

Reconfigurable electronics based on metal-insulator transition: steep-slope switches and high frequency functions enabled by Vanadium Dioxide

THÈSE N° 6949 (2016)

PRÉSENTÉE LE 19 FÉVRIER 2016

À LA FACULTÉ DES SCIENCES ET TECHNIQUES DE L'INGÉNIEUR
LABORATOIRE DES DISPOSITIFS NANOÉLECTRONIQUES
PROGRAMME DOCTORAL EN MICROSYSTÈMES ET MICROÉLECTRONIQUE

ÉCOLE POLYTECHNIQUE FÉDÉRALE DE LAUSANNE

POUR L'OBTENTION DU GRADE DE DOCTEUR ÈS SCIENCES

PAR

Wolfgang Amadeus VITALE

acceptée sur proposition du jury:

Dr G. Boero, président du jury
Prof. M. A. Ionescu, Prof. C. Dehollain, directeurs de thèse
Prof. S. Datta, rapporteur
Prof. S. Ramanathan, rapporteur
Prof. A. Skrivervik, rapporteuse



ÉCOLE POLYTECHNIQUE
FÉDÉRALE DE LAUSANNE

Suisse
2016

To my family.

Acknowledgements

As I began typing these very words, I started realizing I am about to reach the end of the amazing journey that has been this PhD, filled of memorable experiences that helped me learn more about science, about life, about myself, in a way that would have not been possible otherwise. I would like to acknowledge first of all Prof. Adrian Ionescu for giving me this opportunity, and for the freedom I had throughout my PhD. It was a great pleasure and a honor to work with him and earn his trust.

I am very grateful to my thesis co-advisor, Prof. Catherine Dehollain, always willing to encourage me when things seemingly did not work as expected. I would like to acknowledge the members of the jury for the valuable feedback on my work and their time to examine it: Prof. Shriram Ramanathan from Purdue University (USA), Prof. Suman Datta from University of Notre Dame (USA), Prof. Anja Skrivervik from EPFL and Dr. Giovanni Boero, president of the jury, from EPFL.

During my PhD I had the pleasure to work with many brilliant researchers, who helped me greatly in my projects and from whom I always had a lot to learn.

First of all, I will always be grateful to Clara Moldovan and Michele Tamagnone, some of the best memories of this PhD came from having the chance to work with them.

Special thanks to Dr. Montserrat Fernández-Bolaños, she was extremely supportive helping me in my first steps as a researcher, and I considered her a role model at the beginning of this journey.

This work would not have been possible without the support of Dr. Andreas Schüler and Dr. Antonio Paone from LESO-PB at EPFL, who believed in my projects on vanadium dioxide and let me use the sputtering chamber in their laboratory. All my gratitude to Prof. Juan Mosig for the collaborations with LEMA and the use of their equipment and simulation tools. I consider myself lucky for having been part of the Nanolab at EPFL. It has been a nice, supporting environment, and for this reason I would like to thank all the current and previous members met throughout all these years. I am particularly grateful to my friends Arnab, Emanuele and Mariazel. I could always count on you, it wouldn't have been the same without you guys.

Acknowledgements

Special thanks to Clara, she was an amazing friend, co-worker and office mate during all these years. She was always there for me to share my dreams, fears, excitements throughout the PhD, and I will always cherish the good times spent together.

Finally, I would like to thank my family, Rosario, Lucia, Igor and Dimitri for their everlasting support. I love you.

Lausanne, December 2015

Wolfgang

Abstract

The vast majority of disruptive innovations in science and technology has been originated from the discovery of a new material or the way its properties have been exploited to create novel devices and systems. New advanced nanomaterials will have a lasting impact over the next decades, providing breakthroughs in all scientific domains addressing the main challenges faced by the world today, including energy efficiency, sustainability, climate and health.

The electronics industry relied over the last decades on the miniaturization process based on the scaling laws of complementary metal-oxide semiconductors (CMOS). As this process is approaching fundamental limitations, new materials or physical principles must be exploited to replace or supplement CMOS technology. The aim of the work in this thesis is to propose the abrupt metal-insulator transition in functional oxides as a physical phenomenon enabling new classes of Beyond CMOS devices. In order to provide an experimental validation of the proposed designs, vanadium dioxide (VO_2) has been selected among functional oxides exhibiting a metal-insulator transition, due to the possibility to operate at room temperature and the high contrast between the electrical properties of its two structural phases.

A CMOS-compatible sputtering process for uniform large scale deposition of stoichiometric polycrystalline VO_2 has been optimized, enabling high yield and low variability for the devices presented in the rest of the thesis. The high quality of the film has been confirmed by several electrical and structural characterization techniques, including atomic force microscopy (AFM), Kelvin probe force microscopy (KPFM) and X-ray diffraction (XRD).

The first class of devices based on the MIT in VO_2 presented in this work is the steep-slope electronic switch. A quantitative study of the slope of the electrically induced MIT (E-MIT) in 2-terminal VO_2 switches is reported, including its dependence on temperature. Moreover, the switches present excellent ON-state conduction independently of temperature, suggesting MIT VO_2 switches as promising candidates for steep-slope, highly conductive, temperature stable electronic switches. A novel design

Abstract

for the shape of the electrodes used in VO₂ switches has been proposed, targeting a reduction in the actuation voltage necessary to induce the E-MIT. The electrothermal simulations addressing this effect have been validated by measurements.

The potential of the MIT in VO₂ for reconfigurable electronics in the microwave frequency range has been expressed by the design, fabrication and characterization of low-loss, highly reliable, broadband VO₂ radio-frequency (RF) switches, novel VO₂ tunable capacitors and RF tunable filters. The newly proposed tunable capacitors overcome the frequency limitations of conventional VO₂ RF switches, enabling filters working at a higher frequency range than the current state-of-the-art. An alternative actuation method for the tunable capacitors has been proposed by integrating microheaters for local heating of the VO₂ region, and the design tradeoffs have been discussed by coupled electrothermal and electromagnetic simulations.

The last device presented in this work operates in the terahertz (THz) range; the MIT in VO₂ has been exploited to demonstrate for the first time the operation of a modulated scatterer (MST) working at THz frequencies. The proposed MST is the first THz device whose working principle is based on the actuation of a single VO₂ junction, in contrast to commonly employed VO₂ metasurfaces.

Key words: Complementary metal-oxide-semiconductor (CMOS), metal-insulator transition (MIT), functional oxides, Beyond CMOS, vanadium dioxide (VO₂), sputtering, electrical characterization, atomic force microscopy (AFM), Kelvin probe force microscopy (KPFM), X-ray diffraction (XRD), steep slope, temperature dependence, electrothermal simulations, electromagnetic simulations, reconfigurable electronics, microwaves, radio-frequency (RF), RF switches, tunable capacitors, tunable filters, terahertz, modulated scatterer (MST).

Sommario

La stragrande maggioranza delle innovazioni rivoluzionarie in scienza e tecnologia ha avuto come origine la scoperta di nuovi materiali o un diverso uso delle loro proprietà per realizzare nuovi dispositivi e sistemi. Si prevede che nuovi nanomateriali avanzati avranno un impatto a lungo termine nei prossimi decenni, portando a innovazioni in tutti i domini scientifici rivolti allo sviluppo di strategie sostenibili per le maggiori problematiche del mondo attuale.

Negli ultimi decenni il progresso dell'industria elettronica si è basato su processi di miniaturizzazione ben definiti per la tecnologia *complementary metal-oxide semiconductor* (CMOS). Dato che questo processo è in corso di raggiungere i suoi limiti fondamentali, si pone il problema di individuare nuovi materiali o principi fisici per sostituire o supportare la tecnologia CMOS. L'obiettivo di questa tesi consiste nel proporre la transizione metallo-isolante osservata in alcuni ossidi funzionali come un fenomeno fisico in grado di dare origine a una nuova classe di dispositivi *Beyond CMOS*. Per convalidare sperimentalmente i progetti proposti, il diossido di vanadio (VO_2) è stato selezionato tra i vari ossidi funzionali che presentino una transizione metallo-isolante, poiché permette di lavorare a temperatura ambiente ed è caratterizzato da un forte contrasto in proprietà elettriche per le sue due fasi.

Un processo di polverizzazione catodica compatibile con la tecnologia CMOS è stato ottimizzato per produrre una deposizione uniforme a larga scala di VO_2 policristallino stoichiometrico. Questo processo ha permesso di realizzare dispositivi ad alta affidabilità e bassa variabilità, presentati nel seguito della tesi. L'alta qualità del film sottile depositato in questo modo è stata confermata da diverse tecniche di caratterizzazione elettrica e strutturale, tra cui la microscopia a forza atomica, la microscopia a forza di sonda Kelvin e la cristallografia a raggi X.

Il primo dispositivo basato sulla transizione metallo-isolante presentato in questa tesi è l'interruttore elettronico ad alta pendenza a 2 terminali. Il dispositivo è stato caratterizzato con particolare cura per la dipendenza dalla temperatura della pendenza della transizione originata da un segnale elettrico. Inoltre, gli interruttori presentano alta

Sommario

conducibilità una volta attivati, indipendentemente dalla temperatura, suggerendo che questi dispositivi possano essere dei candidati molto promettenti per realizzare interruttori ad alta pendenza, alta conduttività e stabili con la temperatura. Una nuova forma degli elettrodi per questi interruttori basati sul VO₂ è stata proposta per ridurre la tensione di attuazione necessaria per originare la transizione metallo-isolante. Le simulazioni elettrotermiche riguardanti questo effetto sono state confermate da misure elettriche.

Il potenziale della transizione metallo-isolante nel VO₂ per il campo dell'elettronica riconfigurabile a microonde è stato espresso progettando, fabbricando e caratterizzando interruttori a radiofrequenza con basse perdite, condensatori riconfigurabili innovativi e filtri a microonde riconfigurabili. I condensatori riconfigurabili basati sul VO₂, proposti per la prima volta in questo lavoro, permettono di superare i limiti in frequenza degli interruttori a radiofrequenza in VO₂, permettendo di progettare filtri in una banda di frequenze più alta dello stato dell'arte attuale. Successivamente è stato proposto un metodo di attuazione alternativo per i condensatori riconfigurabili, basato su microradiatori integrati per scaldare localmente le regioni di VO₂, e le caratteristiche di progetto sono state discusse tramite simulazioni elettrotermiche ed elettromagnetiche.

L'ultimo dispositivo presentato in questo lavoro opera a frequenze terahertz; la transizione metallo-isolante è stata usata per dimostrare per la prima volta un modulated scatterer a frequenze terahertz. Questo modulated scatterer è il primo dispositivo a frequenze terahertz il cui principio di funzionamento si basa su una singola giunzione in VO₂.

Parole chiave: *Complementary metal-oxide-semiconductor* (CMOS), transizione metallo-isolante, ossidi funzionali, *Beyond CMOS*, diossido di vanadio (VO₂), polverizzazione catodica, caratterizzazione elettrica, microscopia a forza atomica, microscopia a forza di sonda Kelvin, cristallografia a raggi X, alta pendenza, dipendenza dalla temperatura, simulazioni elettrotermiche, simulazioni elettromagnetiche, elettronica riconfigurabile, microonde, radiofrequenza, interruttori a radiofrequenza, condensatori riconfigurabili, filtri riconfigurabili, terahertz, modulated scatterer (MST).

List of Publications

This thesis is based on work published in the following papers.

1. W. A. Vitale †, M. Tamagnone †, N. Émond, B. Le Drogoff, S. C. Capdevila, A. Skrivervik, M. Chaker, J. R. Mosig, and A. M. Ionescu, “Terahertz modulated scatterer technique enabled by current actuated vanadium dioxide switches,” *Applied Physics Letters*, under review, 2016, † equal contributions.
2. W. A. Vitale, L. Petit, C. F. Moldovan, M. Fernández-Bolaños, A. Paone, A. Schüler, and A. M. Ionescu, “Electrothermal actuation of vanadium dioxide for tunable capacitors and microwave filters with integrated microheaters,” *Sensors and Actuators A: Physical*, Jan. 2016.
3. W. A. Vitale, C. F. Moldovan, M. Tamagnone, A. Paone, A. Schuler, and A. M. Ionescu, “Steep-Slope Metal–Insulator–Transition VO₂ Switches With Temperature-Stable High I_{ON} ,” *IEEE Electron Device Letters*, vol. 36, no. 9, pp. 972–974, Sep. 2015.
4. W. A. Vitale, C. F. Moldovan, A. Paone, A. Schüler, and A. M. Ionescu, “Fabrication of CMOS-compatible abrupt electronic switches based on vanadium dioxide,” *Microelectronic Engineering*, vol. 145, pp. 117–119, Sep. 2015.
5. W. A. Vitale, M. Fernandez-Bolanos, C. F. Moldovan, A. Paone, A. Schüler, and A. M. Ionescu, “Tunable capacitors and microwave filters based on vanadium dioxide metal-insulator transition,” oral presentation in 18th International Conference on Solid-State Sensors, Actuators and Microsystems (TRANSDUCERS), pp. 311–314, 2015.
6. W. A. Vitale, A. Paone, C. F. Moldovan, A. Schuler, and A. M. Ionescu, “Growth optimization of vanadium dioxide films on SiO₂/Si substrates,” oral presentation in 40th Micro and Nano Engineering, 2014.

List of Publications

7. W. A. Vitale, A. Paone, M. Fernandez-Bolanos, A. Bazigos, W. Grabinski, A. Schuler, and A. M. Ionescu, “Steep slope VO₂ switches for wide-band (DC-40 GHz) reconfigurable electronics,” oral presentation in 72nd Device Research Conference, pp. 29–30, 2014.

A full list of publications is provided at the end of the thesis.

Contents

Acknowledgements	i
Abstract	iii
List of figures	xiii
List of tables	xxiii
List of symbols	xxv
List of units	xxix
Acronyms and Abbreviations	xxxi
Elements and Materials	xxxv
1 Introduction	1
1.1 Beyond CMOS: functional oxides for reconfigurable electronics	3
1.1.1 Adaptive oxide electronics	3
1.1.2 Resistive switching materials	4
1.1.3 Functional oxides exhibiting a metal-insulator transition	5
1.2 Vanadium Dioxide for reconfigurable electronics	6
1.3 Structure of the thesis	8
2 CMOS-compatible VO₂ sputtering and device integration	11
2.1 Introduction on VO ₂ thin film deposition methods	11
2.1.1 Influence of the substrate on VO ₂ deposition	13
2.1.2 VO ₂ deposition techniques	14
2.2 VO ₂ sputtering on Si/SiO ₂ substrates	15
2.2.1 Deposition and process parameters	15
2.2.2 VO ₂ thin film characterization	17

Contents

2.3	CMOS-compatible electronic switches	24
2.3.1	Fabrication	25
2.3.2	Current actuation of VO ₂ switches	25
2.4	Summary	30
3	VO₂ MIT for steep-slope electronic switches	33
3.1	Introduction on VO ₂ electronic switches	33
3.1.1	E-MIT characterization	33
3.1.2	Applications	37
3.1.3	VO ₂ for steep-slope switches	39
3.2	Abrupt switching in voltage-actuated VO ₂ switches	42
3.3	Steep slope characterization	46
3.4	Low voltage VO ₂ switches	50
3.4.1	Device concept	51
3.4.2	Electrothermal simulations	53
3.4.3	Fabrication	64
3.4.4	Electrical characterization	66
3.4.5	Measurements at cryogenic temperatures	69
3.5	Summary	71
4	VO₂ MIT for reconfigurable RF functions	75
4.1	Introduction	75
4.1.1	Figures of merit for RF tunable devices	77
4.1.2	High frequency tuning elements	78
4.1.3	VO ₂ for reconfigurable RF electronics	84
4.2	VO ₂ wide-band RF switches	88
4.2.1	Fabrication	89
4.2.2	DC actuation	90
4.2.3	RF characterization	91
4.2.4	Reliability	96
4.2.5	Optimization	98
4.3	Tunable capacitors and microwave filters	100
4.3.1	VO ₂ tunable capacitors	100
4.3.2	VO ₂ microwave tunable filters	102
4.3.3	Switchable bandstop filters	107
4.3.4	Electrothermal actuation with integrated microheaters	108
4.4	Summary	115

5	VO₂ MIT for reconfigurable THz functions	119
5.1	Introduction	119
5.1.1	Terahertz characterization of VO ₂	120
5.1.2	VO ₂ devices and applications in the THz range	122
5.2	VO ₂ modulated scatterer for THz applications	123
5.2.1	Introduction: applications and theory	124
5.2.2	Design and simulations	126
5.2.3	Fabrication	138
5.2.4	Measurements	139
5.3	Conclusion	144
 6	 Conclusions and perspectives	 145
6.1	Conclusions	145
6.2	Future work	148
6.3	Perspectives	150
Bibliography		178
List of Publications		179
Curriculum Vitae		183

List of Figures

1.1	Moore's law, showing the exponential increase of the transistor count in microprocessors from different semiconductor chip makers.	2
1.2	Dependence on temperature of VO ₂ resistivity, crystal structure and electrical band diagram.	7
2.1	Phase diagram of the vanadium-oxygen system. Adapted from [40]. . .	12
2.2	Resistivity ratio obtained by T-MIT in VO ₂ and V _n O _{2n-1} phases [41]. . .	12
2.3	UHV Sputtering chamber at LESO-PB, EPFL.	16
2.4	4-point probes measurement setup.	18
2.5	VO ₂ electrical resistivity dependence on temperature for non-optimal O ₂ flows.	19
2.6	VO ₂ electrical resistivity dependence on temperature in the optimized case, showing a reconfigurability higher than 3 decades and a steep transition at ~ 68°C. Inset: d(-log ρ)/dT curves while heating and cooling the VO ₂ film, showing a narrow hysteresis of ~ 7°C.	19
2.7	SEM image of the sputtered VO ₂ thin film, showing an average grain size larger than 100 nm.	20
2.8	XRD spectrum showing the preferential orientations of the deposited polycrystalline VO ₂ film.	21
2.9	Schematic diagram of an atomic force microscope.	22
2.10	Measurement setup and working principle of a Kelvin Probe Force Microscope, illustrating three possible configurations for the tip-sample interaction and the corresponding band diagrams. a) Tip not in contact, applied V _{AC} . b) Tip in contact, applied V _{AC} . c) Tip in contact, applied V _{AC} + V _{DC}	24
2.11	(a) Topography of the film obtained by AFM, showing an average surface roughness of 11 nm. (b) Surface contact potential difference measured by KPFM, used to estimate the VO ₂ work function as ~ 5.125 eV.	24

List of Figures

2.12	Main steps of the fabrication process for VO ₂ planar electronic switches. (a) LPCVD of 400 nm SiO ₂ on Si substrate. (b) Sputtering deposition of 360 nm VO ₂ . (c) Patterning of VO ₂ by optical lithography and ion beam etching. (d) 20/300 nm Cr/Al evaporation patterned by lift-off.	26
2.13	(a) SEM image of one of the VO ₂ planar switches used to characterize the E-MIT. The width of the VO ₂ junction is 100 μm, the length is 7.5 μm. (b) FIB cross-section view of the device, showing the thickness of the VO ₂ layer obtained after 2 h of RF magnetron sputtering deposition as described in section 2.2.1; platinum layer on top used for FIB preparation.	26
2.14	Electrical characterization of the E-MIT by current actuation in a VO ₂ switch	27
2.15	Effect of the VO ₂ switch geometry on the IV characteristics the resistance in the off-state.	28
2.16	Effect of the VO ₂ switch geometry on the resistance in the off-state. Dashed lines: measurements; solid lines: model.	28
2.17	Increase in resistance ratio and width of the actuated region achievable by E-MIT, by increasing the DC current bias I_{DC} . The optical micrographs show the increase in actuated area with increasing current: the darker regions correspond to VO ₂ transitioned to the metallic state. $W = 90\mu\text{m}, L = 7.5\mu\text{m}$	29
2.18	IV characteristics for a VO ₂ switch ($W = 90\mu\text{m}, L = 7.5\mu\text{m}$) actuated by current bias up to 100 mA.	29
3.1	Device cross sections and energy band diagrams corresponding to OFF and ON state in three major classes of switches: (a) MOSFET, (b) Tunnel FET and (c) VO ₂ MIT switch.	41
3.2	Qualitative comparison of the MOSFET, TFET and VO ₂ switch in terms of subthreshold swing abruptness.	41
3.3	Top-view of a fabricated VO ₂ two-terminal switch ($W = 50\mu\text{m}, L = 7.5\mu\text{m}$).	43
3.4	Biasing scheme used for the E-MIT with a resistor in series, in the (a) current actuation and (b) voltage actuation case.	43
3.5	Dependence of intrinsic switch resistance $R_{VO_2} = V_{int}/I$ on the intrinsic power P_{int} dissipated in the VO ₂ switch ($W = 50\mu\text{m}, L = 7.5\mu\text{m}$) by applying a DC voltage or current source at room temperature. (A) Power threshold for metal-insulator transition. (A-A'): E-MIT by voltage actuation. (A-A''): E-MIT by current actuation.	44

3.6	Dependence of the intrinsic switch resistance $R_{VO_2} = V_{int}/I$ on the intrinsic power P_{int} dissipated in the VO ₂ switch by applying a DC voltage source at different temperatures, from 25 °C to 55 °C.	45
3.7	Mean value and standard deviation of the switching power depending on temperature, for the transition increasing V_{DC} (insulator to metal, corresponding to P_{act}) and decreasing V_{DC} (back to the insulating state).	45
3.8	Abrupt switching based on VO ₂ E-MIT, shown by IV curves at different temperatures for the VO ₂ switch with a resistor in series.	46
3.9	Current dependence on the intrinsic voltage drop on the VO ₂ switch at different temperatures, with iso-power curves showing the power dissipation spike in correspondence of the E-MIT.	47
3.10	Dependence of intrinsic switch resistance $R_{VO_2} = V_{int}/I$ on the intrinsic voltage V_{int}	47
3.11	High-resolution IV curves (1 mV incremental steps) for voltages around the E-MIT, at temperatures near the thermal transition. The full hysteresis cycle is not shown due to the limited maximum number of points allowed by the measurement setup.	48
3.12	Dependence on temperature of the slope and the actuation voltage of the VO ₂ abrupt switch.	49
3.13	Dependence on temperature of the current in the ON state and the actuation current.	50
3.14	a) Schematic diagram of the proposed low-voltage VO ₂ switch. The metal spikes (length L_s , width W_s) allow increasing locally the magnitude of the electric field. b) Flat-junction VO ₂ switch employed for performance comparison, having the same length L and width W of the device with spikes.	52
3.15	a) Full geometry domain for the electrothermal simulations used to estimate the efficiency of the increased electric field in correspondence of the metal spikes to actuate the VO ₂ switch at a lower voltage as compared to conventional flat VO ₂ junctions with the same length, assuming an electrothermal actuation model based purely on Joule heating. Grid labels in μm . b) Dense mesh profile in correspondence of the spikes location. The mesh minimum element size has been fixed to 4 nm, for spikes with width $W_s = 40\text{ nm}$ and length $L_s = 400\text{ nm}$	54
3.16	Electric field on the top surface of a VO ₂ switch with flat electrodes for an applied voltage $V_{DC} = 7\text{ V}$, with zoom on the VO ₂ region.	56

List of Figures

3.17 a) Electric field profile for different voltage levels along the length of the switch, from the interface with one metal electrode ($x = 0\mu\text{m}$) to the other ($x = 1\mu\text{m}$), on top of the VO_2 surface and in the middle of the junction ($y = 10\mu\text{m}$). The curves pre-actuation correspond to voltage steps of 0.5V. b) Temperature profile along the length of the switch. c) Dependence of the maximum VO_2 temperature in function of the applied voltage, for $V_{\text{DC}} < V_{\text{act}}$. d) IV characteristics, obtained applying a limiting series resistor $R_s = 50\ \Omega$	57
3.18 a) Electric field on the top surface of a VO_2 switch with electrodes employing spikes to increase locally the electric field; applied voltage $V_{\text{DC}} = 7\text{V}$; spike aspect ratio $\text{AR} = 2$. b) Zoom on the spike, showing an increase in electric field with the spike aspect ratio.	58
3.19 Simulation results and linear interpolation of the field increase factor (ratio between the maximum electric field in junctions with spikes and the one in flat junctions) in function of the spike aspect ratio.	59
3.20 Electric field profile for $V_{\text{DC}} = 7\text{V}$ along the length of the switch in the middle of its width, comparing flat junctions and junctions with spikes with different aspect ratios. Inset: zoom on the first 50 nm away from the junction.	59
3.21 Electric field profile for $V_{\text{DC}} = 7\text{V}$ along the length of the switch, 500 nm away from the middle of its width, comparing flat junctions and junctions with spikes with different aspect ratios. The shaded regions correspond to the additional length with respect to the flat junctions due to the insertion of the spikes on both sides ($L_S = 400\text{ nm}$).	60
3.22 Temperature profile for $V_{\text{DC}} = 7\text{V}$ along the length of the switch in the middle of its width, comparing a flat junction and a junction with a spike with $\text{AR} = 10$. The high field induced at the spike is effective only near the interface with VO_2	60
3.23 a) Electric field profile for different voltage levels along the length of a switch with spikes ($\text{AR} = 10$), from the tip of a spike ($x = 0\mu\text{m}$) to the other ($x = 1\mu\text{m}$), on top of the VO_2 surface and in the middle of the junction ($y = 10\mu\text{m}$). The curves pre-actuation correspond to voltage steps of 0.5V. b) Temperature profile along the length of the switch. c) Dependence of the maximum VO_2 temperature in function of the applied voltage, for $V_{\text{DC}} < V_{\text{act}}$. d) IV characteristics, obtained applying a limiting series resistor $R_s = 50\ \Omega$	61

3.24 a) Electric field on the top surface of a VO ₂ switch with electrodes employing spikes along the whole width of the junction; applied voltage $V_{DC} = 6.5V$; spike aspect ratio $AR = 10$	62
3.25 a) Electric field profile for different voltage levels along the length of a switch with spikes ($AR = 10$) along the whole width of the junction, from the tip of a spike ($x = 0\mu m$) to the other ($x = 1\mu m$), on top of the VO ₂ surface and in the middle of the junction ($y = 10\mu m$). The curves pre-actuation correspond to voltage steps of 0.5 V. b) Temperature profile along the length of the switch. c) Dependence of the maximum VO ₂ temperature in function of the applied voltage, for $V_{DC} < V_{act}$. d) IV characteristics, obtained applying a limiting series resistor $R_S = 50\Omega$	63
3.26 Process flow for the VO ₂ switches with spikes fabricated at INRS. a) Substrate preparation. b) VO ₂ PLD deposition, performed for more thicknesses, from 100 nm to 500 nm. c) Patterning of 100 nm thick Cr/Cu/Au electrodes by e-beam lithography and lift-off.	65
3.27 a-b) SEM images of the 500 nm thick VO ₂ film deposited by PLD on sapphire. c-d) SEM images of the 100 nm thick VO ₂ film deposited by PLD on a Si/SiO ₂ substrate.	66
3.28 a) Top-view of a fabricated VO ₂ two-terminal switch ($W = 50\mu m$, $L = 7.5\mu m$). b) Zoom on the spikes, showing extremely sharp profiles.	66
3.29 VO ₂ electrical resistivity dependence on temperature, showing a reconfigurability higher than 3 decades and a steep transition at $\sim 73^\circ C$. Inset: $d(-\log \rho)/dT$ curves while heating and cooling the VO ₂ film, showing a narrow hysteresis of $\sim 7^\circ C$	67
3.30 Histogram representation and gaussian fitting of the distribution of the actuation voltage for VO ₂ switches ($W = 20\mu m$, $L = 10\mu m$) employing flat junctions or junctions with spikes ($W_S = 200\text{ nm}$, $L_S = 800\text{ nm}$). Bin size: 2 V.	68
3.31 Comparison of IV characteristics for devices with or without spikes ($W_S = 200\text{ nm}$, $L_S = 800\text{ nm}$) along the junctions, keeping constant the width $W = 20\mu m$ and the length L . a) $L = 10\mu m$. b) $L = 2\mu m$	68
3.32 Dependence on temperature of the OFF-state resistance for devices with or without spikes ($W_S = 200\text{ nm}$, $L_S = 800\text{ nm}$) along the junctions, keeping constant the width $W = 20\mu m$ and the length $L = 10\mu m$. Inset: ratio between the OFF-state resistance of devices with flat junctions and the one of devices with junctions with spikes.	70

List of Figures

3.33 Full actuation cycle measured at 77 K for a VO ₂ switch with spikes ($W = 20\mu\text{m}$, $L = 2\mu\text{m}$, $W_S = 200\text{ nm}$, $L_S = 800\text{ nm}$), showing E-MIT at ultra-low power.	71
4.1 Characteristics, cross-sections, equivalent circuits in ON and OFF states and symbols for a) PIN diodes, b) FET RF switches and c) capacitive RF MEMS.	79
4.2 Schematic diagram of a VO ₂ RF switch in series configuration on a CPW.	89
4.3 Main steps of the fabrication process for VO ₂ planar RF switches. (a) LPCVD of 300 nm a-Si and 500 nm SiO ₂ on HR-Si substrate. (b) Sputtering deposition of 360 nm VO ₂ . (c) Patterning of VO ₂ by optical lithography and ion beam etching. (d) 20/300 nm Cr/Al evaporation patterned by lift-off.	89
4.4 SEM top view of a VO ₂ RF switch ($W = 80\mu\text{m}$, $L = 7.5\mu\text{m}$).	90
4.5 I - V characteristics and extracted resistance in insulating and conductive states for 8 instances of a voltage-actuated VO ₂ RF switch ($W = 80\mu\text{m}$, $L = 7.5\mu\text{m}$) with $R_s = 220\Omega$ in series in order to limit the I_{ON} current.	91
4.6 Current I_{act} and voltage V_{act} triggering the E-MIT for different device geometries (standard deviation on 6 devices for each configuration). a) Dependence of V_{act} on W . b) Dependence of V_{act} on L . c) Dependence of I_{act} on L . d) Dependence of I_{act} on W	92
4.7 Dependence of insertion loss on DC current for a $W = 80\mu\text{m}$, $L = 7.5\mu\text{m}$ VO ₂ RF switch.	93
4.8 Dependence of insertion loss and return loss at 40 GHz on DC current for a $W = 80\mu\text{m}$, $L = 7.5\mu\text{m}$ VO ₂ RF switch.	93
4.9 a) S -parameter for VO ₂ RF switches with fixed $W = 100\mu\text{m}$ and variable L (from $7.5\mu\text{m}$ to $17.5\mu\text{m}$). Solid lines: measurements; dotted lines: model. b) Equivalent lumped circuit.	94
4.10 Insertion loss and isolation at 40 GHz for all devices configurations.	95
4.11 Dependence of insertion loss on device width (W varying from $40\mu\text{m}$ to $90\mu\text{m}$, $L = 7.5\mu\text{m}$) using T-MIT or E-MIT.	96
4.12 Variability for 32 instances of the $W = 100\mu\text{m}$, $L = 12.5\mu\text{m}$ switch.	96
4.13 Reliability dependence on rise time of the applied voltage.	97
4.14 Lifetime dependence on current density and duty cycle.	97
4.15 Insertion loss and isolation for RF switches with variable length, using pure VO ₂ ($\rho_{\text{ON}} = 1.5 \times 10^{-3}\Omega\text{ cm}$, $\rho_{\text{OFF}} = 5\Omega\text{ cm}$ or W -doped VO ₂ ($\rho_{\text{ON}} = 5.26 \times 10^{-4}\Omega\text{ cm}$, $\rho_{\text{OFF}} = 5 \times 10^{-1}\Omega\text{ cm}$).	99

4.16 Improvement in contrast between isolation and insertion loss at 42 GHz using W-doped VO ₂ ($\rho_{\text{ON}} = 5.26 \times 10^{-4} \Omega \text{ cm}$, $\rho_{\text{OFF}} = 5 \times 10^{-1} \Omega \text{ cm}$) as compared to pure VO ₂ ($\rho_{\text{ON}} = 1.5 \times 10^{-3} \Omega \text{ cm}$, $\rho_{\text{OFF}} = 5 \Omega \text{ cm}$).	99
4.17 a) Schematic diagram of a VO ₂ tunable capacitor loaded on a CPW in series configuration. The capacitive gap between the signal lines can be tuned from g_{OFF} (VO ₂ in insulating state) to g_{ON} (VO ₂ in conducting state). b) Effects of thermal actuation on the resistivity and series capacitance. The resistivity transition occurs in the shaded area, outside of which a low and high capacitance states are well defined. c) Equivalent lumped circuit.	101
4.18 SEM top view of a VO ₂ tunable capacitor ($w = 100 \mu\text{m}$, $g_{\text{OFF}} = 60 \mu\text{m}$, $g_{\text{ON}} = 20 \mu\text{m}$) loaded in series configuration on a CPW, with zoom on the active area.	101
4.19 S_{21} -parameter measurements of a VO ₂ tunable capacitor ($w = 100 \mu\text{m}$, $g_{\text{OFF}} = 60 \mu\text{m}$, $g_{\text{ON}} = 10 \mu\text{m}$) matched to the equivalent lumped circuit shown in Figure 4.17 (b). OFF state: RT. ON state: $T = 80^\circ\text{C}$	102
4.20 a) Schematic diagram of the VO ₂ tunable bandstop resonator; b) SEM top-view of the fabricated device, with dimensions $a = 700 \mu\text{m}$, $w = 200 \mu\text{m}$, $g_{\text{OFF}} = 60 \mu\text{m}$, $g_{\text{ON}} = 10 \mu\text{m}$, false-colored to highlight the VO ₂ and SiO ₂ regions; (c) equivalent lumped circuit.	104
4.21 S-parameter measurements for the fabricated bandstop resonator. . .	105
4.22 Increase in tunability with the $g_{\text{OFF}}/g_{\text{ON}}$ ratio.	105
4.23 Comparison between simulations of a VO ₂ tunable filter ($a = 450 \mu\text{m}$, $w = 200 \mu\text{m}$, $g_{\text{OFF}} = 60 \mu\text{m}$, $g_{\text{ON}} = 10 \mu\text{m}$) and the corresponding "ideal" fixed filters. In the ideal filters VO ₂ is replaced by air in the OFF state, metal in the ON state. Inset: percentage of change of the quality factor and of the resonance frequency with respect to the ideal performance, in function of the $g_{\text{OFF}}/g_{\text{ON}}$ ratio.	106
4.24 Schematic diagram of the VO ₂ switchable bandstop resonator.	107
4.25 Comparison between measurements and simulations for a VO ₂ switchable bandstop filter ($a = 700 \mu\text{m}$, $w = 200 \mu\text{m}$, $g_{\text{OFF}} = 60 \mu\text{m}$). The simulations have been performed both for the VO ₂ filter and the corresponding ideal fixed-frequency filters.	108

List of Figures

- 4.26 Main steps of the proposed fabrication process for VO₂ RF tunable devices with integrated microheaters. (a) LPCVD of 300 nm a-Si and 3 μm SiO₂ on HR-Si substrate. (b) 50 nm NiCr deposition. (c) Deposition and planarization of a thin SiO₂ layer with thickness t_{ins} , used as a variable parameter in the simulations. The first three steps can be considered as preliminary steps to prepare the substrate to proceed with the process flow used for the fabricated RF devices and presented in Figure 4.3, corresponding to the following steps (d-e-f). 109
- 4.27 Simulation domain for the electrothermal calculations to estimate the power needed to induce the metal-insulator transition in a VO₂ region (width w , length l) contacting an Al electrical contact. The power is provided by applying a DC voltage difference to the two highlighted terminals of a NiCr microheater, electrically insulated to VO₂ by a SiO₂ layer. The structure corresponds to one half of the VO₂ tunable capacitor. Grid labels in μm. 110
- 4.28 Distribution of the electrothermally actuated VO₂ region ($w = 100\mu\text{m}$, $l = 25\mu\text{m}$) in function of the power dissipated in the microheater (from 75 mW to 150 mW), represented by 3D isothermal contours starting from $T = T_{\text{MIT}} = 340\text{K}$ and equidistant slice plots along the VO₂ thickness. . . 111
- 4.29 Temperature profile on the top VO₂ surface along its length, from the contact with the metal electrode ($x = 0\mu\text{m}$) to the end ($x = l = 25\mu\text{m}$), simulated at different levels of dissipated power (from 50 mW to 200 mW).112
- 4.30 Temperature profile on the top VO₂ surface along its length, from the contact with the metal electrode ($x = 0\mu\text{m}$) to the end ($x = l = 25\mu\text{m}$), simulated for different oxide thicknesses (from 200 nm to 2 μm, with 100 nm steps). Inset: dependence of actuation power on oxide thickness.112
- 4.31 Dependence of the actuation power density on the aspect ratio of the VO₂ region ($w = 50\mu\text{m}$, l increasing from 11.5 μm to 91 μm). Oxide thickness $t_{\text{ins}} = 150\text{nm}$. Microheater line width 3 μm, spacing 1 μm. . . 113
- 4.32 Electromagnetic simulation domain for an electrothermally actuated VO₂ microwave filter with dimensions $a = 900\mu\text{m}$, $w = 50\mu\text{m}$, $g_{\text{OFF}} = 200\mu\text{m}$, $g_{\text{ON}} = 2\mu\text{m}$. The 50 nm thick NiCr microheater has a serpentine geometry with line width 3 μm and spacing 1 μm. 114

4.33 Comparison between simulations of a VO ₂ tunable filter with integrated microheaters ($a = 900\mu\text{m}$, $w = 50\mu\text{m}$, $g_{\text{OFF}} = 200\mu\text{m}$, $g_{\text{ON}} = 2\mu\text{m}$) and the corresponding "ideal" fixed filters. In the ideal filters VO ₂ is replaced by air in the OFF state, metal in the ON state. Inset: decrease in quality factor and shift in resonance frequency with respect to ideal performance.	114
5.1 General schematic diagram of a THz-TDS setup.	121
5.2 General scenario of an RFID system where the transmitter and receiver antennas of the RFID reader communicate with a MST probe.	125
5.3 Polar plot of $\Gamma_{\text{ON}}^{\text{K}}$ and $\Gamma_{\text{OFF}}^{\text{K}}$ in the ideal case for maximum P_{mod} : the amplitude of the reflection coefficients is 1 and their difference in phase is 180°.	127
5.4 Schematic diagram of the proposed VO ₂ THz MST.	127
5.5 a) Full geometry domain for the electromagnetic simulations performed to optimize the impedance of the bowtie antenna. b) Zoom on the switchable VO ₂ region.	129
5.6 Dependence of the real part of the antenna impedance on the width of the bowtie antenna. The optimized solution for broadband performance ($W_{\text{A}} = 100\mu\text{m}$) is highlighted in green.	130
5.7 Dependence of the imaginary part of the antenna impedance on the width of the bowtie antenna. The optimized solution ($W_{\text{A}} = 100\mu\text{m}$), showing negligible values with respect to the real part, is highlighted in green.	130
5.8 Polar plot of $\Gamma_{\text{ON}}^{\text{K}}$ and $\Gamma_{\text{OFF}}^{\text{K}}$ for selected values of W_{A} , from 20 μm to 100 μm . The minimum of $\Delta\Gamma^{\text{K}}$ is plotted in dashed lines for all values of W_{A} , the maximum only for the optimal value $W_{\text{A}} = 100\mu\text{m}$	131
5.9 Dependence of $\Delta\Gamma^{\text{K}}$ on frequency for all the simulated values of W_{A} . The optimized solution for broadband performance ($W_{\text{A}} = 100\mu\text{m}$) is highlighted in green.	132
5.10 Dependence of the real part of the antenna impedance on the width of the VO ₂ switch.	133
5.11 Dependence of the imaginary part of the antenna impedance on the width of the VO ₂ switch.	133
5.12 Polar plot of $\Gamma_{\text{ON}}^{\text{K}}$ and $\Gamma_{\text{OFF}}^{\text{K}}$ for all the simulated values of W , from 2 μm to 8 μm and keeping constant $L = 2\mu\text{m}$, $W_{\text{A}} = 100\mu\text{m}$ and $L_{\text{A}} = 60\mu\text{m}$. Minimum of $\Delta\Gamma^{\text{K}}$ plotted in dashed lines in the best ($W = 4\mu\text{m}$) and worst ($W = 2\mu\text{m}$) case.	134

List of Figures

5.13	Dependence of $\Delta\Gamma^K$ on frequency for all the simulated values of W . The optimized solution for broadband performance starting from 0.7 THz ($W = 4\mu\text{m}$) is highlighted in red.	135
5.14	Dependence on frequency of the impedance of the large bowtie antenna.	136
5.15	a) Polar plot of Γ_{ON}^K and Γ_{OFF}^K for the optimized large bowtie antenna ($L_A = 300\mu\text{m}$, $W_A = 400\mu\text{m}$, $L = 2\mu\text{m}$, $W = 4\mu\text{m}$). b) Dependence on frequency of $\Delta\Gamma^K$	137
5.16	Polar plot of Γ_{ON}^K and Γ_{OFF}^K for the THz MST on HR-Si for selected values of W , from $4\mu\text{m}$ to $16\mu\text{m}$ and keeping constant $L = 2\mu\text{m}$, $W_A = 100\mu\text{m}$ and $L_A = 60\mu\text{m}$. Minimum of $\Delta\Gamma^K$ plotted in dashed lines in the best ($W = 12\mu\text{m}$) and worst ($W = 4\mu\text{m}$) case.	138
5.17	Dependence of $\Delta\Gamma^K$ on frequency for the THz MST on HR-Si for selected values of W	138
5.18	Top view of the characterized VO_2 THz MST.	139
5.19	Current actuation of the VO_2 switch used as a tunable load for the VO_2 THz MST.	140
5.20	Measurement setup for reflective THz-TDS.	141
5.21	Nominal power spectrum of the THz spectrometer used in this work, measured with a reference mirror.	141
5.22	Differential signal and noise floor for incidence at 45° and reception at -10° from the normal. The measurements have been normalized with respect to the mirror power. The results are obtained averaging 1000 cycles.	142
5.23	a) Noise floor and b) modulated signal imaging at 0.32 THz. The measurements are obtained averaging 100 cycles.	143
5.24	Radiation pattern of the VO_2 THz MST.	143

List of Tables

1.1	List of functional oxides exhibiting a metal-insulator transition.	6
2.1	Optimized process parameters for reactive magnetron sputtering of VO ₂ on Si/SiO ₂ substrates.	17
3.1	Material properties used for the electrothermal simulations.	55
4.1	Comparison of figures of merit for VO ₂ RF switches.	86
4.2	Comparison of figures of merit for VO ₂ RF tunable filters.	88
4.3	Material properties used for the electrothermal simulations.	110
5.1	Substrate properties used for design and electromagnetic simulations.	128
5.2	Dependence on W of the antenna and tunable load impedances.	134
5.3	Impedances of the antenna and tunable load for the MST on HR-Si.	137

List of symbols

Symbol	Units	Description
AR	1	Spike aspect-ratio in a low-voltage VO ₂ switch
a	m	VO ₂ DGS resonator size
a_B	m	Effective Bohr radius
C_d	F	MOSFET depletion capacitance
C_{eq}	F	VO ₂ RF switch parasitic capacitance
C_{ox}	F	MOSFET oxide capacitance
C_p	F	Shunt capacitance of the VO ₂ tunable capacitor
C_s	F	Series capacitance of the VO ₂ tunable capacitor
d	m	Interatomic distance
E_R	Vm ⁻¹	Electric field of the received signal in THz-TDS
E_{ref}	Vm ⁻¹	Electric field of the reference signal in THz-TDS
E_T	Vm ⁻¹	Electric field of the transmitted signal in THz-TDS
e	C	Electron charge
F_ω	N	Electrostatic force monitored in KPFM
f_0	Hz	VO ₂ filter resonance frequency
f_{0-OFF}	Hz	VO ₂ filter resonance frequency in the insulating state
f_{0-ON}	Hz	VO ₂ filter resonance frequency in the conducting state
G_{MT}	1	Gain from the modulated scatterer to the transmitter
G_{MR}	1	Gain from the modulated scatterer to the receiver
G_{RM}	1	Gain from the receiver to the modulated scatterer
G_{TM}	1	Gain from the transmitter to the modulated scatterer
g_{OFF}	m	VO ₂ capacitor gap in the insulating state
g_{ON}	m	VO ₂ capacitor gap in the conducting state

List of symbols

I_{act}	A	Actuation current
I_{d}	A	Drain current
I_{DC}	A	DC current source
I_{ON}	A	VO ₂ switch current in the conducting state
J_{ON}	Am ⁻²	VO ₂ switch current density in the conducting state
L	m	VO ₂ switch length
L_{A}	m	MST bowtie antenna length
L_{S}	m	Spike length in a low-voltage VO ₂ switch
n_{c}	m ⁻³	Critical carrier density for the Mott transition
P_{act}	W	Actuation power
P_{h}	W	Power dissipated using a microheater
P_{hd}	Wm ⁻²	Power density dissipated using a microheater
P_{int}	W	Power dissipated in a VO ₂ device
P_{mod}	W	Power of the signal modulated by the MST
P_{T}	W	Power emitted by the transmitter antenna
Q	1	Quality factor
R^2	1	Coefficient of determination
R_{s}	Ω	Series resistance
R_{OFF}	Ω	VO ₂ resistance in the insulating state
R_{ON}	Ω	VO ₂ resistance in the conducting state
R_{RM}	m	Distance from the receiver antenna to the MST
R_{TM}	m	Distance from the transmitter antenna to the MST
R_{VO2}	Ω	VO ₂ switch resistance
S	V/dec	VO ₂ OFF-ON transition slope
SS	V/dec	Subthreshold swing
$S_{11-\text{ON}}$	dB	Return loss
$S_{21-\text{OFF}}$	dB	Isolation
$S_{21-\text{ON}}$	dB	Insertion loss
T	K	Temperature
T_{MIT}	K	Metal-Insulator Transition temperature
TR	1	Tunability of a reconfigurable device

$TR_{\%}$	1	Relative tunability of a reconfigurable device
T_r	1	Transmittance
t	m	VO ₂ switch thickness
t_{ins}	m	Thickness of the microheater insulating layer
V_{act}	V	Actuation voltage
V_{AC}	V	AC voltage source amplitude
V_{DC}	V	DC voltage source
V_{int}	V	Voltage drop on VO ₂ switch
V_g	V	Gate voltage
W	m	VO ₂ switch width
W_A	m	MST bowtie antenna width
W_S	m	Spike width in a low-voltage VO ₂ switch
w	m	VO ₂ tunable capacitor width
Z_A	Ω	Impedance of the modulated scatterer antenna
Z_L	Ω	Impedance of the modulated scatterer tunable load
Z_{OFF}	Ω	VO ₂ impedance in the insulating state
Z_{ON}	Ω	VO ₂ impedance in the conducting state
Z_{VO_2}	Ω	VO ₂ switch impedance
Z_{opt}	Ω	Optimal value for the real part of Z_A
Γ^K	1	Kurokawa's reflection coefficient
Γ_{OFF}^K	1	Kurokawa's reflection coefficient with VO ₂ in OFF state
Γ_{ON}^K	1	Kurokawa's reflection coefficient with VO ₂ in ON state
ϵ_r	1	Effective dielectric constant
ΔT	K	Hysteresis width in VO ₂ resistivity
$\Delta \Gamma^K$	1	Distance between Γ_{OFF}^K and Γ_{ON}^K
θ	1	X-ray angle of incidence in XRD
λ	m	Wavelength
ρ	Ωm	Electrical resistivity
σ	$S m^{-1}$	Electrical conductivity
σ_R	Ω	Standard deviation of VO ₂ resistance
ϕ_{sample}	eV	Sample work function

List of symbols

ϕ_{tip}	eV	KPFM Tip work function
Ψ_{S}	V	Surface potential
ω	rad	Angular frequency

List of units

Name	Symbol	SI base units form	Quantity
Ampere	A	A	Electric current
Bar	bar	$1 \times 10^5 \text{ N m}^{-2}$	Pressure
Coulomb	C	As	Electric charge
Degree of arc	°	1	Angle
Degree Celsius	°C	K – 273.15	Temperature
Electronvolt	eV	$1.6 \times 10^{-19} \text{ kg m}^2 \text{ s}^{-2}$	Energy
Farad	F	$\text{kg}^{-1} \text{ m}^{-2} \text{ s}^4 \text{ A}^2$	Electric capacitance
Hertz	Hz	s^{-1}	Frequency
Hour	h	3600 s	Time
Inch	"	$2.54 \times 10^{-2} \text{ m}$	Length
Kelvin	K	K	Temperature
Kilogram	kg	kg	Mass
Meter	m	m	Length
Minute	min	60 s	Time
Ohm	Ω	$\text{kg m}^2 \text{ s}^{-3} \text{ A}^{-2}$	Electric resistance
Revolutions per minute	rpm	$1/60 \text{ s}^{-1}$	Rotation frequency
Second	s	s	Time
Standard cubic centimeters per minute	sccm	$\text{m}^3 \text{ s}^{-1}$	Flow
Volt	V	$\text{kg m}^2 \text{ s}^{-3} \text{ A}^{-1}$	Voltage
Watt	W	$\text{kg m}^2 \text{ s}^{-3}$	Power

Acronyms and Abbreviations

AC	Alternate Current
ADS	Advanced Design System
AFM	Atomic Force Microscopy
ALD	Atomic Layer Deposition
APCVD	Atmospheric-Pressure Chemical Vapor Deposition
a.u.	Arbitrary unit
CMOS	Complementary Metal-Oxide-Semiconductor
CPW	Coplanar Waveguide
CVD	Chemical Vapor Deposition
DC	Direct Current
DGS	Defected Ground Structure
EDLT	Electric Double-Layer Transistor
EFM	Electrostatic Force Microscopy
E-MIT	Electrically Induced Metal-Insulator-Transition
EPFL	École Polytechnique Fédérale de Lausanne
ESD	Electrostatic Discharge
e.g.	exempli gratia
et al.	et alii (and others)
FET	Field Effect Transistor
FIB	Focused Ion Beam

Acronyms and Abbreviations

FTIR	Fourier Transform Infrared Spectroscopy
HFSS	High Frequency Structural Simulator
IBE	Ion Beam Etching
IC	Integrated Circuit
IMOS	Impact Ionization MOSFET
IoT	Internet of Things
IT	Information Technology
INRS	Institut National de la Recherche Scientifique
IP3	Third Order Intercept Point
ITRS	International Technology Roadmap for Semiconductors
i.e.	id est (that is)
KPFM	Kelvin Probe Force Microscopy
LPCVD	Low-Pressure Chemical Vapor Deposition
LTO	Low Temperature Oxide
MEMS	Microelectromechanical Systems
MIT	Metal-Insulator Transition
MOCVD	Metal-Organic Chemical Vapor Deposition
MOSFET	Metal-Oxide-Semiconductor Field-Effect-Transistor
MoM	Method of Moments
MST	Modulated Scatterer
NDR	Negative Differential Resistance
PCB	Printed Circuit Board
PID	Proportional Integral Derivative
PLD	Pulsed Laser Deposition
PNA	Programmable Network Analyzer
RF	Radio Frequency

RFID	Radio Frequency Identification
RRAM	Resistive Random Access Memory
RT	Room Temperature
Rx	Receiver antenna
SEM	Scanning Electron Microscope
SI	International System of Units
SIMS	Secondary Ion Mass Spectroscopy
SMU	Source Monitor Unit
SNR	Signal to Noise Ratio
SPDT	Single-Pole Double-Throw
SPNT	Single-Pole N-Throw
SPST	Single-Pole Single-Throw
SRR	Split Ring Resonator
THz- TDS	Terahertz Time Domain Spectroscopy
TFET	Tunnel FET
THz	Terahertz
T-MIT	Thermally Induced Metal-Insulator-Transition
TMO	Transition Metal Oxide
TRL	Thru-Reflect-Line
Tx	Transmitter antenna
UHV	Ultra High Vacuum
VCO	Voltage Control Oscillator
XRD	X-ray Diffraction Analysis

Elements and Materials

Al	Aluminum
Al₂O₃	Sapphire
Ar	Argon
Au	Gold
BaTiO₃	Barium Titanate
Ba_xSr_{1-x}TiO₃	Barium Strontium Titanate (BST)
(C₅H₇O₂)₄V	Vanadium Acetylacetonate
Cr	Chromium
Cu	Copper
Fe₃O₄	Iron(II,III) Oxide (Magnetite)
GaN	Gallium Nitride
Gd₂O₃	Gadolinium Oxide
HfLaO_x	Hafnium-Lanthanum Oxide
HfO₂	Hafnium Oxide
LaCoO₃	Lanthanum Cobaltite Oxide
MgF₂	Magnesium Fluoride
NbO	Niobium Monoxide
NbO₂	Niobium Dioxide
NdNiO₃	Neodymium Nickel Oxide
NiCr	Nickel Chromium

Elements and Materials

O₂	Dioxygen
PbZr_xTi_{1-x}O₃	Lead Zirconate Titanate (PZT)
Pd	Palladium
PrNiO₃	Praseodymium Nickelate
Pt	Platinum
PtIr₅	Platinum Iridium ₅
Si	Silicon
Si₃N₄	Silicon Nitride
SiO₂	Silicon Dioxide
SmNiO₃	Samarium Nickelate
SrTiO₃	Strontium Titanate (STO)
TiO₂	Titanium Dioxide
Ti₂O₃	Titanium Sesquioxide
Ti₃O₅	Titanium Pentoxide
V	Vanadium
VO₂	Vanadium Dioxide
VOCl₃	Vanadium Oxychloride
VO(OC₃H₇)₃	Vanadyl Tri-Isopropoxide
ZrO_x	Zirconium Oxide

1 Introduction

The exponential growth in performance of electronic devices since the invention of the first working transistor in 1947 [1] has promoted revolutionary enhancements in information technology (IT), from the early days of radio and television up to the current era of the Internet of Things (IoT). The IT revolution has dramatically influenced our interaction with the world and society in ways unforeseeable just few decades ago.

The technological improvements necessary to sustain the ever-increasing IT requirements have been achieved for more than 40 years, since the invention of the Integrated Circuit (IC) in 1958 [2], by increasing the transistor density on a chip. This trend has been predicted by Moore's Law of scaling of silicon ICs [3], according to which the transistor density in an IC has doubled approximately every two years, as shown in Figure 1.1.

The increase in transistor density in this time frame has been possible for decades focusing mostly on device miniaturization, following the Metal-Oxide-Semiconductor Field-Effect-Transistor (MOSFET) scaling rules introduced by Dennard in 1974 [4]. However, this approach became obsolete with the advent of nanotechnology, since the behavior of nanoelectronic devices requires more complex models for which it is not possible to apply simple scaling rules.

While approaching the scaling limits of conventional Complementary Metal-Oxide-Semiconductor (CMOS) technology, new strategies are proposed by the annual reports of the International Technology Roadmap for Semiconductors (ITRS) [5] in order to keep improving the performance of electronic devices. These approaches are broadly categorized in three classes: *More Moore*, *More than Moore* and *Beyond CMOS*.

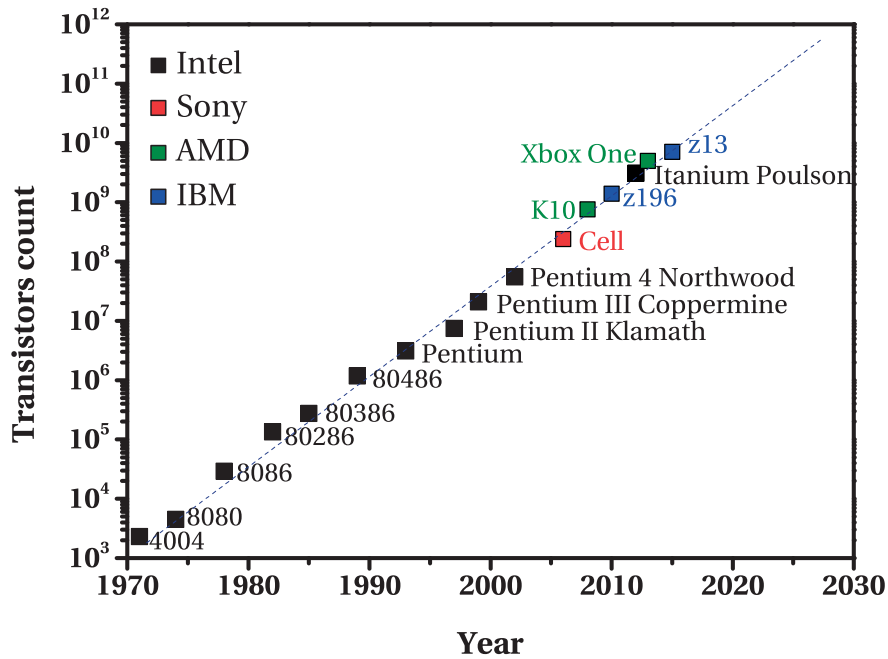


Figure 1.1 – Moore’s law, showing the exponential increase of the transistor count in microprocessors from different semiconductor chip makers.

The *More Moore* strategy is based on keep following Moore’s Law by exploiting technology boosters for advanced CMOS devices, like high-mobility channel materials, high-k dielectrics, multi-gate structures, strain engineering, and so forth.

On the other hand, *More than Moore* solutions target other challenges not directly related to miniaturization and speed, such as energy efficiency or functional diversification. The corresponding devices do not necessarily scale in density according to Moore’s Law, but provide additional value implementing advanced functions, e.g. integrated sensing and actuating, high-frequency communication and energy management.

Lastly, *Beyond CMOS* refers to alternative technologies developed in parallel to CMOS and able to exhibit superior performance in different domains. These technologies can be based on the study of the properties of new materials, or on the exploitation of completely different information processing methods based on state variables other than electric charge, such as spin orientation, phase state, strongly correlated electron state, and so on.

The aim of this thesis was to identify a promising *Beyond CMOS* technology for re-

1.1. Beyond CMOS: functional oxides for reconfigurable electronics

configurable electronics and assess its potential for applications considering all the aspects of the design process, from the growth of the required materials to the benchmarking with alternative technologies.

1.1 Beyond CMOS: functional oxides for reconfigurable electronics

One of the most promising *Beyond CMOS* strategies consists in exploiting the so-called functional oxides. In CMOS technology, oxides are used just as electrical insulators with a well controlled dielectric constant to control the field effect and separate devices. In contrast to conventional oxides, functional oxides can be used in different ways, such as transparent conductors for stretchable electronics [6] or non-volatile memory elements [7].

Complex oxides were studied over the last century mainly from a materials science point of view; the first functional properties that were exploited for applications were ferroelectricity (in BaTiO_3) and piezoelectricity (in $\text{PbZr}_x\text{Ti}_{1-x}\text{O}_3$). The technological advancements allowing to realize thin films of complex oxides enabled novel functionalities in electronics, increasing dramatically the research interest in this field [8, 9]. In many cases, the properties of functional oxide thin films are highly dependent on interface and defects, so atomic layer deposition (ALD) is recommended as a growth technique to have a good control of crystallinity and defect density [10].

1.1.1 Adaptive oxide electronics

Among the several options offered by working with functional oxide thin films, what is most interesting for reconfigurable electronics is the possibility to tune some of their properties (internal states). This research area is commonly called adaptive oxide electronics.

Functional oxides present several clear advantages that make them suitable for reconfigurable electronics, including fast switching speed, scalability to low dimension, long retention time of the modified internal state, potential CMOS compatibility and possible implementation of novel functionalities.

The internal states that can be reconfigured in a relevant way for electronic devices

Chapter 1. Introduction

depend on the structure and properties of the functional oxide, and can include electric resistivity, permittivity, polarization, magnetization and optical transmission. The change in internal state is induced by an external perturbation, which can be of different nature, including electric, magnetic, thermal or optical excitations. After the excitation is removed, the material can keep or not the modified internal state.

The choice of a suitable functional oxide for the applications of interest starts from the desired combination of tunable internal states and corresponding excitations. The wide range of materials in this class allows to choose any combination among the elements of the previous lists. Among the several possibilities favorable for reconfigurable electronics, for this thesis it was decided to investigate materials showing tunability of the resistivity by electrical excitations. This decision has been taken for two main reasons: firstly, regarding the perturbation, it is preferable to keep the same kind of excitation used for most alternatives for reconfigurable electronics, in order to provide a more meaningful comparison of different technologies; secondly, limiting the choice to the internal states tunable by electric perturbations, working with electrical resistivity provides the largest margins of improvement in terms of applications.

1.1.2 Resistive switching materials

Resistive switching functional oxides are usually classified and characterized according to several parameters, whose combination determines their suitability to different applications:

- *number of tunable states*: some resistive switching materials offer the possibility to tune their resistivity continuously, while others only in discrete steps (two or more).
- *resistive ratio*: ratio between the highest and lowest achievable values of resistivity; values as high as 1×10^6 have been measured for HfLaO_x [11] and Gd₂O₃ [12].
- *switching speed*: maximum time needed to change the resistivity from one value to another; in most cases it ranges from few nanoseconds to few tens of nanoseconds, resulting in a fast switching mechanism as compared to other technology solutions for RF reconfigurable electronics.

1.1. Beyond CMOS: functional oxides for reconfigurable electronics

- *retention time*: time limit for a material to keep a tuned resistivity value; it is generally highly dependent on the material and on the temperature.
- *endurance*: number of sustainable switching cycles between different resistivity values before structural failure.

It must be noted that most of the materials in this category have not been characterized for radio frequency applications, since they are mostly exploited for resistive switching random access memories (RRAM) working with direct current, for instance using TiO_2 [13]. One of the objectives of this thesis consists in developing a technology that can be used for devices in very different frequency ranges, from DC to terahertz. For this reason, it is important to make sure that the conduction mechanisms in the low resistance state of the material are not limited in frequency in our range of interest. Moreover, the dielectric constant of the material in the high resistivity state must be considered to predict the effect of parasitic capacitances at high frequencies.

1.1.3 Functional oxides exhibiting a metal-insulator transition

One of the most remarkable effects exploited in oxide electronics is the one used for the devices presented in this thesis: the Metal-Insulator Transition (MIT). Even in this case the tunable internal state is the electrical resistivity, but there is no retention of the tuned state after the excitation is removed.

MIT oxides are broadly categorized in three classes according to the physics underlying the transition mechanism: in Peierls insulators the MIT occurs due to electron-phonon interactions, in Anderson insulators it is due to disorder-induced localization, while in Mott-Hubbard insulators it is caused by electron-electron interactions. This phenomenon is observed in several transition metal oxides (TMO) behaving as strongly correlated electron systems, in which metallic properties due to high charge concentration can be inhibited by the repulsion of electrons and their resulting localization at each atomic site [14].

The MIT in strongly correlated electron systems can be originated by external stimuli of different nature, e.g. electric field, optical excitation, magnetic field and pressure. However, the most straightforward way to observe the phase transition is by thermal triggering in TMOs behaving as insulators below the transition temperature T_{MIT} , and as conductors above. The effect of excitations of different nature is generally

cumulative, therefore for device applications it is preferable to select MIT oxides with a value of T_{MIT} only slightly higher than room temperature. Some of the most studied functional oxides exhibiting the MIT are reported in Table 1.1, ordered by T_{MIT} .

Table 1.1 – List of functional oxides exhibiting a metal-insulator transition.

Material	T_{MIT}
Fe_3O_4	121 K
PrNiO_3	135 K
NdNiO_3	201 K
VO_2	340 K
SmNiO_3	403 K
Ti_3O_5	448 K
LaCoO_3	500 K
Ti_2O_3	400 K to 600 K
NbO_2	1081 K

1.2 Vanadium Dioxide for reconfigurable electronics

Vanadium Dioxide (VO_2) is a paradigmatic example of a strongly correlated electron system, exhibiting a MIT in correspondence of a structural phase transition at the temperature $T_{\text{MIT}} = 340$ K, accompanied by a steep change in electrical resistivity and near-infrared transmission [15–17]. This behavior is qualitatively described in Figure 1.2, showing the following effects obtained by decreasing the temperature below T_{MIT} :

1. phase transition from a tetragonal rutile structure with regularly spaced vanadium atoms ($V-V = 2.87 \text{ \AA}$) to a monoclinic phase with alternate shorter (2.65 \AA) and longer (3.12 \AA) $V-V$ distances;
2. opening of an energy gap $E_g \approx 0.6$ eV in the vanadium 3d conduction band;
3. step increase in resistivity, reaching up to 5 orders of magnitude in bulk VO_2 .

Since the discovery of the MIT in VO_2 more than 50 years ago, this material has been widely-studied by a large community of theoretical and experimental condensed-matter and materials scientists, in order to unravel the physics underlying its switching mechanism. In fact, the exact nature of the physical mechanisms responsible of the MIT in VO_2 is still under debate, with different research groups divided on the question

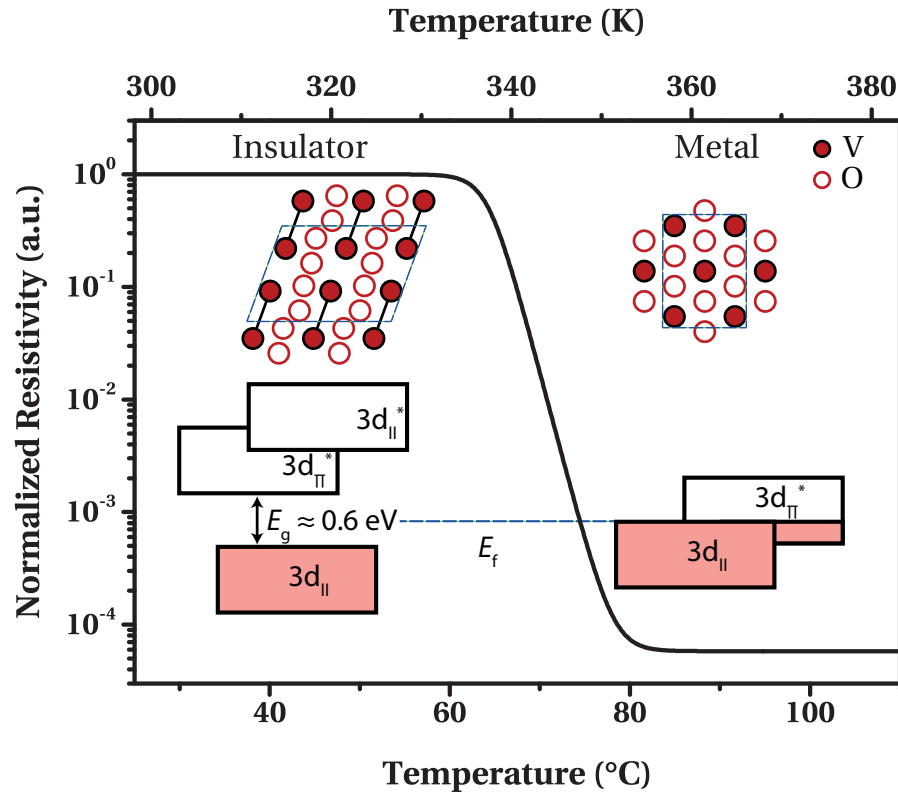


Figure 1.2 – Dependence on temperature of VO_2 resistivity, crystal structure and electrical band diagram.

whether the structural phase transition is sufficient to explain the insulating nature of the low temperature phase (Peierls transition), or whether strongly correlated electron states play a dominant role (Mott-Hubbard transition) [18], as suggested by most recent findings [19–22].

In parallel to this field of research, VO_2 has attracted interest in terms of possible device applications, due to the fact that, differently from the majority of functional oxides exhibiting a MIT, the transition occurs near room temperature (RT). More recently, increasing research interest in VO_2 has been induced by the possibility to trigger the MIT by excitations of nature other than thermal, with the demonstration of electrical, optical and strain-assisted transitions. The electrically-induced metal-insulator transition (E-MIT) is particularly interesting due to the report of ultrafast switching times (of the order of few ns [23]), allowing to envision promising solutions for oxide electronics [24].

As a consequence, several applications for VO_2 have been proposed in a broad range of fields: thermal sensors [25], chemical sensors [26], optical modulators [27–29],

Chapter 1. Introduction

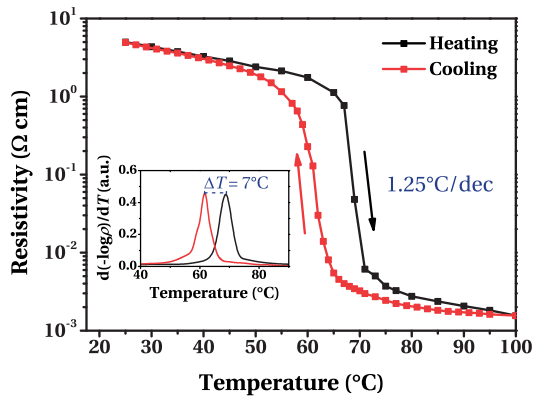
optoelectronic memories [30], memristive elements [31, 32], metamaterials [33, 34], all-thermal solid state devices [35], fast switches for logic [36] and high-frequency switches [37].

In conclusion, VO₂ has been selected for this thesis as a promising material to develop a *Beyond CMOS* technology for reconfigurable electronic devices working in a wide frequency range, addressing applications ranging from DC to the terahertz regime.

1.3 Structure of the thesis

This thesis is structured as follows:

Chapter 2: CMOS-compatible VO₂ sputtering and device integration

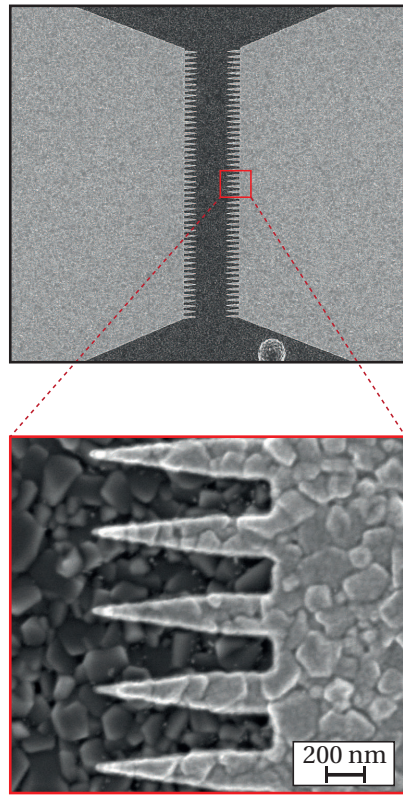


This chapter reports the development of a technology for CMOS-compatible VO₂ electronic switches, exploited for most of the devices characterized in the rest of the thesis. The chapter starts with an introduction on the challenges related to the deposition of high quality VO₂ thin films and a brief review on different deposition methods. In this work, reactive magnetron sputtering has been optimized to achieve stoichiometric polycrystalline VO₂ on Si/SiO₂ sub-

strates. The quality of the film is assessed by structural and electrical characterization. Planar 2-terminal VO₂ electronic switches with different geometrical parameters have been fabricated as test structures to characterize the electrically-induced MIT.

Chapter 3: VO₂ MIT for steep-slope electronic switches

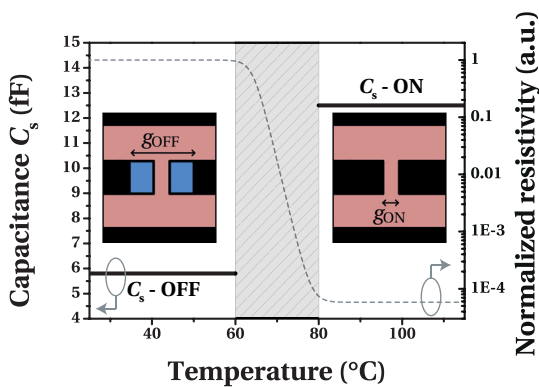
Highly conductive, temperature stable steep-slope switches are discussed in detail in this chapter. After a general introduction on previous work on VO₂ electronic switches, their applications and the main active fields of research, the potential of VO₂ for steep-slope switches is discussed by a comparison with alternative technologies.



The fabricated VO₂ 2-terminal switches are electrically actuated, comparing the operation with current or voltage bias and discussed in the context of the electrothermal actuation model based on Joule heating. The measurements of the slope and of the current in the ON state are performed in a wide temperature range, allowing to assess for the first time their low temperature dependence. The second part of the chapter is devoted to the study of an optimized electrode shape for the VO₂ switches, designed in order to decrease their actuation voltage. The design is driven by electrothermal simulations, and the working principle is validated by the electrical characterization of the fabricated devices. The chapter is concluded by measurements at cryogenic temperatures, performed to

provide further insights on the role of the electric field in the E-MIT in VO₂ switches.

Chapter 4: VO₂ MIT for reconfigurable RF functions



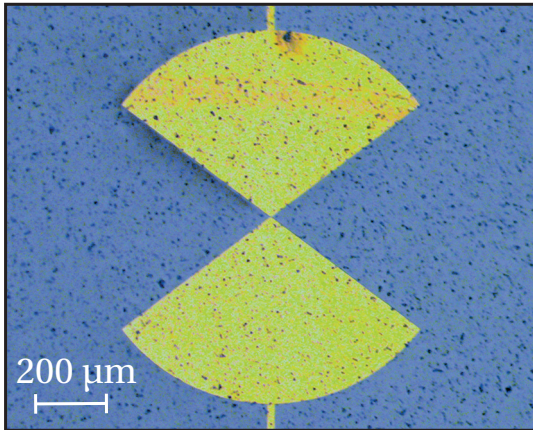
This chapter presents the design, fabrication and characterization of different devices based on the MIT in VO₂ as enabler of tunable high-frequency functions. After a general introduction on the available technologies for RF reconfigurable electronics, compared in terms of the relevant figures of merit, the state of the art of VO₂ RF switches and tunable filters is discussed. CMOS-compatible, low-loss,

highly reliable VO₂ RF switches are thoroughly characterized up to 40 GHz, discussing the dependence of the insertion loss on the DC bias current, the effect of the para-

Chapter 1. Introduction

sitic components and the comparison between electrical and thermal actuation. A possible optimization step for the RF switches is proposed, discussing the possibility to dope VO_2 to increase its conductivity in both the structural phases. In the second part of the chapter, novel digitally tunable capacitors are introduced, fabricated and characterized by thermal actuation. The VO_2 tunable capacitors are then exploited to design tunable and switchable bandstop filters operating at higher frequency ranges than what demonstrated in other works based on conventional VO_2 RF switches. The chapter is concluded with the discussion of an alternative actuation method for VO_2 tunable capacitors and filters, studying by coupled electrothermal and electromagnetic simulations the feasibility of integrating microheaters for local heating of the VO_2 regions.

Chapter 5: VO_2 MIT for reconfigurable THz functions



In this chapter it is reported for the first time a modulated scatterer working in the THz range, enabled by the VO_2 MIT. After a general introduction on the properties of THz electromagnetic radiation and a review on the state-of-the-art of VO_2 THz devices, the VO_2 THz modulated scatterer is presented. The main design equations of the modulated scatterer are discussed and an optimization process based on electromagnetic simulations is performed. The resulting fabricated design is characterized up to 2 THz

using terahertz time domain spectroscopy, and the working principle of the device is validated measuring a modulated signal much higher than the noise floor up to around 0.8 THz, confirming for the first time THz operation for a modulated scatterer.

Chapter 6: conclusions and perspectives

The last chapter summarizes the main contributions of the thesis and discusses short-term and long-term goals for further investigations related to MIT and VO_2 devices.

2 CMOS-compatible VO₂ sputtering and device integration

This chapter presents the VO₂ sputtering deposition method developed at EPFL and its integration in a CMOS-compatible process for reconfigurable electronics based on VO₂ MIT. This process has been employed for steep-slope VO₂ switches (chapter 3), VO₂ RF switches (section 4.2), VO₂ tunable capacitors (section 4.3.1) and VO₂ microwave tunable filters (section 4.3.2).

2.1 Introduction on VO₂ thin film deposition methods

Several techniques have been explored in order to achieve high-quality, cost-efficient and reproducible deposition of VO₂ thin films.

The quality of the deposited VO₂ thin films for reconfigurable electronics is assessed in comparison to the electrical characteristics of bulk VO₂ single crystals [38, 39], exhibiting a steep decrease in resistivity of 5 orders of magnitude (typically from 10 Ω cm to 10⁻⁴ Ω cm) at $T_{MIT} = 340 \pm 1$ K and a very narrow hysteresis width (0.5–2 K) observed for T_{MIT} in heating-cooling cycles.

Unfortunately the deposition of VO₂ thin films is a challenging task, currently constituting a very active field of research with different proposed solutions and optimization strategies. Part of the difficulty in the process is due to the fact that, as illustrated in Figure 2.1, VO₂ is not the only stable vanadium oxide phase. Due to the multiple valence states of Vanadium, other oxide phases, like the ones described by the general formulas V_nO_{2n-1} (n = 2, 3, 4, 5, 6, 8) and V_nO_{2n+1} (n = 2, 6) are also possible, complicating the goal of achieving pure stoichiometric VO₂ thin films.

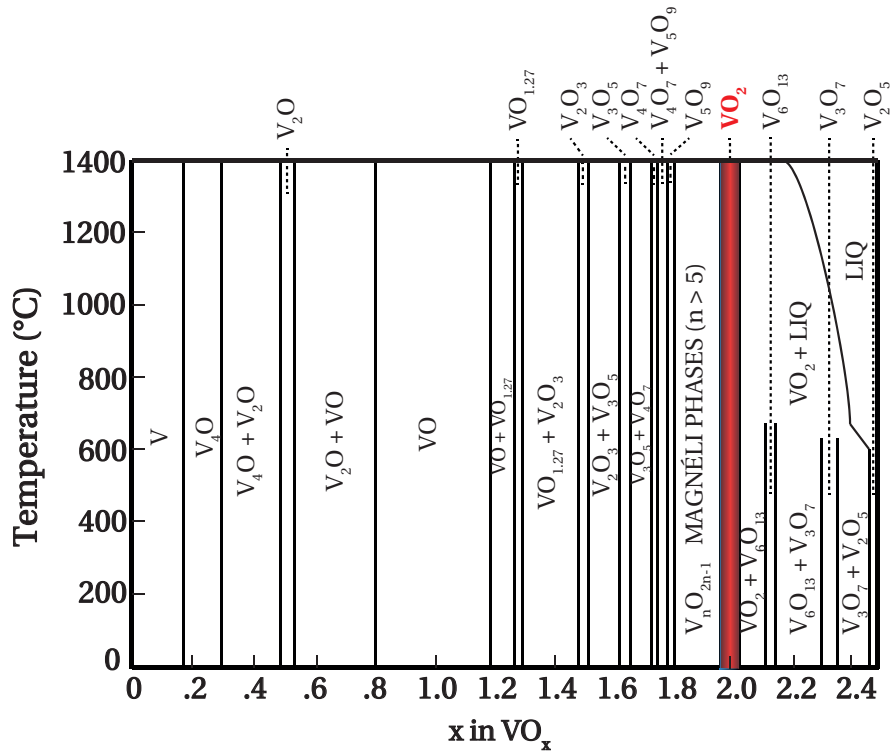


Figure 2.1 – Phase diagram of the vanadium-oxygen system. Adapted from [40].

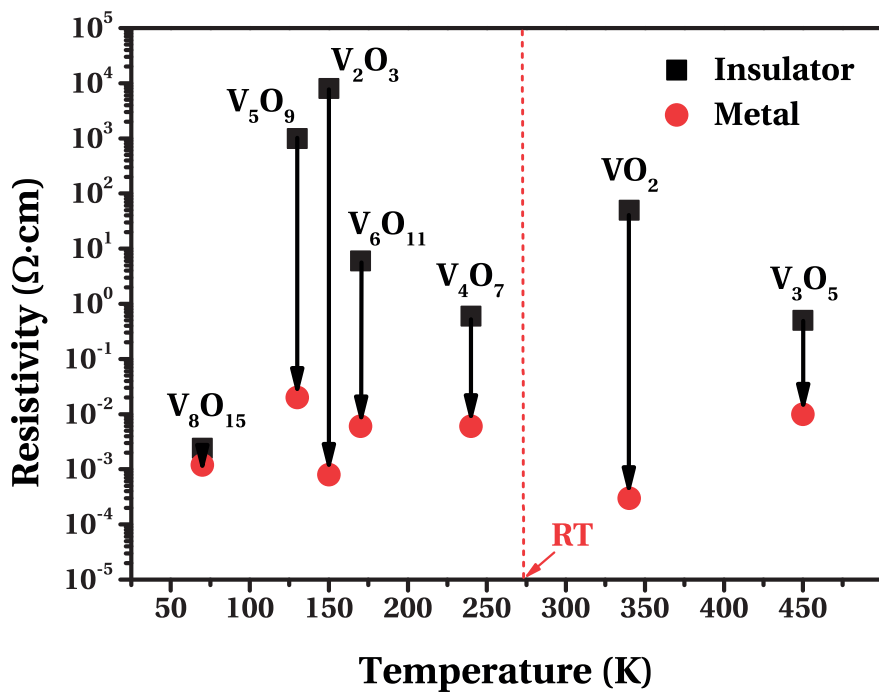


Figure 2.2 – Resistivity ratio obtained by T-MIT in VO₂ and V_nO_{2n-1} phases [41].

2.1. Introduction on VO₂ thin film deposition methods

The influence of stoichiometry on the quality of the MIT in VO₂ [40] is due to the fact that other intermediate phases exhibit metal-insulator transitions with different characteristics, as shown in Figure 2.2, with most of the phases having a T_{MIT} lower than room temperature. Therefore, only VO₂ films with good stoichiometry can present a high resistivity modulation effect at temperatures practical for reconfigurable electronics. Despite these challenges, high-quality VO₂ thin films have been deposited on a variety of substrates and exploiting different deposition techniques.

2.1.1 Influence of the substrate on VO₂ deposition

The properties of VO₂ thin films are strongly affected by their crystallinity, interface to the substrate and localized strain, therefore in order to obtain MIT characteristics as close as possible to those of bulk VO₂ single crystals it is necessary to be able to grow high-quality epitaxial thin films [42].

Heteroepitaxy of VO₂ has been achieved with different deposition techniques, but the choice of the substrate is limited by the need to match the lattice constant and the angle of the lattice vectors with the ones of the monoclinic VO₂ crystal system. An added complication is present for the deposition techniques working at high temperature, because of the possible mismatch in thermal expansion coefficient between VO₂ and substrate, and because of the structural phase transition of VO₂ while cooling down to room temperature after deposition, which can induce a variety of defects and dislocations due to stress.

Despite these difficulties, epitaxial VO₂ thin films have been grown on Magnesium Fluoride (MgF₂) [43], Titanium Dioxide (TiO₂) [44–46] and Sapphire, the single crystal form of Aluminium Oxide (Al₂O₃). Sapphire is the preferred choice due to its easy availability, good stability at high temperatures, lower reactivity with oxides, and especially, good matching between its hexagonal lattice and the monoclinic form of VO₂. As a consequence, VO₂ thin films grown on Sapphire can exhibit MITs with resistivity ratios higher than 4 orders (typically from 10 Ω cm to 10⁻⁴ Ω cm) and narrow hysteresis window $\Delta T < 2$ K [43, 47–50], with particularly good results (ratio of 9.4×10^4) working on the R-cut plane (10 $\bar{1}$ 2) of Sapphire [51].

Working with other substrates does not allow to grow epitaxial VO₂ thin films, and the MIT characteristics of the resulting polycrystalline VO₂ are generally degraded both in terms of resistivity ratio and hysteresis width.

2.1.2 VO₂ deposition techniques

The most common deposition techniques employed for VO₂ thin films are the following:

- *Pulsed Laser Deposition* (PLD) is a thin film deposition technique particularly suited for oxides, and it is based on focusing a pulsed laser beam on a target inside a vacuum chamber. The vaporized material is deposited on the substrate facing the target. In the VO₂ case, the target is generally pure Vanadium, and the deposition happens in a Argon (Ar) - Dioxygen (O₂) atmosphere. The substrate is generally heated at temperatures ranging from 300 °C to 600 °C [47, 48, 52–55] but depositions at room temperature have also been reported [56, 57].

Due to the relatively simple configuration setup compared to other deposition techniques, high quality VO₂ thin films can be deposited with good reliability; as a consequence, PLD has become one of the most common deposition techniques among research groups working on VO₂. However, this process cannot cover large areas and presents drawbacks in terms of uniformity and surface cleanliness, therefore it is mostly used for prototyping.

- *Magnetron Sputtering* is based on generating a plasma by ionizing a process gas, usually Ar, in a vacuum chamber. The ions from the plasma are accelerated towards the target by the applied electric field between the magnetron (cathode) and the substrate (anode); the high energy of the impact makes so that atoms from the target are ejected and can deposit on the substrate. By introducing another gas in the chamber it is possible to induce chemical reactions between the gas and the atoms ejected from the target (*reactive magnetron sputtering*), allowing for instance to obtain oxides from metallic targets.

In the case of VO₂, reactive magnetron sputtering is normally performed at temperatures of the order of 500 °C in a Ar – O₂ atmosphere. While the most common choice for the target is pure vanadium [40, 58–69], thin film depositions using VO₂ [43, 70] or V₂O₅ [71, 72] targets are also reported in the literature. Compared to other techniques, sputtering provides advantages in terms of film uniformity and scalability to larger substrate sizes.

- *Chemical Vapor Deposition* (CVD) is based on exposing the substrate to one or more volatile precursors, which produce the thin film by a chemical reaction on the surface of the substrate. CVD was the first reported deposition method for

VO₂ thin films [73], using vanadium oxychloride (VOCl₃) as a precursor. In most of the cases the preferred CVD technique for VO₂ is metal-organic chemical vapor deposition (MOCVD), employing organometallic precursors like vanadium acetylacetonate (C₅H₇O₂)₄V or vanadyl tri-isopropoxide (VO(OC₃H₇)₃).

CVD is still considered as one of the most convenient ways to deposit VO₂, and high quality thin films were obtained both using atmospheric-pressure CVD (APCVD) [74, 75] and low-pressure CVD (LPCVD) [76–78].

- Other employed techniques are the *sol-gel method* [79–88], *vanadium oxidation* [89–94], *post-deposition annealing* of VO_x films [95] and *ALD* [11, 96–100].

2.2 VO₂ sputtering on Si/SiO₂ substrates

One of the main goals in research on VO₂ electronics consists in extending CMOS by realizing VO₂ devices with novel or improved functionalities with fully controlled integration capability on advanced CMOS platforms. For this reason, one of the objectives of this thesis was to develop a CMOS-compatible technology for VO₂ electronic devices. The choice of sputtering as a deposition technique allowed us to perform large-scale depositions, suitable for device variability and reliability studies.

In order to ensure CMOS compatibility, it was necessary to optimize sputtering deposition on Silicon Dioxide-coated Silicon (Si/SiO₂) substrates. As explained in section 2.1.1, this substrate choice prevents to form epitaxial films, and polycrystalline VO₂ thin films exhibit worse MIT electrical characteristics. In fact, VO₂ deposited on standard Si/SiO₂ substrates has shown in several reports a MIT with relatively low resistivity ratio, around 2 orders of magnitude [40, 68, 71], due to homogeneity and crystallinity issues generally ascribed to lattice mismatch [53].

2.2.1 Deposition and process parameters

VO₂ thin films were deposited by reactive magnetron sputtering on Si/SiO₂ substrates of a 5.08 cm diameter pure V target (Lesker 99.5 %), using the ultra-high-vacuum (UHV) sputtering chamber at the Solar Energy and Building Physics Laboratory (LESO-PB) at EPFL [101], shown in Figure 2.3.

High vacuum (8×10^{-8} mbar) was achieved in the chamber using a turbomolecular

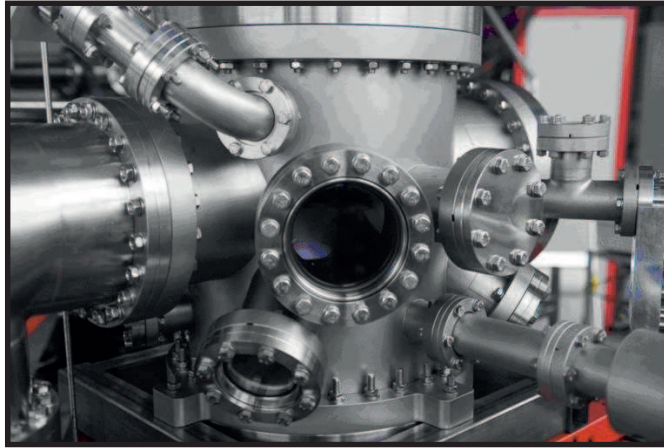


Figure 2.3 – UHV Sputtering chamber at LESO-PB, EPFL.

pump (Oerlikon TMP600C); the pumping rate was then reduced and kept constant during the deposition.

The substrate was annealed at a heating rate of 30 °C/min up to 490 °C and kept at constant temperature during the deposition; this value has been selected in order to ensure a good crystallinity for the deposited film. To improve the uniformity of the deposition, the substrate was rotated at a constant speed of 15 rpm and the distance from the target was optimized at 4 cm with 10° angle [102].

The inert gas used for plasma formation (99.999 % pure Ar) was introduced in the chamber and a mass flow controller was used to keep the flow stable at 12.5 sccm. The plasma was formed by applying 150 W RF power on the V target using a MKS RPG-50 power supply. Before introducing the reactive gas (99.995 % pure O₂), a pre-sputtering step was performed (with the substrate protected by a shutter) in order to clean the outermost layers of the target.

The O₂ concentration is the most critical parameter influencing the composition of the deposited VO_x film. In order to improve the stoichiometry of the VO₂ film, subsequent depositions were performed in order to optimize the values of the deposition pressure (2×10^{-3} mbar) and the initial O₂ flow (2.41 sccm). The pressure in the chamber was accurately monitored using a pressure sensor (Vacom Atmion ATS35C) and we used a lambda-probe (Zirox XS22) in combination with a Proportional Integral Derivative (PID) controller to have a feedback control on the O₂ flow that would ensure constant O₂ partial pressure.

2.2. VO₂ sputtering on Si/SiO₂ substrates

The deposition time was generally 2 h, then, after stopping the plasma, the substrate was brought back to room temperature at a cooling rate of 30 °C/min. Table 2.1 summarizes the optimized process parameters, obtained after multiple tests on the effect of the oxygen flow.

Table 2.1 – Optimized process parameters for reactive magnetron sputtering of VO₂ on Si/SiO₂ substrates.

Parameter	Value
Target	Vanadium
Temperature	490 °C
Power	150 W
Base pressure	8×10^{-8} mbar
Deposition pressure	2×10^{-3} mbar
Argon flow	12.5 sccm
Oxygen flow	2.41 sccm
Deposition time	2 h

2.2.2 VO₂ thin film characterization

In order to assess the quality of the films deposited using the process parameters summarized in Table 2.1, we performed several electrical and structural characterization techniques, as detailed in the following sections.

Electrical characterization

The electrical resistivity ρ of VO₂ was measured by 4-point probes measurements on the as-deposited VO₂ film using an HP 4156C semiconductor parameter analyzer and a control on the substrate temperature up to 100 °C. As shown in Figure 2.4, the probes are placed in line with a fixed interspace s . In this configuration, and assuming that s is much higher than the VO₂ thickness t , it can be shown that the film resistivity can be easily calculated as:

$$\rho = 4.53t \frac{V}{I} \quad (2.1)$$

where I is the constant current passing through the outer probes and V is the voltage measured between the inner probes.

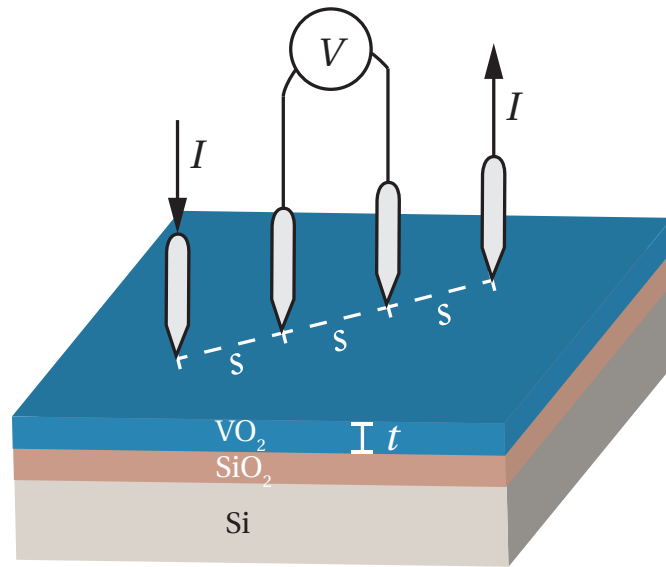


Figure 2.4 – 4-point probes measurement setup.

This method provides a fast qualitative analysis of the composition of the deposited VO_x films, in contrast to more time-consuming X-ray diffraction (XRD) analyses: good quality, stoichiometric VO₂ should undergo a transition of more than 3 orders of magnitude in resistivity at around 67 °C. Measuring the resistivity after each deposition allows to fine-tune the process parameters in order to obtain stoichiometric VO₂.

Figure 2.5 shows the results of the electrical characterization for non-optimal VO₂ depositions. Slight deviations from the optimal initial O₂ flow do not prevent to observe a resistance modulation in the deposited VO₂ films. The VO₂ film obtained with a higher initial O₂ flow (2.43 sccm) presents a resistance ratio of 85, decreasing from 13.2 Ω cm to 1.54 × 10⁻¹ Ω cm while increasing the temperature from 25 °C to 100 °C. A lower initial O₂ flow (2.39 sccm) produced a more conductive VO₂ film, with lower resistivity values both in the insulating and metallic state. The resistivity at 25 °C was 1.5 × 10⁻¹ Ω cm and the one at 100 °C was 8.64 × 10⁻⁴ Ω cm, resulting in a resistance ratio of 1.73 × 10².

As shown by the results in Figure 2.6, a resistivity ratio of more than 3 decades (3.33 × 10³) was obtained in the optimized film, for which it is possible to observe a resistivity decrease from 5 Ω cm to 1.5 × 10⁻³ Ω cm increasing the temperature from 25 °C to 100 °C. The steepness of the transition (1.25 °C/dec) and the small hysteresis window observed in the heating/cooling cycle (~ 7 °C, measured plotting d(-log ρ)/dT in the inset of Figure 2.6) are other indicators of the good quality of the

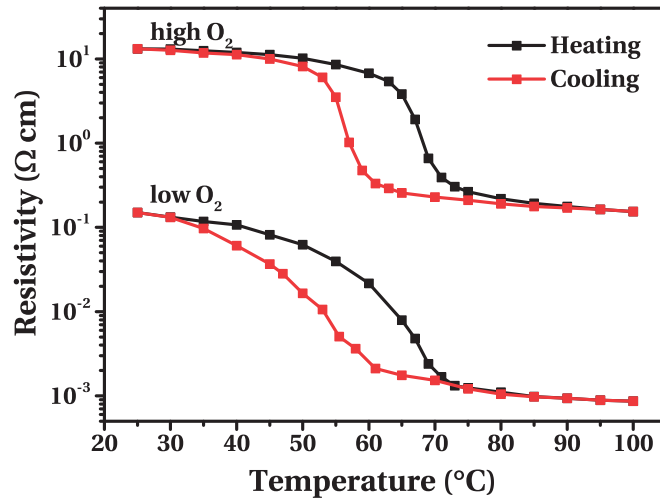


Figure 2.5 – VO₂ electrical resistivity dependence on temperature for non-optimal O₂ flows.

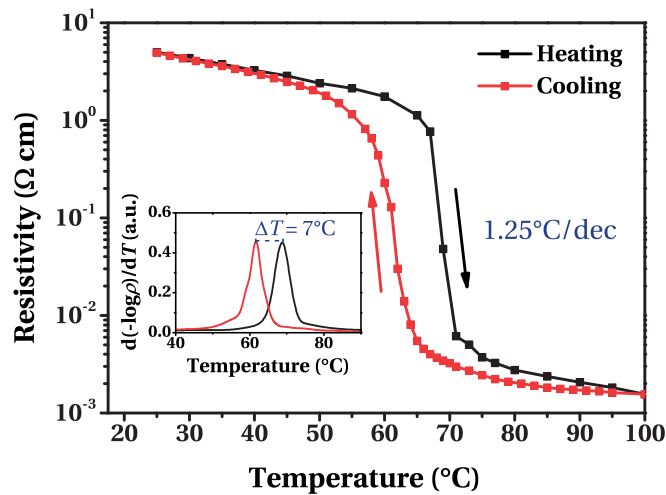


Figure 2.6 – VO₂ electrical resistivity dependence on temperature in the optimized case, showing a reconfigurability higher than 3 decades and a steep transition at ~ 68°C. Inset: $d(-\log \rho)/dT$ curves while heating and cooling the VO₂ film, showing a narrow hysteresis of ~ 7°C.

film.

Scanning electron microscope analysis

Scanning electron microscope (SEM) analysis is based on the use of a high energy electron beam which allows to achieve higher imaging resolution than standard

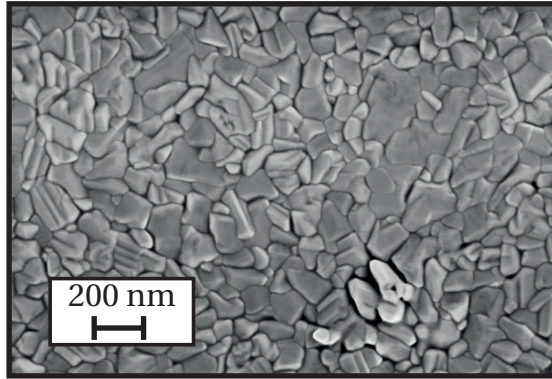


Figure 2.7 – SEM image of the sputtered VO₂ thin film, showing an average grain size larger than 100 nm.

optical microscopy. High energy electrons irradiate the sample and the image is obtained from the information on the detected backscattered electrons (reflected by elastic collision at the surface) and secondary electrons (emitted from the sample).

SEM imaging of VO₂ films was performed in the Center of MicroNanoTechnology (CMi) at EPFL using SEM Zeiss Merlin, with a configuration optimized for information on surface structure. We used an In-Lens detector, efficient for high-resolution imaging using secondary electrons, and set a low working distance of 3 mm and an acceleration voltage of 1 kV. The results in Figure 2.7 show the good homogeneity and crystallinity of the deposited VO₂ film, with grains larger than 100 nm, consistent with the state of the art for sputtered VO₂ [63] and contributing to the good electrical properties of the observed metal-insulator transition [103].

X-ray diffraction analysis

XRD is a powerful non-destructive technique used to investigate the atomic and molecular structure of crystals, based on observing the intensity of monochromatic X-ray beams scattered from a sample in function of the angle of incidence θ . Constructive diffraction is possible only if the Bragg's law is satisfied:

$$n\lambda = 2d \sin\theta \quad (2.2)$$

where n is an integer, λ is the wavelength of the X-ray source and d is the distance between atomic planes. By sweeping θ , Bragg's law is satisfied by different spacings d in polycrystalline materials. Therefore, the position of the peaks in a plot of the

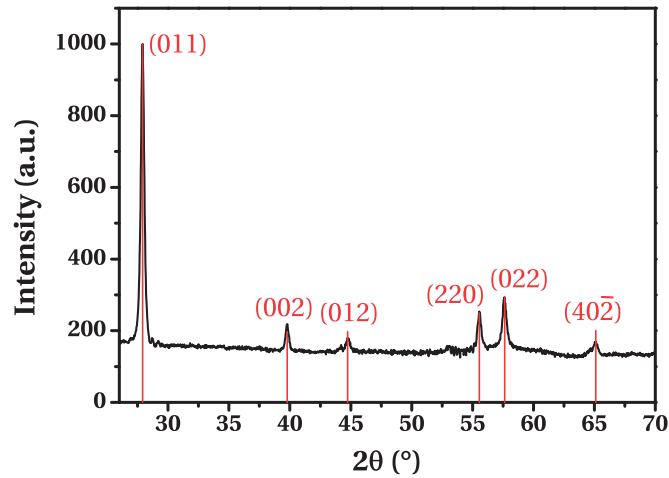


Figure 2.8 – XRD spectrum showing the preferential orientations of the deposited polycrystalline VO₂ film.

diffraction intensity versus θ allows to obtain information on the crystal structure of the material. Moreover, the width of the peaks is related to the preferred crystal orientation (texture) and other structural parameters, such as average grain size, strain and crystal defects.

XRD analyses of the optimized sputtered VO₂ thin films were performed at the department of Physics in EPFL (Rigaku equipment with a CuK α X-ray radiation) in the Bragg-Brentano configuration, in order to investigate their crystallinity and stoichiometry. The XRD spectrum reported in Figure 2.8 shows a correspondence with the power diffraction data of some crystal lattice planes of VO₂ ([0,1,1], [0,0,2], [0,1,2], [2,2,0], [0,2,2], [4,0,-2]) presented in the literature [104], confirming the successful deposition of pure polycrystalline VO₂. The absence of the other peaks suggests preferential orientation or possible strain of crystallites.

Atomic force microscopy and Kelvin probe force microscopy

Atomic Force Microscopy (AFM) is a high-resolution structural characterization technique used to obtain information on the topography of a sample at the nanometric scale. Figure 2.9 illustrates a typical AFM measurement setup. AFM is based on detecting the forces between a sharp tip at the end of a cantilever and the sample to be investigated, placed in close proximity to the tip. Depending on the situation, these forces can be of different nature (e.g. Van der Waals forces, electrostatic forces, chemical bonding, etc.). In the non-contact mode, which we used for the VO₂ char-

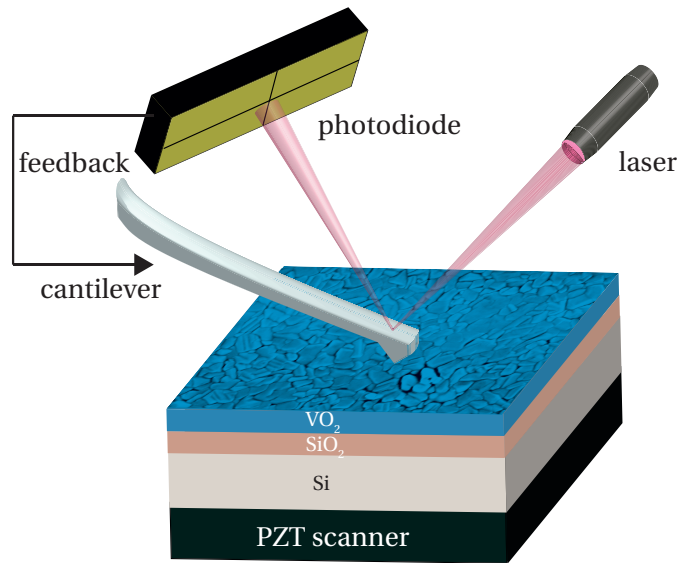


Figure 2.9 – Schematic diagram of an atomic force microscope.

acterization, the tip does not touch the surface, and the cantilever, supported by a piezoelectric element, oscillates close to its resonance frequency (usually of the order of 100 kHz). The forces between the tip and the surface produce a decrease in the resonance frequency of the cantilever, which can be detected using a laser and a photodiode array. The laser is focused on the reflective back of the cantilever, and the deflected beam is detected by the photodiodes. As the cantilever is moved in the xy -plane defining the sample surface, the change in topography induces a change in resonance frequency which is detected as a difference in the signal detected by the photodiodes. A feedback control is used to maintain a constant force or height between the tip and the sample throughout the scanning operation, and the corresponding height information is registered in function of the xy coordinates to obtain a topographical map of the sample.

Kelvin Probe Force Microscopy (KPFM) is a variant of AFM which provides quantitative values for the sample work function ϕ_{sample} . Figure 2.10 shows the working principle and biasing scheme used for KPFM characterization. At first, the tip is far from the sample, and an electrical modulation $V_{\text{AC}} \sin(\omega t)$ is applied to the cantilever (Figure 2.10 (a)) matching its resonance frequency. When the tip is put in electrical contact with the sample (Figure 2.10 (b)), the Fermi levels of the tip and the sample align and the electrostatic force has a component modulated at ω , proportional to

the contact potential difference V_{CPD} between the tip and the sample [105]:

$$F_{\omega} = -\frac{dC}{dz} V_{\text{CPD}} V_{\text{AC}} \sin(\omega t) \quad (2.3)$$

where C is the capacitance between the tip and the sample and z is their separation. V_{CPD} is due to the difference in work function of the tip and sample materials:

$$V_{\text{CPD}} = \frac{\phi_{\text{tip}} - \phi_{\text{sample}}}{e} \quad (2.4)$$

where e is the electron charge. By applying a DC bias voltage in series to the AC component (Figure 2.10 (c)), equation 2.3 is modified as:

$$F_{\omega} = \frac{dC}{dz} [V_{\text{DC}} - V_{\text{CPD}}] V_{\text{AC}} \sin(\omega t) \quad (2.5)$$

Therefore, the value of V_{CPD} can be determined by adjusting the bias voltage V_{DC} such that F_{ω} is minimized. By knowing V_{CPD} and ϕ_{tip} and after calibration procedures, it is possible to extract ϕ_{sample} .

AFM and KPFM characterizations were performed in the Division of Micro- and Nanostructures Metrology at Wrocław University of Technology, Poland, using a Veeco/Bruker NanoMan VS Scanning Probe Microscope with NanoScope V controller. The characterization was performed in two scanning steps. In the first step the topography contour is recorded. In the second step the feedback loop is open and the piezo scanner is repeating the contour recorded in the first step while measuring V_{CPD} . A PPP-EFM PtIr5 coated tip from Nanosensors with ~ 75 kHz resonance frequency was used at a scan height of 10 nm. The topography plot in Figure 2.11 (a) obtained by AFM reveals an average surface roughness of 11 nm. The contact potential difference V_{CPD} measured between the tip (~ 5 eV work function) and the VO₂ surface, shown in Figure 2.11 (b), is used to estimate the VO₂ work function as ~ 5.125 eV, consistent with other values found in the literature for VO₂ in the insulating state [106, 107].

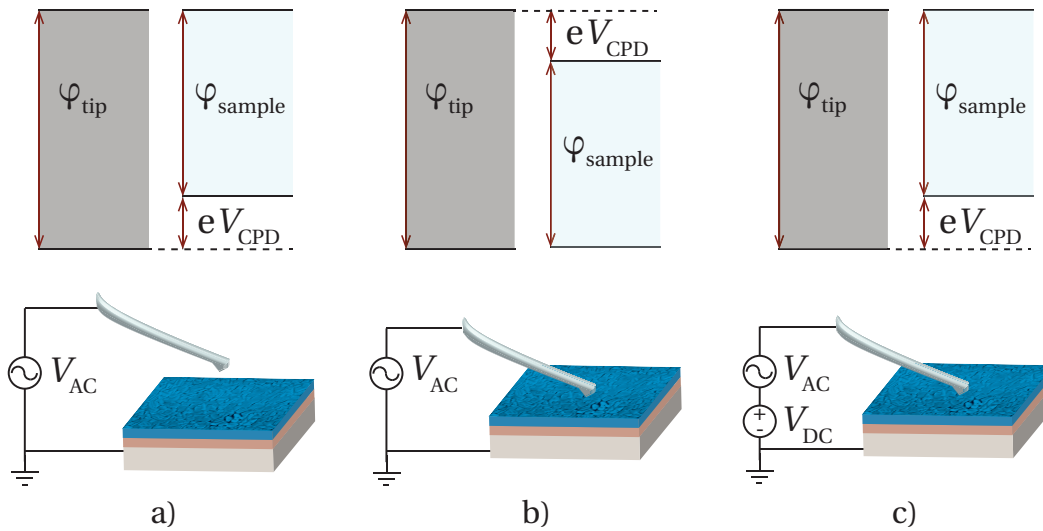


Figure 2.10 – Measurement setup and working principle of a Kelvin Probe Force Microscope, illustrating three possible configurations for the tip-sample interaction and the corresponding band diagrams. a) Tip not in contact, applied V_{AC} . b) Tip in contact, applied V_{AC} . c) Tip in contact, applied $V_{AC} + V_{DC}$.

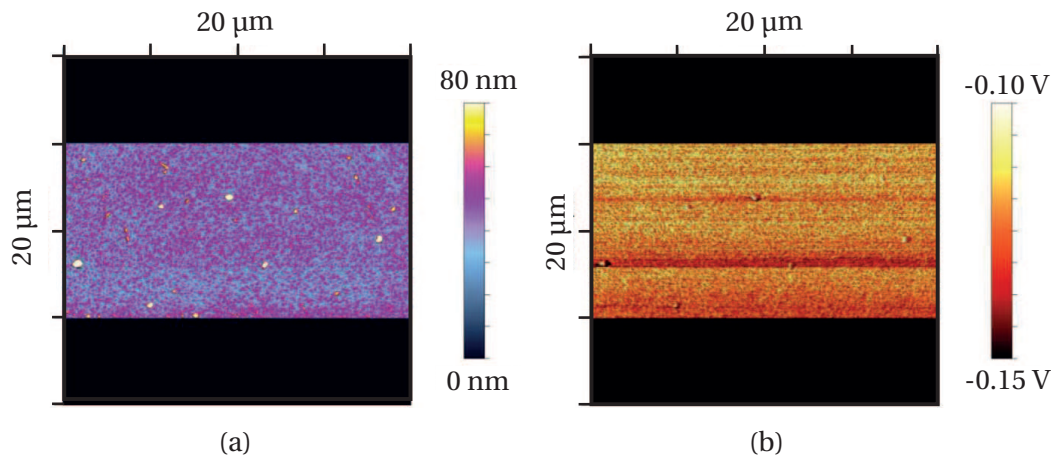


Figure 2.11 – (a) Topography of the film obtained by AFM, showing an average surface roughness of 11 nm. (b) Surface contact potential difference measured by KPFM, used to estimate the VO₂ work function as ~ 5.125 eV.

2.3 CMOS-compatible electronic switches

In this section we present the characterization of the E-MIT in CMOS-compatible VO₂ electronic switches, with the aim to provide guidelines for integration in CMOS circuits.

2.3.1 Fabrication

Figure 2.12 shows the main steps of the fabrication process for the VO₂ planar switches used as E-MIT test structures. The fabrication was performed in CMi at EPFL, except for the VO₂ deposition step. The process starts with the deposition of a 400 nm low temperature (425 °C) SiO₂ layer (LTO) by LPCVD (Centrotherm furnace) on top of a 4'' silicon substrate (Figure 2.12a). A 360 nm VO₂ thin film is then deposited by reactive magnetron sputtering (Figure 2.12b) as described in section 2.2.1.

A photolithography step for VO₂ patterning was performed coating a 1.2 μm thick AZ1512 positive photoresist (EVG150), exposed in hard contact mode (Süss Microtec MA6). The VO₂ film was patterned (Figure 2.12c) by ion beam etching (IBE, Veeco Nexus IBE350). IBE provides a simple alternative to plasma etching techniques based on fluorine or chlorine chemistry [108], but it requires precise characterization of the etching rate, because of the low selectivity of the process with respect to the underlying SiO₂ layer. The results from the etch tests and the use of Secondary Ions Mass Spectroscopy (SIMS) for real-time end point detection allowed to prevent overetching of the SiO₂ layer.

The process ends with a lift-off procedure to define the metal contacts. First it is deposited a double-layer photoresist (700 nm LOR and AZ1512, coated with EVG150), then a 300 nm thin film of Al is deposited by thermal evaporation (Leybold Optics LAB 600H) with 20 nm Chromium (Cr) adhesion layer.

Figure 2.13 shows the top view (a) and cross-section (b) of a finalized planar switch with width $W = 100\mu\text{m}$ and length $L = 7.5\mu\text{m}$. The cross-section analysis was performed by Focused Ion Beam (FIB, FEI Nova 600 NanoLab) etch and SEM imaging.

2.3.2 Current actuation of VO₂ switches

The electrically induced MIT in a VO₂ switch can be achieved by injecting a DC current across its terminals, as shown in Figure 2.14. A resistor R_s in series to the switch is included in order to suppress the oscillations caused by the negative differential resistance [109]. The measurements were performed with a HP 4156C semiconductor parameter analyzer.

By increasing the current I passing through the VO₂ switch, its resistance $R_{\text{VO}_2} = V_{\text{int}} / I$ (where V_{int} is the voltage drop on the switch) slowly decreases, until reaching the E-

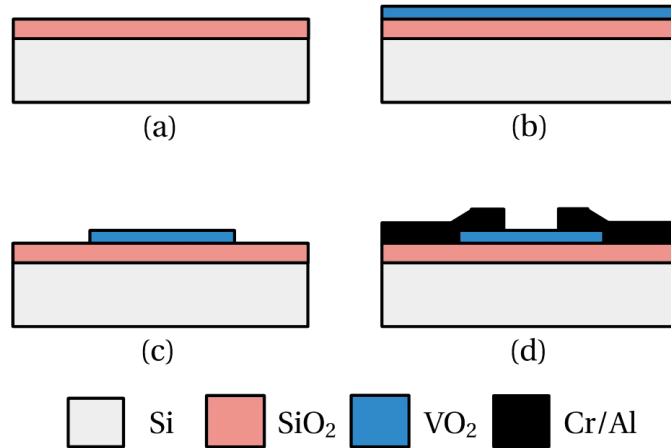


Figure 2.12 – Main steps of the fabrication process for VO₂ planar electronic switches. (a) LPCVD of 400 nm SiO₂ on Si substrate. (b) Sputtering deposition of 360 nm VO₂. (c) Patterning of VO₂ by optical lithography and ion beam etching. (d) 20/300 nm Cr/Al evaporation patterned by lift-off.

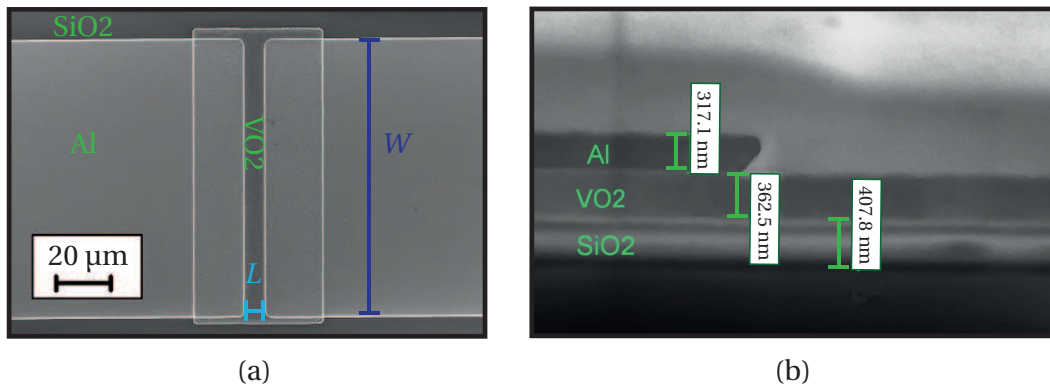


Figure 2.13 – (a) SEM image of one of the VO₂ planar switches used to characterize the E-MIT. The width of the VO₂ junction is 100 μm, the length is 7.5 μm. (b) FIB cross-section view of the device, showing the thickness of the VO₂ layer obtained after 2 h of RF magnetron sputtering deposition as described in section 2.2.1; platinum layer on top used for FIB preparation.

MIT in correspondence of the power dissipation level necessary to reach the transition temperature T_{MIT} . We define the actuation current I_{act} and the actuation voltage V_{act} as the values respectively of I and V_{int} in correspondence of which the E-MIT is triggered. We identify V_{act} , I_{act} and the resistance in insulating and metallic states (respectively R_{OFF} and R_{ON}) as the most important parameters for compact modeling of the VO₂ switch and integration in CMOS circuits.

In order to study the effects of scaling on the performance of VO₂ switches, we fabri-

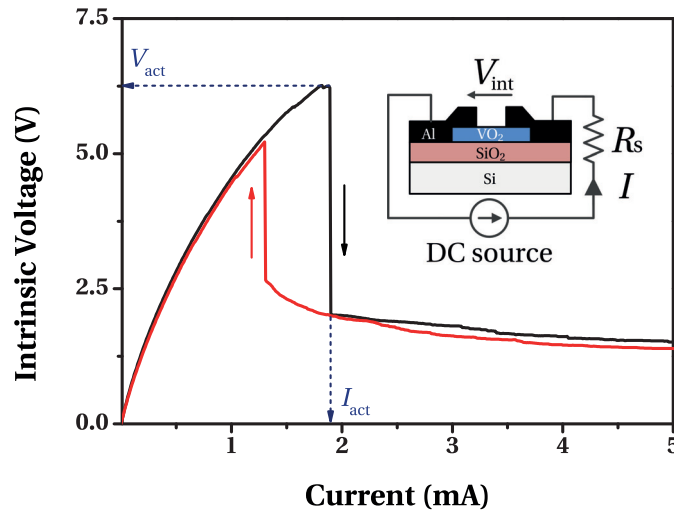


Figure 2.14 – Electrical characterization of the E-MIT by current actuation in a VO_2 switch with $W = 100\mu\text{m}$ and $L = 7.5\mu\text{m}$. Inset: biasing scheme including a DC current source I_{DC} and a series resistor $R_s = 1\text{ k}\Omega$.

cated devices with different geometries (VO_2 junction width W ranging from $50\mu\text{m}$ to $100\mu\text{m}$, length L from $7.5\mu\text{m}$ to $17.5\mu\text{m}$) and characterized them by DC current actuation up to 5 mA. In Figure 2.15 we show the effect of scaling W and L on the IV characteristics of different VO_2 switches. A reference device ($W = 80\mu\text{m}$, $L = 7.5\mu\text{m}$) switches at $I_{\text{act}} = 1.89\text{ mA}$ and shows an $R_{\text{OFF}} = 8.5\text{ k}\Omega$. We observed that the actuation current density J_{act} has a low dependence on the switch geometry. Therefore, increasing W , and by consequence the cross-section of the device, increases the required current to reach the same J_{act} , so we measure higher I_{act} values. In the explored geometry variation, I_{act} is in the range from 1.43 mA to 2.46 mA. Changing L has a negligible effect on I_{act} , while V_{act} changes linearly as expected from the change in resistance of the switch.

The results on the resistance in the OFF state, calculated for low applied power, are summarized in Figure 2.16. As expected, R_{OFF} increases linearly with the length and decreases linearly with the width. However, the resistance in the ON state R_{ON} shows no dependence on W while sweeping I_{DC} up to values slightly higher than I_{act} . This is due to the fact that for the considered devices an $I_{\text{DC}} = 5\text{ mA}$ is insufficient to switch the whole volume of the device: a thin conductive filament is formed [110] while the rest of the junction remains in the insulating state, causing a limit in the decrease of R_{ON} by increasing W .

This effect is shown in Figure 2.17: higher I_{DC} bias values increase the width of the

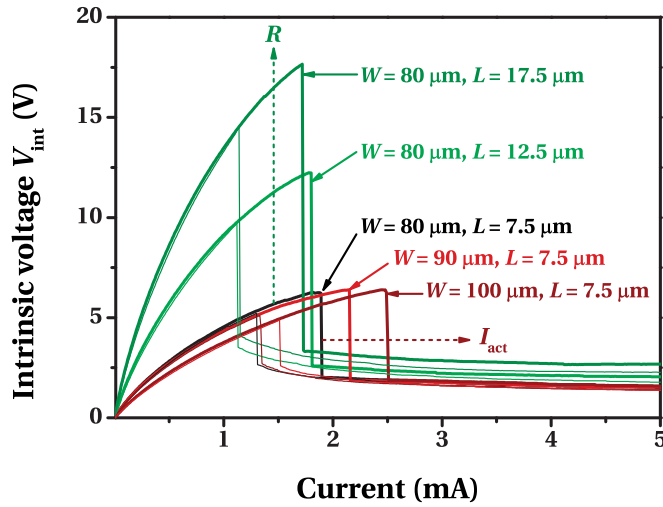


Figure 2.15 – Effect of the VO₂ switch geometry on the IV characteristics the resistance in the off-state.

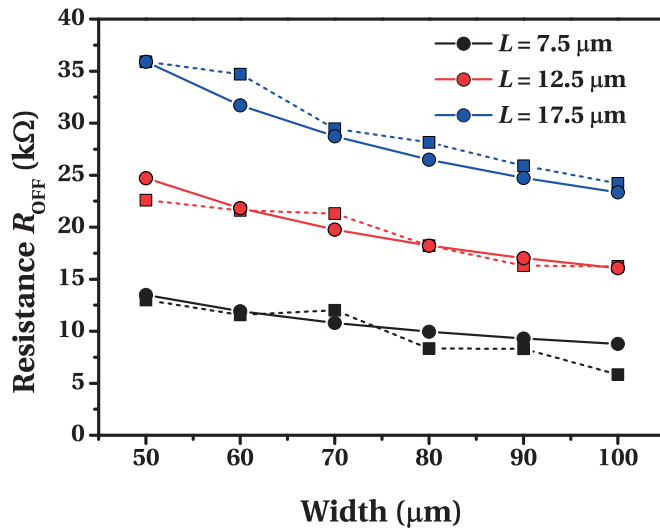


Figure 2.16 – Effect of the VO₂ switch geometry on the resistance in the off-state. Dashed lines: measurements; solid lines: model.

conductive region, as shown in the optical microscope images for selected values of I_{DC} , and as a consequence the R_{OFF}/R_{ON} ratio is improved.

We measured the improvement in R_{OFF}/R_{ON} ratio for increasing I_{DC} bias values up to 100 mA and compared it to the improvement expected from measuring the width of the actuated region. The results are in good agreement with the model. The effectively actuated width increases linearly with I_{DC} , and for the considered switch ($W = 90\mu\text{m}, L = 7.5\mu\text{m}$) an effective width higher than 25% ensures a resistance

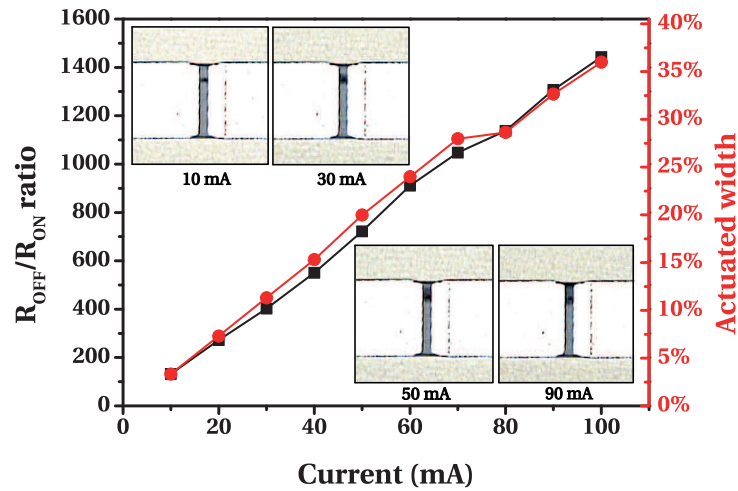


Figure 2.17 – Increase in resistance ratio and width of the actuated region achievable by E-MIT, by increasing the DC current bias I_{DC} . The optical micrographs show the increase in actuated area with increasing current: the darker regions correspond to VO_2 transitioned to the metallic state. $W = 90\mu\text{m}$, $L = 7.5\mu\text{m}$.

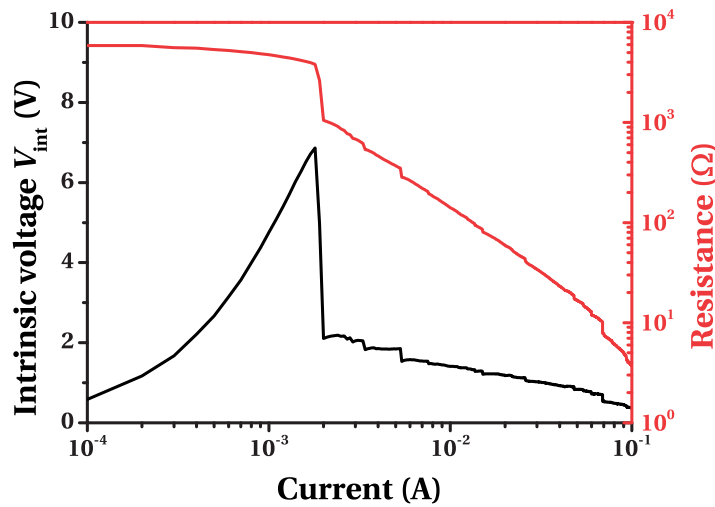


Figure 2.18 – IV characteristics for a VO_2 switch ($W = 90\mu\text{m}$, $L = 7.5\mu\text{m}$) actuated by current bias up to 100 mA.

ratio higher than 3 orders of magnitude. Figure 2.18 shows the IV characteristics for the same switch up to the highest value of I_{DC} used for the characterization (100 mA), for which we obtain a resistance ratio $> 1.44 \times 10^3$. This value is comparable to the one achieved with thermal actuation (3.33×10^3) and represents a significant improvement with respect to previously reported VO_2 electrical switches on Si/ SiO_2 substrates [36, 111], limited to resistance ratios $< 1.3 \times 10^2$.

2.4 Summary

This chapter presented the technology developed at EPFL for CMOS-compatible electronic switches, exploited for steep-slope VO₂ switches (chapter 3), VO₂ RF switches (section 4.2), VO₂ tunable capacitors (section 4.3.1) and VO₂ microwave tunable filters (section 4.3.2). After a short introduction on the problem of achieving high quality deposition of VO₂ thin films and a brief review of the possible deposition methods, the optimized growth conditions for RF magnetron sputtering on Si/SiO₂ substrates are presented.

The structural characterization of the VO₂ thin films was performed using different techniques (XRD, SEM, AFM, KPFM) to reveal the good crystallinity and stoichiometry of the film. The electrical characterization confirmed the excellent quality of the optimized VO₂ film, employing thermal actuation to observe a metal-insulator transition with a resistivity modulation higher than 3 orders of magnitude.

A CMOS-compatible process for planar VO₂ switches on Si/SiO₂ substrates was developed to characterize the electrically-induced metal-insulator transition. Devices with different lengths and widths were fabricated in order to study the dependence of the resistance and the actuation current on the geometry of the device.

The main contributions of this chapter can be summarized as follows:

Optimization of sputtering for high-quality VO₂ thin films on Si/SiO₂ substrates. The feasibility of using reactive magnetron sputtering as a uniform, large-scale deposition technique for high-quality VO₂ thin films on Si/SiO₂ substrates has been demonstrated. The use of a lambda-probe in combination with a PID controller allowed to have a feedback loop to ensure a constant O₂ partial pressure in the sputtering chamber, necessary for the good stoichiometry of the VO₂ film. The film exhibited a resistance ratio of 3.33×10^3 , decreasing from $5 \Omega \text{ cm}$ to $1.5 \times 10^{-3} \Omega \text{ cm}$ increasing the temperature from 25°C to 95°C , and a hysteresis of $\sim 7^\circ \text{C}$. These values are comparable to the ones achievable with PLD of polycrystalline VO₂, without its drawbacks in terms of homogeneity for large-scale depositions.

Development of a CMOS-compatible technology for VO₂ electronic switches. The presented sputtering method was exploited to fabricate planar VO₂ electronic switches on Si/SiO₂ substrates, using a fabrication process suitable for integra-

tion with CMOS technology. The devices show a resistance ratio $> 1.44 \times 10^3$, more than one order of magnitude higher than previously reported VO₂ switches on Si/SiO₂ substrates. In conclusion, we achieved the positive reassessment of VO₂ sputtering deposition on Si/SiO₂ substrates, paving the way to a CMOS compatible VO₂ technology.

3 VO₂ MIT for steep-slope electronic switches

This chapter presents the fabrication and characterization of 2-terminal VO₂ devices working as steep-slope electronic switches, with specific focus on the study of the temperature dependence of the slope and the ON current I_{ON} , the assessment of the actuation voltage and possible techniques to reduce it.

3.1 Introduction on VO₂ electronic switches

The high contrast in electrical resistivity between the insulating (OFF) and conducting (ON) states of VO₂ and the fast achievable switching time induced increasing research interest in the applications of VO₂ for electronic devices.

3.1.1 E-MIT characterization

In order to properly exploit VO₂ for electronic switches, it is of foremost importance to have an accurate model of the E-MIT, from the investigation of the switching mechanisms to the characterization of key figures of merit for different applications.

This section is devoted to the summary of the most recent updates on the characterization of the E-MIT in 2-terminal VO₂ planar switches and 3-terminal VO₂ transistors. Some of the most important research topics in this context are the following:

- *Investigation of the switching mechanism*: the nature of switching mechanism in VO₂ has been one of the most important topics to unravel since the first experiments involving the E-MIT in VO₂ switches. One of the main objectives

in the first reports on the characterization of the MIT in VO₂ switches driven by an external electric field has been the attempt to prove that the switching event can be modeled in concordance with the Mott criterion, according to which the MIT is initiated once reached a critical carrier density n_c in the VO₂ volume [112–114]:

$$n_c = (0.25/a_B)^3 \approx 3 \times 10^{18} \text{ cm}^{-3} \quad (3.1)$$

where $a_B = \hbar^2 \epsilon_r / m^* e^2$ is the effective Bohr radius in VO₂, \hbar is the reduced Planck constant, ϵ_r is the VO₂ effective dielectric constant, m^* is the effective electron mass and e is the electron charge.

The Mott criterion has been successfully used to model the MIT in different systems, including for instance heavily doped semiconductors and high-temperature superconductors. The validity of the Mott criterion in VO₂ has been demonstrated at first by reaching n_c with photogeneration of carriers using femtosecond laser excitations [115, 116]. In order to show that the Mott criterion can be used also to describe the E-MIT in VO₂, some encouraging measurements were performed in 3-terminal switches with direct carrier avalanche injection in a VO₂ channel [117] or in conventional planar 2-terminal switches [118].

However, the most convincing and comprehensive works on modeling the E-MIT in VO₂ switches, including the effect of temperature, bias conditions and device geometries are based on Joule heating [119, 120], according to which the increase in temperature due to the power dissipation induced by the current flowing in the device is sufficient to describe the switching dynamics.

Most recent works on modeling the E-MIT switching mechanisms propose improvements on the Joule heating based model, summarized as follows:

- whilst the Joule heating model can be used to accurately describe the switching dynamics for gradual transitions, in which the voltage is swept continuously from 0 up to values above the actuation voltage and back to 0, different models might be necessary to explain abrupt transitions in which the voltage sweep starts from values above the actuation voltage. For instance, in [121] it is shown how the onset of abrupt transitions can be modeled by the electric-field induced Poole-Frenkel effect, subsequently supported by Joule heating, while [111] suggests that abrupt transitions are initiated by carrier injection;

3.1. Introduction on VO₂ electronic switches

- other reports argue that even in gradual transitions, well predicted by the Joule heating model, it is possible to identify other mechanisms anticipating or concurring with the electrothermal actuation, such as the electric field effect [122] or carrier injection [123, 124].
- *Switching time analysis*: one of the main reasons for which VO₂ has attracted increasing research interest among the possible Beyond CMOS solutions is the potential to achieve ultra-fast switching times. In fact, the optically induced MIT has been characterized as having switching times of the order of ~ 100 fs using optical pump-probe methods [116, 125], terahertz pump-probe methods [126] or time-resolved XRD [127].

The characterization of the E-MIT switching time is generally done by applying a voltage pulse to a 2-terminal VO₂ switch and measuring the rise time of the current, from 10 % to 90 % of its maximum value. One of the first works on the characterization of VO₂ terminal switches reported the possibility to have rise times as low as 9 ns in 3 μm long switches, by measuring the dependence of the rise time on the value of the resistor R_s in series to the VO₂ switch in the circuit, and extrapolating the time for $R_s = 0$ [128]. However, concerns on the validity of this method were raised, due to the fact that it assumes that the VO₂ channel can be simply modeled by a variable resistor in parallel to a constant parasitic capacitor, while impedance spectroscopy measurements reveal a better fit to multiple RC networks in series, consistent with the observation of multiple domain boundaries even in epitaxially grown VO₂ thin films [129].

In a more recent work the switching time was reduced by characterizing VO₂ switches with channel lengths $< 1 \mu\text{m}$ [23]. Using a switch 125 nm long and $R_s = 50 \Omega$ it was measured a rise time as low as 4.5 ns. Furthermore, the delay time (defined as the time difference at 10 % of the applied and measured signals) was found to be as low as 4.5 ns. Out-of-plane switches, with VO₂ thin films deposited between a top and bottom metal electrode, might provide lower switching times. A switching time of 1.9 ns, defined as the time necessary to obtain a decrease in resistance by 90 % in log scale was reported for an out-of-plane switch using 400 nm thick polycrystalline VO₂ [36]. These values are still around four orders of magnitude higher than the lower theoretical bound for the E-MIT in VO₂, estimated as being of the order of 0.5 ps [130].

- *Reliability*: one of the main concerns regarding the possibility to exploit VO₂ for industrial applications consists in the possible degradation of the device

performance with increasing number of switching cycles. This concern is due to the change in crystal structure in correspondence of the Joule heating induced E-MIT, which might cause structural damage in the film after a large number of cycles.

In order to address this possible issue, some reports on VO₂ 2-terminal switches have included reliability tests, with results summarized as follows:

- neither the switch resistance ratio nor the switching time are affected by the voltage-triggered E-MIT after 2×10^3 cycles [36];
 - E-MIT by current actuation has been proven to be a more reliable operation mode with respect to voltage actuation, improving considerably the device lifetime [131];
 - the possibility to use voltage actuation without degrading the resistance ratio has been demonstrated up to 2×10^{10} cycles [132].
- *Field effect in 3-terminal devices:* the observation of a field-effect induced metal-insulator transition in 3-terminal VO₂ devices with a gate voltage affecting the channel conductivity has been object of considerable research effort since the first reports on the E-MIT. However, a first convincing report on the modulation of the VO₂ channel conductivity in presence of a gate bias voltage was published only in 2010 using a conventional MOSFET structure with VO₂ as the semiconductor [133]. This work provided an important contribution to the investigation of the switching mechanism in VO₂, but the performance of the proposed device was far from realizing the full potential of the E-MIT in VO₂, with the conductivity modulation observable only at temperatures very near to T_{MIT} (T between 60 °C and 65 °C), and limited to a relative increase of only 0.26 %. In fact, further work on modeling this kind of device has ruled out the possibility to fully switch the VO₂ channel using conventional MOSFET structures, since the metal phase would not extend for more than ~ 1 nm before reaching the oxide breakdown voltage [41, 134]. A recent work on field-effect in 3-terminal VO₂ devices reported a conductance modulation up to 0.6 %/V at 80 K ascribed to strongly localized field-induced carriers [135]. Alternative structures were investigated, for instance exploiting the field effect induced by trapped charges at the interface between silicon nitride (Si₃N₄) and VO₂ in a Si/SiO₂/Si₃N₄/VO₂ heterostructure [136]. Even in this case, though, the performance was far from ideal, with the gate effect assessed by a reported decrease in transition temperature of only ~ 2 °C.

3.1. Introduction on VO₂ electronic switches

An alternative approach, which collected increasing interest in the last 3 years and it is currently considered the most promising to improve the performance of 3-terminal VO₂ devices with gate operation, consists in exploiting ionic liquid electrolyte gating in electric double-layer transistor (EDLT) structures. The EDLT configuration allows to obtain a ultrahigh electric field at the interface between the ionic liquid and VO₂, which might induce the MIT by electron correlation effects. This effect was used to interpret the results obtained in [137] and [138], where it was obtained a resistance ratio higher than 2 orders of magnitude. However, further work on ionic liquid gating demonstrated that the high change in resistance in this kind of structures is not due to the electron correlation effects, but to the creation of oxygen vacancies in presence of strong electric field [139–141].

A recent work introduced a new approach on gating VO₂, exploiting the carrier distribution in the space charge region of a p-n heterojunction formed by a p-doped gallium nitride (GaN) layer and a VO₂ thin film grown on top of it [142]. This structure allowed to obtain a clear, repeatable resistance switching behavior (ratio ~8) ascribable to electron correlation effects.

3.1.2 Applications

Different families of electronic devices based on the E-MIT in VO₂ have been proposed. Some of the main applications and corresponding results are summarized as follows:

- *MIT tunnel junctions*: VO₂ can be exploited to obtain switchable tunnel junctions, in which tunneling is enabled only in the conducting state; this method has been demonstrated in [143], where the junction is made by a stack of a metal (palladium, Pd), an insulator (1.6 nm hafnium oxide, HfO₂) and VO₂ (3.8 nm). A different working principle is exploited in [144], where the tunneling current in a Platinum (Pt)/HfO₂/VO₂ stack is tuned thanks to the change in VO₂ work function (from 5.2 eV in the insulating state to 5.3 eV in the conducting state).
- *Oscillators*: the observation of self-oscillations generated by the electrical actuation in VO₂ switches led to the investigation of possible applications of the E-MIT for compact oscillating circuits without inductive components. The characterization of the negative differential resistance (NDR) region in the IV characteristics of VO₂ switches and the conditions to exploit it for the genera-

tion of self-oscillations were performed by several research groups, achieving a well-controlled oscillation frequency < 1 MHz [145–149]. Models for the control of the electrical oscillation properties (amplitude and frequency) were provided in function of the voltage bias [145–148], current bias [149], external RC components [147], VO₂ switch geometry [148] and temperature [148].

Despite possible concerns about the device lifetime, due to the observation of narrow high-temperature channels in a brief part of the oscillation cycle, consistent with the analysis of the instantaneous dissipated power in the VO₂ switch [150], more advanced applications were achieved by coupling multiple VO₂ oscillators. Since the discovery of synchronized charge oscillations in capacitively coupled VO₂ switches [151], these structures were proposed for multiphase oscillator arrays [152], non-boolean neuroinspired computation and pattern recognition applications [153–155].

- *Memories*: the possibility to switch VO₂ between two distinct phases with high resistivity ratio, fast switching time, good cycling endurance and long relaxation times is of great interest for memory applications [92].

One of the most promising applications consists in replacing diodes as selector devices in cross bar nonvolatile memory arrays, used to reduce parasitic currents from unaddressed memory elements when performing reading/writing operations [156,157]. The performance of VO₂ as a selector device was evaluated by measurements using as memory elements niobium monoxide (NbO) [158] and zirconium oxide (ZrO_x) / (HfO_x) [159].

- *Memristive elements*: VO₂ could be of interest for applications requiring memristors [9], since the observation of memristive behavior in 2-terminal VO₂ switches [160–164].
- *Electrostatic discharge protection*: in order to protect circuits from electric surges and electrostatic discharge (ESD), it is possible to employ voltage-dependent varistors, whose resistance would drop abruptly in presence of a high applied voltage. Therefore, voltage-triggered E-MIT in VO₂ can be exploited for this application, as demonstrated in [165], where the geometry of the VO₂ switch was optimized in order to sustain ESD protection tests with ESD voltages up to 3.3 kV with fast response times (< 20 ns). On a related note, a similar application was demonstrated using VO₂ switches to limit microwave power [166].

- *High frequency functions*: the high contrast in resistance between the two VO₂ phases attracted increasing research interest in the context of high frequency reconfigurable electronics. This is one of the main fields addressed in this thesis, and it is developed in chapter 4 for microwave and chapter 5 for terahertz applications.
- *Steep-slope switches*: the abrupt nature of the phase transition in VO₂ is considered promising for steep-slope switches, and it is the main application studied in this chapter. In fact, one of the main objectives in validating VO₂ for Beyond CMOS devices is to demonstrate steep-slope operation, in order to overcome the problem of high power consumption in advanced and high-performance CMOS technology, as better explained in the next section.

3.1.3 VO₂ for steep-slope switches

In conventional CMOS scaling, with the objective to keep following Moore's law, the device concept and the role of metal, oxide and semiconductor materials are unchanged, but properly engineered in order to keep reducing the device dimensions. Periodically, some technology boosters were introduced, like high-mobility channel materials (e.g. III-V semiconductors), high-k dielectrics (e.g. HfO₂), multi-gate structures and so on, but the device concept (MOSFET) remained the same. Instead, in a new Beyond CMOS switch both the device concept and the materials will change.

Conventional scaling of CMOS transistors allowed to obtain extraordinary improvements in terms of switching speed, device density, functionality and cost, but aggressive scaling down to gate lengths of the order of tens of nanometers caused problems in terms of process variability and high leakage power with significantly degraded I_{ON}/I_{OFF} ratio, currently considered the main issues of advanced CMOS [167].

For this reason, recent review papers [168, 169] have highlighted the need for new devices that could complement CMOS with improvements in terms of energy efficiency and novel functionality. One of the key targets in this direction is the reduction of the subthreshold swing SS , which in conventional MOSFET structures is limited by the thermionic carrier injection mechanism to 60 mV/dec at room temperature, as

Chapter 3. VO₂ MIT for steep-slope electronic switches

obtained by the following physics-based equation [170]:

$$SS = \frac{dV_g}{d\Psi_s} \frac{d\Psi_s}{d(\log_{10} I_d)} \cong \left(1 + \frac{C_d}{C_{ox}}\right) \frac{kT}{e} \ln 10 > \frac{kT}{e} \ln 10 \cong 60 \frac{\text{mV}}{\text{dec}} \Big|_{T=300\text{K}} \quad (3.2)$$

where Ψ_s is the surface potential, V_g is the gate voltage, I_d is the drain current, kT/e is the thermal voltage and C_d and C_{ox} are respectively the depletion and the oxide capacitance. The development of subthermal subthreshold swing switches (so called because of the possibility to have a $SS < 60 \text{ mV/dec}$ at room temperature), also known as steep slope switches, would allow to scale down the supply voltage, and therefore enable future low-power design [171].

In order to obtain steep slope switches, one possibility consists in decreasing the first factor of the SS equation, $dV_g/d\Psi_s$ (body factor); this approach has been exploited in the negative capacitance transistor [172] and using electro-mechanical gates with movable electrodes [173]. Despite experimentally demonstrated small SS values, in both cases the supporting technology is still far from maturity. The other possibility to enable subthermal SS operation consists in decreasing the second factor, $d\Psi_s/d(\log_{10} I_d)$, which implies the modification of the carrier injection mechanism. For instance, alternative mechanisms that can be exploited for this purpose are impact ionization (IMOS switch [174]) and quantum mechanical band-to-band tunneling mechanism in tunnel FETs (TFETs) [175].

Despite TFET arguably being the most promising steep slope device at the moment, with experimentally demonstrated subthreshold swings of the order of 30-40 mV/dec, this device has strong limitations in terms of low I_{ON} current and frequency operation. Therefore, the question about a new Beyond CMOS steep-slope switch remains open, and it is of foremost importance to investigate the E-MIT in VO₂ as an alternative solution to overcome the limits of thermionic injection.

Figure 3.1 compares the structure and the simplified band diagram of three among the aforementioned switches, with three different principles: (a) the MOSFET, (b) the TFET and (c) the MIT three-terminal switch. While in the case of the MOSFET and the TFET the charge carriers are concentrated in the channel and balanced by the charge on the gate oxide, in the VO₂ switch the whole volume is converted to the metallic phase once triggered the MIT and the whole metallic mobile charge is available for

3.1. Introduction on VO₂ electronic switches

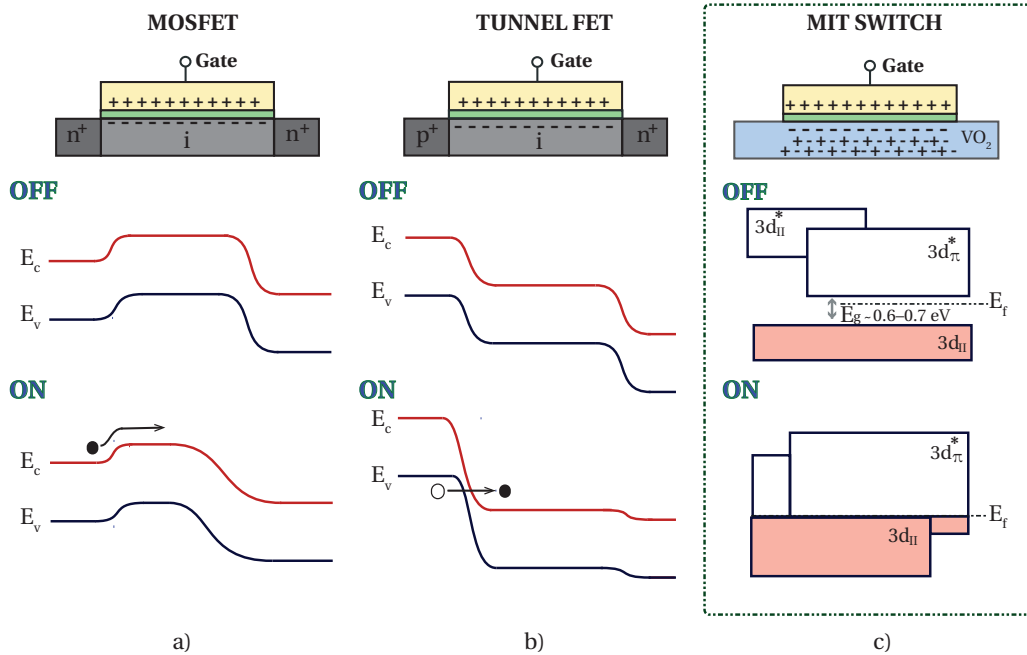


Figure 3.1 – Device cross sections and energy band diagrams corresponding to OFF and ON state in three major classes of switches: (a) MOSFET, (b) Tunnel FET and (c) VO₂ MIT switch.

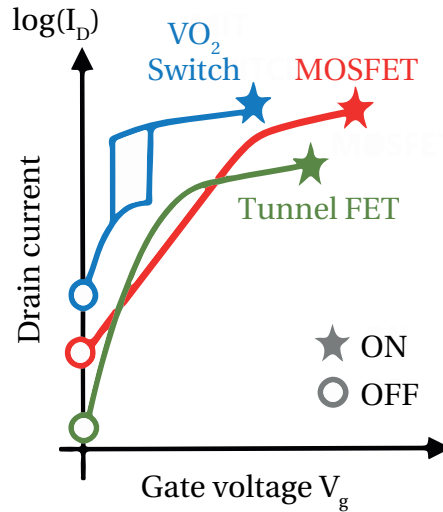


Figure 3.2 – Qualitative comparison of the MOSFET, TFET and VO₂ switch in terms of subthreshold swing abruptness.

conduction, balanced by the background ion charge. When comparing the transfer characteristics of the 3 families of switches, qualitatively represented in Figure 3.2, it is possible to draw the following conclusions on the complementarity of the VO₂ 3-terminal switch to the other devices:

- *I_{ON} current*: the MIT switch and the MOSFET are capable of delivering high *I_{ON}* current normalized per width and therefore ensure high performance in terms of speed, while the TFET reaches values 2-3 orders of magnitude lower, needing complex band-gap engineering of heterojunctions to offer reasonable levels of current.
- *I_{OFF} current*: the TFET has better current blocking capability in the OFF state than the MOSFET, while the VO₂ MIT switch has a higher leakage component due to the relatively low bandgap (~ 0.6–0.7 eV).
- *Steep slope*: the MOSFET is limited by thermionic injection of carriers to $SS = 60 \text{ mV/dec}$ at room temperature, with degrading performance at higher T . The TFET has lower dependence on temperature but shows difficulties in achieving slopes of the order of 30 mV/dec at room temperature, while the abrupt nature of the E-MIT in VO₂ holds great potential for going well below this value.

In this context, the objective of this chapter is to further characterize the slope of the E-MIT in VO₂ switches: steep-slope switches based on VO₂ E-MIT have been presented in previous contributions, but no detailed quantitative analysis on the limits of steepness of the electrical transition between the two structural phases and its dependence on temperature have ever been reported in the literature.

3.2 Abrupt switching in voltage-actuated VO₂ switches

VO₂ planar switches were fabricated using the process flow described in section 2.3.1. The data reported in the following sections correspond to a device with width $W = 50 \mu\text{m}$ and length $L = 7.5 \mu\text{m}$ (shown in Figure 3.3), and the electrical characterization was performed using a HP 4156C semiconductor parameter analyzer.

In order to induce the E-MIT, the biasing scheme shown in Figure 3.4 (a) was used for the current actuation case and the one in Figure 3.4 (b) for the voltage actuation. In both cases, a DC source (voltage V_{DC} or current I_{DC}) is applied to the series connection of the VO₂ switch and the resistor R_s , whose value depends on whether it is used the voltage or the current source, as detailed in the following discussion. The voltage drop on the switch is defined as the intrinsic voltage, $V_{\text{int}} = V - IR_s$, where V and I are the voltage and current for the series connection, respectively.

3.2. Abrupt switching in voltage-actuated VO₂ switches

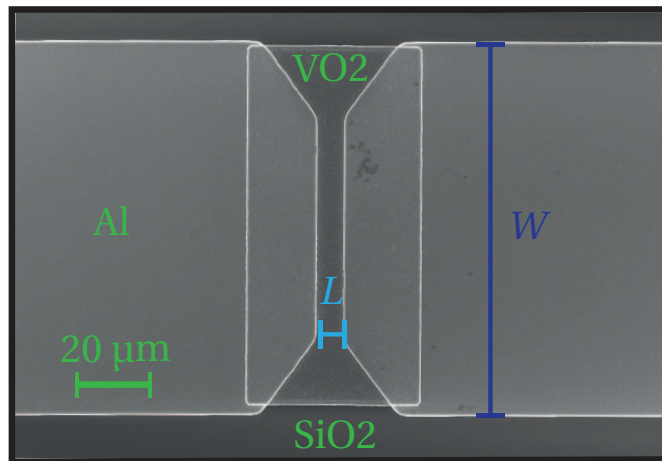


Figure 3.3 – Top-view of a fabricated VO₂ two-terminal switch ($W = 50\mu\text{m}$, $L = 7.5\mu\text{m}$).

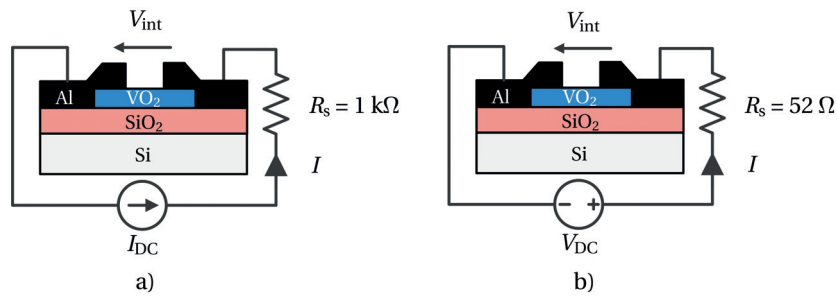


Figure 3.4 – Biasing scheme used for the E-MIT with a resistor in series, in the (a) current actuation and (b) voltage actuation case.

The physical mechanism responsible of the abrupt transition in the IV characteristics of VO₂ switches is the sudden decrease in resistivity observed once reaching the actuation voltage V_{act} of the switch, and it can be modeled by Joule heating [119, 120]. This electrothermal actuation is achieved when the power dissipated in the device $P_{\text{int}} = V_{\text{int}}I$ is producing a material heating above the transition temperature, $T_{\text{MIT}} = 68^\circ\text{C}$.

Figure 3.5 shows the dependence of the switch resistance R_{VO_2} on the intrinsic power dissipated in the device due to the application of a DC voltage or current source, with measurements done at room temperature. In both cases, the applied power gradually increases the temperature of the device, until a conductive filamentary path is created at the onset of the E-MIT.

Once the metallic state is triggered, the resulting power dissipated in the device depends on whether a current or voltage source is used. In the current actuation case,

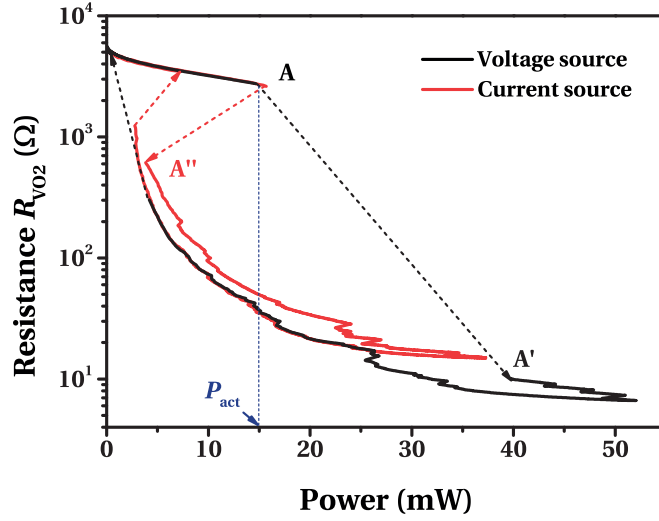


Figure 3.5 – Dependence of intrinsic switch resistance $R_{VO_2} = V_{int}/I$ on the intrinsic power P_{int} dissipated in the VO₂ switch ($W = 50\mu\text{m}$, $L = 7.5\mu\text{m}$) by applying a DC voltage or current source at room temperature. (A) Power threshold for metal-insulator transition. (A-A'): E-MIT by voltage actuation. (A-A''): E-MIT by current actuation.

the decreased resistance in the metallic state induces a drop in V_{int} , limiting the power dissipated in the device and therefore the increase in temperature. As a consequence, the resistance drop in correspondence of the E-MIT is relatively low (factor of 3.1). In the voltage actuation case, the decreased resistance causes a further increase in current, inducing a spike in dissipated power and temperature which allows exploiting the R_{VO_2} modulation for a steep current transition from OFF to ON state.

The results shown in figure 3.5 refer to the intrinsic properties of the VO₂ switching region, therefore they are independent of the value of R_s . In the voltage source case we selected $R_s = 52\Omega$, high enough to limit the current in the ON state, preventing excessive overheating, and low enough to be comparable with R_{VO_2} in the ON state, in order to preserve the high resistance modulation provided by the VO₂ switching region. In the current source case we selected $R_s = 1\text{ k}\Omega$, high enough to suppress the oscillations caused by the VO₂ negative differential resistance region [109].

Temperature-dependent properties of the VO₂ switches have been measured by heating the substrate gradually up to the metal-insulator transition. Figure 3.6 shows the dependence of the VO₂ resistance on the dissipated power P_{int} at different temperatures, from 25 °C to 55 °C, using voltage actuation. As expected, the power needed to heat the VO₂ region up to T_{MIT} and therefore induce the E-MIT is decreasing with

3.2. Abrupt switching in voltage-actuated VO₂ switches

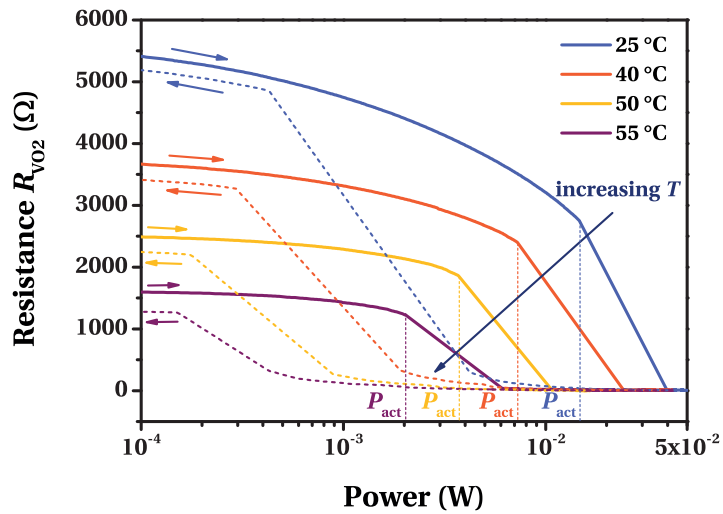


Figure 3.6 – Dependence of the intrinsic switch resistance $R_{VO_2} = V_{int}/I$ on the intrinsic power P_{int} dissipated in the VO₂ switch by applying a DC voltage source at different temperatures, from 25 °C to 55 °C.

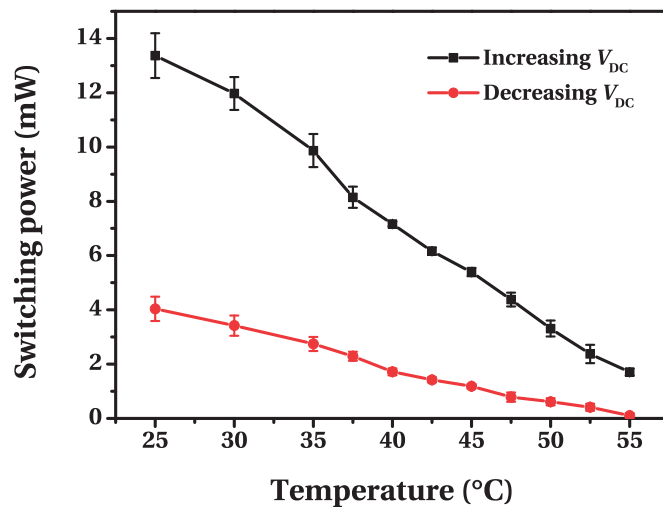


Figure 3.7 – Mean value and standard deviation of the switching power depending on temperature, for the transition increasing V_{DC} (insulator to metal, corresponding to P_{act}) and decreasing V_{DC} (back to the insulating state).

temperature. Furthermore, the resistance drop in correspondence of the transition is large and abrupt even when approaching T_{MIT} , demonstrating the potential of voltage-actuated VO₂ for temperature-stable abrupt switching applications. Figure 3.7 shows the actuation power P_{act} at different temperatures, including results for the transition back to the insulating state. In both cases the dependence is linear, in accordance with the Joule heating model.

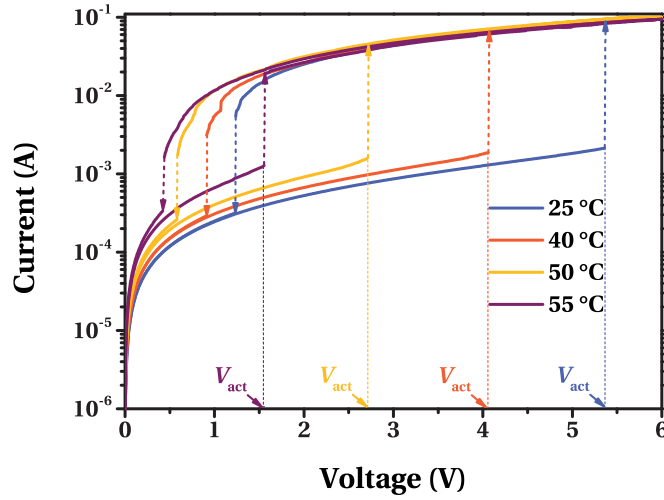


Figure 3.8 – Abrupt switching based on VO₂ E-MIT, shown by IV curves at different temperatures for the VO₂ switch with a resistor in series.

3.3 Steep slope characterization

Figure 3.8 shows the IV characteristics at different temperatures for the same switch ($W = 50\mu\text{m}$, $L = 7.5\mu\text{m}$), actuated with a DC voltage source, using $R_s = 52\Omega$. Due to the lower needed P_{act} , the actuation voltage decreases from 5.36 V at 25 °C to 1.55 V at 55 °C, including the voltage drop on R_s . In order to more accurately show the behavior of the isolated VO₂ switch, independent of the value of R_s , in Figure 3.9 it is shown the measured current as a function of the intrinsic voltage V_{int} and iso-power curves corresponding to the power thresholds P_{act} at different temperatures, decreasing from 11.8 mW at 25 °C to 1.9 mW at 55 °C.

Due to the small value of R_s as compared to R_{VO_2} in the OFF state, the voltage drop on the series resistance is negligible, and the intrinsic actuation voltage is comparable to the previously reported V_{act} , decreasing from 5.25 V at 25 °C to 1.48 V at 55 °C.

Figure 3.10 shows the dependence of R_{VO_2} on the intrinsic voltage at different temperatures. The switch resistance ratio is defined as the ratio between the value of R_{VO_2} right before actuation and the one right after; this definition is possible due to the abruptness of the E-MIT, without intermediate points measured between the OFF and ON state. We report a switch resistance ratio higher than 10^2 in the whole range of studied temperatures, from 310.1 (2466.1 Ω /7.9 Ω) at 25 °C to 102.7 (1643 Ω /16 Ω) at 55 °C.

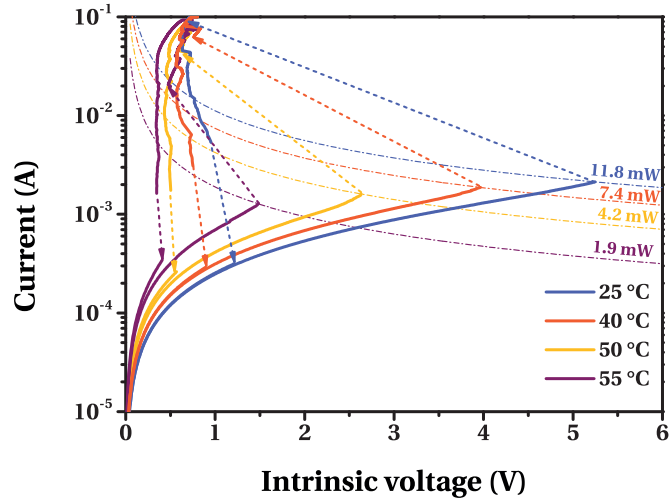


Figure 3.9 – Current dependence on the intrinsic voltage drop on the VO₂ switch at different temperatures, with iso-power curves showing the power dissipation spike in correspondence of the E-MIT.

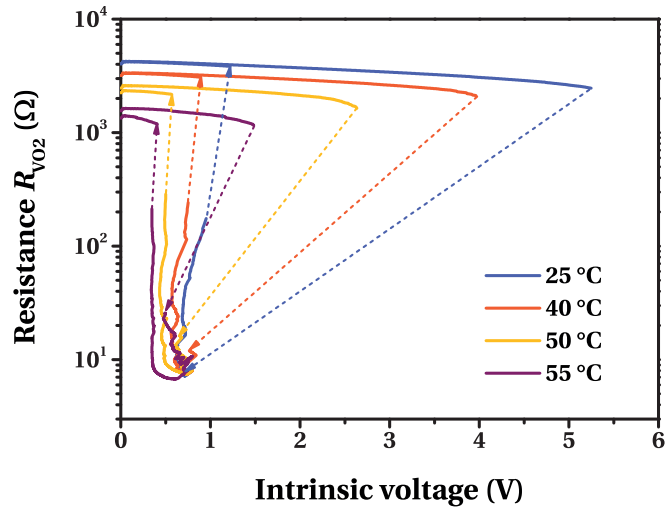


Figure 3.10 – Dependence of intrinsic switch resistance $R_{VO_2} = V_{int}/I$ on the intrinsic voltage V_{int} .

The IV characteristics reported in Figure 3.8 show a sudden increase in current for small variations of V_{DC} around V_{act} . In order to quantify the steepness of this transition, the slope S is calculated similarly to the subthreshold swing in a diode switch, as the increase in V_{DC} at the onset of the E-MIT necessary to have an increase in current by

Chapter 3. VO₂ MIT for steep-slope electronic switches

one decade in a log-lin plot; this corresponds to the following definition:

$$S = \left[\frac{d(\log_{10} I)}{dV_{DC}} \right]^{-1} \Big|_{V_{DC}=V_{act}} \quad (3.3)$$

For better accuracy in the calculation of the slope, the measurements were performed at the maximum resolution available with the equipment in use, i.e. with 1 mV incremental steps. High-resolution IV measurements at different temperatures (shown in Figure 3.11 for T approaching T_{MIT}) demonstrate that S is extremely abrupt (< 1 mV/dec) and it has very little dependence on temperature below 50 °C. This unique behavior is observed for the first time and suggests that in a three-terminal embodiment, for instance by using an electrothermal heating electrode as a gate, such a MIT switch could offer a unique temperature-stable solution for 1 mV/dec logic switching.

The high-resolution IV curves in Figure 3.11, measured from 50 °C to 60 °C, show that even if the slope is more dependent on temperature, from 50 °C to 57 °C it is still possible to observe an abrupt increase in current higher than one decade at the E-MIT, and the slope is degraded only by the decrease in resistance ratio. Further approaching T_{MIT} , the steepness of the switch is severely affected by partial switching events distributed in a wider voltage range.

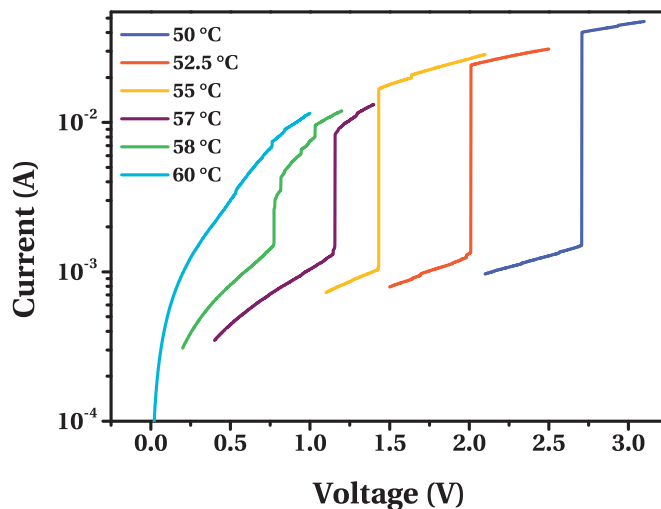


Figure 3.11 – High-resolution IV curves (1 mV incremental steps) for voltages around the E-MIT, at temperatures near the thermal transition. The full hysteresis cycle is not shown due to the limited maximum number of points allowed by the measurement setup.

3.3. Steep slope characterization

Figure 3.12 summarizes the results on the temperature dependence of the slope and the actuation voltage. The reported S values can be considered deep-sub-thermal, varying from 0.24 mV/dec at 25 °C to 0.38 mV/dec at 50 °C, with a low dependence on temperature below 50 °C ($< 5.5 \mu\text{V}^\circ\text{C}/\text{dec}$). The actuation voltage is decreasing with the temperature, as expected, because less injected power is requested to induce the E-MIT at higher temperatures.

Another remarkable fact observable in Figure 3.9 is the high level of current in the ON state of the switch, I_{ON} , reaching values higher than 1.8 mA/ μm at 5.5 V. Furthermore, as shown in Figure 3.13, the dependence of I_{ON} on temperature is very little ($2.7 \mu\text{A}^\circ\text{C}/\mu\text{m}$) suggesting a high stability versus temperature of the switch conductivity in the ON state. These values, normalized per width, offer a direct comparison with other steep slope devices, showing the capacity of MIT switches to provide high levels of current, similar to advanced CMOS.

On the other hand, the main drawback is the reported high current before the MIT transition, I_{act} , also plotted in Figure 3.13, which with the same normalization per unit width is 43 $\mu\text{A}/\mu\text{m}$, quasi-stable in the considered temperature range. This relatively high current in the OFF state can be reduced by doping VO_2 with elements increasing its sheet resistivity [176].

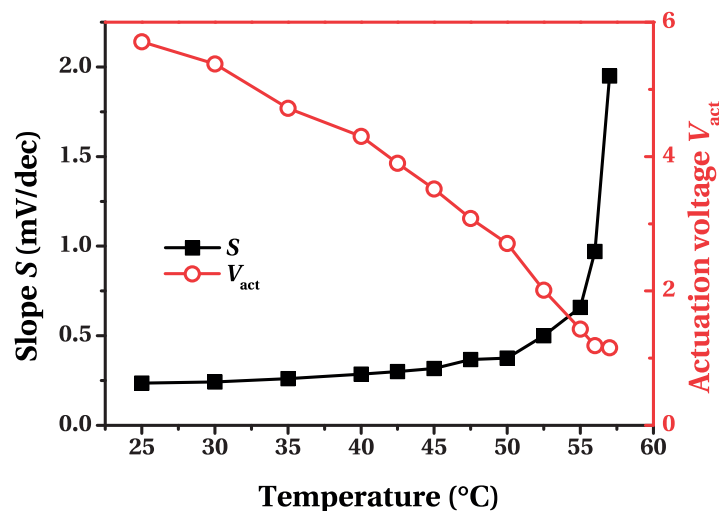


Figure 3.12 – Dependence on temperature of the slope and the actuation voltage of the VO_2 abrupt switch.

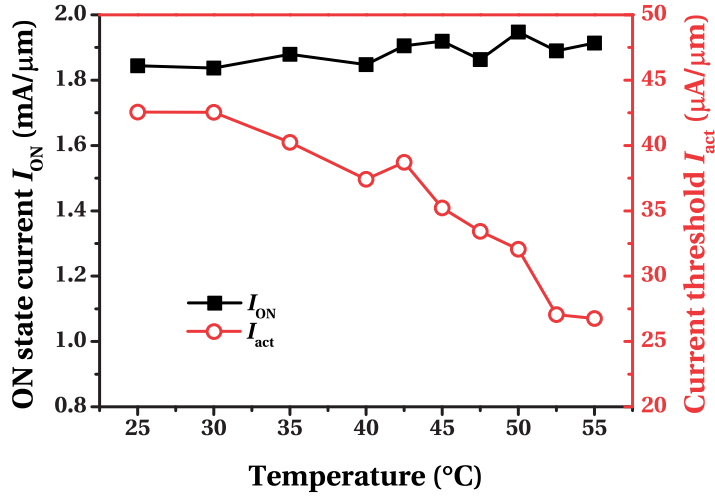


Figure 3.13 – Dependence on temperature of the current in the ON state and the actuation current.

3.4 Low voltage VO₂ switches

The results presented in the previous sections encourage further investigations for the use of VO₂ for applications requiring steep-slope switches. An important figure of merit to evaluate the performance of the switch is the actuation voltage, which must be minimized in order for the VO₂ switches to be attractive for industrial applications. As shown in Figure 3.9, the actuation voltage for the characterized switch ($W = 50\mu\text{m}$, $L = 7.5\mu\text{m}$) is lower than 5.5 V at room temperature.

A possible way to decrease the actuation voltage consists in decreasing the length of the switch, in concordance with the electrothermal actuation model based on Joule heating. The power required to actuate the VO₂ switch can be expressed as:

$$P_{act} = \alpha W t L \Delta T \quad (3.4)$$

$$\Delta T = T_{MIT} - T \quad (3.5)$$

where α is the thermal conductance to the environment. Expressing P_{act} in terms of the actuation voltage we obtain:

$$\frac{V_{\text{act}}^2}{R_{\text{VO}_2}} = \alpha L W t \Delta T \quad (3.6)$$

$$V_{\text{act}} = \sqrt{\alpha L W t \Delta T R_{\text{VO}_2}} \quad (3.7)$$

$$R_{\text{VO}_2} = \rho_{\text{VO}_2} \frac{L}{W t} \quad (3.8)$$

substituting (3.8) in (3.7) we obtain:

$$V_{\text{act}} = \sqrt{\alpha \Delta T \rho_{\text{VO}_2} L} \quad (3.9)$$

showing that for the purely Joule heating-based model the actuation voltage is linearly proportional to the length of the switch, in concordance with the measurements shown in Figure 2.15. A previous work on VO₂ junctions with sub-micrometer lengths reported actuation voltages as low as 1.1 V [23]; moreover, a study on the scalability of V_{act} with L for VO₂ nano-gap junctions highlighted the importance of the work function difference between VO₂ and the metal contact, explaining the extrapolation of non-zero values for V_{act} when $L \rightarrow 0$ [111].

In this work we consider a different approach for the reduction of V_{act} , optimizing the metal contact geometry to focus the electric field at specific locations of the VO₂ junction.

3.4.1 Device concept

Figure 3.14 (a) shows the schematic diagram of the proposed device; conventional metal-VO₂ contacts like the ones shown in Figure 3.3 are extended with triangular-shaped “spikes” protruding on the VO₂ junction. The aim of this section is to prove that VO₂ switches with spikes actuate by E-MIT at a lower voltage than conventional flat junctions with the same length. As shown in Figure 3.14 (b), for fair comparison the length L is measured starting and ending at the tip of the spikes.

The working principle of the proposed device consists in exploiting the fact that in an irregularly-shaped conductor, in conditions of electrostatic equilibrium, excess

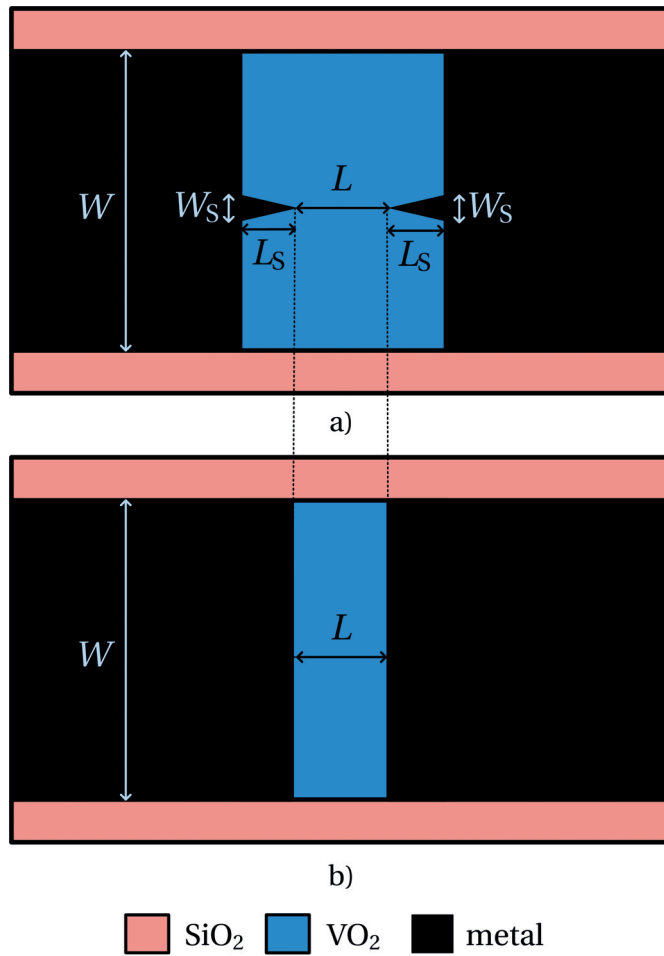


Figure 3.14 – a) Schematic diagram of the proposed low-voltage VO₂ switch. The metal spikes (length L_s , width W_s) allow increasing locally the magnitude of the electric field. b) Flat-junction VO₂ switch employed for performance comparison, having the same length L and width W of the device with spikes.

electric charges accumulate with higher density in regions of larger curvature. This larger charge quantity, combined with the fact that the charge repulsive forces will be mostly directed perpendicular to the surface, results in producing a stronger electric field in locations where the conductor is most curved.

As a consequence, the electric field profile for the VO₂ switch structure in Figure 3.14 (a) will have its maximum at the tip of the spikes, where the radius of curvature is minimized.

The temperature reached at equilibrium depends on the obtained electric field, as

shown hereinafter. The total power dissipated P in the VO₂ region is given by:

$$P = \int_V \vec{J} \cdot \vec{E} dV \quad (3.10)$$

where V is the volume of the VO₂ region, \vec{J} is the current density and \vec{E} is the electric field. In each point of the material the local formulation of Ohm's law states that:

$$\vec{J} = \sigma \vec{E} \quad (3.11)$$

where σ is the conductivity of VO₂. By substituting (3.11) in (3.10) we obtain:

$$P = \int_V \sigma |\vec{E}|^2 dV \quad (3.12)$$

showing that the power dissipated, and therefore the temperature increase, will be higher in regions of higher electric field. If the local temperature increase is high enough to initiate the E-MIT, the VO₂ region in the proximity of the tip of the spike will transition to the metallic state, extending the length of the spike and decreasing the effective length of the switch. This mechanism would constitute a positive feedback increasing the electric field for the same voltage and creating a conductive filament connecting the metal electrodes in correspondence of the spike location.

3.4.2 Electrothermal simulations

In order to validate the proposed working principle, electrothermal simulations have been performed using the finite element method (FEM) in COMSOL Multiphysics. Figure 3.15 (a) shows the full simulated geometry. The boundaries of the simulation domain are far enough from the active region so that the results are unchanged if the domain is extended. As shown in Figure 3.15 (b), the tetrahedral mesh has been refined in the proximity of the metal spikes, in order to properly simulate the effect of the increased curvature, occurring in the range of few tens of nanometers.

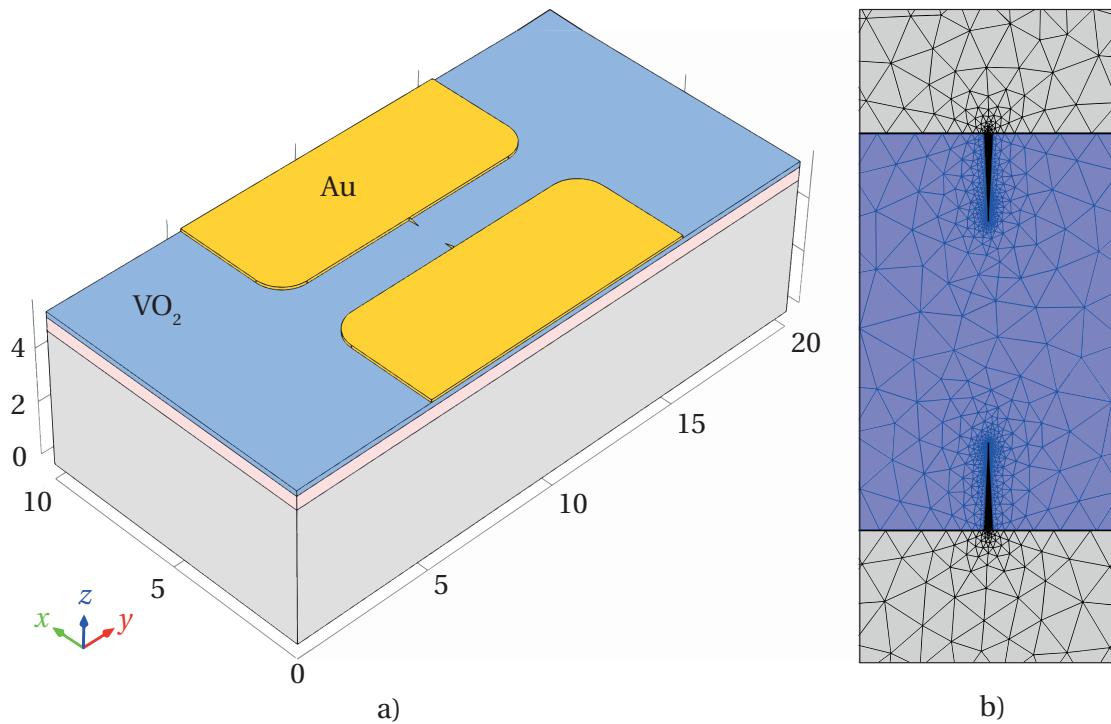


Figure 3.15 – a) Full geometry domain for the electrothermal simulations used to estimate the efficiency of the increased electric field in correspondence of the metal spikes to actuate the VO₂ switch at a lower voltage as compared to conventional flat VO₂ junctions with the same length, assuming an electrothermal actuation model based purely on Joule heating. Grid labels in μm . b) Dense mesh profile in correspondence of the spikes location. The mesh minimum element size has been fixed to 4 nm, for spikes with width $W_s = 40 \text{ nm}$ and length $L_s = 400 \text{ nm}$.

The substrate is made of $5 \mu\text{m}$ thick silicon, extended on a $10 \times 20 \mu\text{m}$ area. A 500 nm SiO₂ layer on top of the substrate acts as an electrical insulator. The VO₂ layer is 200 nm thick and its electrical conductivity is introduced as a temperature-dependent function, obtained using a cubic interpolation of the experimental results shown in Figure 2.6.

In this way the coupled FEM electrical and thermal simulations require multiple iterations to calculate the VO₂ resistance change due to Joule heating and as a consequence the change in current, until convergence is reached. The metal electrodes are made by 200 nm gold (Au), patterned to create junctions with constant width and length ($W = 10 \mu\text{m}$, $L = 1 \mu\text{m}$) and spikes with variable aspect ratio $AR = L_s/W_s$. In order to isolate the effect of the spikes, the corners of the contacts are shaped with a quarter of circumference with a radius of $1 \mu\text{m}$.

Table 3.1 – Material properties used for the electrothermal simulations.

Material	Electrical conductivity (S/m)	Relative permittivity	Thermal conductivity (Wm ⁻¹ K ⁻¹)	Heat capacity (Jkg ⁻¹ K ⁻¹)
Si	/	11.7	130	700
SiO ₂	/	4.2	1.4	730
VO ₂	from 20 to 6.4 × 10 ⁴	30	6	690
Au	45.6 × 10 ⁶	1	317	129

All the material parameters used for the electrothermal simulation are summarized in Table 3.1.

The simulations are performed in steady-state conditions, applying a constant potential difference between the two Au contacts. The heat dissipation is modeled by fixing the temperature at the bottom of the substrate to room temperature $T_0 = 293.15$ K and by adding convective heat flux boundary conditions on the top surfaces. The heat loss due the convection can be calculated as:

$$P = hA(T - T_{\text{ext}}) \quad (3.13)$$

where h is the convection heat transfer coefficient, A is the exposed surface area and T_{ext} is the external temperature, set to $T_0 = 293.15$ K. For the following simulations, h has been fixed to $5 \text{ Wm}^{-1} \text{ K}^{-2}$.

Simulations of flat junctions

A first set of simulations was performed to assess the electric field distribution in flat junctions and its effect on the temperature profile and the resulting actuation voltage. These results are used as a reference to benchmark the performance of VO₂ switches with spikes.

Figure 3.16 shows the electric field on the top surfaces of a VO₂ switch with flat junction, for a simulated geometry with the dimensions shown in Figure 3.15 (a) and an applied voltage $V_{\text{DC}} = 7$ V, close to the actuation voltage. As expected for flat electrodes, the electric field is constant along the width of the switch, and it

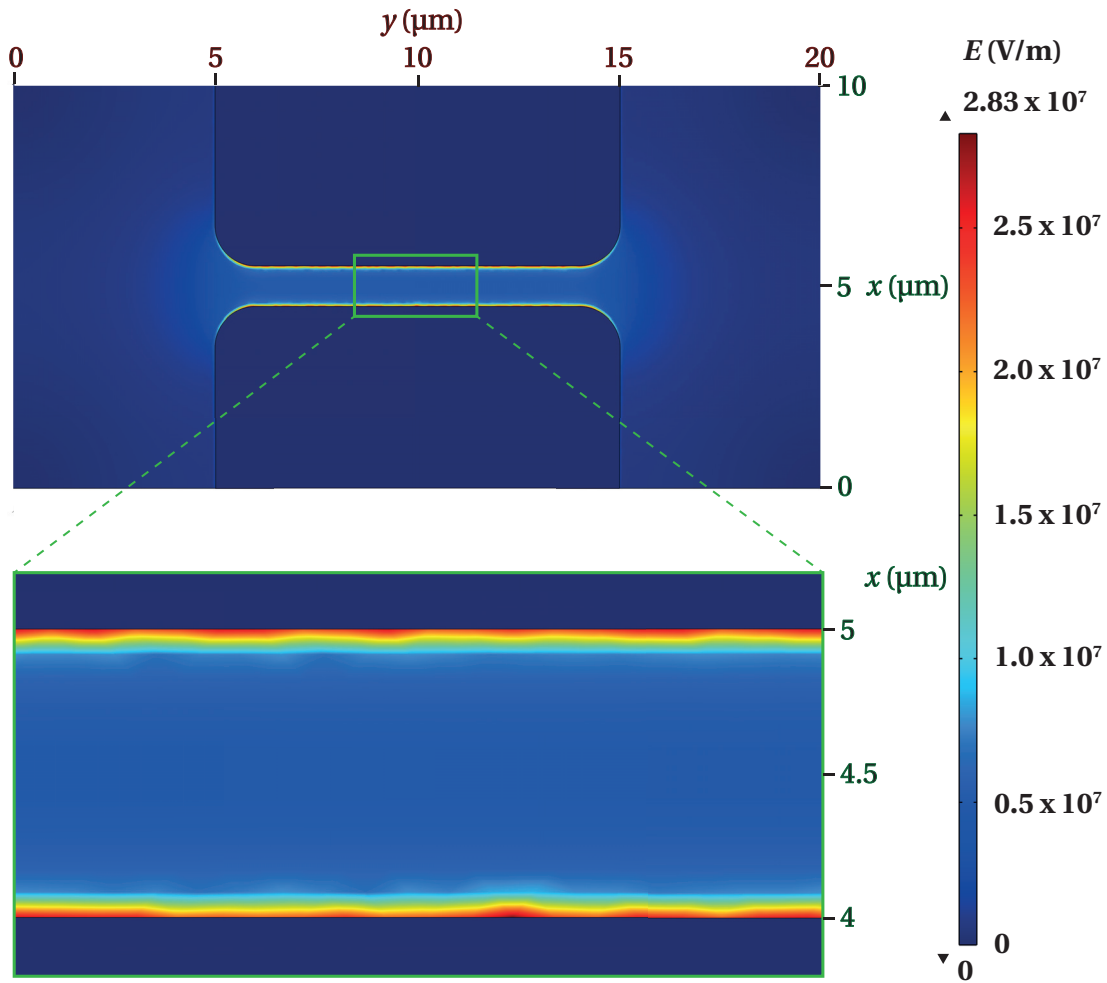


Figure 3.16 – Electric field on the top surface of a VO₂ switch with flat electrodes for an applied voltage $V_{DC} = 7\text{V}$, with zoom on the VO₂ region.

decreases going further from the interface with the metal electrode, from a maximum of $2.83 \times 10^7\text{V/m}$ at the interface ($x = 0\mu\text{m}$) to a minimum of $5.04 \times 10^6\text{V/m}$ in the middle ($x = 0.5\mu\text{m}$).

In order to assess the actuation voltage a parametric sweep was introduced in the simulation, with minimum step voltage of 0.1 V; the results are summarized in Figure 3.17, showing the actuation voltage $V_{act} = 7.2\text{V}$. The results in function of the position along the x -axis in the junction (corresponding to the length of the device) are calculated on a line on top of the VO₂ surface and in the center of the y -axis (corresponding to the width).

Figure 3.17 (a) shows the electric field profile along the length of the switch for different

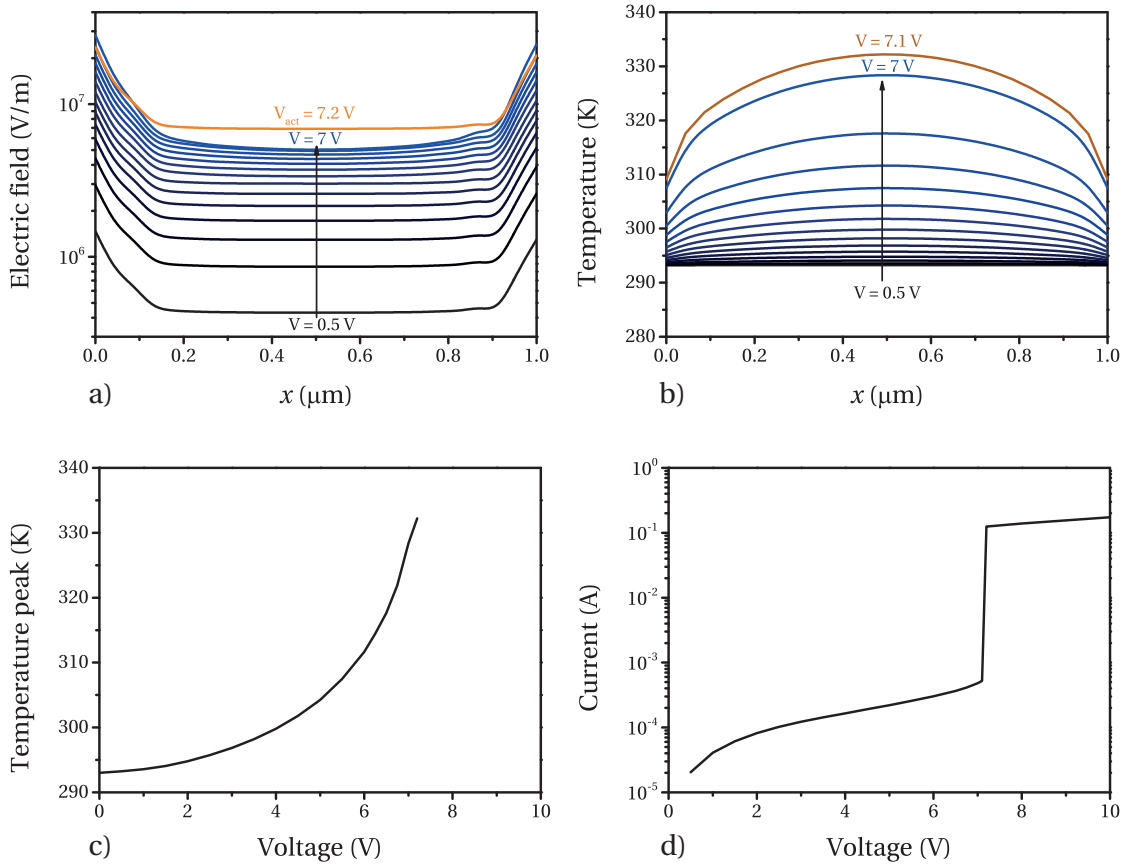


Figure 3.17 – a) Electric field profile for different voltage levels along the length of the switch, from the interface with one metal electrode ($x = 0 \mu\text{m}$) to the other ($x = 1 \mu\text{m}$), on top of the VO₂ surface and in the middle of the junction ($y = 10 \mu\text{m}$). The curves pre-actuation correspond to voltage steps of 0.5 V. b) Temperature profile along the length of the switch. c) Dependence of the maximum VO₂ temperature in function of the applied voltage, for $V_{\text{DC}} < V_{\text{act}}$. d) IV characteristics, obtained applying a limiting series resistor $R_s = 50 \Omega$.

voltage levels before actuation (0.5 V steps) and in correspondence of $V_{\text{DC}} = V_{\text{act}} = 7.2 \text{ V}$, showing that the field drops rapidly in the first 100 nm away from the interface with the metal electrodes.

Figure 3.17 (b) shows the temperature profile along the length of the switch for different voltage levels before actuation. The temperature peak is in the middle of the junction ($x = 0.5 \mu\text{m}$) and, as better shown in 3.17 (c), it increases at a higher rate for voltage levels approaching V_{act} . Due to the absence of a limiting series resistor and the low aspect ratio of the switch ($W/L = 10$), the very high current for voltages $V_{\text{DC}} \geq V_{\text{act}}$ causes temperature values beyond the VO₂ melting point (1967 °C [177]).

Chapter 3. VO₂ MIT for steep-slope electronic switches

Figure 3.17 (d) shows the IV characteristics of the switch for V_{DC} swept up to 10 V and applying a series resistor of 50 Ω to limit the current in the VO₂ metal state, showing a steep increase of more than two decades in correspondence of the E-MIT.

Simulations of junctions with spikes

Another set of simulations was performed for the geometry domain shown in Figure 3.15 (a) using spikes with constant length ($L_S = 400$ nm) and variable width, in order to study the effect of the spike aspect ratio $AR = L_S / W_S$. Figure 3.18 (a) shows the electric field on the top surfaces for $V_{DC} = 7$ V and $AR = 2$.

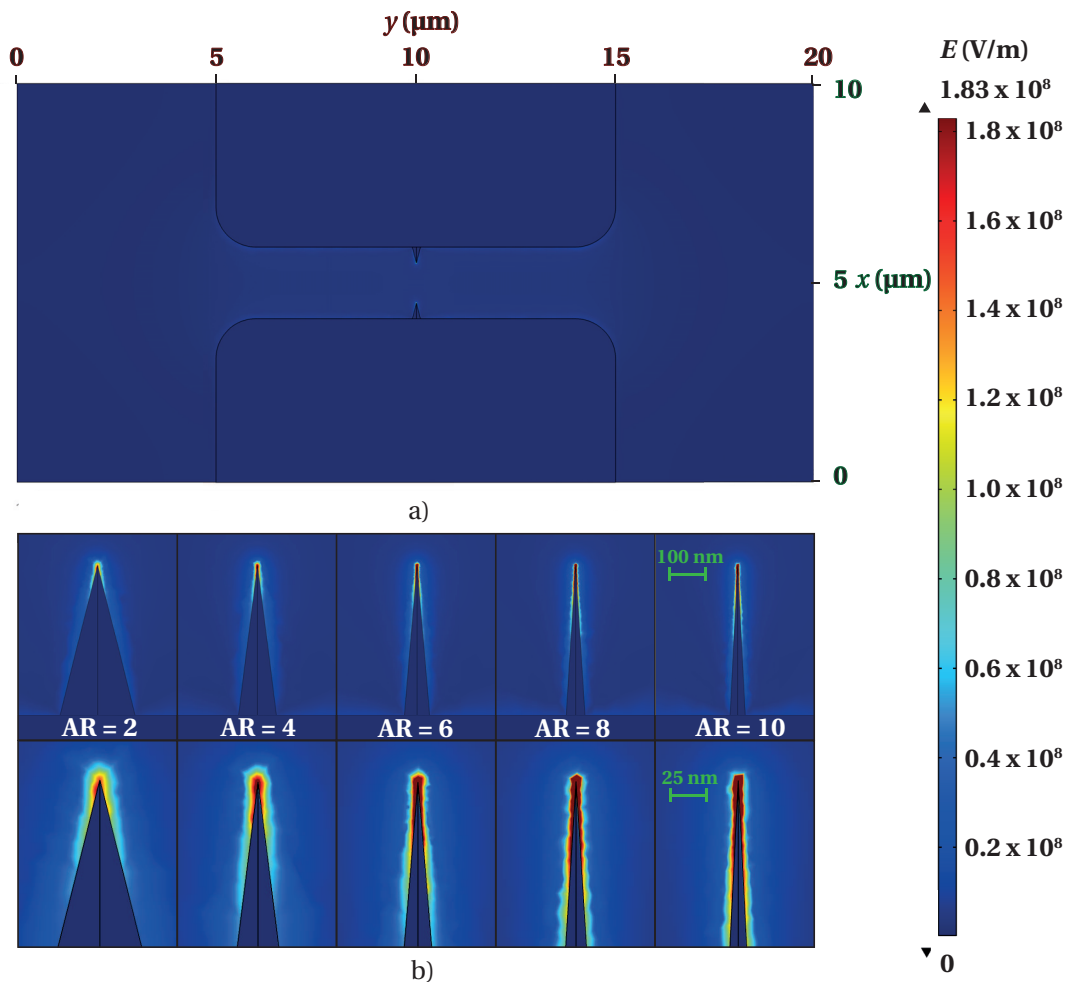


Figure 3.18 – a) Electric field on the top surface of a VO₂ switch with electrodes employing spikes to increase locally the electric field; applied voltage $V_{DC} = 7$ V; spike aspect ratio $AR = 2$. b) Zoom on the spike, showing an increase in electric field with the spike aspect ratio.

The maximum of the electric field is located as expected in correspondence of the tip of the spike, and its value (1.83×10^8 V/m) is more than 6 times higher than the one obtained in flat junctions with the same V_{DC} . Figure 3.18 (b) provides a zoomed view of the electric field in the proximity of the spikes. The spike aspect ratio AR is increased from 2 to 10, showing the possibility to reach higher electric fields using narrower spikes.

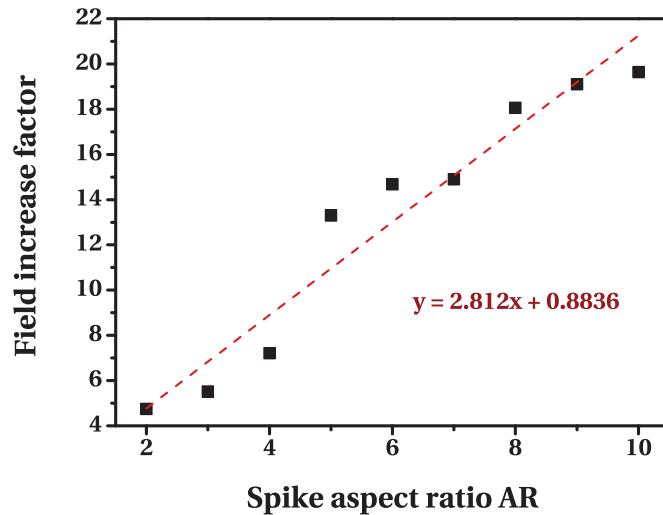


Figure 3.19 – Simulation results and linear interpolation of the field increase factor (ratio between the maximum electric field in junctions with spikes and the one in flat junctions) in function of the spike aspect ratio.

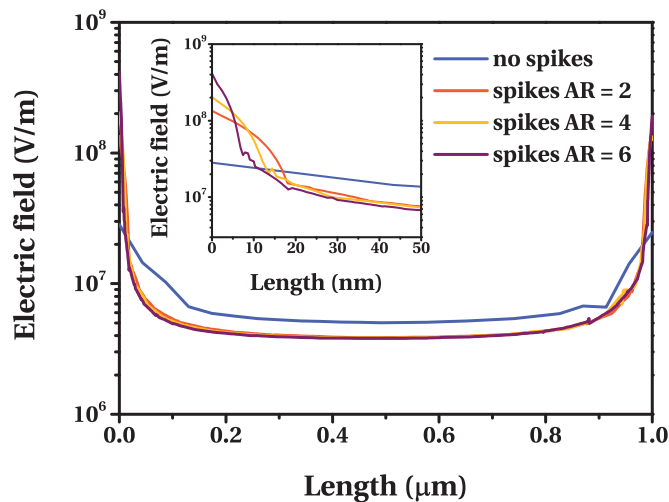


Figure 3.20 – Electric field profile for $V_{DC} = 7V$ along the length of the switch in the middle of its width, comparing flat junctions and junctions with spikes with different aspect ratios. Inset: zoom on the first 50 nm away from the junction.

Chapter 3. VO₂ MIT for steep-slope electronic switches

The ratio of the maximum electric fields for junctions with spikes and flat junctions is plotted in function of the spike aspect ratio in Figure 3.19 keeping constant $V_{DC} = 7V$, reaching values as high as 20. The results show that the improvement in the field increase factor can be fitted with a linear function (coefficient of determination $R^2 = 0.9403$).

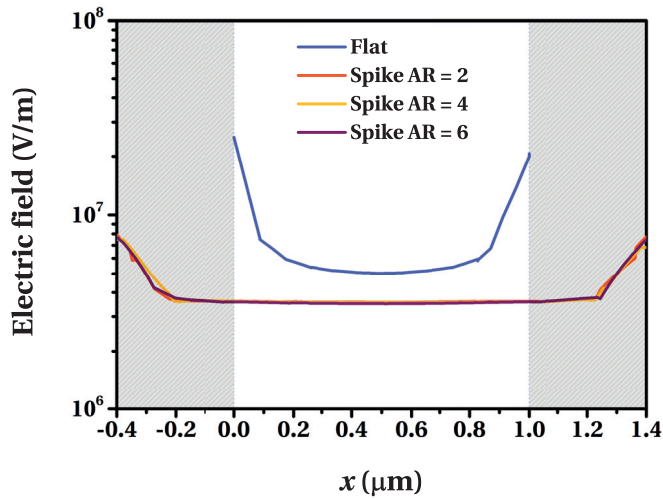


Figure 3.21 – Electric field profile for $V_{DC} = 7V$ along the length of the switch, 500 nm away from the middle of its width, comparing flat junctions and junctions with spikes with different aspect ratios. The shaded regions correspond to the additional length with respect to the flat junctions due to the insertion of the spikes on both sides ($L_S = 400\text{ nm}$).

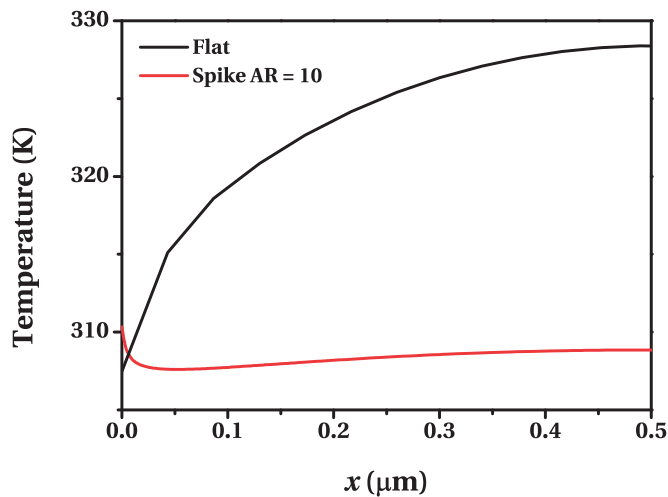


Figure 3.22 – Temperature profile for $V_{DC} = 7V$ along the length of the switch in the middle of its width, comparing a flat junction and a junction with a spike with AR = 10. The high field induced at the spike is effective only near the interface with VO₂.

3.4. Low voltage VO₂ switches

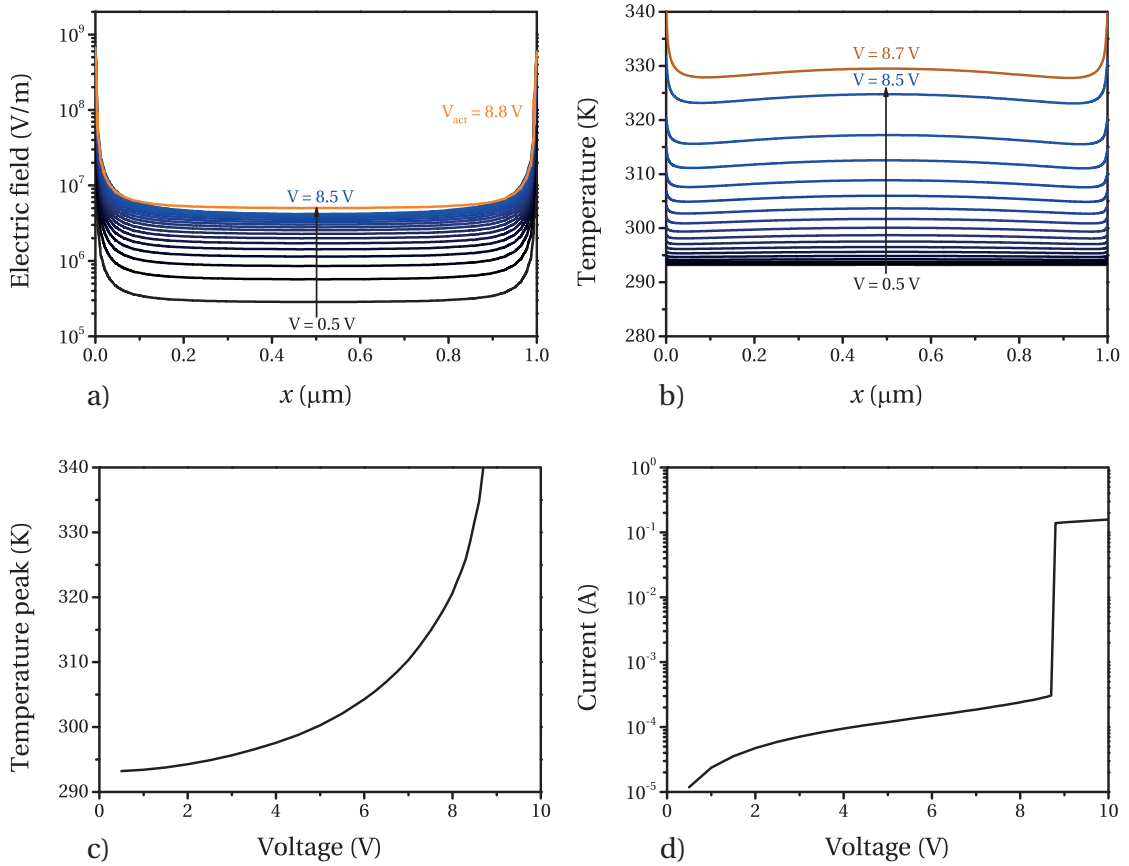


Figure 3.23 – a) Electric field profile for different voltage levels along the length of a switch with spikes ($AR = 10$), from the tip of a spike ($x = 0 \mu\text{m}$) to the other ($x = 1 \mu\text{m}$), on top of the VO₂ surface and in the middle of the junction ($y = 10 \mu\text{m}$). The curves pre-actuation correspond to voltage steps of 0.5 V. b) Temperature profile along the length of the switch. c) Dependence of the maximum VO₂ temperature in function of the applied voltage, for $V_{\text{DC}} < V_{\text{act}}$. d) IV characteristics, obtained applying a limiting series resistor $R_s = 50 \Omega$.

Figure 3.20 shows the electric field profile along the length of the switch for different spike aspect ratios, compared to the one obtained using flat junctions, while keeping constant $V_{\text{DC}} = 7 \text{ V}$. As better shown in the inset, the electric field at the interface is highly dependent on AR, but the effect of the spike vanishes around 20 nm away from the junction. All the field profiles overlap around 150 nm away.

These results confirm that the spikes allow to increase locally the electric field for the same applied voltage. However, as shown in Figure 3.21, in which the electric field profile across the length of the switch is plotted for a line 500 nm away from the middle of the width, the added junction length due to the insertion of the spike causes

Chapter 3. VO₂ MIT for steep-slope electronic switches

a considerable decrease in the electric field far from the center of the device with respect to the flat junction.

This drawback results ultimately in a lower peak temperature for the device with spikes, as shown in Figure 3.22, where the temperature profile along the length of the switch in the middle of its width is plotted for a flat junction and a junction with spikes (AR = 10) at $V_{DC} = 7V$. The VO₂ temperature is indeed higher at the tip of the spike with respect to the interface with the flat junction, but the temperature peak for the flat junction (located at $x = 0.5\mu m$) is much higher, due to the higher total dissipated power.

Figure 3.23 summarizes the results for a junction with spikes with AR = 10. Figure 3.23 (a) shows that the electric field can be more than two orders of magnitude higher at the tip of the spike with respect to the center. As a consequence, differently from what observed for flat junctions, the temperature peak is obtained at the interface with the electrode (Figures 3.23 (b-c)). The IV characteristics in Figure 3.23 (d) show the actuation voltage $V_{act} = 8.8V$.

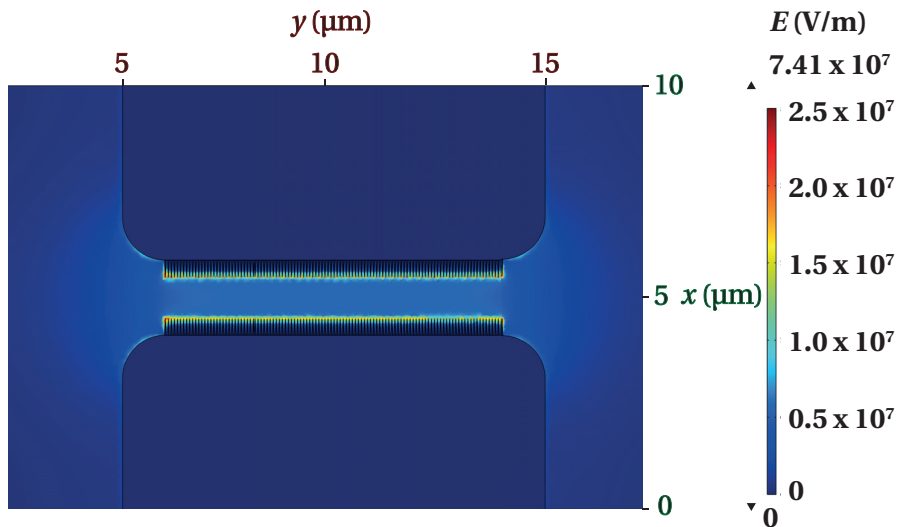


Figure 3.24 – a) Electric field on the top surface of a VO₂ switch with electrodes employing spikes along the whole width of the junction; applied voltage $V_{DC} = 6.5V$; spike aspect ratio AR = 10.

Simulations of junctions with multiple spikes

A possible way to limit the drawback explained above, resulting in a higher actuation voltage for the junction with spikes, consists in minimizing the ratio L_S/L in order

to decrease the excess length due to the insertion of the spikes. However, increasing L beyond 1 μm , even if convenient for a validation of the concept, would probably end up in too high actuation voltages for both kind of junctions. On the other hand, decreasing L_s below 400 nm while keeping high aspect ratios could be prohibitive from a fabrication point of view.

Another approach, followed in the rest of the discussion and validated by experimental results, consists in adding multiple spikes along the whole width of the junction. Figure 3.24 shows the simulation of the electric field distribution on the surface of this structure for $V_{\text{DC}} = 6.5\text{V}$, reaching a higher peak electric field than the flat junction case.

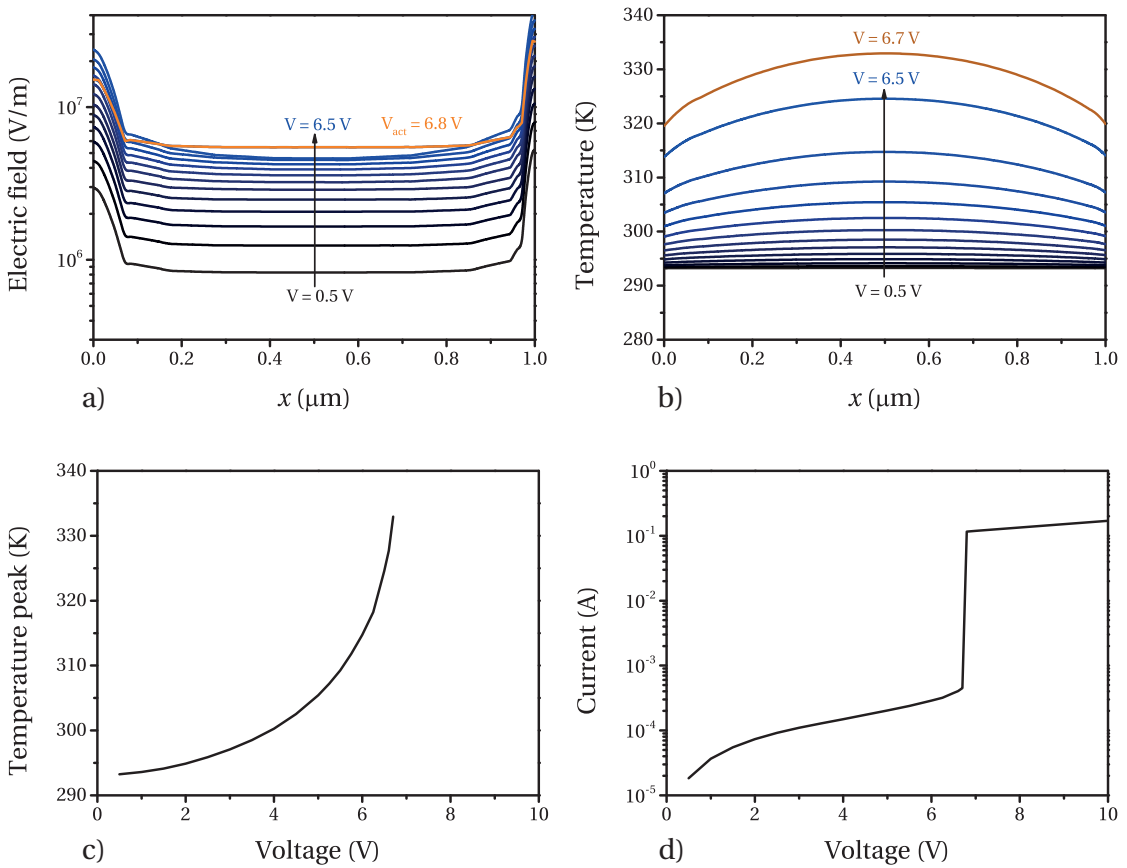


Figure 3.25 – a) Electric field profile for different voltage levels along the length of a switch with spikes ($\text{AR} = 10$) along the whole width of the junction, from the tip of a spike ($x = 0\mu\text{m}$) to the other ($x = 1\mu\text{m}$), on top of the VO₂ surface and in the middle of the junction ($y = 10\mu\text{m}$). The curves pre-actuation correspond to voltage steps of 0.5 V. b) Temperature profile along the length of the switch. c) Dependence of the maximum VO₂ temperature in function of the applied voltage, for $V_{\text{DC}} < V_{\text{act}}$. d) IV characteristics, obtained applying a limiting series resistor $R_s = 50\ \Omega$.

Chapter 3. VO₂ MIT for steep-slope electronic switches

An additional advantage following this approach is related to process variability issues. Due to resolution limits in lithography processes, the fabricated spikes will not be as sharp as in the design, and the radius of curvature would be affected by the process variability; therefore including multiple spikes would maximize the chance to have at least a spike with a radius of curvature lower than the target specification.

This design, simulated for the same geometry used for flat junctions and junctions with single spikes, results in a lower actuation voltage $V_{\text{act}} = 6.8\text{V}$. For comparison purposes, the electric field on the top surfaces of the device, shown in Figure 3.24, is calculated for a bias voltage before actuation, $V_{\text{DC}} = 6.5\text{V}$.

The results on the performance of the device are summarized in Figure 3.25, showing similar temperature distributions to the flat junction case (maximum in the middle: $x = 0.5\mu\text{m}$) but with higher values for the same applied V_{DC} , confirming that this approach is promising for the implementation of low-voltage VO₂ switches.

3.4.3 Fabrication

The fabrication process was carried out in the Laboratory of Micro- and Nanofabrication (LMN) at the Institut National de la Recherche Scientifique (INRS), University of Quebec. In a first fabrication run, based on the process flow shown in figure 3.26, 500 nm thick epitaxial VO₂ was grown on a 1'' circular sapphire substrate (Al₂O₃(1 $\bar{1}$ 02) orientation) by Pulsed Laser Deposition using a Krypton Fluoride laser (wavelength $\lambda = 248\text{nm}$) at a repetition rate of 10 Hz. The vanadium metal target was ablated with a laser fluence of $2\text{J}/\text{cm}^2$. Before starting the deposition, the chamber was pumped down to 1.33×10^{-6} mbar. During the deposition, the pressure was kept constant at 3.6×10^{-2} mbar, with a constant oxygen flow of 5 sccm. The substrate temperature was set to 550 °C, and the target-to-substrate distance was 6.5 cm. In order to improve the film homogeneity, the substrate was rotated during deposition.

Figure 3.27 (a) shows the SEM top view of the deposited 500 nm VO₂ thin film. The VO₂ film presents good crystallinity, with the zoom in Figure 3.27 (b) showing a grain size as high as 600 nm. However, differently from the films obtained with sputtering, the surface is covered by μm -sized droplets characteristic of thin films deposited by PLD [178].

The electrodes are made of a 100 nm thick Cr/Cu/Au metal stack. Electron beam

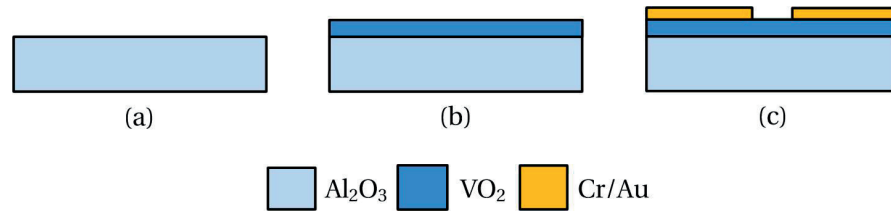


Figure 3.26 – Process flow for the VO₂ switches with spikes fabricated at INRS. a) Substrate preparation. b) VO₂ PLD deposition, performed for more thicknesses, from 100 nm to 500 nm. c) Patterning of 100 nm thick Cr/Cu/Au electrodes by e-beam lithography and lift-off.

lithography and lift-off were employed to obtain the very high resolution features required to minimize the radius of curvature of the spikes. However, the high size and density of droplets on the 500 nm VO₂ surface did not allow to properly pattern the metal electrodes, particularly in correspondence of the spikes. A possible way to decrease the size and density of the droplets consists simply in reducing the deposition time.

This is the approach that was followed for a second fabrication run, in which a 100 nm thick polycrystalline VO₂ film was deposited by PLD on a 1 square in Si/SiO₂ substrate. As shown in Figure 3.28 (c), using the same scale as Figure 3.28 (a), the density of droplets has been significantly reduced. As a consequence of the lower thickness, the VO₂ grain size observable in Figure 3.28 (d) is smaller than what obtained for the 500 nm film.

Figure 3.28 reports the SEM top view of a final device, showing that the droplets density in the 100 nm film has been reduced enough to allow the realization of devices without droplets interfering with their active region.

Using this process, devices with constant width ($W = 20\mu\text{m}$) and different lengths (L varying from $2\mu\text{m}$ to $10\mu\text{m}$) have been realized, both with spikes and without spikes. Furthermore, the devices with spikes present a geometrical variation on the spike length (L_s varying from $400\mu\text{m}$ to $1600\mu\text{m}$) and its aspect ratio (AR varying from 3 to 6). Moreover, 12 instances of the same device variation were included in the layout, in order to consider variability effects on the device performance.

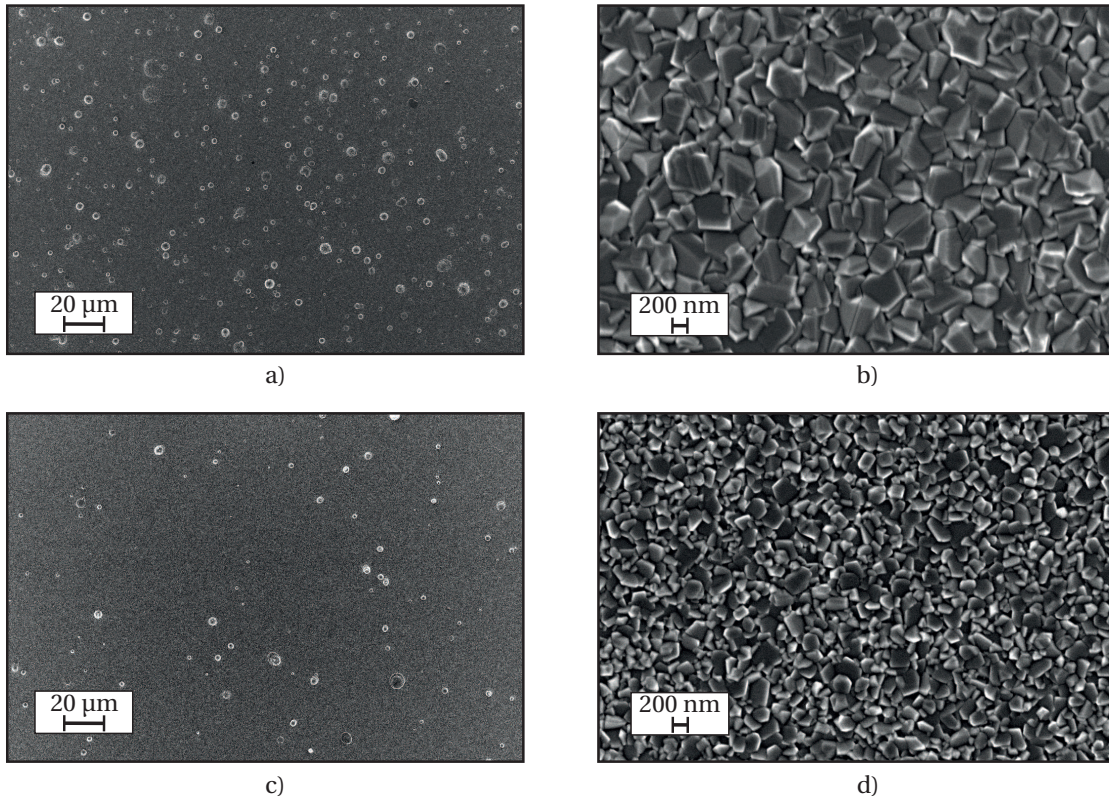


Figure 3.27 – a-b) SEM images of the 500 nm thick VO₂ film deposited by PLD on sapphire. c-d) SEM images of the 100 nm thick VO₂ film deposited by PLD on a Si/SiO₂ substrate.

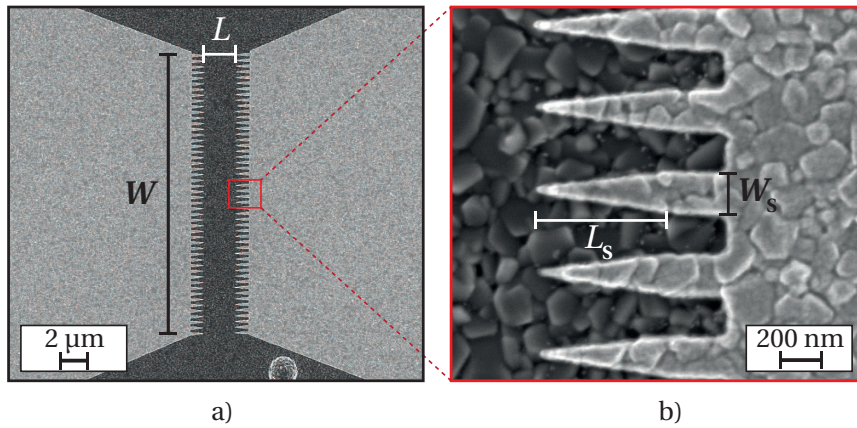


Figure 3.28 – a) Top-view of a fabricated VO₂ two-terminal switch ($W = 50\mu\text{m}$, $L = 7.5\mu\text{m}$). b) Zoom on the spikes, showing extremely sharp profiles.

3.4.4 Electrical characterization

First of all, the deposited 100 nm VO₂ thin film was characterized by 4-point probes measurements as described in section 2.2.2. The resistivity curve shown in Figure 3.29

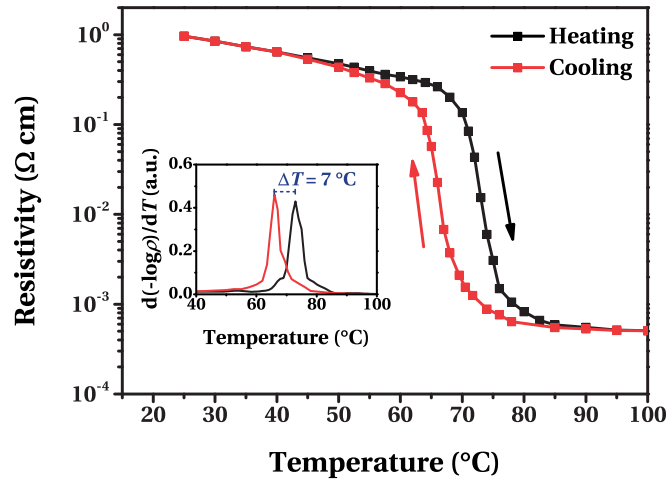


Figure 3.29 – VO₂ electrical resistivity dependence on temperature, showing a reconfigurability higher than 3 decades and a steep transition at $\sim 73^\circ\text{C}$. Inset: $d(-\log \rho)/dT$ curves while heating and cooling the VO₂ film, showing a narrow hysteresis of $\sim 7^\circ\text{C}$.

confirms the good quality of the deposited film, with a reconfigurability of more than 3 orders of magnitude.

DC measurements were performed at room temperature using the biasing scheme in Figure 3.4 (b) as described in section 3.2, with a series resistor $R_s = 10\text{k}\Omega$. The objective of the IV characterization consists in comparing the voltage necessary to switch the devices with spikes with the one required for conventional flat junctions, expecting to observe a lower actuation voltage thanks to the high electric field at the tip of the spikes.

In order to consider variability effects in the discussion of the results, more instances of the same device variation were measured, both for flat junctions and junctions with spikes. Figure 3.30 shows the histogram representation of the distribution of the actuation voltage for $L = 10\mu\text{m}$ long devices; the width of the spikes is $W_s = 200\text{nm}$ and the length $L_s = 800\text{nm}$. The data has been fitted to gaussian distributions.

The results show higher variability in the actuation voltage than what obtained using the sputtering process optimized in EPFL (see for instance Figure 4.5), but there is a clear trend in the reduction of the actuation voltage when employing the spikes. The distribution for the devices with spikes is fitted to a gaussian with average 20.1 V and standard deviation 5.1 V, while for the flat junctions the average is 25.8 V and the standard deviation 7.3 V.

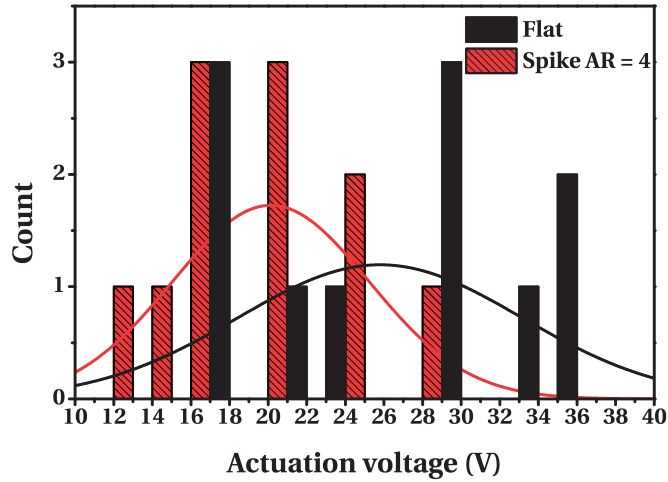


Figure 3.30 – Histogram representation and gaussian fitting of the distribution of the actuation voltage for VO₂ switches ($W = 20\mu\text{m}$, $L = 10\mu\text{m}$) employing flat junctions or junctions with spikes ($W_S = 200\text{ nm}$, $L_S = 800\text{ nm}$). Bin size: 2 V.

Figure 3.31 (a) shows the comparison of the IV characteristics for devices using flat junctions or junctions with spikes, selecting from the ones included in Figure 3.30 ($L = 10\mu\text{m}$) the ones that undergo the E-MIT at the lowest actuation voltage. We observe a decrease in V_{act} from 16.6 V to 12.4 V, corresponding to a 25.3 % reduction. Figure 3.31 (b) shows the same comparison for shorter devices ($L = 2\mu\text{m}$); in this case we obtain a 38.3 % reduction in actuation voltage, decreasing from 8.6 V to 5.3 V.

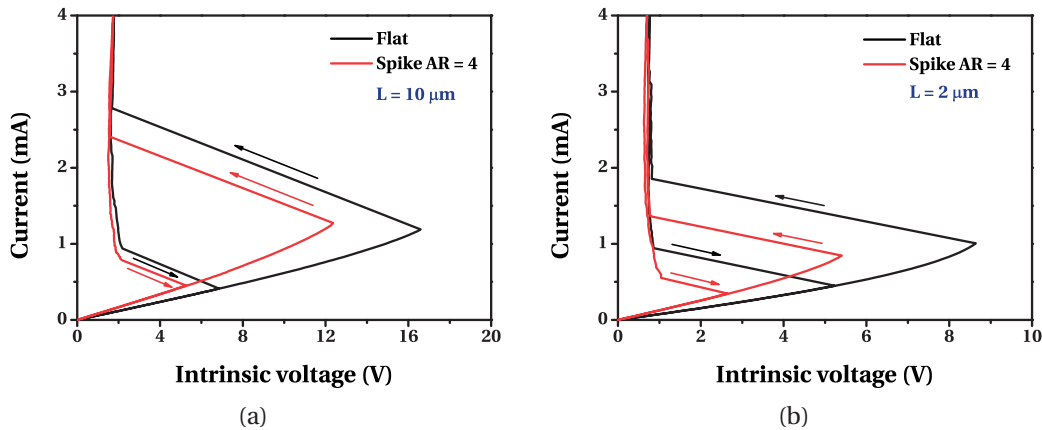


Figure 3.31 – Comparison of IV characteristics for devices with or without spikes ($W_S = 200\text{ nm}$, $L_S = 800\text{ nm}$) along the junctions, keeping constant the width $W = 20\mu\text{m}$ and the length L . a) $L = 10\mu\text{m}$. b) $L = 2\mu\text{m}$.

The measurements presented in this section validate the use of spikes along the metal

electrodes at the interface with VO₂ as a method to decrease the actuation voltage in VO₂ switches. However, the actuation voltage achieved in the best cases is still too high to consider these devices as low-voltage switches. A possible way to decrease the actuation voltage, based on the electrothermal actuation model by Joule heating, consists in decreasing the length of the switch or the VO₂ resistivity, as expressed in Equation (3.12). Another approach would consist in identifying conditions in which the electric field plays a more important role in the actuation event.

3.4.5 Measurements at cryogenic temperatures

The results at room temperature presented above prove that the spikes can be used to decrease the actuation voltage in VO₂ switches. However, since their working principle is based on the high electric field created on the tip of the spikes, a higher difference in actuation voltage with respect to flat junctions could be observed in conditions in which the MIT is mainly driven by the electric field.

A previous work on VO₂ characterization at cryogenic temperatures has proven that the actuation voltage for a VO₂ switch measured at 77 K was less than two times higher than what observed at room temperature, while using a model based purely on Joule heating it was predicted a 43-fold increase [179]. These findings suggested the importance of non-thermal voltage-driven transitions occurring in VO₂, not easily observable at room temperature since being concomitant with electrothermal actuation mechanisms, but crucial to explain the actuation dynamics at 77 K.

For this reason, we decided to further investigate the behavior of VO₂ switches at cryogenic temperatures, expecting to observe a larger improvement in actuation voltage using the spikes.

Cryogenic measurements were performed in a Süss Microtec cryogenic prober chamber (PMC 150) at EPFL. This tool allows high vacuum (better than 1×10^{-5} mbar) for on-wafer measurements in a broad temperature range from 4 K (using liquid helium) to 400 K. Liquid nitrogen was used to cool the substrate temperature down to 77 K.

Figure 3.32 shows the dependence of the OFF-state resistance of 2 μm long VO₂ switches with and without spikes. Coherently with earlier studies [38, 39, 180], the resistance of VO₂ at temperatures far from T_{MIT} is found to be exponentially decreasing with temperature, reaching values 4 orders of magnitude higher than what measured

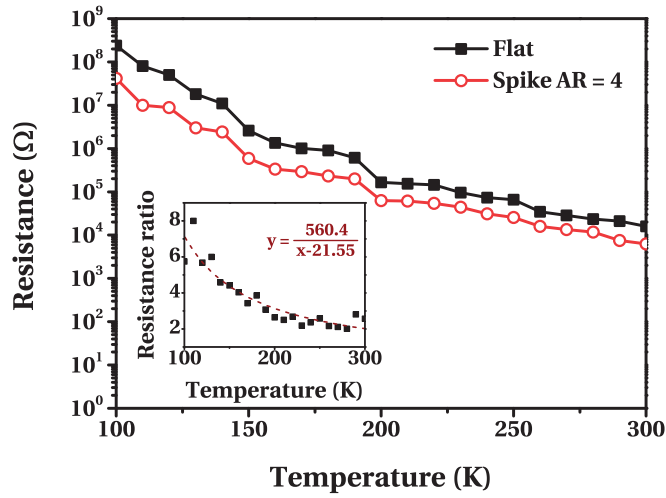


Figure 3.32 – Dependence on temperature of the OFF-state resistance for devices with or without spikes ($W_S = 200$ nm, $L_S = 800$ nm) along the junctions, keeping constant the width $W = 20$ μ m and the length $L = 10$ μ m. Inset: ratio between the OFF-state resistance of devices with flat junctions and the one of devices with junctions with spikes.

at room temperature. The inset shows the increase in resistance observed in devices with flat junctions with respect to devices with spikes, which fits well to an inversely proportional dependence on temperature from 100 K to 300 K.

Differently from what observed in [179], the devices were not actuated for voltage levels few times higher than what obtained at room temperature, therefore it was necessary to increase the voltage sweep up to values higher than 80 V. However, the devices appear to actuate at remarkably low power levels, incompatible with a model based purely on Joule heating. For instance, Figure 3.33 shows an actuation event measured at 77 K for a device with spikes ($W_S = 200$ nm, $L_S = 800$ nm), actuating at $P_{act} = 64.4$ μ W ($V_{act} = 75.2$ V, $I_{act} = 0.85$ μ A), while switches at room temperature actuate for power levels of the order of the mW.

The device reported in Figure 3.33 was damaged during the first IV characterization, and it was not possible to actuate it for a second cycle, persisting on a high-resistance state. Other devices were damaged directly in correspondence of the actuation event, therefore in their case it was not possible to observe the low-resistance state. Devices were damaged despite the presence of a current-limiting series resistance $R_S = 10$ k Ω , suggesting that it would be necessary to decrease the actuation voltage for reliable operation.

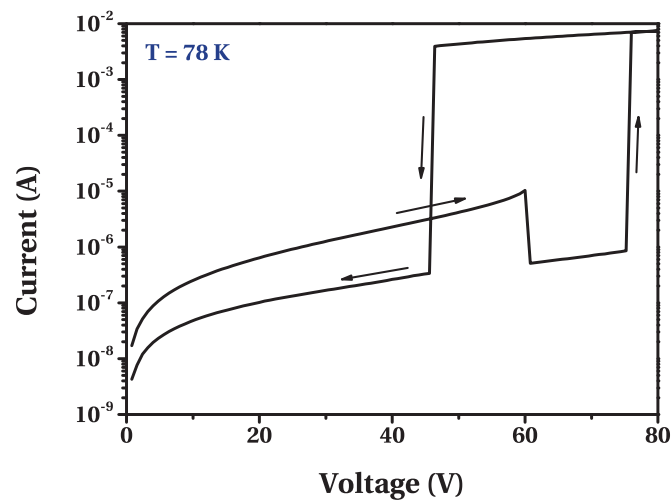


Figure 3.33 – Full actuation cycle measured at 77 K for a VO₂ switch with spikes ($W = 20\mu\text{m}$, $L = 2\mu\text{m}$, $W_S = 200\text{nm}$, $L_S = 800\text{nm}$), showing E-MIT at ultra-low power.

3.5 Summary

This chapter presented the fabrication and characterization of VO₂ steep-slope switches operating in a broad temperature range. After an introduction on the literature on VO₂ electronic switches, the main fields of research and their applications, the potential of VO₂ for steep-slope switches was discussed. Steep-slope switches based on the metal-insulator transition in VO₂ have been compared to other technologies such as MOSFET and TFET in terms of slope, I_{ON} current and I_{OFF} current, suggesting that the VO₂ based MIT switch is a promising candidate for a new Beyond CMOS switch able to overcome the limits of thermionic injection.

VO₂ 2-terminal switches were fabricated at EPFL exploiting the optimized sputtering process presented in section 2.2.1 and the process flow in section 2.3.1. Current and voltage actuation methods were compared and discussed in the context of the electrothermal actuation model based on Joule heating, showing how voltage actuation provides a power dissipation spike in correspondence of the E-MIT ensuring very high resistance ratios between the two states.

The slope of the transition was defined and measured in a broad temperature range, assessing quantitatively for the first time its low temperature dependence up to 50 °C. The devices operate as deep subthermal switches up to 57 °C, close to the VO₂ transition temperature. Moreover, we observed a very low dependence on temperature of the high I_{ON} current in VO₂ switches from 25 °C to 60 °C, confirming the good

Chapter 3. VO₂ MIT for steep-slope electronic switches

temperature stability of the proposed device.

The second part of the chapter was devoted to the study of an optimized electrode shape to decrease the actuation voltage in VO₂ switches. We proposed the use of triangular-shaped “spikes” protruding on the VO₂ junction as a way to increase the electric field peak (located on the tip of the spike) for the same applied voltage with respect to conventional flat junctions. Electrothermal simulations, in which the E-MIT is based purely on Joule heating, show that this effect would help decreasing the actuation voltage. Moreover, this kind of electrodes could help distinguish conditions in which the E-MIT is initiated by other mechanisms related to the electric field.

The devices were fabricated in INRS using VO₂ deposited by PLD and characterized at EPFL. Measurements at room temperature confirm the working principle validated by simulations. Moreover, measurements at cryogenic temperatures were performed in order to provide further insights on the role of the electric field in the E-MIT in VO₂ switches.

The main contributions of this chapter can be summarized as follows:

Comprehensive study of the E-MIT slope in VO₂ switches. Previous contributions on steep-slope switches based on VO₂ E-MIT did not report detailed quantitative analyses on the limits of the steepness of the electrical transition between the two VO₂ structural phases. For better insights into the performance of VO₂ switches from this point of view, we fabricated CMOS-compatible two-terminal switches and measured E-MIT actuation events with high-resolution voltage sweeps (1 mV steps), obtaining transition slopes as low as 0.24 mVdec⁻¹ at room temperature.

Moreover, we experimentally reported for the first time the dependence of the slope on the temperature, increasing only up to 0.38 mVdec⁻¹ at 50 °C, corresponding to a T dependence $< 5.5 \mu\text{V}^\circ\text{C}/\text{dec}$. Moreover, the devices show excellent ON-state conduction, with $I_{\text{ON}} = 1.8 \text{ mA}/\mu\text{m}$ at 5.5 V for the whole range of investigated temperatures. These results recommend MIT VO₂ switches as future candidates for steep-slope, highly conductive, temperature-stable switches.

Method to decrease V_{act} by generating high electric fields in VO₂ switches. We proposed an alternative electrode shape to reduce the actuation voltage in VO₂ switches. Electrothermal simulations in COMSOL Multiphysics proved that

including triangular-shaped metal “spikes” along the electrode sides on the VO₂ junction allows to reach the transition temperature T_{MIT} at lower voltages with respect to what obtainable with standard “flat” junctions. This effect is due to the higher electric field induced on the tip of the spikes, which depends on the spike radius of curvature. The device working principle was validated by DC measurements at room temperature comparing the actuation voltage in standard flat junctions with the one observed in devices with spikes of the same length. More instances of the same geometrical variation were measured to take into account the process variability. For the 10 μm long switches, the devices with flat junctions actuated on average at 25.8 V, while the devices with spikes actuated on average at 20.1 V. By considering only the devices which actuate at lower voltage, we obtain a 25.3 % reduction in actuation voltage for the 10 μm long devices (from 16.6 V to 12.4 V) and a 38.3 % reduction in actuation voltage for the 2 μm long devices (from 8.6 V to 5.3 V). Moreover, the devices with spikes were measured at cryogenic temperatures in order to investigate possible alternative actuation mechanisms based on the electric field effect, with Joule heating relegated to a minor role. Most of the devices measured at 77 K were irreparably damaged due to the very high voltage levels required to actuate, however for one of the devices it was possible to observe a full actuation cycle, with the E-MIT occurring at a remarkably low actuation power, $P_{\text{act}} = 64.4 \mu\text{W}$ ($V_{\text{act}} = 75.2 \text{V}$, $I_{\text{act}} = 0.85 \mu\text{A}$), while switches measured at room temperature actuate for power levels of the order of the mW. This low actuation power cannot be predicted by conventional models based on Joule heating and needs to be confirmed by further characterization, potentially providing more insights into alternative actuation mechanisms based on the electric field effect in VO₂.

4 VO₂ MIT for reconfigurable RF functions

This chapter presents the fabrication and characterization of reconfigurable radio frequency (RF) devices based on the metal-insulator transition in VO₂.

We first propose a CMOS-compatible, low-loss, highly-reliable VO₂ RF switch. The VO₂ RF switch has been thoroughly characterized and compared to the respective state-of-the-art and alternative competing technologies in terms of the main figures of merit defined in Section 4.1.1.

In the second part of the chapter we present a novel tunable capacitor based on VO₂ and its application for microwave tunable filters.

4.1 Introduction

Microwaves are a form of electromagnetic radiation covering the spectrum from 300 MHz to 300 GHz. This range of frequencies corresponds to wavelengths λ decreasing from 100 cm to 0.1 cm. As a consequence, working in this part of the spectrum means that the wavelength of the signals is comparable to the size of the equipment, therefore it is not possible to use exclusively lumped-circuit models based on discrete components (e.g. resistors, capacitors, inductors). Instead, distributed circuit elements and the theory of transmission lines have been developed to accurately design and analyse microwave circuits and propagation [181].

Microwave technology is exploited for different applications, such as radar systems, telecommunications, satellite navigation, radio astronomy, heating and power applications. The aim of this chapter is to further explore the potential of VO₂ (and

Chapter 4. VO₂ MIT for reconfigurable RF functions

MIT materials in general) for reconfigurable RF devices, with particular focus on devices suitable for wireless communication systems and their subsystems (e.g. antennas, filters, matching networks, etc.). Microwaves are particularly suited for wireless communication systems because they are more easily focused into narrow beams than lower-frequency radio waves, they allow higher data transmission rates and the antenna size is miniaturized, decreasing proportionally to the wavelength. Moreover, long-distance terrestrial telecommunications are possible since microwaves are strongly absorbed by the atmosphere only at wavelengths shorter than about 1.5 cm (i.e. above 20 GHz).

Devising and exploiting tunable RF devices is of foremost importance for wireless communication systems, for three main purposes:

- *switching networks between subsystems*: RF switches are used in virtually any wireless communication system. Single-pole double-throw (SPDT) and double-pole double-throw (DPDT) switches are generally used to route the signals between different subsystems (e.g. transmit-receive switches in transceivers), while single-pole N-throw (SPNT) switches are used mainly to select different elements in amplifier or filter banks.
- *subsystems requiring reconfigurability*: some subsystems inherently require reconfigurable devices for their functionality, like for instance phase shifters and voltage-controlled oscillators (VCOs). Phase shifters are microwave networks able to provide a controllable phase shift of the RF signal; this function is enabled by reconfigurable RF elements, like SPNT switches to select transmission lines with variable lengths, or tunable capacitors used as variable loading on a fixed line. VCOs provide an oscillating signal at a frequency controlled by voltage, and they can be realized exploiting voltage-tunable capacitors; improving the quality of the capacitor allows to increase the tunability and the achievable frequency range.
- *reconfigurable subsystems*: tunable RF devices can be used to introduce reconfigurable properties in subsystems (e.g. reconfigurable antennas, reconfigurable matching networks, etc.). For instance, one of the aims of this chapter is to design microwave tunable filters based on the metal-insulator transition in VO₂ (Section 4.3). Microwave tunable filters are among the most important components in wireless communications systems, due to their ability to control the spectral profile of the transmitter and the receiver while excluding undesirable

narrowband signals, without employing bulky filter banks. The development of a low-cost, miniaturized, reliable technology for analog and digital control of microwave filters is of foremost importance for the next generations of wireless communication systems.

4.1.1 Figures of merit for RF tunable devices

In order to compare the advantages and drawbacks of different technologies for RF reconfigurable electronics, we introduce the following figures of merit:

- *Tunability*: any RF tunable device functionality is based on the ability to modify one of its properties f (e.g. equivalent resistance or capacitance), in function of an applied signal x . We define the tunability TR of the device as:

$$\text{TR} = \frac{f(x = x_{\max})}{f(x = 0)} \quad (4.1)$$

where x_{\max} is the x value providing the maximum change in f . The relative tunability $\text{TR}_{\%}$ is then defined as:

$$\text{TR}_{\%} = \frac{f(x = x_{\max}) - f(x = 0)}{f(x = 0)} \quad (4.2)$$

- *Loss*: low loss is often one of the most stringent specifications in the design of RF tunable devices, with clear advantages for any microwave circuit (e.g. low phase noise in oscillators, high gain and low power consumption in amplifiers).

In RF switches as a figure of merit the loss is usually quantified using the S-parameters: for instance, for a simple SPST switch, the main figures of merit are the insertion loss $S_{21-\text{ON}}$ and the isolation $S_{21-\text{OFF}}$. In tunable capacitors it is more appropriate to use the quality factor Q definition:

$$Q = \frac{1}{\omega RC} \quad (4.3)$$

where $\omega = 2\pi f$ is the angular frequency, C is the equivalent series capacitance and R is the equivalent series resistance.

- *Power consumption*: since nowadays most wireless communication systems are portable and battery operated, reducing DC power consumption is a concern of

foremost importance. Using low-power tunable devices can significantly reduce the battery weight and size or increase the battery lifetime.

- *Tuning speed*: another important figure of merit is the speed with which the device tunable property (e.g. resistance, capacitance, etc.) is reconfigured from the minimum value to the maximum and vice versa. Tuning speed is especially important for applications requiring fast switching, such as high data rate telecommunications and radar detection in scenarios where the target is small and in close range.
- *Linearity*: in a linear system, the input and the output signal have the same frequency. In most RF devices, though, nonlinear effects cause intermodulation distortion of the output signal, whose spectrum will present frequencies different from the ones of the input. One of the most common ways to quantify the linearity of the RF tunable device consists in calculating the third order intercept point (IP3). IP3 is calculated by using two sinusoidal signals as inputs of the RF device, at closely spaced frequencies ω_1 and ω_2 ; the output signal will include not only the fundamental frequencies, but also the harmonics $n\omega_1$, $n\omega_2$, and the intermodulation products $\pm m\omega_1 \mp n\omega_2$, where m and n are integer numbers. The third order intermodulation products $2\omega_1 - \omega_2$ and $2\omega_2 - \omega_1$ are particularly important because closely located to the fundamental frequency. IP3 is then calculated as the input signal power for which the output power at the fundamental frequency is equal to the one of the third order intermodulation product.
- *Power handling capability*: for some applications it is important to have devices with high power handling capability, evaluated as the maximum input power that does not cause irreversible breakdown or unacceptable levels of distortion at the output.

4.1.2 High frequency tuning elements

In order to discuss the potential of VO₂ for RF reconfigurable electronics, we first introduce the most studied alternatives for RF tunable devices based on different technologies. Figure 4.1 presents the typical characteristics, device cross-sections and simplified equivalent circuits for the most common options for RF switches: PIN diodes, FET switches and RF MEMS. Their functionality and the one of other technologies is described in detail in the following list:

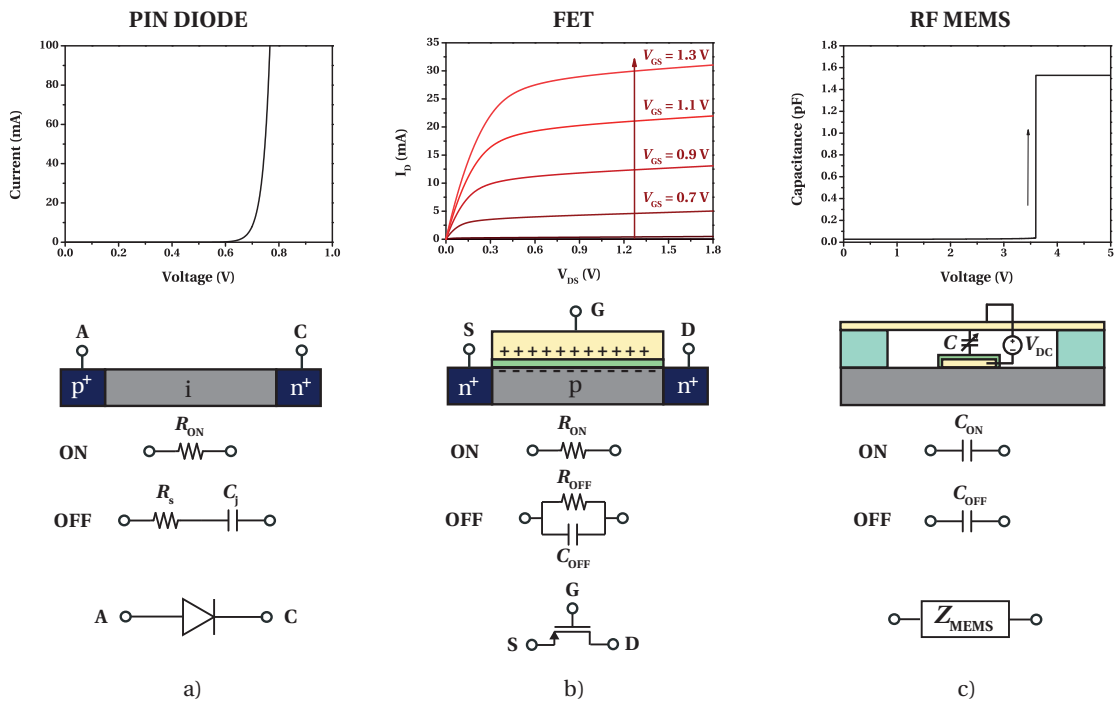


Figure 4.1 – Characteristics, cross-sections, equivalent circuits in ON and OFF states and symbols for a) PIN diodes, b) FET RF switches and c) capacitive RF MEMS.

- PIN diodes:* a PIN diode is a semiconductor device that behaves as a variable resistance at microwave frequencies. The device is made of an undoped intrinsic semiconductor region between a p-doped semiconductor and n-doped semiconductor region [182], as shown in Figure 4.1 (a). The PIN diode is operated in two well defined states by controlling the bias voltage on its terminals: under forward bias the device is in the ON state and can be modeled by a low resistance, while under reverse bias (OFF state) it behaves as a series connection of a resistance and a low capacitance, allowing isolation from RF signal up to a certain frequency limit. The ON state resistance is linearly dependent on the DC current, while the OFF state capacitance depends on the reverse bias. PIN diodes are introduced in the microwave circuit in series configuration if low insertion loss is the main concern, while they are used in shunt configuration if high isolation is more important.

The main advantages of PIN diodes are the high tunability, fast tuning speed and easy integration, while the main drawback is the loss at high frequency with respect to other technologies. Linearity issues are more important in reverse biased conditions, where the capacitance varies with the bias voltage

and the distortion increases with increasing frequency. The power handling capability is limited by breakdown voltage and power dissipation capability, due to temperature-dependent effects in the behavior of semiconducting materials.

The high contrast between the two states made PIN diodes widely used in reconfigurable microwave circuits to selectively include or exclude different components, like fixed-value reactance elements for lumped/distributed filters [183] or extension stubs for electrically coupled resonator filters [184, 185].

- *FET RF switches*: Field effect transistors are three-terminal semiconductor devices that can be used as RF switches with similar functionality to the one of PIN diodes. The gate voltage is used as a control signal to switch between the low (ON) and high (OFF) impedance states (Figure 4.1 b). Differently from PIN diodes, where the ON state is due to a DC current, FET RF switches require virtually no DC power in both states. Moreover, the OFF state capacitance is not a strong function of the reverse voltage.

In terms of performance, FET RF switches generally achieve faster switching time than PIN diodes but have higher insertion loss (higher ON resistance) and lower isolation (higher OFF capacitance). Silicon FETs can handle high RF power at low frequency, but their performance drops off dramatically at high frequency. Differently from silicon, gallium arsenide (GaAs) is highly resistive due to its wide energy band gap (1.424 eV at 300 K) and it has a high dielectric constant, making it better suited for microwave applications. Moreover, GaAs FETs have improved performance due to a higher saturated electron velocity and higher electron mobility with respect to silicon.

As a consequence, the emergence of GaAs has enabled the widespread development of monolithic microwave integrated circuits (MMIC), in which active and passive components are fabricated on the same substrate. MMICs provide functional diversification on a single chip, low cost, compact size and easier packaging with respect to previous hybrid solutions for integration (active and lumped passive components connected to distributed circuit components by wire bonding).

- *Semiconductor varactors*: another functionality offered by semiconductor devices for RF reconfigurable systems consists in the possibility to tune a capacitance with voltage. This functionality can be achieved with reverse-biased $p - n$ diodes, in which the junction capacitance is tuned by voltage due to the increase

in width of the depletion layer, or using MOSFETs, in which the gate capacitance depends on voltage [186].

Semiconductor varactors have been widely used for reconfigurable RF electronics because of their high analog capacitance tuning, compact size (high capacitance density of the order of $10 \text{ fF}/\mu\text{m}^2$), ease of integration and fast tuning speed. On the other hand, this class of devices generally suffers of poor linearity and a significant decrease of the quality factor with frequency. Working on GaAs substrates allows to decrease the series parasitic resistance and as a consequence improve the Q with respect to devices on silicon. Another way to decrease the equivalent series resistance in MOS varactors consists in decreasing the channel length (i.e. reducing the distance between source and drain contacts); however, short channel devices have lower tunability due to the increased influence of the overlap capacitance between the gate and the source/drain terminals, which is not tunable.

In conclusion, semiconductor varactors are very well suited for applications involving low-loss, compact, planar microwave circuits with high degree of reconfigurability in the low GHz range [187–189].

- *Ferroelectric varactors*: ferroelectric materials present a spontaneous electric polarization that can be reversed by applying an external electric field. Since the polarization curve is highly nonlinear for low electric fields, the dielectric permittivity is tunable with the applied field. As a consequence, varactors can be made using ferroelectric thin films in interdigital or parallel-plate capacitors. The tunability increases with the value $\epsilon(0)$ of the dielectric permittivity for no applied field [190].

Some of the most studied ferroelectric materials for varactors are SrTiO_3 (STO) and $\text{Ba}_x\text{Sr}_{1-x}\text{TiO}_3$ (BST). STO has good properties for microwave tunable applications, namely low loss and very high dielectric permittivity, but only at cryogenic temperatures. At room temperature, the dielectric permittivity is not high enough to achieve a good tunability with reasonable values for the electric field. BST is better suited for reconfigurable RF circuits because it is possible to work at room temperature: the dependence on temperature of $\epsilon(0)$ has a peak that can be shifted by modifying the barium concentration; a high concentration of barium allows shifting the peak to room temperature, therefore achieving maximum tunability, but also the loss will increase.

The main advantages of BST parallel-plate varactors are compact size, high tun-

ability for low power consumption, fast tuning speed and good power handling. The main limitations are the poor linearity (comparable to the one of semiconductor varactors) and the low quality factor at high frequency. BST varactors have been successfully employed for microwave tunable filters [191–193], phase shifters [194, 195] and other applications for RF reconfigurable electronics.

- *RF MEMS switches and tunable capacitors*: microelectromechanical systems (MEMS) are a class of devices in which electrical functions are implemented by mechanical components with dimensions ranging from few to few hundred micrometers. RF MEMS exploit the movement of some of their components to process RF signals. The movement can be induced by different actuation mechanisms, such as electrostatic, electromagnetic, magnetostatic, thermal or piezoelectric, with different advantages and drawbacks. Electrostatic actuation is the most common choice for RF MEMS, with significant advantages in terms of power consumption, size and switching time [196, 197].

Electrostatically actuated RF MEMS switches can be realized exploiting suspended mechanical components that can put in contact two sections of a transmission line in function of an applied bias, as shown in Figure 4.1 (c). RF MEMS can be integrated both in series or shunt configuration. If the contact is made between two electrically conductive parts the switch is referred as “ohmic”, while if there is a dielectric in between the switch is called “capacitive”. Both in ohmic switches and capacitive switches the OFF state can be modeled by a low parasitic capacitance depending on the air gap between the transmission line section and the MEMS movable electrode on top of it; in the ON state the ohmic switch behaves as a low resistance (depending on the quality of the contact), while the capacitive switch behaves as a high capacitance (depending on the thickness of the dielectric layer). The high achievable tunability in capacitive RF MEMS switches allows to obtain two well-defined states in a frequency range in which the low capacitance blocks the RF signal and the high capacitance allows its transmission.

As aforementioned, in electrostatically actuated RF MEMS the position of the movable electrode depends on the applied bias. Both positive and negative voltages induce an attractive force that reduces the distance between the electrodes until an instability point is reached and the movable electrode collapses on the fixed one (pull-in event). If operated in a voltage range before pull-in, RF MEMS can be also used as tunable capacitors, with a continuous tuning ratio up to a

theoretical limit of 1.5:1 in conventional parallel-plate configurations.

The main advantages of RF MEMS with respect to alternative solutions based on semiconducting or ferroelectric materials are very low power consumption (virtually zero for capacitive switches) and low loss at high frequency, resulting in switches with better contrast between insertion loss and isolation and varactors with improved quality factor. Moreover, RF MEMS can handle high RF power, present very good linearity and can be fabricated using CMOS-compatible processes.

The main limitation of RF MEMS switches in terms of performance is the relatively high switching time. Electrostatic actuation is faster with respect to other methods, but still much slower than semiconductor and ferroelectric devices, being typically in the range from 1 μ s to 100 μ s. Optimized mechanical designs and material engineering allows to decrease considerably the switching time with respect to conventional RF MEMS architectures, reaching values as low as 50 ns [198] for capacitive switches and 300 ns [199] for ohmic switches. Even lower values could be achieved using graphene as a suspended membrane [200–202]. Moreover, despite negligible DC leakage current through the dielectric layer in capacitive switches, the required power can be increased by the need for voltage upconverters (e.g. capacitive DC-DC charge pumps) to reach the bias level needed for pull-in. Regarding electrostatically actuated RF MEMS tunable capacitors, the main drawback with respect to alternative solutions is the low tunability, requiring more complex designs to overcome the 1.5:1 limit of conventional parallel-plate configurations [203, 204].

Other drawbacks for RF MEMS are related to technological aspects, such as reliability and packaging. Reliability issues can affect the lifetime of RF MEMS switches due to mechanical fatigue of the suspended membrane, contact damage, stiction and dielectric charging [205, 206]. Moreover, the performance of RF MEMS can be severely affected by the environment (vapor, oxygen, contamination), reducing the quality of the contact or causing stiction. For this reason, hermetic packaging is often required, significantly increasing the cost of the device.

In conclusion, RF MEMS switches and tunable capacitors are good candidates for RF reconfigurable circuits working at frequencies in which semiconductor and ferroelectric devices are too lossy and for which switching times $> 1 \mu$ s are acceptable. Tunable microwave filters are a good example of the high perfor-

mance and flexibility of RF MEMS [207–212].

4.1.3 VO₂ for reconfigurable RF electronics

The optimization of a low-cost, miniaturized, reliable technology for analog and digital control in RF front ends is of foremost importance for the development of the next generations of wireless communication systems. Several technologies have been proposed for the realization of reconfigurable RF circuits, as presented in the previous section. Two of the most commonly employed solutions, semiconductor FET RF switches and varactors are generally limited by high insertion loss at frequencies > 10 GHz, while RF MEMS are affected by reliability issues and complex integration.

Even though VO₂ has been extensively studied since more than 40 years in terms of material properties and several applications in different fields have been investigated, the potential of this material for RF reconfigurable electronics has not been fully explored, providing promising opportunities for innovation in this field. This section is devoted to a detailed review of the state-of-the-art of reconfigurable RF functions based on VO₂, in order to identify potential areas of improvement.

VO₂ RF switches

Progress in the characterization of the thermoelectrical MIT in VO₂ has generated increasing research interest in the possibility to exploit it for reconfigurable RF electronics. The high contrast in resistivity achievable in VO₂ with thermoelectrical actuation allowed envisioning a fast, compact RF switch with low insertion loss independent of frequency, operating at room temperature without sophisticated packaging.

The first demonstration of a VO₂ RF switch was reported in 2007 by Dumas-Bouchiat et al. [213] at the University of Limoges, presenting microwave characterization of RF switches based on VO₂ deposited by pulsed laser deposition on sapphire substrates. Both series and shunt RF switches were characterized up to 35 GHz with good contrast between insertion loss and isolation in the whole frequency range. This work demonstrated the feasibility of RF switches exploiting the resistivity change due to the MIT in VO₂; however, RF characterization was based exclusively on thermal actuation, heating the whole substrate above VO₂ transition temperature.

The first paper focused on electrically actuated VO₂ RF switches was published in

2010 by Crunteanu et al. [131] at the University of Limoges. Even in this case VO₂ was deposited by pulsed laser deposition on sapphire substrates. Electrical actuation, applying a voltage difference at the two terminals of the switch, is more practical from a device perspective, but the RF characterization up to 25 GHz presented worse performance in terms of insertion loss and isolation with respect to the previous work on thermally actuated VO₂ switches. Moreover, the actuation voltage was relatively high ($V_{\text{act}} = 20\text{V}$) and the switch failed after 16.25×10^6 actuation cycles.

Further work on modeling and characterization of electrically actuated VO₂ RF switches was performed at Harvard University in 2013 by Ha et al. [214]. The VO₂ thin film was deposited by reactive magnetron sputtering on sapphire. In this case the RF measurements were performed only up to 13 GHz, but it was shown that the electrical actuation can provide the same resistive ratio as the thermal one. Moreover, a more comprehensive characterization with respect to previous works was reported, including the transient analysis of electrical switching to demonstrate ultrafast switching time, the dependence of insertion loss on the limit bias current and as a consequence on the power consumption, the dependence between input and output RF power (linear up to 27 dBm) and the extraction of fitting parameters for the equivalent lumped circuit.

An alternative approach was proposed from Teledyne Scientific Company, published by Hillman et al. [215] in 2014. In this work the VO₂ junction (deposited by reactive magnetron sputtering on sapphire) was actuated by using an integrated microheater for local actuation. The whole device was realized using a benzocyclobutene (BCB) based 3-metal MMIC process, providing RF and DC interconnections. Using integrated microheaters allows to decrease the power consumption of the switch by 2 orders of magnitude with respect to previously reported solutions without compromising its RF results, exhibiting excellent performance up to 110 GHz.

In this thesis we focused on exploiting the process presented in section 2.2 to fabricate and characterize for the first time a Si RF CMOS compatible VO₂ RF switch. The state-of-the-art of VO₂ RF switches including this work is summarized in Table 4.1, showing the comparison of the main figures of merit.

Chapter 4. VO₂ MIT for reconfigurable RF functions

Table 4.1 – Comparison of figures of merit for VO₂ RF switches.

	Dumas- Bouchiat et al. (2007)	Crunteanu et al. (2010)	Ha et al. (2013)	Hillman et al. (2014)	Vitale et al. (2015) (this work)
Size	W = 160 μm L = 500 μm	W = 50 μm L = 10 μm	W = 25 μm L = 10 μm	W = 20 μm L = 20 μm	W = 80 μm L = 7.5 μm
Substrate	Al ₂ O ₃ (C)	Al ₂ O ₃ (C)	Al ₂ O ₃ (C)	Al ₂ O ₃ (C)	Si/SiO ₂
VO₂ deposition method	PLD	PLD	Reactive Magnetron Sputtering	Reactive Magnetron Sputtering	Reactive Magnetron Sputtering
Actuation method	T = 400 K	V _{act} = 20 V	V _{act} = 29 V	V _{ON} = 2 V	V _{ON} = 15 V
Insertion loss	-2.5 dB (35 GHz)	-4 dB (25 GHz)	-2.95 dB (13 GHz)	-0.5 dB (110 GHz)	-0.7 dB (40 GHz)
Isolation	-25 dB (35 GHz) -37 dB (10 GHz)	-16 dB (25 GHz) -22 dB (10 GHz)	-25 dB (13 GHz) -28 dB (10 GHz)	-15 dB (110 GHz) -37 dB (10 GHz)	-9.6 dB (40 GHz) -20.5 dB (10 GHz)
Switching time	< 100 ns	n.a.	14.1 ± 2.7 ns	n.a.	< 400 ns
Power consumption	P _{ON} > 2.1 W ¹	n.a.	P _{ON} > 2.0 W ²	P _{ON} = 20 mW	P _{ON} = 1.5 W ³
Power handling	n.a.	n.a.	27 dBm ⁴	n.a.	n.a.
Reliability	n.a.	16.25 x 10 ⁶ cycles ⁵	n.a.	n.a.	> 1 x 10 ⁹ cycles

¹ Estimated from electrical characterization: $I_{ON} > 130$ mA, $V_{ON} > V_{act} = 16$ V. RF measurements were performed using thermal actuation. ² Calculated from electrical characterization: $I_{ON} = 70$ mA, $V_{ON} > V_{act} = 29$ V. ³ Reducible to $P_{ON} = 260$ mW ($I_{ON} = 20$ mA, $V_{ON} = 13$ V) for an insertion loss of -2.75 dB at 40 GHz. ⁴ Maximum RF input power P_{in} for which the power at the output increases linearly. ⁵ Better reliability achieved with current actuation ($I_{act} = 1$ mA, $> 260 \times 10^6$ cycles), but limited to currents not high enough to provide the same R_{ON} used for RF measurements.

VO₂ RF tunable filters

Previous work on VO₂ RF tunable filters was mainly led by a research group in the University of Limoges. The first work on the use of VO₂ switches for reconfigurable microwave filters was reported by Givernaud et al. [216] in 2008, presenting a switchable bandstop filter. VO₂ switches were integrated in electrical resonators coupled to a microstrip, normally producing a bandstop response from 9 GHz to 16 GHz. When thermally actuated ($T = 353\text{K}$, ON state), VO₂ switches short the resonator, allowing transmission of the signal. However, the insertion loss in the ON state is relatively high, reaching -10 dB in the characterized frequency range. A similar filter topology and functionality was later reported by Crunteanu et al. [217], but controlling the VO₂ switches by electrical actuation without a detrimental effect on the filter performance.

A tunable bandpass filter based on VO₂ was presented in 2009 by Bouyge et al. [218]. The bandpass response, characterized from 1 GHz to 20 GHz is produced by two coupled split ring resonators. Electrically actuated VO₂ switches are employed to selectively connect metallic patches to the resonator, modifying their center frequency (6.4 % tunability) without affecting the insertion loss ($\sim -4\text{ dB}$).

The first VO₂ tunable bandstop filter was reported by Bouyge et al. [219] in 2010, characterized from 1 GHz to 16 GHz and reconfigured by VO₂ thermal actuation. The center frequency was tuned from 9.7 GHz to 9 GHz (7.2 % tunability) with a low insertion loss ($\sim -1\text{ dB}$) in the whole frequency range.

In conclusion, RF filters exploiting VO₂ switches on sapphire have been successfully demonstrated, but the center frequency was limited to values $< 12.5\text{ GHz}$. One of the aims of this work is to extend the center frequency of VO₂ tunable filters exploiting the CMOS-compatible technology presented in chapter 2.

The state-of-the-art of VO₂ RF tunable filters is summarized in Table 4.2, including this work.

Other applications

Additional applications of VO₂ for RF reconfigurable electronics are the following:

- *reconfigurable antennas*: a VO₂ switch integrated in the layout of a bowtie antenna has been exploited to digitally tune its resonance frequency [220];

Chapter 4. VO₂ MIT for reconfigurable RF functions

Table 4.2 – Comparison of figures of merit for VO₂ RF tunable filters.

		Crunteanu et al. (2008)	Givernaud et al. (2008)	Bouyge et al. (2009)	Bouyge et al. (2010)	Vitale et al. (2015) (this work)
Function		Switchable bandstop	Switchable bandstop	Tunable bandpass	Tunable bandstop	Tunable bandstop
Area		54.4 mm ²	31.5 mm ²	63 mm ²	17.5 mm ²	4.4 mm ²
Substrate		Al ₂ O ₃ (C)	Al ₂ O ₃ (C)	Al ₂ O ₃ (C)	Al ₂ O ₃ (C)	Si/SiO ₂
VO₂ deposition method		PLD	PLD	PLD	PLD	Reactive Magnetron Sputtering
Actuation method		V _{act} = 50 V	T = 353 K	V _{act} = 60 V	T > T _{MIT}	T = 353 K
Frequency range		5 to 15 GHz	9 to 16 GHz	1 to 18 GHz	1 to 16 GHz	1 to 40 GHz
Center frequency	OFF	10.4 GHz	12.5 GHz	9.4 GHz	9.7 GHz	22.5 GHz
	ON	n.a	n.a	8.8 GHz (6.4%)	9 GHz (7.2%)	19.8 GHz (12%)
Max. insertion loss	OFF	-6 dB	-10 dB	-4.1 dB	-0.9 dB	-1.8 dB
	ON	-10 dB	-9.5 dB	-4.1 dB	-1 dB	-1.8 dB
Min. rejection level	OFF	-34 dB	-47 dB	-17 dB	-31.6 dB	-17.2 dB
	ON	n.a.	n.a.	-14.5 dB	-33.2 dB	-18.8 dB

- *power limiting devices*: VO₂ switches can be used as broadband tunable receiver protectors [166, 221] exploiting the RF power - induced MIT.

4.2 VO₂ wide-band RF switches

This section describes the fabrication and characterization of VO₂ RF switches on high-resistivity silicon (HR-Si) substrates. This work demonstrates for the first time the feasibility of high-performance, CMOS-compatible VO₂ microwave switches.

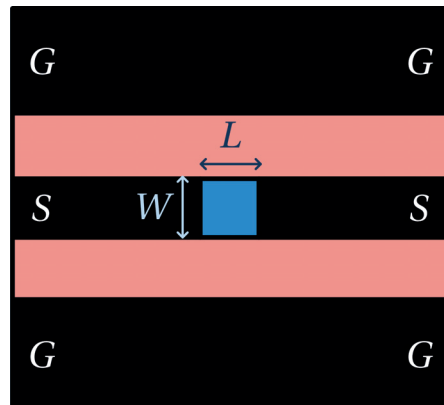


Figure 4.2 – Schematic diagram of a VO₂ RF switch in series configuration on a CPW.

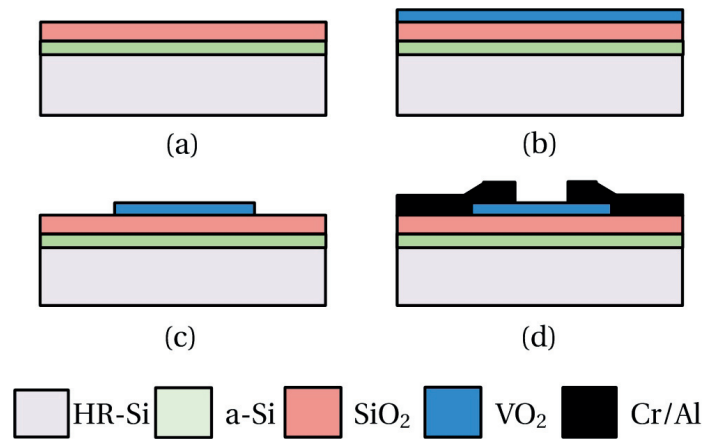


Figure 4.3 – Main steps of the fabrication process for VO₂ planar RF switches. (a) LPCVD of 300 nm a-Si and 500 nm SiO₂ on HR-Si substrate. (b) Sputtering deposition of 360 nm VO₂. (c) Patterning of VO₂ by optical lithography and ion beam etching. (d) 20/300 nm Cr/Al evaporation patterned by lift-off.

4.2.1 Fabrication

VO₂ microwave switches were fabricated in series configuration on a coplanar waveguide (CPW), as shown in the diagram in Figure 4.2. The good uniformity of the optimized sputtering process allowed to compare the performance of devices on a full 4" wafer, enabling variability, reliability and geometry variation analysis. The length L of the switch was varied from 7.5 μm to 17.5 μm with 2.5 μm steps, while the width W varied from 40 μm to 100 μm with 10 μm steps, keeping constant the dimensions of the CPW (100 μm wide signal line with 60 μm gap distance to the 255 μm wide ground planes).

The main steps of the process flow for VO₂ RF switch, represented in Figure 4.3, are

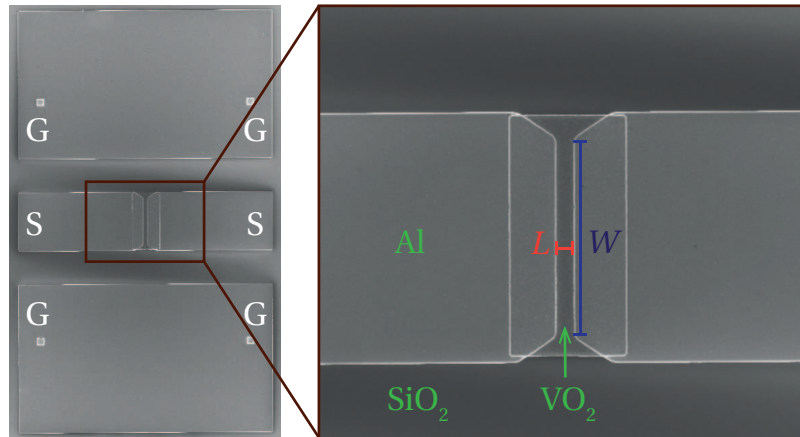


Figure 4.4 – SEM top view of a VO₂ RF switch ($W = 80\mu\text{m}$, $L = 7.5\mu\text{m}$).

analogous to what described in section 2.3.1, except for the different substrate. RF switches were fabricated on a high-resistivity silicon substrate ($> 10\text{ k}\Omega\text{ cm}$) in order to reduce substrate RF loss. To further improve the RF performance, a layer of 300 nm amorphous silicon (a-Si) was deposited on the substrate before the LTO deposition. The a-Si passivation layer, deposited through an optimized LPCVD process, inhibits the conductive layer that intrinsically appears at the Si/SiO₂ interface, therefore reducing RF loss [222]. The temperature used in the following steps of the process is limited to values $< 500\text{ }^\circ\text{C}$, therefore there is no risk of recrystallization of the a-Si layer. Figure 4.4 shows the SEM top view of a fabricated VO₂ RF switch, with a zoom on the switching region.

4.2.2 DC actuation

In order to assess the performance of the E-MIT in the fabricated RF switches, the switches were actuated with a DC voltage bias and a resistor in series $R_s = 220\Omega$ used to prevent overheating of the VO₂ junction, as described in section 3.2. The electrical characterization was performed using a HP 4156C semiconductor parameter analyzer.

Figure 4.5 shows the results of the voltage actuation by IV characteristics and resistance plots of 8 instances of a $W = 80\mu\text{m}$, $L = 7.5\mu\text{m}$ VO₂ RF switch. The average value of the extracted resistance with no applied bias is $14.4\text{ k}\Omega$ (standard deviation $\sigma_R = 1.15\text{ k}\Omega$), decreasing down to $21.3\text{ }\Omega$ ($\sigma_R = 2.5\text{ }\Omega$) in the metal phase. In all the cases the resistance ratio (between maximum and minimum of the extracted R_{VO_2}) was higher than 2 orders of magnitude, 676.1 in average and 824.1 in the best case, confirming

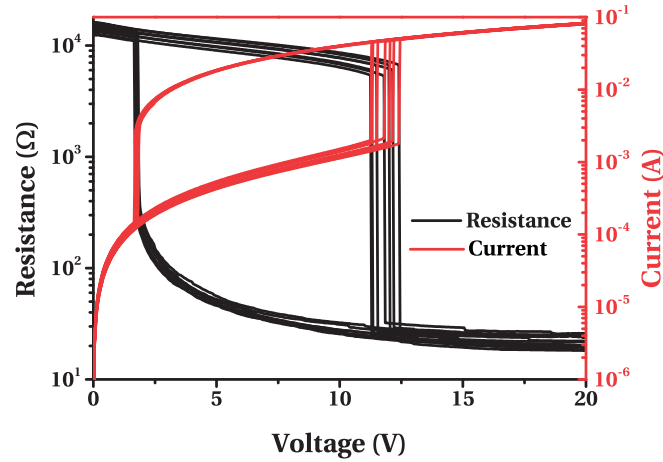


Figure 4.5 – I - V characteristics and extracted resistance in insulating and conductive states for 8 instances of a voltage-actuated VO₂ RF switch ($W = 80\mu\text{m}$, $L = 7.5\mu\text{m}$) with $R_s = 220\Omega$ in series in order to limit the I_{ON} current.

the good quality of the E-MIT.

A study on the dependence of the actuation voltage V_{act} and current I_{act} on the device geometry was performed by fabricating switches with different W (from $40\mu\text{m}$ to $100\mu\text{m}$) and L (from $7.5\mu\text{m}$ to $17.5\mu\text{m}$), for a total of 21 device configurations, replicated in 32 chips on the wafer. The results are summarized in Figure 4.6. The actuation voltage is found to be independent of the width (Figure 4.6 a) and linearly dependent on the length (Figure 4.6 b), varying from an average of 12.1 V for $7.5\mu\text{m}$ to 25.1 V for $17.5\mu\text{m}$. The actuation current instead is independent of the length (Figure 4.6 c) and it shows a linear increase with the width from $40\mu\text{m}$ to $80\mu\text{m}$, while for longer widths the rate of increase is reduced (figure 4.6 d).

4.2.3 RF characterization

The RF characterization was performed up to 40 GHz using an Agilent E8361A programmable network analyzer (PNA), with the DC bias applied by a HP 4156C semiconductor parameter analyzer connected to the internal bias-Ts of the PNA. The calibration was performed using two on-wafer Thru-Reflect-Line (TRL) kits, to cover the frequency ranges from 1 GHz to 8 GHz and from 8 GHz to 40 GHz.

While the OFF state of the switch is easily defined by performing the measurements with no applied DC bias, in order to define the ON state it is necessary to study the

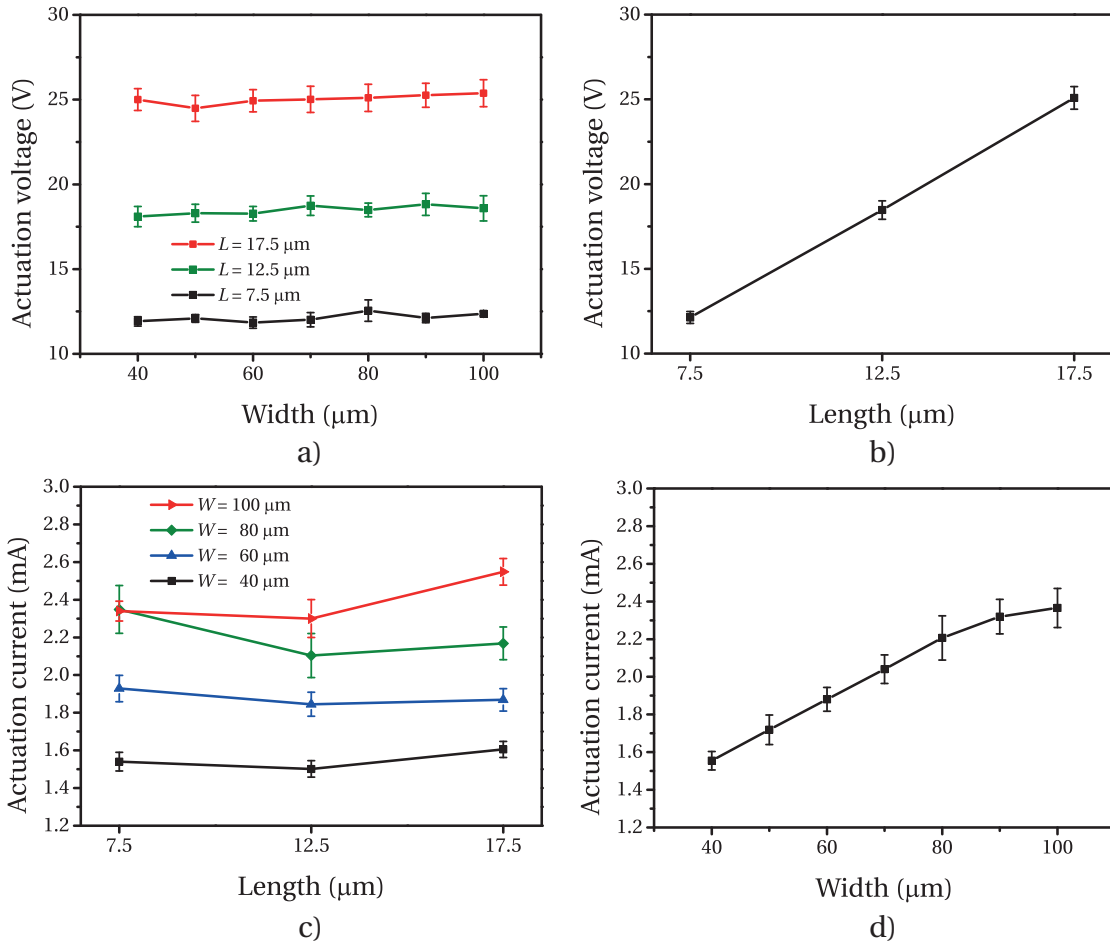


Figure 4.6 – Current I_{act} and voltage V_{act} triggering the E-MIT for different device geometries (standard deviation on 6 devices for each configuration). a) Dependence of V_{act} on W . b) Dependence of V_{act} on L . c) Dependence of I_{act} on L . d) Dependence of I_{act} on W .

dependence on the applied bias. For instance, Figure 4.7 shows the dependence of the insertion loss S_{21-ON} on the DC current flowing on a VO₂ RF switch ($W = 80 \mu\text{m}$, $L = 7.5 \mu\text{m}$). The switches were voltage-actuated as described earlier, but the value of R_s was decreased in order to increase the achievable current values after actuation. For more precise control, the current compliance parameter of the source monitor units (SMUs) of the semiconductor parameter analyzer was set to change for different measurements from 20 mA to 100 mA with 5 mA steps.

As shown in Figure 4.7, the insertion loss is flat in the whole frequency range (from 1 GHz to 40 GHz) and it improves from -2.7 dB for $I = 20$ mA to -0.6 dB for $I = 100$ mA. The results are summarized in Figure 4.8, where it is possible to see that both the

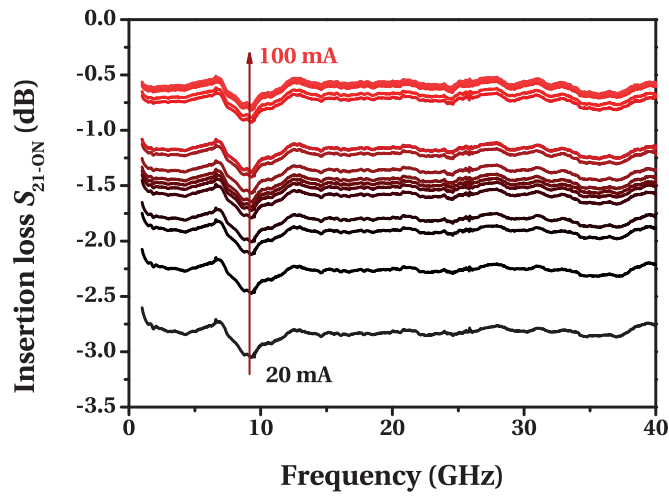


Figure 4.7 – Dependence of insertion loss on DC current for a $W = 80\mu\text{m}$, $L = 7.5\mu\text{m}$ VO₂ RF switch.

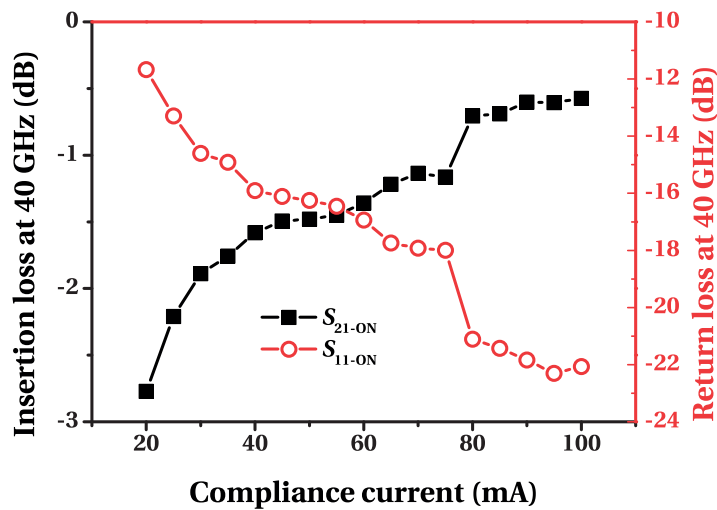


Figure 4.8 – Dependence of insertion loss and return loss at 40 GHz on DC current for a $W = 80\mu\text{m}$, $L = 7.5\mu\text{m}$ VO₂ RF switch.

insertion loss and the return loss S_{11-ON} do not show significant improvements for current values $> 80\text{ mA}$. For the results shown next in this section, the ON state is defined for a DC current $I_{ON} = 100\text{ mA}$, corresponding to a current density of the order of $J_{ON} = 5 \times 10^5\text{ Acm}^{-2}$.

Figure 4.9 (a) shows the S-parameters in OFF and ON states for devices with different L and fixed $W = 100\mu\text{m}$. The devices show good performance up to 40 GHz, with an insertion loss better than -1 dB for $L = 7.5\mu\text{m}$, return loss $\sim 20\text{ dB}$ and isolation

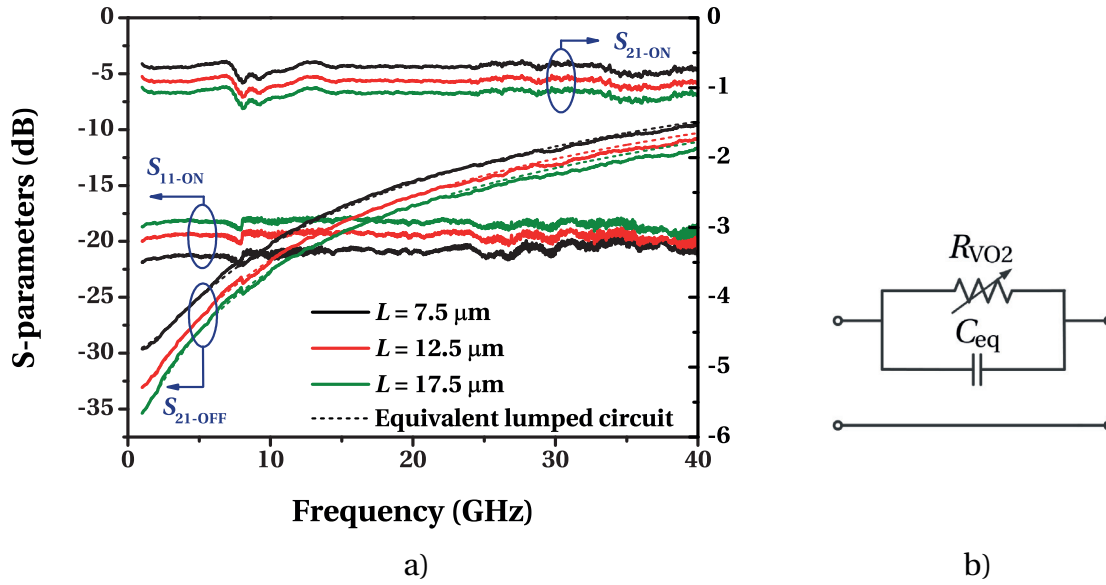


Figure 4.9 – a) S-parameter for VO₂ RF switches with fixed $W = 100\mu\text{m}$ and variable L (from $7.5\mu\text{m}$ to $17.5\mu\text{m}$). Solid lines: measurements; dotted lines: model. b) Equivalent lumped circuit.

$S_{21\text{-OFF}}$ better than -10 dB.

The S-parameter measurements have been matched to the equivalent lumped circuit shown in Figure 4.9 (b) using Agilent Advanced Design System (ADS). The good agreement between the data and the fit proves that the VO₂ RF switch can be well modeled by a parallel RC network; the resistive component is variable and corresponds to R_{VO_2} , while the capacitive component C_{eq} is fixed and corresponds to the parasitic capacitance between the Al metal contacts.

In the VO₂ conductive state R_{ON} is of the order of few tens of Ohm; such a low value ensures a flat insertion loss, independent of frequency up to 40 GHz. In the insulating state, and in the considered range of geometries, the behavior of the VO₂ RF switch is heavily affected by the parasitic capacitance C_{eq} , deteriorating the isolation level at high frequency. In fact, even employing a VO₂ thin film with higher resistivity in the isolating state (and therefore higher R_{OFF}), the isolation at high frequency would be dominated by C_{eq} due to the proximity of the metal contacts. S-parameter measurements in the OFF state allowed to extract the parameters of the equivalent lumped circuit. R_{OFF} increases linearly with L (from $5.15\text{ k}\Omega$ to $9.45\text{ k}\Omega$ for $W = 40\mu\text{m}$, from $3.05\text{ k}\Omega$ to $6.35\text{ k}\Omega$ for $W = 100\mu\text{m}$), while C_{eq} is dominated by the VO₂ film region under the Al contacts and less dependent on the geometry of the air gap

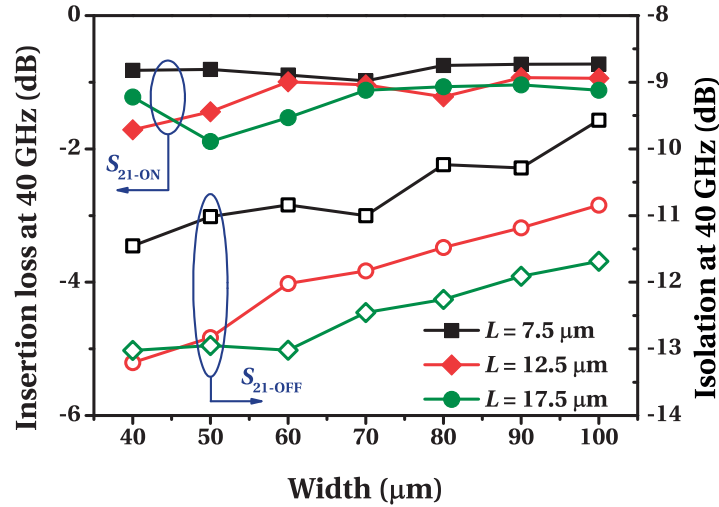


Figure 4.10 – Insertion loss and isolation at 40 GHz for all devices configurations.

(varying from 11.5 fF to 9.9 fF for $W = 40\mu\text{m}$, from 15 fF to 11.7 fF for $W = 100\mu\text{m}$).

Figure 4.10 illustrates the effect of W and L in the considered geometry range on the trade-off between the insertion loss and the isolation, with their values reported at 40 GHz. Decreasing L improves the insertion loss (lower R_{ON}), but worsen the isolation (higher C_{eq}). Similarly, for larger widths the parasitic capacitance C_{eq} increases, degrading the isolation level, but there is no clear improvement on the insertion loss.

This behavior suggests that the current level used to define the ON state ($I = 100\text{ mA}$, equivalent to the limit of the SMU) is insufficient to switch completely the wider VO₂ junctions, consistent with what observed in the optical microscopy analysis reported in Figure 2.17, in which the conductive filament formed in a 100 μm wide VO₂ switch actuated by a 100 mA current was covering $\sim 35\%$ of its width. As a consequence, the narrowest switches provide the best trade-off in terms of $S_{21-\text{ON}}/S_{21-\text{OFF}}$ ratio.

Figure 4.11 shows the comparison in the performance of the switch between thermal and electrical actuation. T-MIT provides slightly better insertion loss and higher dependence on W (decreasing from -0.6 dB at $W = 40\mu\text{m}$ to -0.35 dB at $W = 100\mu\text{m}$ for $7.5\mu\text{m}$ long switches). These results demonstrate that to optimize the switch design it is crucial to model the width of the actuated region and the respective needed power. Finally, we investigate the variability of the VO₂ RF switch by measuring 32 instances of the same device ($W = 100\mu\text{m}$, $L = 12.5\mu\text{m}$) on different regions of the wafer. Figure 4.12 shows the results in terms of insertion loss and isolation, from which it was possible to extract $R_{\text{ON}} = 12 \pm 3\Omega$ and $R_{\text{OFF}} = 8.25 \pm 2.25\text{ k}\Omega$.

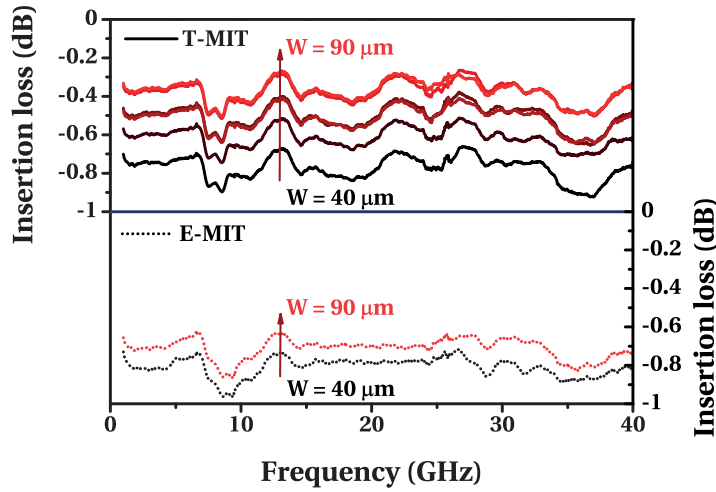


Figure 4.11 – Dependence of insertion loss on device width (W varying from $40\ \mu\text{m}$ to $90\ \mu\text{m}$, $L = 7.5\ \mu\text{m}$) using T-MIT or E-MIT.

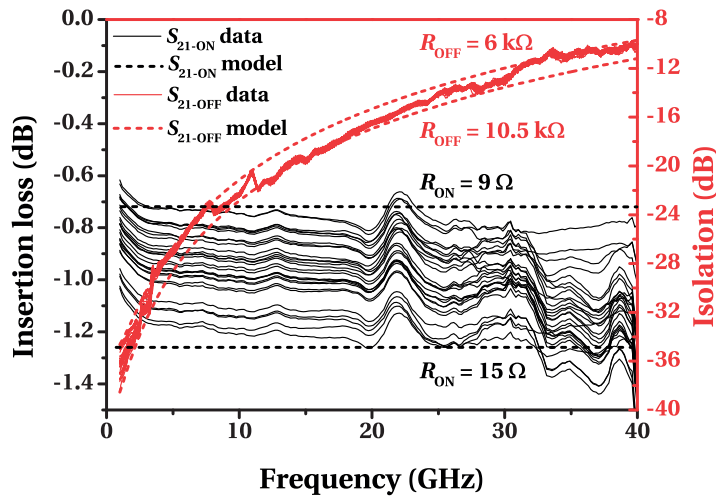


Figure 4.12 – Variability for 32 instances of the $W = 100\ \mu\text{m}$, $L = 12.5\ \mu\text{m}$ switch.

4.2.4 Reliability

The reliability of the VO₂ RF switch was studied by actuating it repeatedly with a voltage pulse train with the following characteristics:

- amplitude of 15 V, sufficient to reach the current compliance of the SMU set to define the ON state of the switch ($I_{\text{ON}} = 100\ \text{mA}$, $J_{\text{ON}} = 5 \times 10^5\ \text{A cm}^{-2}$);
- period of 200 μs ;
- duty cycle of 50 %;

- rise time as low as 100 ns.

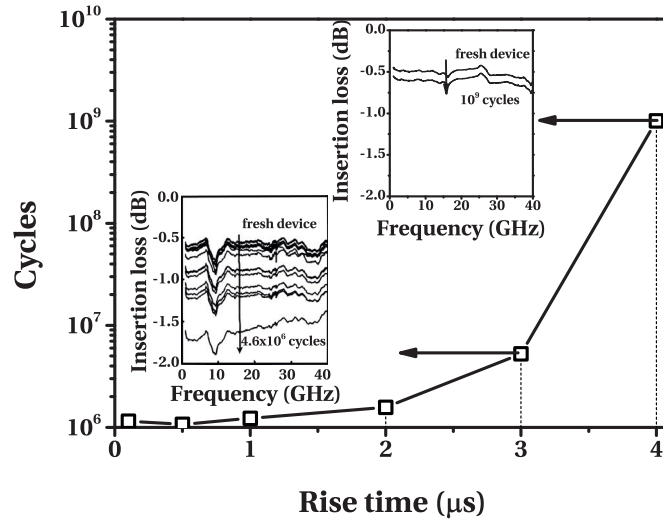


Figure 4.13 – Reliability dependence on rise time of the applied voltage.

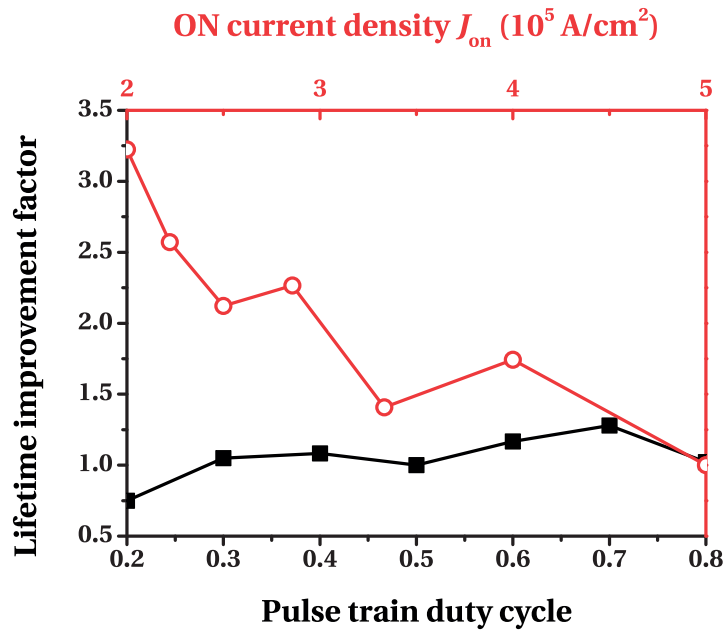


Figure 4.14 – Lifetime dependence on current density and duty cycle.

Figure 4.13 shows the results of the reliability tests in function of the rise time of the voltage pulses. We can observe that the lifetime of the switch in terms of actuation cycles can be dramatically improved by increasing the rise time, and it was possible to reach more than 10⁹ cycles without failure or significant degradation in the insertion loss, before the testing was stopped because of time constraints.

We further study the dependence of the lifetime of the switch on the properties of the voltage pulse train used to actuate it, with results summarized in Figure 4.14. Whilst the value of the duty cycle shows no connection to the reliability of the switch, the lifetime can be improved by decreasing J_{ON} , showing the existence of a trade-off between endurance and insertion loss of the VO₂ RF switch.

From the results of Figures 4.13 and 4.14 it is possible to conclude that the E-MIT can induce structural damage to the VO₂ film if the transition is too abrupt, while there is no dependence on the ON-time of the switch.

4.2.5 Optimization

As shown by the results in Figures 4.9 (a), in the characterized devices the isolation level is dominated by the parasitic capacitance C_{eq} in parallel to the VO₂ resistance, due to the proximity of the metal contacts. Increasing the length of the switch, and as a consequence the distance between the metal contacts, would improve the performance of the switch in terms of isolation at high frequency, but only at the cost of a higher insertion loss. These observations lead us to consider that, differently from DC switches where the main figure of merit expressed in the resistivity curve of the VO₂ material is the R_{OFF}/R_{ON} ratio, in RF switches it could be more important to have a higher conductivity in the ON state, even at the cost of a lower resistivity ratio.

For instance, in a previous work carried on at LESO-PB in EPFL it has been demonstrated how to increase the VO₂ conductivity in both states by tungsten doping (W:VO₂), reporting the values of $\rho_{ON} = 5.26 \times 10^{-4} \Omega \text{ cm}$ and $\rho_{OFF} = 5 \times 10^{-1} \Omega \text{ cm}$ [69]. In the rest of this section we show by HFSS simulations how the performance of RF switches would be improved by using W:VO₂ even if the resistivity ratio is lower than the one of the deposited pure VO₂ ($\rho_{ON} = 1.5 \times 10^{-3} \Omega \text{ cm}$, $\rho_{OFF} = 5 \Omega \text{ cm}$). Figure 4.15 shows the S-parameter simulations for VO₂ series RF switches (schematic diagram shown in Figure 4.2) with variable lengths ($L = 10 \mu\text{m}$ and $L = 100 \mu\text{m}$), using the resistivity values measured for pure VO₂ and tungsten-doped VO₂. For the short device ($L = 10 \mu\text{m}$), the ON state is conductive enough both for pure VO₂ and doped VO₂ to ensure very low insertion loss. In the OFF state, at low frequency the VO₂ device outperforms the doped VO₂ one, due to the higher R_{OFF} , but at frequencies high enough ($> 26 \text{ GHz}$ in this case) the isolation level is the same due to the high parasitic capacitance, confirming that the benefits of having a high R_{OFF}/R_{ON} ratio are reduced at higher frequencies.

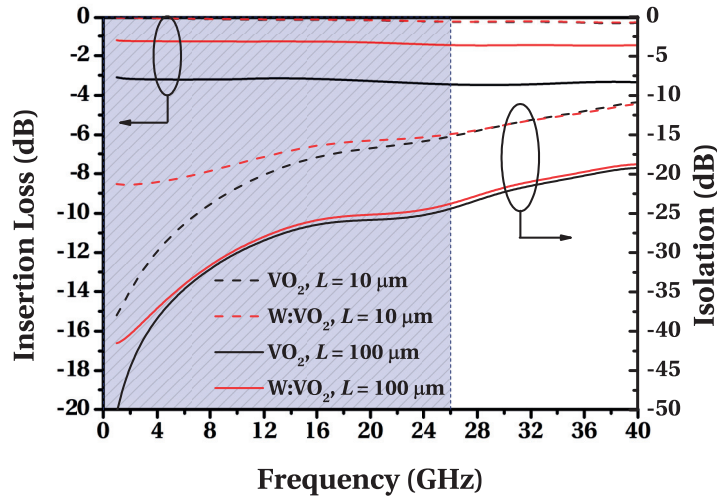


Figure 4.15 – Insertion loss and isolation for RF switches with variable length, using pure VO₂ ($\rho_{ON} = 1.5 \times 10^{-3} \Omega \text{ cm}$, $\rho_{OFF} = 5 \Omega \text{ cm}$) or W-doped VO₂ ($\rho_{ON} = 5.26 \times 10^{-4} \Omega \text{ cm}$, $\rho_{OFF} = 5 \times 10^{-1} \Omega \text{ cm}$).

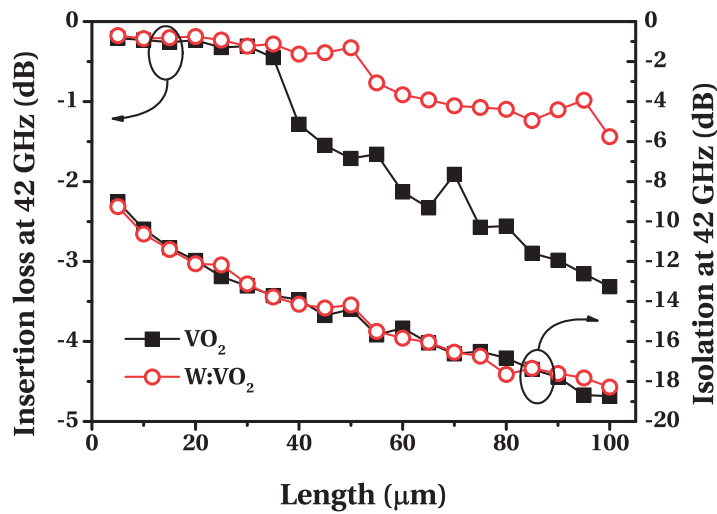


Figure 4.16 – Improvement in contrast between isolation and insertion loss at 42 GHz using W-doped VO₂ ($\rho_{ON} = 5.26 \times 10^{-4} \Omega \text{ cm}$, $\rho_{OFF} = 5 \times 10^{-1} \Omega \text{ cm}$) as compared to pure VO₂ ($\rho_{ON} = 1.5 \times 10^{-3} \Omega \text{ cm}$, $\rho_{OFF} = 5 \Omega \text{ cm}$).

Moreover, the long devices ($L = 100 \mu\text{m}$) exhibit the same isolation for frequencies higher than 6 GHz, regardless of the better R_{OFF} for pure VO₂, while the insertion loss is significantly improved in doped VO₂ in the whole frequency range, due to the lower R_{ON} .

Figure 4.16 summarizes the simulation results, comparing the dependence on L

(varying from 5 μm to 100 μm) of the insertion loss and isolation at 42 GHz for RF switches employing doped VO₂ or pure VO₂. By increasing L , the insertion loss in VO₂ switches increases at a higher rate with respect to W:VO₂ due to the higher R_{ON} , while the lower R_{OFF} in W:VO₂ switches does not affect the isolation with respect to VO₂ because in both cases the limiting factor is the parasitic capacitance.

4.3 Tunable capacitors and microwave filters

As aforementioned in section 4.1.3, the implementation of tunable filters and other RF functions employing VO₂ switches has been usually limited to frequencies ~ 10 GHz due to the relatively high parasitic capacitance between metal contacts, degrading the switch isolation as confirmed by the measurements in section 4.2.3. Considering this problem, in this section it is introduced the VO₂ tunable capacitor as an alternative solution to already established technologies like RF MEMS and semiconductor varactors, presenting their advantages in terms of ease of integration, design and performance at high frequency. The proposed devices overcome the frequency limitations of VO₂ RF switches while keeping their advantages in terms of insertion loss, as demonstrated by the fabrication and characterization of microwave tunable bandstop filters working in the K band (from 18 GHz to 27 GHz), presented in section 4.3.2.

4.3.1 VO₂ tunable capacitors

The working principle of the VO₂ tunable capacitor consists in exploiting the MIT in VO₂ to tune the length of capacitive gaps in transmission lines. For instance, a possible configuration is depicted in the diagram in Figure 4.17 (a), where a pair of VO₂ patterned regions is used to selectively define the length of a series capacitive gap in a CPW. The length of the capacitive gap depends on the VO₂ phase, varying from g_{OFF} at room temperature to g_{ON} at $T > T_{\text{MIT}}$ when VO₂ transitions to the metallic state. The effects of the MIT on the VO₂ capacitor are qualitatively illustrated in Figure 4.17 (b). Increasing the temperature above T_{MIT} induces a decrease in VO₂ resistivity with magnitude and steepness depending on the quality of the VO₂ film. The series capacitor C_s switches from a low value when the film is insulating to a high value when the film is highly conducting. Symmetric series gaps in CPWs are accurately modeled by a Π circuit, including parasitic capacitors C_p for the parallel branches. Therefore the VO₂ tunable capacitor can be modeled by the equivalent lumped circuit

4.3. Tunable capacitors and microwave filters

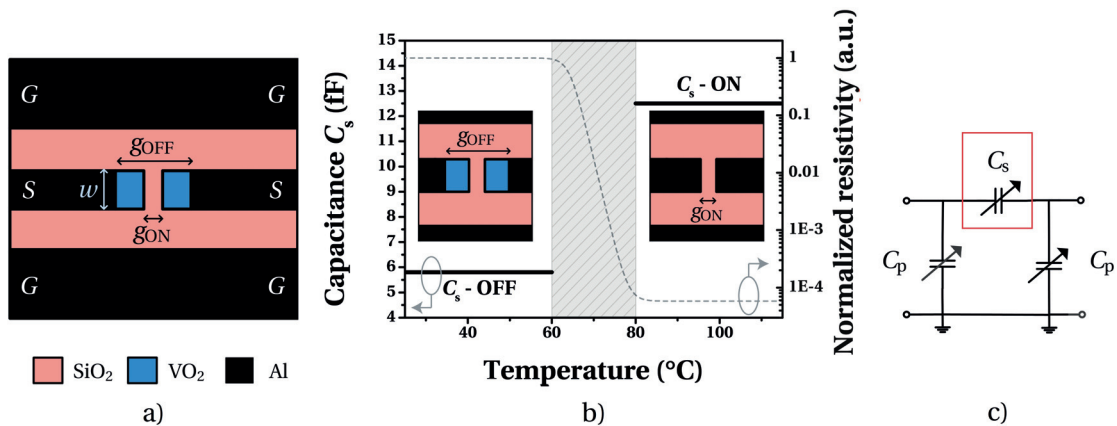


Figure 4.17 – a) Schematic diagram of a VO₂ tunable capacitor loaded on a CPW in series configuration. The capacitive gap between the signal lines can be tuned from g_{OFF} (VO₂ in insulating state) to g_{ON} (VO₂ in conducting state). b) Effects of thermal actuation on the resistivity and series capacitance. The resistivity transition occurs in the shaded area, outside of which a low and high capacitance states are well defined. c) Equivalent lumped circuit.

shown in Figure 4.17 (c) where the tunability is due to the MIT in VO₂: the decrease in length from g_{OFF} to g_{ON} leads to an increase in C_s and a decrease in C_p [223]. The VO₂ tunable capacitors have been fabricated on HR-Si substrates ($> 10 \text{ k}\Omega \text{ cm}$) as described on section 4.2.1. Figure 4.18 shows a SEM top view of a capacitor with a width $w = 100 \mu\text{m}$ and a gap varying from $g_{\text{OFF}} = 60 \mu\text{m}$ to $g_{\text{ON}} = 20 \mu\text{m}$.

Tunable capacitors have been characterized by S-parameter measurements up to 40 GHz using an Agilent E8361A PNA. Like in the case of VO₂ RF switches, TRL on-wafer calibration has been performed in order to remove the systematic measurement

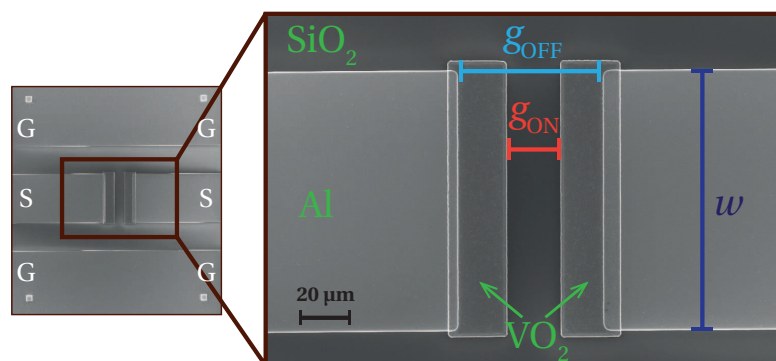


Figure 4.18 – SEM top view of a VO₂ tunable capacitor ($w = 100 \mu\text{m}$, $g_{\text{OFF}} = 60 \mu\text{m}$, $g_{\text{ON}} = 20 \mu\text{m}$) loaded in series configuration on a CPW, with zoom on the active area.

errors and de-embed parasitic coupling to the substrate. The measurements were performed in a PMC 150 prober chamber and the tunability of VO₂ has been achieved by thermal actuation. The wafer is heated from the chuck, connected to a thermally isolated heat exchanger, which contains a thermal sensor used to monitor the temperature of the substrate. A DC heater is used to set the temperature of the whole substrate to values exceeding T_{MIT} , allowing to control the phase of the VO₂ regions. A first set of measurements is performed at room temperature, with the VO₂ regions in the insulating state (OFF state); these measurements are then compared to the ones performed at $T = 80^\circ\text{C}$, with the VO₂ regions in the conducting state (ON state). Figure 4.19 shows the S_{21} -parameter measurements for a VO₂ tunable capacitor with $w = 100\mu\text{m}$, $g_{OFF} = 60\mu\text{m}$, $g_{ON} = 10\mu\text{m}$. The measurements are in good agreement to the fit done in Agilent ADS using the equivalent lumped circuit shown in Figure 4.17 (c). The isolation at 40 GHz changes from -18 dB to -12 dB as a consequence of the increase in C_s (from 5.8 fF to 12.5 fF) and decrease in C_p (from 4 fF to 1 fF).

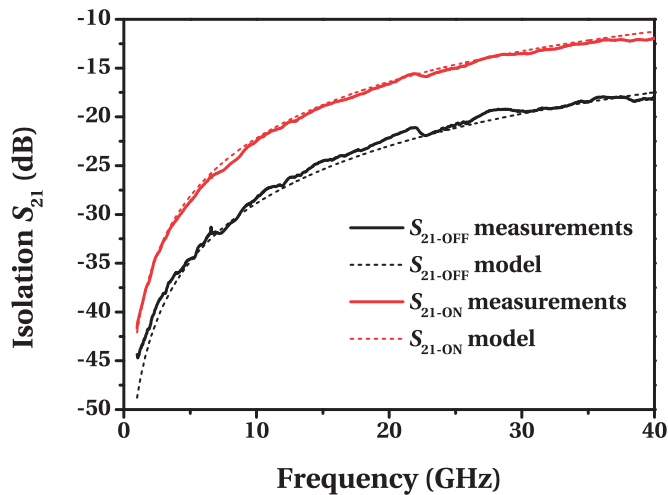


Figure 4.19 – S_{21} -parameter measurements of a VO₂ tunable capacitor ($w = 100\mu\text{m}$, $g_{OFF} = 60\mu\text{m}$, $g_{ON} = 10\mu\text{m}$) matched to the equivalent lumped circuit shown in Figure 4.17 (b). OFF state: RT. ON state: $T = 80^\circ\text{C}$.

4.3.2 VO₂ microwave tunable filters

One of the main strengths of the proposed VO₂ tunable capacitor is the ease of integration in the design of reconfigurable high-frequency circuits. For instance, any planar fixed-frequency microwave filter based on capacitive-coupled resonators [224–226] can be made reconfigurable using VO₂ tunable capacitors in a straightforward manner

4.3. Tunable capacitors and microwave filters

by the following design procedure. First, a fixed-frequency filter with geometry F_{OFF} is designed to target a specified center frequency $f_{0-\text{OFF}}$. Next, VO_2 regions are added to extend its layout (e.g. decreasing the length of capacitive gaps) from F_{OFF} to F_{ON} . Ideally, when VO_2 is insulating the performance of the original filter is not affected, having the same center frequency $f_{0-\text{OFF}}$. When VO_2 is conducting, instead, the center frequency is tuned to $f_{0-\text{ON}}$, correspondent to the response of a fixed-frequency metal filter with geometry F_{ON} .

Following this approach, for instance VO_2 tunable bandstop filters can be designed using defected ground structures (DGS) on CPWs [227–237], etching regular patterns in the ground planes to introduce rejection bands depending on their geometry. The main advantages of this kind of tunable filter consist in the flexibility in achievable design specifications and ease of fabrication, requiring only two photolithography steps (patterning for the metal layer and the VO_2 layer).

As a proof of concept, VO_2 tunable resonators have been fabricated using the DGS structure shown in figure 4.20, which includes the schematic diagram, the SEM top view and the equivalent lumped circuit, constituted by a LC parallel resonator connecting the CPW in series configuration. The resonance frequency $f_0 = 1/(2\pi\sqrt{LC})$ of the DGS structure used in this work depends on the geometry of the etched region as specified in the following [228, 233]:

- increasing the size a of the square etched region increases the inductance of the equivalent parallel resonator, therefore the resonance frequency decreases;
- increasing the size g of the capacitive gap decreases the equivalent capacitance, and as a consequence the resonance frequency increases;
- increasing the width w of the capacitive gap increases the equivalent capacitance, therefore the resonance frequency decreases.

In the fabricated VO_2 tunable resonators the dimensions a ($700\ \mu\text{m}$) and w ($200\ \mu\text{m}$) are fixed. However, the length g of the capacitive gap can be reconfigured, ranging from $g_{\text{OFF}} = 60\ \mu\text{m}$ in the VO_2 insulating state to $g_{\text{ON}} = 10\ \mu\text{m}$ in the VO_2 conducting state.

This effect is demonstrated by the S -parameter measurements in Figure 4.21, which shows a shift in the resonance frequency due to the VO_2 MIT, from $f_{0-\text{OFF}} = 22.5\ \text{GHz}$

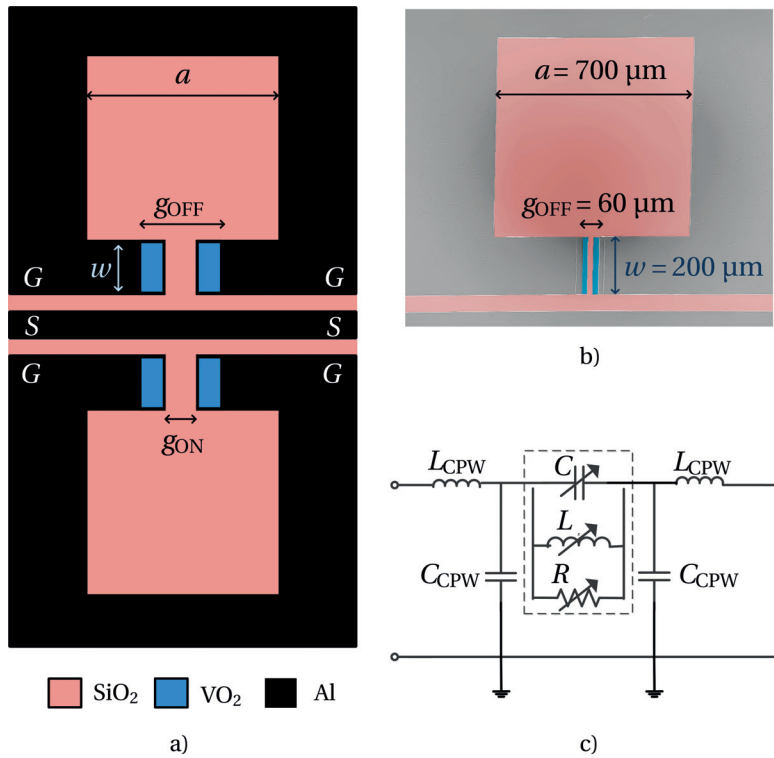


Figure 4.20 – a) Schematic diagram of the VO₂ tunable bandstop resonator; b) SEM top-view of the fabricated device, with dimensions $a = 700 \mu\text{m}$, $w = 200 \mu\text{m}$, $g_{OFF} = 60 \mu\text{m}$, $g_{ON} = 10 \mu\text{m}$, false-colored to highlight the VO₂ and SiO₂ regions; (c) equivalent lumped circuit.

to $f_{0-ON} = 19.8 \text{ GHz}$, corresponding to a tunability of $\frac{|f_{0-ON} - f_{0-OFF}|}{f_{0-OFF}} = 12\%$. The filter maintains excellent RF performance in both states, as well as a constant bandwidth. The return loss is about -1.5 dB at the center frequency, the isolation is 17.2 dB in the OFF state and 18.8 dB in the ON state, and the insertion loss is better than -2 dB in the lower and higher conducting bands up to 40 GHz , showing the suitability of VO₂ tunable capacitors for high frequency microwave filters.

For a better insight into the behavior of the filter, 3D full-wave electromagnetic simulations were performed in Ansys HFSS as reported in the following. Figure 4.22 shows the dependence of the tunability on the g_{OFF}/g_{ON} ratio, by performing simulations keeping constant $g_{OFF} = 60 \mu\text{m}$ and varying g_{ON} from $30 \mu\text{m}$ to $8 \mu\text{m}$; all the other filter layout dimensions ($a = 700 \mu\text{m}$, $w = 200 \mu\text{m}$) are unchanged and correspond to the ones used for the fabricated device. Increasing the g_{OFF}/g_{ON} ratio increases the capacitance ratio in the equivalent circuit shown in Figure 4.20 (c), allowing to achieve a higher shift in f_0 as confirmed by the simulations. In the same figure are reported

4.3. Tunable capacitors and microwave filters

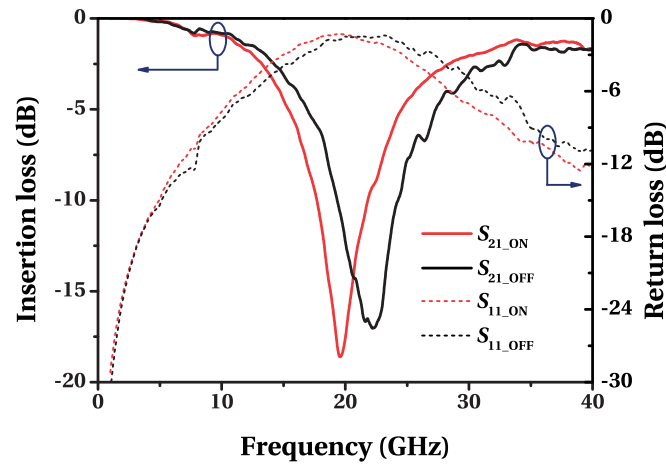


Figure 4.21 – S-parameter measurements for the fabricated bandstop resonator.

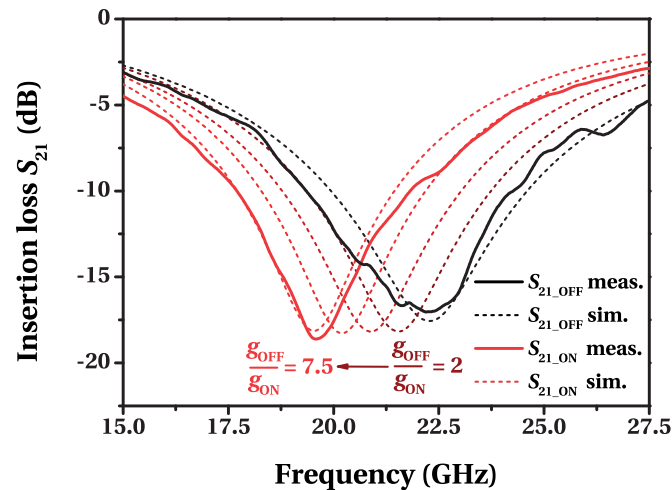


Figure 4.22 – Increase in tunability with the $g_{\text{OFF}}/g_{\text{ON}}$ ratio.

for comparison the measurements of the fabricated resonator. The measurements in the OFF state are in good agreement with the simulation results. The ON state measurements match well the simulation using the ratio $g_{\text{OFF}}/g_{\text{ON}} = 7.5$, instead of $g_{\text{OFF}}/g_{\text{ON}} = 6$ as designed. This suggests that g_{ON} in the fabricated filter was lower than expected, ultimately resulting in a higher tunability.

In order to better assess the suitability of this approach for high-frequency reconfigurable electronics, it is possible to perform electromagnetic simulations to quantify how much the filter performance is degraded due to the fact that VO_2 is not an ideal conductor in the metallic state, nor an ideal insulator in the insulating state. For this purpose, electromagnetic simulations of a reconfigurable VO_2 filter in the ON and OFF

Chapter 4. VO₂ MIT for reconfigurable RF functions

state are compared with the respective corresponding ideal fixed-frequency filters:

- the simulation of the VO₂ filter in the ON state is compared with the filter obtained replacing VO₂ by the conductor used for the metal layer (i.e. the F_{ON} filter used in the design procedure);
- the simulation of the VO₂ filter in the OFF state is compared with the filter obtained replacing VO₂ by air (i.e. the F_{OFF} filter).

The results of this analysis for a VO₂ RF filter with the structure shown in Figure 4.20 (a) and dimensions $a = 450\mu\text{m}$, $w = 200\mu\text{m}$, $g_{\text{OFF}} = 60\mu\text{m}$, $g_{\text{ON}} = 10\mu\text{m}$ are shown in Figure 4.23. The VO₂ tunable filter shows 13.1 % tunability in center frequency, from 30.6 GHz to 26.6 GHz, with negligible deterioration in performance with respect to the fixed-frequency filters caused by the non-ideality of the VO₂ insulating and conductive states.

The inset in Figure 4.23 shows that the shift in resonance frequency with respect to the ideal filters is less than 3.2 % in the explored range of $g_{\text{OFF}}/g_{\text{ON}}$ ratios (from 3.75 to 10), while the decrease in quality factor is less than 10 % in the OFF state, 7 % in the ON state.

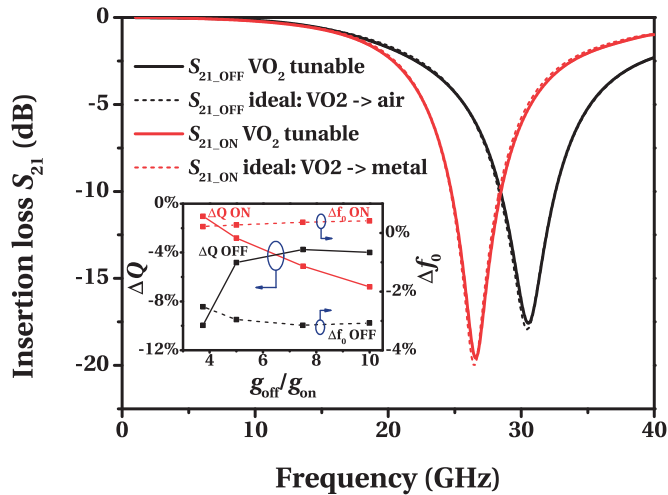


Figure 4.23 – Comparison between simulations of a VO₂ tunable filter ($a = 450\mu\text{m}$, $w = 200\mu\text{m}$, $g_{\text{OFF}} = 60\mu\text{m}$, $g_{\text{ON}} = 10\mu\text{m}$) and the corresponding "ideal" fixed filters. In the ideal filters VO₂ is replaced by air in the OFF state, metal in the ON state. Inset: percentage of change of the quality factor and of the resonance frequency with respect to the ideal performance, in function of the $g_{\text{OFF}}/g_{\text{ON}}$ ratio.

4.3.3 Switchable bandstop filters

A different filtering function can be achieved by modifying the filter structure shown in Figure 4.20 (a) such that $g_{\text{ON}} = 0$, i.e. the capacitive gap is completely filled in the ON state and the resonator in the equivalent circuit in Figure 4.20 (c) is shorted. Therefore, this filter structure is expected to present a bandstop response in the OFF state that can be inhibited by actuating VO_2 .

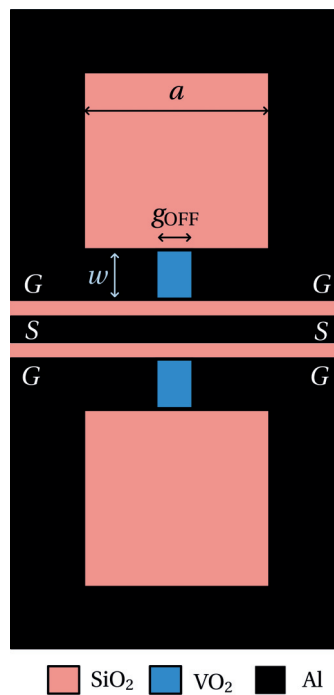


Figure 4.24 – Schematic diagram of the VO_2 switchable bandstop resonator.

This kind of filter has been fabricated and characterized up to 40 GHz as shown in Figure 4.25, where the S_{21} -parameter measurements in ON and OFF state are compared to the corresponding HFSS electromagnetic simulations and the ideal fixed-frequency filter performance. The filter geometry is $a = 700\mu\text{m}$, $w = 200\mu\text{m}$, $g_{\text{OFF}} = 60\mu\text{m}$. Even in this case it is possible to notice that the simulations show similar results for the VO_2 tunable filter and the corresponding ideal fixed-frequency filters, showing a bandstop resonance around 22.5 GHz in the OFF state and very low insertion loss in the ON state. The RF measurements show a similar trend, with a resonance frequency in the OFF state around 22 GHz, comparable to the simulation results and the measurements in the OFF state of the tunable bandstop filters with the same geometry. The transmission is reduced both in the OFF and ON states, but the insertion loss in the ON state is still relatively low, being better than -2.5 dB up to

40 GHz.

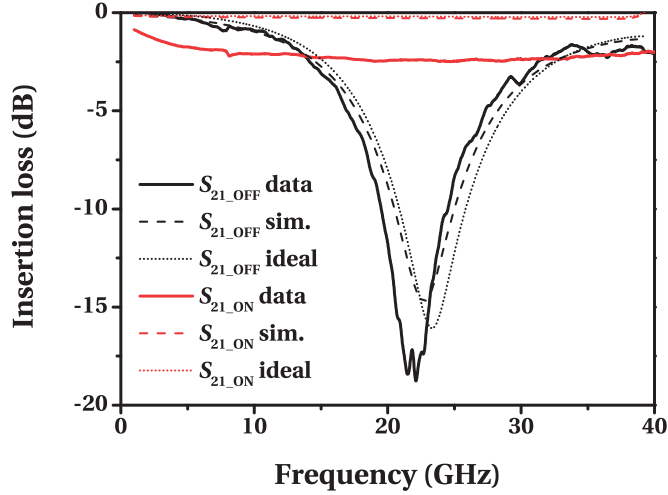


Figure 4.25 – Comparison between measurements and simulations for a VO₂ switchable bandstop filter ($a = 700\mu\text{m}$, $w = 200\mu\text{m}$, $g_{\text{OFF}} = 60\mu\text{m}$). The simulations have been performed both for the VO₂ filter and the corresponding ideal fixed-frequency filters.

4.3.4 Electrothermal actuation with integrated microheaters

The measurements presented in the previous section are based on VO₂ tunability through thermal actuation by heating the whole substrate. This method provides a validation of the working principle of the VO₂ tunable capacitor and microwave filters, but presents limitations in terms of required power and switching speed. In order to address these issues, we envision in this section a fully integrated design for electrical control of the capacitor and filter tuning through locally injected power via micro-heaters. Electrothermal actuation by external localized heat sources has been proposed as an alternative to electrothermal actuation by Joule heating in the VO₂ region, and successfully implemented for low-loss RF switches [215], low voltage compact plasmonic switches [238] and infrared filters [239].

The design procedure for VO₂ RF tunable devices following this approach involves multiple iterations in the optimization of the microheater structure, requiring electrothermal simulations to minimize the power necessary to actuate the VO₂ region, and electromagnetic simulations to ensure that the parasitic coupling to the microheater does not significantly hinder the performance of the device.

4.3. Tunable capacitors and microwave filters

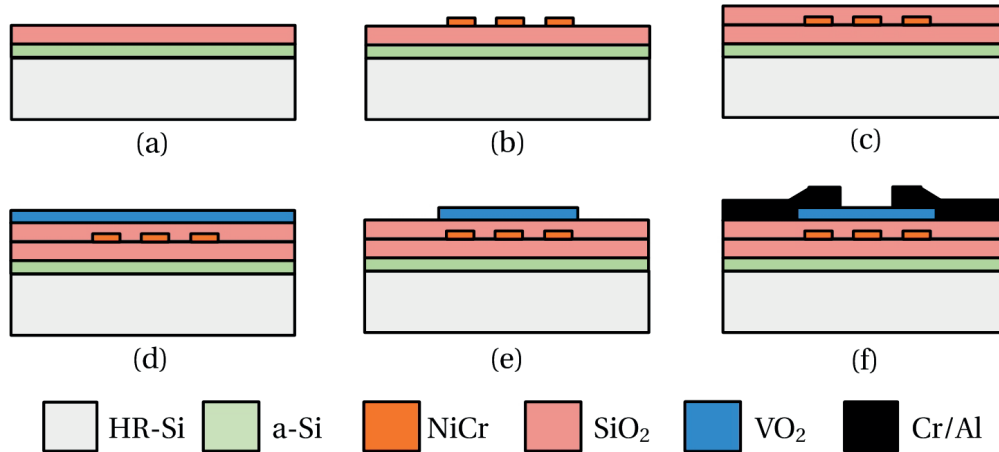


Figure 4.26 – Main steps of the proposed fabrication process for VO₂ RF tunable devices with integrated microheaters. (a) LPCVD of 300 nm a-Si and 3 μm SiO₂ on HR-Si substrate. (b) 50 nm NiCr deposition. (c) Deposition and planarization of a thin SiO₂ layer with thickness t_{ins} , used as a variable parameter in the simulations. The first three steps can be considered as preliminary steps to prepare the substrate to proceed with the process flow used for the fabricated RF devices and presented in Figure 4.3, corresponding to the following steps (d-e-f).

Figure 4.26 shows a modified process flow, which allows to integrate microheaters in VO₂ RF tunable devices. The choice of nickel chromium (NiCr) as a material for the microheater is due to its long term durability, CMOS compatibility and high electrical resistivity [240], which is an important parameter to minimize parasitic coupling to VO₂, preventing undesirable modification of the behavior of the device.

Electrothermal simulations have been performed in COMSOL Multiphysics in order to estimate the total dissipated power needed to heat above the transition temperature both VO₂ regions of the tunable capacitor. Figure 4.27 shows the full simulated geometry; the symmetry of the device across its length is exploited to simulate only one half of the structure, assuming that the power needed to actuate both the VO₂ regions composing the tunable capacitor is the double of the simulation results. The boundaries of the simulation domain are far enough from the active region so that the results are unchanged if the domain is extended.

The heat capacity of VO₂ is set to 690 J kg⁻¹ K⁻¹ and its thermal conductivity to 6 W m⁻¹ K⁻¹ [39]. All the other material parameters necessary for the simulations are summarized in Table 4.3.

The lower boundary of the HR-Si substrate is set to a constant temperature of 293.15 K,

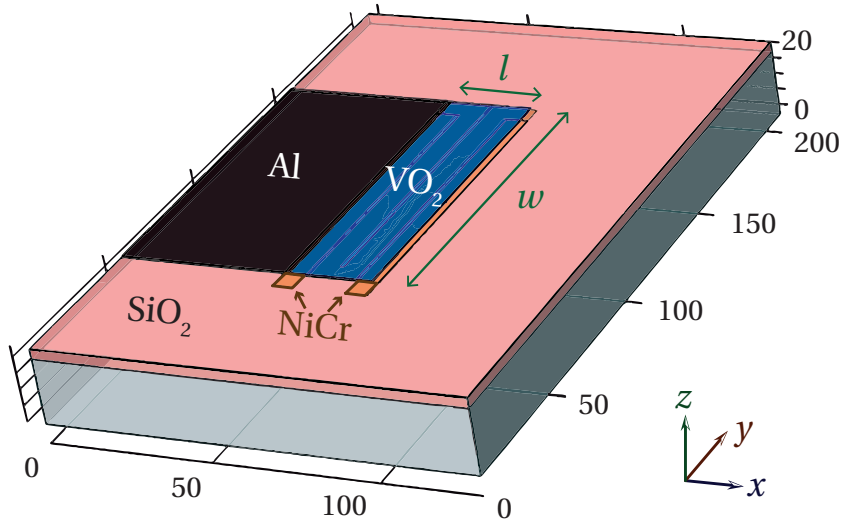


Figure 4.27 – Simulation domain for the electrothermal calculations to estimate the power needed to induce the metal-insulator transition in a VO₂ region (width w , length l) contacting an Al electrical contact. The power is provided by applying a DC voltage difference to the two highlighted terminals of a NiCr microheater, electrically insulated to VO₂ by a SiO₂ layer. The structure corresponds to one half of the VO₂ tunable capacitor. Grid labels in μm .

Table 4.3 – Material properties used for the electrothermal simulations.

Material	Electrical conductivity (S/m)	Thermal conductivity ($\text{Wm}^{-1}\text{K}^{-1}$)	Heat capacity ($\text{Jkg}^{-1}\text{K}^{-1}$)
HR-Si	/	130	700
SiO ₂	/	1.4	730
NiCr	4×10^5	17	500
VO ₂	20	6	690
Al	35.5×10^6	237	904

acting as a heat sink, while all the other external thermal boundaries are set to a convective heat flux with a heat transfer coefficient of $5 \text{ Wm}^{-2}\text{K}^{-1}$. The simulations were performed under steady-state conditions, applying a constant potential difference to the two terminals of the microheater.

Figure 4.28 shows the 3D profile of the electrothermally actuated VO₂ region for different levels of dissipated power P_{h} ; the VO₂ patterned film has dimensions $w = 100 \mu\text{m}$, $l = 25 \mu\text{m}$, corresponding to the fabricated tunable capacitor ($l = (g_{\text{OFF}} - g_{\text{ON}})/2$), and the oxide has thickness $t_{\text{ins}} = 200 \text{ nm}$. The microheater has a serpentine pattern, using $6.5 \mu\text{m}$ wide lines with $1 \mu\text{m}$ spacing.

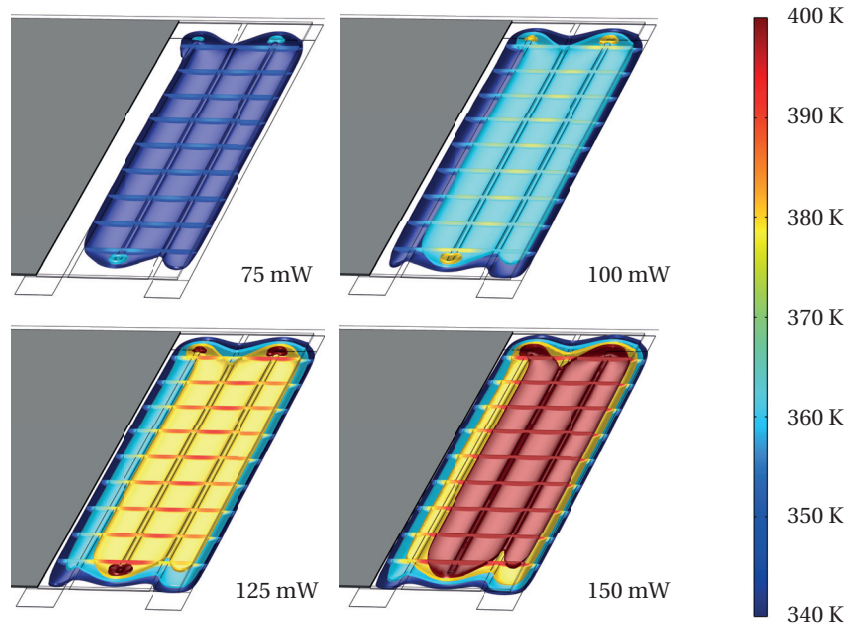


Figure 4.28 – Distribution of the electrothermally actuated VO₂ region ($w = 100\mu\text{m}$, $l = 25\mu\text{m}$) in function of the power dissipated in the microheater (from 75 mW to 150 mW), represented by 3D isothermal contours starting from $T = T_{\text{MIT}} = 340\text{ K}$ and equidistant slice plots along the VO₂ thickness.

The results in Figure 4.28 show that a power $P_h = 75\text{ mW}$ is sufficient to actuate $\sim 70\%$ of the VO₂ area, with only the region in proximity of the metal electrode being below 340 K. As better shown in Figure 4.29, the Al electrode acts as a heat sink due to its high thermal conductivity and the VO₂ temperature drops steeply when the distance from the electrode is less than $2.5\mu\text{m}$. For this geometry, corresponding to an area of $250\mu\text{m}^2$, a dissipated power $P_h = 200\text{ mW}$ is necessary to increase up to 340 K the temperature at the interface between metal and VO₂. This value, normalized per area ($P_{\text{hd}} = P_h/(wl) = 80\mu\text{W}\mu\text{m}^{-2}$), is comparable to the power needed for electrothermally actuated VO₂ devices using microheaters [215, 238].

Figure 4.30 shows the dependence of the temperature profile on the thickness t_{ins} of the oxide between the microheater and the VO₂ region. By increasing t_{ins} the VO₂ temperature profile is more uniform but lower in average and in particular on the contact with the metal. Therefore lower t_{ins} values allow to decrease the actuation power P_{act} , defined as the P_h necessary to reach the transition temperature in the entire volume of the VO₂ film. This is better shown in the inset of Figure 4.30, where P_{act} is decreasing from 211.1 mW to 187.28 mW while decreasing t_{ins} from $2\mu\text{m}$ to $0.2\mu\text{m}$.

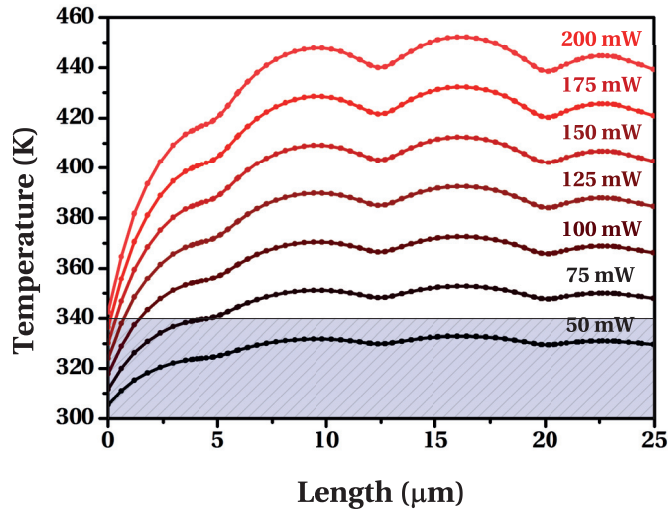


Figure 4.29 – Temperature profile on the top VO₂ surface along its length, from the contact with the metal electrode ($x = 0\mu\text{m}$) to the end ($x = l = 25\mu\text{m}$), simulated at different levels of dissipated power (from 50 mW to 200 mW).

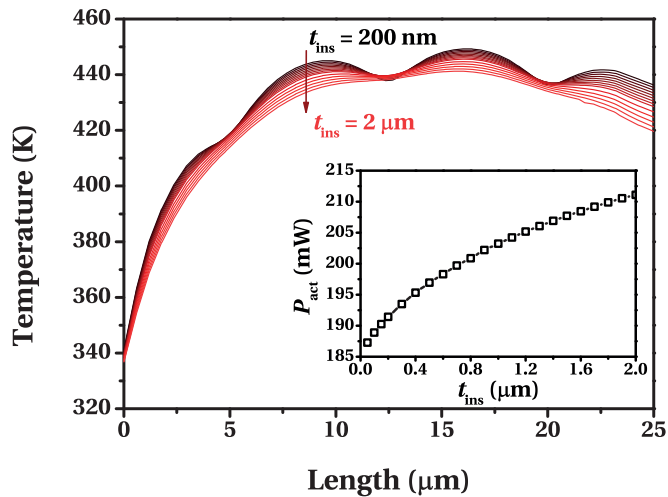


Figure 4.30 – Temperature profile on the top VO₂ surface along its length, from the contact with the metal electrode ($x = 0\mu\text{m}$) to the end ($x = l = 25\mu\text{m}$), simulated for different oxide thicknesses (from 200 nm to 2 μm, with 100 nm steps). Inset: dependence of actuation power on oxide thickness.

In order to decrease the effect of the metal contact on the energy efficiency of the device, it is possible to increase the aspect ratio l/w of the VO₂ region to be actuated. Figure 4.31 shows how the actuation power density for a VO₂ region with $w = 50\mu\text{m}$ decreases from $103.7\mu\text{W}/\mu\text{m}^2$ to $76.1\mu\text{W}/\mu\text{m}^2$ by increasing l from $11.5\mu\text{m}$ to $91\mu\text{m}$.

Following these considerations, a microwave filter with integrated microheaters to

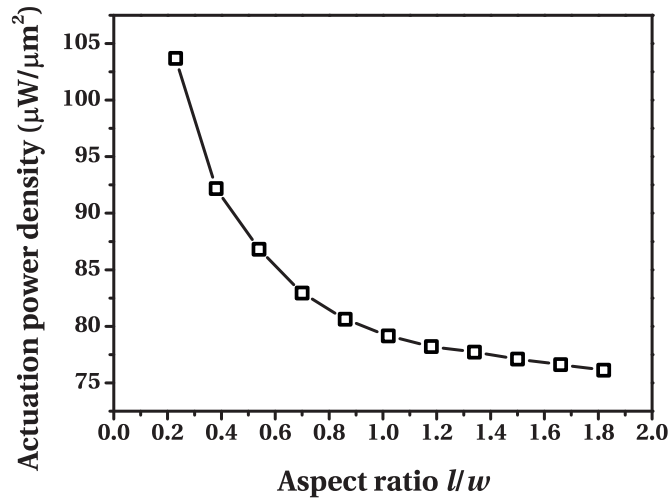


Figure 4.31 – Dependence of the actuation power density on the aspect ratio of the VO₂ region ($w = 50\mu\text{m}$, l increasing from $11.5\mu\text{m}$ to $91\mu\text{m}$). Oxide thickness $t_{\text{ins}} = 150\text{nm}$. Microheater line width $3\mu\text{m}$, spacing $1\mu\text{m}$.

actuate VO₂ regions having aspect ratio $l/w > 1$ has been designed and simulated in HFSS up to 40 GHz. Figure 4.32 shows the full electromagnetic simulation domain, including the bias lines to the microheater used to actuate the VO₂ regions. The filter dimensions are $a = 900\mu\text{m}$, $w = 50\mu\text{m}$, $g_{\text{OFF}} = 200\mu\text{m}$, $g_{\text{ON}} = 2\mu\text{m}$; the high $g_{\text{OFF}}/g_{\text{ON}}$ ratio allows maximizing the tunability of the filter. The thickness of the NiCr microheater line is 50 nm, corresponding to a sheet resistance of $50\Omega/\text{sq}$. The power required to fully actuate a VO₂ region is $P_{\text{act}} = 346\text{mW}$ (corresponding to the actuation voltage $V_{\text{act}} = 81.75\text{V}$), minimized by selecting a low oxide thickness $t_{\text{ins}} = 150\text{nm}$.

Figure 4.33 shows the results of the simulation. The performance of the VO₂ filter with integrated microheater has been compared to the corresponding F_{OFF} and F_{ON} filters (as defined in section 4.3.2). The ideal bandstop filters corresponding to the selected geometry have a resonance frequency of 28 GHz in the OFF state and 23.6 GHz in the ON state, resulting in a tunability of 15.7%. The VO₂ filter with integrated microheaters has similar performance to the ideal filters: the resonance frequency varies by only 4.4% in the OFF state ($f_{0-\text{OFF}} = 26.76\text{GHz}$) and 7.2% ($f_{0-\text{ON}} = 21.9\text{GHz}$) in the ON state, while the rejection level presents a slight decrease, from -14.72dB to -12.04dB in the OFF state and from -14.61dB to -11.93dB in the ON state, suggesting that a further optimization step after the design of the fixed-frequency filters is required in order to take into account the effects of the integration with the microheater. However, the filter performance is not affected in terms of tunability (18.2%),

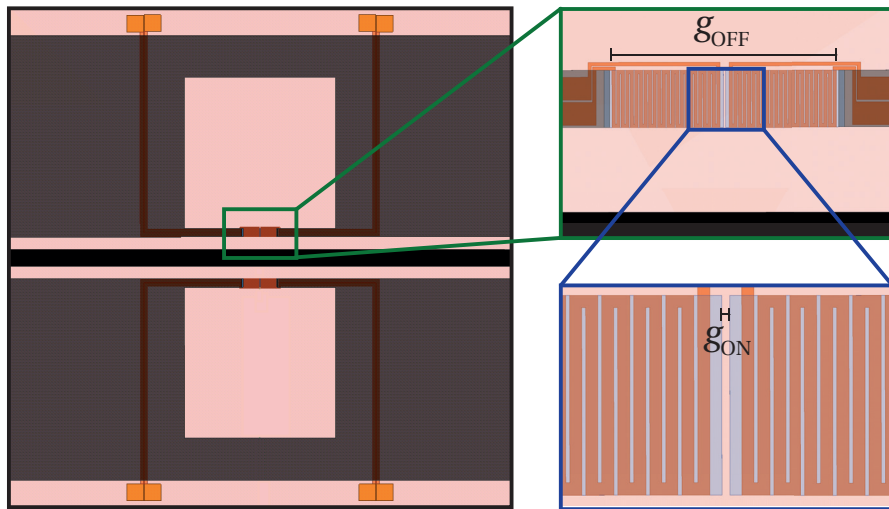


Figure 4.32 – Electromagnetic simulation domain for an electrothermally actuated VO₂ microwave filter with dimensions $a = 900\mu\text{m}$, $w = 50\mu\text{m}$, $g_{\text{OFF}} = 200\mu\text{m}$, $g_{\text{ON}} = 2\mu\text{m}$. The 50 nm thick NiCr microheater has a serpentine geometry with line width $3\mu\text{m}$ and spacing $1\mu\text{m}$.

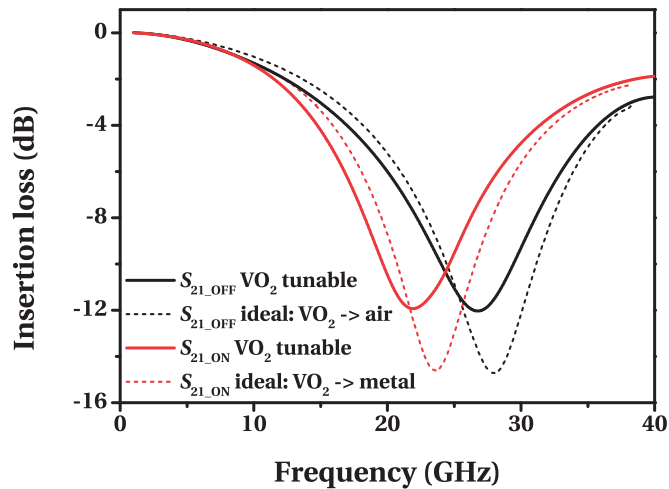


Figure 4.33 – Comparison between simulations of a VO₂ tunable filter with integrated microheaters ($a = 900\mu\text{m}$, $w = 50\mu\text{m}$, $g_{\text{OFF}} = 200\mu\text{m}$, $g_{\text{ON}} = 2\mu\text{m}$) and the corresponding "ideal" fixed filters. In the ideal filters VO₂ is replaced by air in the OFF state, metal in the ON state. Inset: decrease in quality factor and shift in resonance frequency with respect to ideal performance.

demonstrating the potential of the proposed method for electrical control of VO₂ tunable filters in the K band.

4.4 Summary

This chapter presented the design, fabrication and characterization of different devices based on the MIT in VO₂, which enables tunable high-frequency functions. After a general introduction on the different technologies for RF reconfigurable electronics and relevant figures of merit, the state of the art of VO₂ devices in the microwave frequency range has been discussed, with particular focus on RF switches and tunable filters.

VO₂ wide-band RF switches fabricated at EPFL with different geometrical parameters have been thoroughly characterized up to 40 GHz, discussing the dependence of the insertion loss on DC bias current, the effect of parasitic components on the performance at high frequency and the comparison between electrical and thermal actuation. The large scale process exploited for the fabrication of the devices allowed to perform variability and reliability studies.

A possible optimization step for the performance of the RF switches was proposed, discussing the possibility to dope VO₂ to increase its conductivity in both the insulating and metallic phases, with simulations predicting better performance at high frequency even if the resistance ratio is reduced with respect to pure VO₂.

In the second part of the chapter, novel VO₂ tunable capacitors and their use in tunable microwave filters have been discussed. The VO₂ tunable capacitors have been fabricated at EPFL and characterized by thermal actuation, showing two well defined capacitance states according to the phase of VO₂. Using VO₂ tunable capacitors allowed to design and fabricate tunable and switchable bandstop filters working at higher frequency than what previously achieved using conventional VO₂ RF switches. The tunable filters have been characterized up to 40 GHz and their performance has been compared in both the ON and OFF state to the corresponding ideal fixed-frequency filters.

An alternative method to overcome the limitations of thermal actuation in terms of switching speed and required power has been proposed for the VO₂ tunable capacitors and filters, discussing by coupled electrothermal and electromagnetic simulations the feasibility of integrating microheaters for localized heating of the VO₂ regions.

The main contribution of this chapter can be summarized as follows:

Fabrication and characterization of CMOS-compatible VO₂ RF switches. We reported for the first time VO₂ RF switches based on a CMOS-compatible process on Si/SiO₂ substrates. The process has 100 % yield and the VO₂ switches present excellent RF performance, around -0.6 dB S_{21-ON} independent of frequency, -10 dB S_{21-OFF} at 40 GHz, comparable with the state-of-the-art of VO₂ RF switches on sapphire. An extensive study on different geometries for the VO₂ RF switches led to an optimum design with maximized S_{21-ON}/S_{21-OFF} ratio. The large scale process exploited for the fabrication allowed to perform a variability study on 32 instances of the same device ($W = 100\mu\text{m}$, $L = 12.5\mu\text{m}$), obtaining $R_{ON} = 12 \pm 3\Omega$ and $R_{OFF} = 8.25 \pm 2.25\text{k}\Omega$. A reliability study revealed that the lifetime of voltage-actuated VO₂ RF switches is highly dependent on the rise time of the voltage pulse train and it can be slightly improved decreasing the DC current density, while it is not affected by the duty cycle. A lifetime higher than 10^9 cycles was reported for a pulse train with an amplitude of 15 V, a current density of $5 \times 10^5 \text{ A cm}^{-2}$ and a rise time of 4 μs . These results validate VO₂ RF switches as a promising solution for wideband reconfigurable electronics.

Fabrication and characterization of novel VO₂ tunable capacitors. We proposed a new method to exploit VO₂ for RF reconfigurable electronics: the MIT allows tuning the length of a gap between metal lines, and in consequence its parasitic capacitance. Following this approach, a thermally actuated VO₂ tunable capacitor loaded in series configuration on a CPW has been modeled, fabricated and characterized up to 40 GHz. The series capacitor shows two well defined states, switching from 5.8 fF at room temperature to 12.5 fF at temperatures higher than T_{MIT} . The VO₂ tunable capacitors offer an alternative to more commonly employed technologies for RF reconfigurable electronics, presenting lower RF loss at high frequency than semiconductor varactors and easier integration than RF MEMS.

Fabrication and characterization of VO₂ RF tunable filters in the K band. We have demonstrated the potential of VO₂ tunable capacitors for RF reconfigurable electronics by fabricating tunable and switchable bandstop filters working at higher frequency than what already reported using conventional VO₂ RF switches, limited by their parasitic capacitance. The fabricated tunable bandstop filters reached a tunability of 12 % in resonance frequency, from 22.5 GHz to 19.8 GHz, while maintaining excellent RF performance in both states as well as a constant bandwidth. The return loss is about -1.5 dB at the center frequency, the isola-

tion is 17.2 dB in the OFF state and 18.8 dB in the ON state, and the insertion loss is better than -2 dB in the lower and higher conducting bands up to 40 GHz. The fabricated switchable bandstop filter shows a bandstop resonance around 22.5 GHz with high isolation (18 dB) in the OFF state and low insertion loss in the ON state, better than -2.5 dB up to 40 GHz.

The measurements are in good agreement with full-wave 3D electromagnetic simulations, which moreover show that the performance of the VO₂ tunable filter is comparable to the corresponding ideal fixed-frequency filters in both the ON and OFF states. Additional simulations have been performed to optimize the design of the filter, characterizing the dependence of the tunability of the filter on the $g_{\text{OFF}}/g_{\text{ON}}$ ratio of the tunable capacitor.

Study of the integration of microheaters in VO₂ tunable capacitors and filters. We performed a thorough investigation of the feasibility of electrothermal actuation with integrated microheaters, locally heating the VO₂ regions in tunable capacitors and microwave filters. The tradeoff between power needed for actuation and RF performance has been discussed performing simulations with different thicknesses for the oxide used as electrical insulator between the VO₂ regions and the microheater. A tunable microwave filter employing VO₂ capacitors with integrated microheaters for electrothermal actuation has been simulated, showing performance comparable to the corresponding fixed-frequency filters in both the ON and the OFF state: the resonance frequency varies by only 4.4 % in the OFF state ($f_{0\text{-OFF}} = 26.76$ GHz) and 7.2 % ($f_{0\text{-ON}} = 21.9$ GHz) in the ON state, while the rejection level presents a slight decrease, from -14.72 dB to -12.04 dB in the OFF state and from -14.61 dB to -11.93 dB in the ON state. Importantly, the filter performance is not affected in terms of tunability (18.2 %), demonstrating the potential of the proposed method for electrical control of VO₂ tunable filters in the K band.

5 VO₂ MIT for reconfigurable THz functions

This chapter presents the design, fabrication and characterization of a reconfigurable terahertz (THz) device based on the metal-insulator transition in VO₂.

The first terahertz passive modulated scatterer has been demonstrated experimentally using VO₂ as the enabling technology, representing an important step towards the implementation of fast and energy-efficient THz communication applications and novel phase-resolved THz imaging systems.

5.1 Introduction

Vanadium dioxide has proven to be a very promising candidate for the emerging field of terahertz applications, due excellent theoretical upper bounds [241] for reconfigurable figure of merits in this range of frequencies [242]. Terahertz is conventionally defined as the band included between 0.3 and 3 THz, corresponding to the wavelength range going from 1 mm to 100 μm (submillimeter waves). The technology to work in the THz frequency range is still at an early stage: the frequency is too high for conventional electronic devices (used up to the microwave frequency range) and too low to exploit well developed optical technologies (used starting from infrared radiation).

Like microwave and infrared radiation and differently from X-rays, terahertz waves are non-ionizing. Like microwaves, THz radiation can penetrate many non-conducting materials, such as wood, plastic, ceramics, etc.; however, it cannot penetrate water or metal. Moreover, THz waves are strongly attenuated in air, due to the presence of water vapour, which possess strong resonances in THz frequencies.

Chapter 5. VO₂ MIT for reconfigurable THz functions

Terahertz is currently a very fertile research topic for several applications, such as radioastronomy, telecommunications, spectroscopy, imaging and homeland security. Each of these applications exploits important properties of terahertz waves.

THz spectroscopy, for example, can be used to probe molecular dynamics and many-body interactions, which can have characteristic times in the order of picoseconds (1 ps = 1/(1 THz)). Similarly, applications in radioastronomy are motivated by the fact that several resonances of organic molecules lie in the THz band and can hence be used to study the concentration of such molecules in interstellar space. Notably, being these resonances based on the mechanical oscillation of the molecules, isotope identification is also possible, allowing to extract dating information about the studied matter. THz imaging for homeland security finds application in full-body scanners and in remote imaging radars, possible because materials such as clothes and paper are transparent to THz. Importantly, many drugs and explosives have distinctive THz spectra, making THz imaging an even more appealing possibility.

Several technologies have been proposed to exploit the THz band, such as liquid crystals [243], PIN diodes [244], Schottky diodes [245], photoexcited semiconductors [246] and graphene [247]. However, the main obstacle to widespread use of THz communication systems is still the relative lack of available components to generate, manipulate and detect THz waves. Vanadium dioxide is considered a very important technological platform to solve some of these problems.

5.1.1 Terahertz characterization of VO₂

Terahertz time domain spectroscopy

Terahertz time domain spectroscopy (THz-TDS) is the most common characterization technique for materials in the THz frequency range. THz-TDS was introduced in the mid 80s [248, 249], it started to be widely used in the 90s to study material properties [250, 251], and it is currently the main tool for characterization of THz devices, including the modulated scatterer presented in this chapter.

Figure 5.1 shows the general schematic diagram of a THz-TDS system. The spectrometer is powered by a pulse train emitted by a femtosecond laser. Each pulse is splitted into two beam paths, called respectively pump and probe. The pump beam is used to excite the emitter, based on photoconductivity in semiconductors or nonlinear

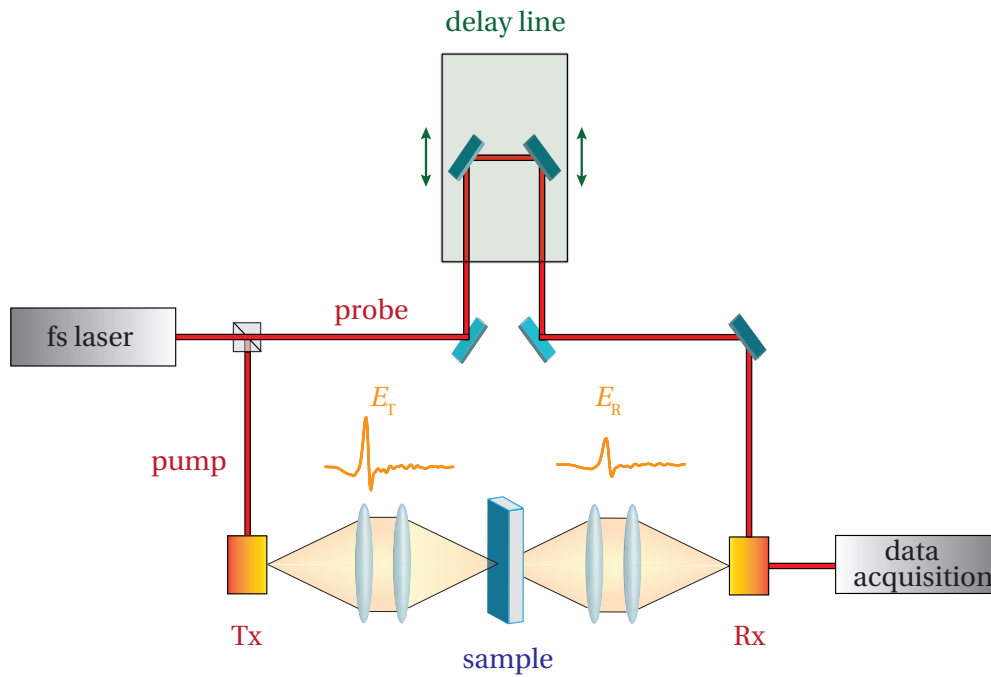


Figure 5.1 – General schematic diagram of a THz-TDS setup.

phenomena in optical crystals. The emitter generates an electromagnetic wave with spectrum centered at several hundreds of GHz. Lenses are used to focus and collimate the generated THz wave through a sample and onto the detector. The detector is conductive and allows to read the electric field of the received signal E_R only when it is struck by the probe pulse. A delay line is applied on the probe beam path in order to control the time in which it reaches the detector, allowing to plot E_R over time.

The complex transmittance T_T of the sample can then be calculated from the Fourier transform of E_R as:

$$T_T(\omega) = \frac{E_R(\omega)}{E_{\text{ref}}(\omega)} \quad (5.1)$$

where $E_{\text{ref}}(\omega)$ is the Fourier transform of a reference signal, transmitted through a medium with known properties. If the transmittance of the material is too low at THz frequencies, the sample can be characterized by the reflected signal.

An alternative technique that can be used for the characterization of materials at THz frequencies is Fourier Transform Infrared Spectroscopy (FTIR). In terms of signal to noise ratio, THz-TDS is advantageous below 3 THz, while FTIR works better above 5 THz [252].

Characterization of THz transmission properties

THz-TDS has been exploited to characterize the VO₂ THz transmission. An intensity modulation depth as high as 98 % over a broadband THz region has been reported for a ~ 120 nm VO₂ thin film grown on r-plane sapphire [51], encouraging the use of VO₂ for THz modulation applications.

A subsequent study on VO₂ transmission in the THz range discovered a dependence of the transmission ratio on the grain size of the VO₂ film: films with smaller grains present a higher modulation of the transmission due to the more compact structure of the film [253].

THz-field induced MIT

Another important field of research related to the characterization of VO₂ using THz waves is the study of the photoinduced MIT.

An early study in this field exploited optical-pump terahertz-probe spectroscopy to investigate the behavior of the photoinduced MIT in VO₂ thin films operated near T_{MIT} , characterizing the dependence on temperature of the fluence required to induce the transition [254].

THz sources generally do not provide enough power to induce the MIT in unpatterned VO₂ thin films. Different solutions have been introduced to increase the field up to levels high enough to study the THz-induced MIT, for instance depositing on the VO₂ film split ring resonators [33] or patterned nanoantennas [255] acting as local resonant THz concentrators.

5.1.2 VO₂ devices and applications in the THz range

The main application of VO₂ in the THz frequency range consists in the realization of tunable metamaterials. Metamaterials are smart materials engineered in order to create electromagnetic responses absent in nature. They are usually made of different materials, presenting repeating patterns smaller than the wavelength of the phenomena they influence.

VO₂ metamaterials are made depositing arrays of metallic resonators or nanoantennas on the VO₂ film. The change in phase of VO₂ can influence the response of the

metamaterial in different ways:

- *polarization*: VO₂ has been exploited to demonstrate THz frequency selective surfaces with reconfigurable polarization characteristics, in which VO₂ was used as an element of a cross resonator. The resonator topology was converted to a slotted dipole after thermal actuation, inhibiting one of the two allowed polarizations in the original resonator [256]. In another case VO₂ was used as a continuous film with tunable conductivity under a metallic grating, acting as a switchable THz linear polarizer [257].
- *resonance frequency*: VO₂ was proposed to tune the resonance frequency in metamaterials. This effect was achieved exploiting the high change in complex permittivity near T_{MIT} in VO₂ films covered by split ring resonator (SRR) arrays [258]. The same structure was studied applying short electric pulses instead of using thermal actuation, showing a memory effect in the response of the metamaterial [160]. A different approach was followed in the realization of a tunable dual-band THz metamaterial bandpass filter [259], exploiting thermally actuated VO₂ switches to modify the geometry of the loop cross dipole resonators used as unit cells of the metamaterial, and as a consequence their resonance frequency.
- *transmission*: a thermally actuated VO₂ film under an array of nanoslot antennas was used to modulate the transmission of the metamaterial, independently of frequency from 0.2 THz to 2 THz [260]. Electrical control (500 V at 333 K) was demonstrated in another work [261], which moreover showed how the transmission tuning is improved in metamaterials employing patterned nanoantennas, compared to bare VO₂ films. The same kind of structure was further characterized by thermal actuation in [262], demonstrating that the dependence of the transmission on temperature can be significantly modified by extreme nanopatterning of the antennas.

5.2 VO₂ modulated scatterer for THz applications

This sections presents a potential application of VO₂ for telecommunication at THz frequencies. As aforementioned in section 5.1, THz waves are attenuated in air because the atmosphere is a strong absorber of THz radiation in specific water vapor absorption bands. However, while this absorption prevents long range radio links, it

might actually prove to be very useful for short range wideband secure telecommunication. In fact, the exponential decay of THz waves would allow two close peers (< 10m) to communicate while a third more distant eavesdropper could not intercept their message due to the too low signal to noise ratio (SNR). Unlike encrypted links, this approach could also mask the presence of the radio link itself, preventing to triangulate the position of the two nodes. This property has made THz communications very interesting for military applications.

5.2.1 Introduction: applications and theory

An electromagnetic scatterer is any device or structure able to scatter an impinging electromagnetic wave in various directions. Effectively, any object with electromagnetic properties different from the surrounding environment behaves as a scatterer. Modulated scatterers (MST) are linear passive electromagnetic devices able to control and change their electromagnetic scattering properties by incorporating a tunable material or lumped element [263]. They find their main applications in radio frequency identification (RFID), functioning as devices that can transmit back a modulated signal when interrogated with a single frequency harmonic impinging wave. This is achieved by modulating in time the tunable element or material, which in turns modulates the scattered field propagating away from the device.

RFID have several applications for tagging objects and goods, for tracking purposes and as anti-theft labels. The working frequency of the most commonly available RFID goes from hundreds of kHz up to millimetre waves, while THz has not been explored yet. More recently, modulated scatterers were considered as an important alternative to classical imaging based on bolometers because they allow the possibility of measuring amplitude and phase of an electromagnetic wave at a single point, while bolometers are limited to amplitude informations. This property could be of great interest while considering an array of MSTs, since having full knowledge of magnitude and phase for each of the pixels of the array would allow further processing (e.g. allowing to re-focus the signal in a post-processing stage), not possible measuring only the received power.

The realization of such devices at THz frequencies has yet to be explored and it could lead to interesting new strategy to perform amplitude and phase imaging at THz frequencies. For these reasons we explored the feasibility of a THz modulated scatterer using a VO₂ switch as the tunable element. It must be noticed that this is the

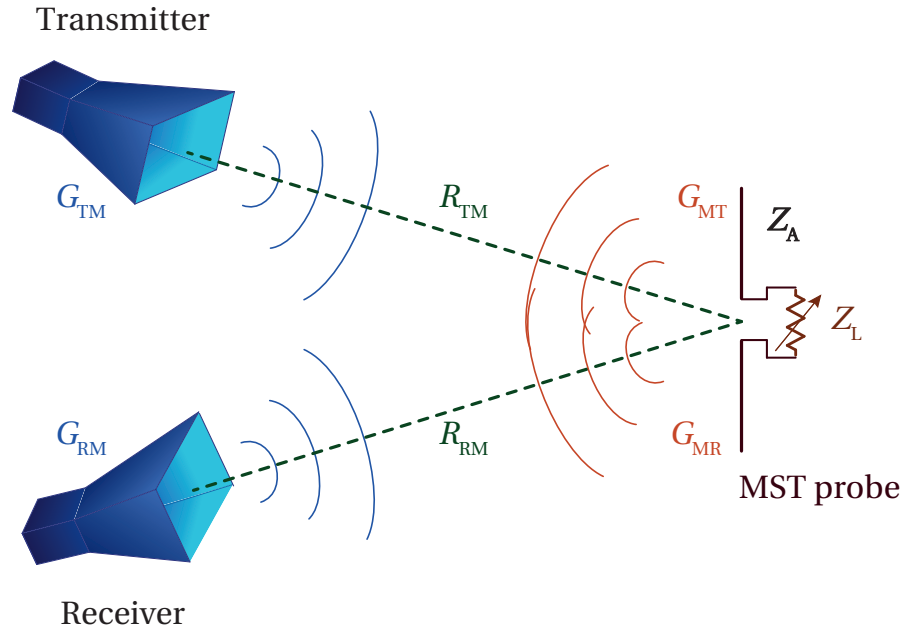


Figure 5.2 – General scenario of an RFID system where the transmitter and receiver antennas of the RFID reader communicate with a MST probe.

first THz reconfigurable device in which the tunability is obtained using a single VO₂ junction, in contrast with the applications presented in section 5.1.2, which exploit VO₂ metasurfaces. The use of a single VO₂ switch in our device is crucial, as it ensures operation even when the interrogation and receiver fields are placed at arbitrary angles with respect to the MST. This is not the case for metasurfaces, which are optimized to preserve the propagation direction of the modulated wave. Furthermore, the use of a single VO₂ switch drastically reduces the power consumption and the response time of the device

Figure 5.2 shows a general RFID scenario compatible with our study, where a reader is communicating with a MST probe. The reader is characterized by the gain G_{TM} of the transmitter antenna towards the MST and the gain G_{RM} of the receiver towards the MST. The MST probe is described by the gain G_{MT} of the MST towards the transmitter, the gain G_{MR} of the MST towards the receiver, the impedance of the antenna Z_A and the tunable load Z_L . In this work, the tunable load is implemented by a VO₂ switch with impedance Z_{VO_2} , which can be reconfigured from the value Z_{OFF} in the insulating state, to Z_{ON} in the conducting state.

The design procedure consists in optimizing the MST antenna and VO₂ switch in order to maximize the power of the modulated signal P_{mod} . This is achieved by

maximizing the difference in the scattered power in the two states of the MST. The MST theory is well known and demonstrates that the power of the modulated signal can be calculated using the modified Friis link budget equation [264]:

$$P_{\text{mod}} = G_{\text{TM}} G_{\text{MT}} G_{\text{MR}} G_{\text{RM}} \left(\frac{\lambda}{4\pi} \right)^4 \frac{1}{R_{\text{TM}}^2 R_{\text{RM}}^2} |\Gamma_{\text{ON}}^{\text{K}} - \Gamma_{\text{OFF}}^{\text{K}}|^2 P_{\text{T}} \quad (5.2)$$

where P_{T} is the power emitted by the transmitter, R_{TM} is the distance from the transmitter to the MST, R_{RM} is the distance from the receiver to the MST, λ is the wavelength and Γ^{K} is known as Kurokawa's reflection coefficient. Γ^{K} expresses the mismatch between the load and the antenna, and it is defined as:

$$\Gamma_{\text{ON}}^{\text{K}} = \frac{Z_{\text{ON}} - Z_{\text{A}}^*}{Z_{\text{ON}} + Z_{\text{A}}} \quad (5.3)$$

$$\Gamma_{\text{OFF}}^{\text{K}} = \frac{Z_{\text{OFF}} - Z_{\text{A}}^*}{Z_{\text{OFF}} + Z_{\text{A}}} \quad (5.4)$$

Equation (5.2) demonstrates that the power of the modulated backscattered signal is directly proportional to the square magnitude of the differential Kurokawa's reflection coefficient ($\Gamma_{\text{ON}}^{\text{K}} - \Gamma_{\text{OFF}}^{\text{K}}$). This quantity can be visualized as the distance $\Delta\Gamma^{\text{K}}$ between $\Gamma_{\text{ON}}^{\text{K}}$ and $\Gamma_{\text{OFF}}^{\text{K}}$ in a polar plot, as shown in Figure 5.3 for the ideal case in which the amplitude of $\Gamma_{\text{ON}}^{\text{K}}$ and $\Gamma_{\text{OFF}}^{\text{K}}$ is 1 and their difference in phase is 180°, resulting in the optimal distance $\Delta\Gamma^{\text{K}} = 2$.

5.2.2 Design and simulations

Figure 5.4 shows the diagram of the proposed implementation of the VO₂ MST. A dipole antenna is patterned on a VO₂ thin film. By applying a DC bias to the two terminals of the antenna, it is possible to switch the VO₂ region connecting them (highlighted in the figure as the “VO₂ tunable” region), which acts as a tunable load, reconfigurable from Z_{OFF} to Z_{ON} .

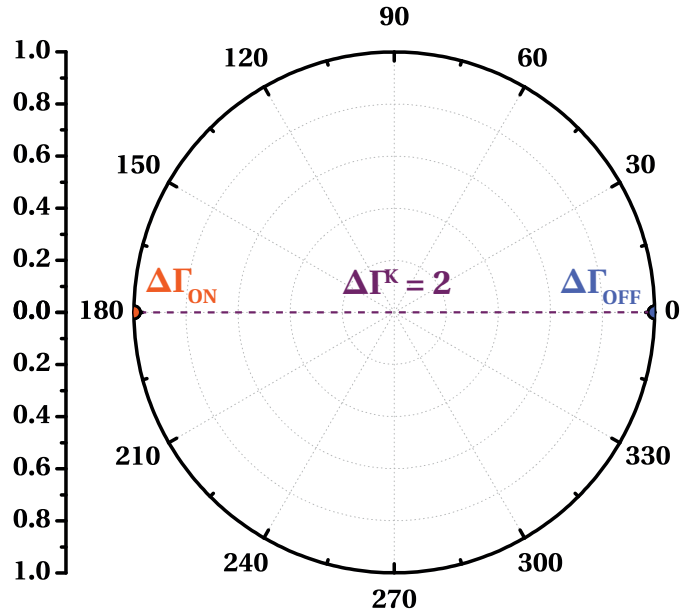


Figure 5.3 – Polar plot of Γ_{ON}^K and Γ_{OFF}^K in the ideal case for maximum P_{mod} : the amplitude of the reflection coefficients is 1 and their difference in phase is 180°.

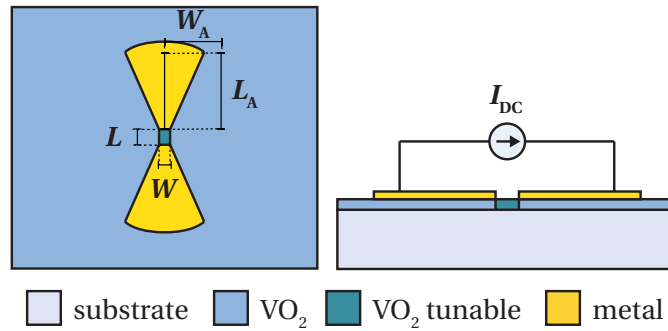


Figure 5.4 – Schematic diagram of the proposed VO₂ THz MST.

In case the load impedances are real, it is possible to prove from equations (5.3) and (5.4) that the differential Kurokawa's reflection coefficient is maximized if the design is based on the following guidelines:

- Z_{OFF} must be as high as possible;
- Z_{ON} must be as low as possible;
- the real part of Z_A must be close to the geometric mean of Z_{OFF} and Z_{ON} :

$$Z_{opt} = \sqrt{Z_{OFF} Z_{ON}};$$
- the imaginary part of Z_A must be negligible with respect to the real part.

Chapter 5. VO₂ MIT for reconfigurable THz functions

While Z_{OFF} and Z_{ON} can be predicted by knowing the resistivity curve of the VO₂ film, its thickness and the geometry of the port (width W and length L), the dependence of Z_A on frequency requires full-wave 3D electromagnetic simulations, performed in Ansys HFSS. The design procedure is complicated by the fact that the geometry of the port does not affect only Z_{OFF} and Z_{ON} , but also Z_A , both in its real and imaginary part.

In order to ensure broadband performance, for the MST antenna it was selected the bowtie topology. The bowtie antenna is a dipole antenna whose geometry is invariant with respect to scaling, a property that, associated with Maxwell's Equations scaling laws, ensures that the behavior of the antenna is theoretically independent of frequency. Actually, real bowtie antennas have finite size and non infinitesimal gap, and these non idealities set bounds on the actual antenna bandwidth.

Regarding the choice of the substrate, two options were considered: sapphire and high-resistivity silicon. Using sapphire allows to obtain higher quality VO₂ films, maximizing the contrast between Z_{OFF} and Z_{ON} ; however, optimizing VO₂ THz MSTs on high-resistivity silicon allows to develop a cheaper fabrication process with better compatibility with other steps. Table 5.1 summarizes the substrate parameters used for the design simulations. The VO₂ thickness was constant at 500 nm and its electrical resistivity depends on the choice of the substrate: for the design on sapphire it varies from $5 \times 10^{-1} \Omega\text{m}$ (insulating state) to $5 \times 10^{-6} \Omega\text{m}$, while for the design on high-resistivity silicon it varies from $2.4 \times 10^{-2} \Omega\text{m}$ to $4.4 \times 10^{-5} \Omega\text{m}$. The bowtie antenna was made of 200 nm thick gold (conductivity $\sigma = 4.1 \times 10^7 \text{ S/m}$).

Table 5.1 – Substrate properties used for design and electromagnetic simulations.

Material	Relative permittivity (1)	VO ₂ resistivity OFF (Ωm)	VO ₂ resistivity ON (Ωm)
Sapphire	10	5×10^{-1}	5×10^{-6}
HR-Si	11.66	2.4×10^{-2}	4.4×10^{-5}

Electromagnetic simulation setup

Figure 5.5 (a) shows the full simulated geometry. For good accuracy of the results, the boundaries of the simulation domain must be extended to a distance from the antenna higher than $\lambda/4$, where λ is calculated for the minimum simulated frequency (e.g. 750 μm for 0.1 THz in air). To improve the accuracy of the results for the radiation

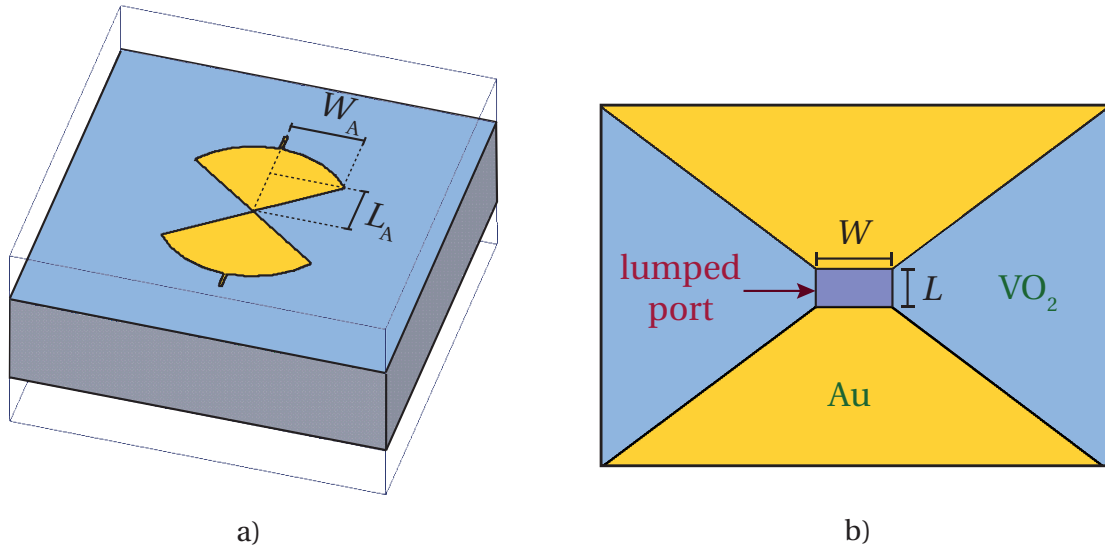


Figure 5.5 – a) Full geometry domain for the electromagnetic simulations performed to optimize the impedance of the bowtie antenna. b) Zoom on the switchable VO₂ region.

pattern, it is necessary to simulate the full substrate thickness and a vacuum region below. However, it must be noted that other electromagnetic simulation softwares, based on the method of moments (MoM), are better suited for the calculation of the radiation pattern.

Figure 5.5 (b) shows a zoom on the antenna gap, connected by the VO₂ tunable load. This region is coincident with the lumped port (impedance = 50 Ω) used to define the excitation. All the outer surfaces of the simulation domain are set to the radiation boundary condition. The mesh was refined through multiple adaptive passes until the change of the S-parameters between two consecutive passes, calculated at the maximum frequency, reached a value < 0.05.

Effect of the antenna shape

A first set of simulations was performed to optimize the shape of the bowtie antenna: the length $L_A = 60\mu\text{m}$ is constant, while the width W_A is a variable parameter going from 20 μm to 100 μm.

The switchable VO₂ junction dimensions were fixed at $L = 2\mu\text{m}$, $W = 4\mu\text{m}$. This geometry corresponds to the impedances $Z_{\text{OFF}} = 5 \times 10^5 \Omega$, $Z_{\text{ON}} = 5\Omega$, resulting in the target impedance $Z_{\text{opt}} = 1.58 \times 10^3 \Omega$ for the real part of Z_A .

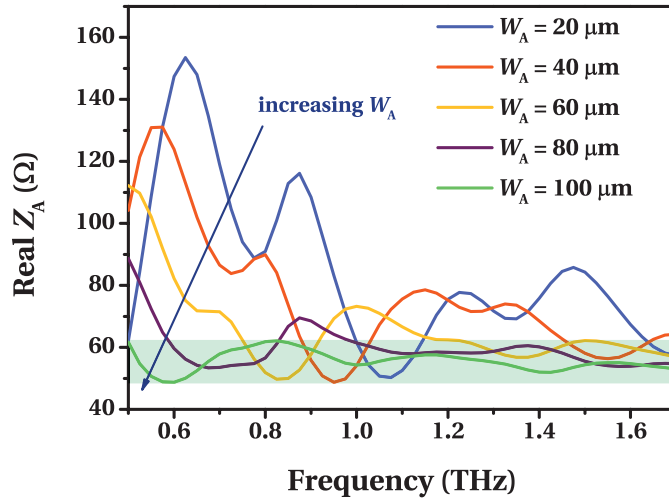


Figure 5.6 – Dependence of the real part of the antenna impedance on the width of the bowtie antenna. The optimized solution for broadband performance ($W_A = 100\mu\text{m}$) is highlighted in green.

Figure 5.6 shows the dependence on W_A of the real part of Z_A . By increasing W_A from 20 μm to 100 μm the antenna broadband behavior is extended: for $W_A = 100\mu\text{m}$, $\text{real}(Z_A)$ has a very low variation ($55.46\Omega \pm 6.68\Omega$) in the whole simulated frequency range (from 0.5 THz to 1.7 THz). Figure 5.7 shows the dependence on W_A of the imaginary part of Z_A : even in this case $W_A = 100\mu\text{m}$ provides the best performance, with the lowest values of $|\text{imag}(Z_A)|$ in the whole frequency range of interest.

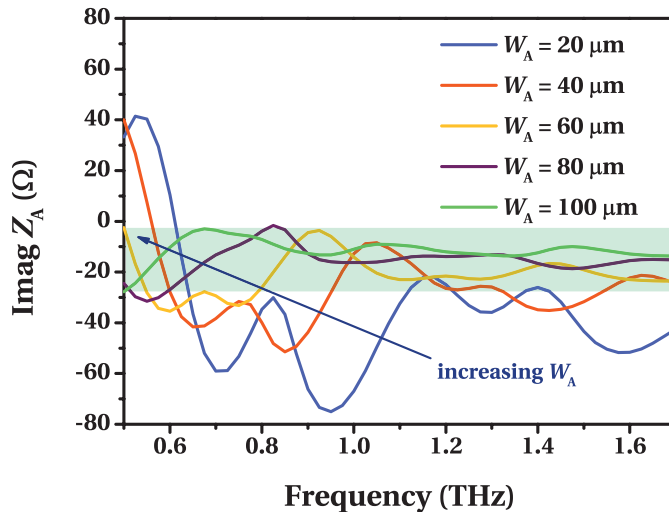


Figure 5.7 – Dependence of the imaginary part of the antenna impedance on the width of the bowtie antenna. The optimized solution ($W_A = 100\mu\text{m}$), showing negligible values with respect to the real part, is highlighted in green.

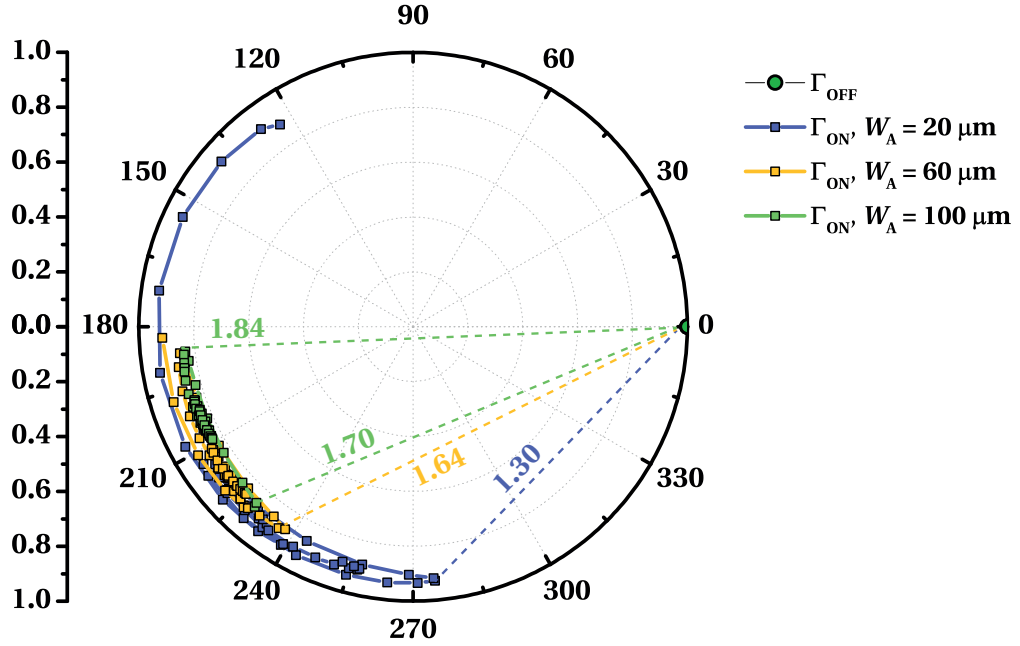


Figure 5.8 – Polar plot of Γ_{ON}^K and Γ_{OFF}^K for selected values of W_A , from $20\ \mu\text{m}$ to $100\ \mu\text{m}$. The minimum of $\Delta\Gamma^K$ is plotted in dashed lines for all values of W_A , the maximum only for the optimal value $W_A = 100\ \mu\text{m}$.

The effects of this optimization process are more clear in the polar plot of Γ^K shown in Figure 5.8. Γ_{OFF}^K shows no dependence on frequency due to the very high value of Z_{OFF} (ideal performance as in Figure 5.3), but the variation of Γ_{ON}^K reduces the value of $\Delta\Gamma^K$ in certain frequency ranges. The minimum of $\Delta\Gamma^K$ increases from 1.3 to 1.7 while increasing W_A from $20\ \mu\text{m}$ to $100\ \mu\text{m}$. The variation in $\text{imag}(Z_A)$ with frequency and its non-negligible values with respect to the real part causes important changes in the phase of Z_A , as a consequence reducing the value of $\Delta\Gamma^K$.

Figure 5.9 shows the dependence of $\Delta\Gamma^K$ on frequency for all the simulated values of W_A . The non-optimal solutions present dips in the frequency response, with extension decreasing in function of W_A .

Effect of the VO₂ switch width

Once defined the optimal ratio between length and width of the antenna to obtain an impedance Z_A with real part quasi-independent of frequency and negligible imaginary part, the next step of the design procedure consists in optimizing the VO₂ switch used as the tunable load. As concluded from the design equations presented in section 5.2.1, Z_{OFF} should be much higher and Z_{ON} should be much lower than the real part

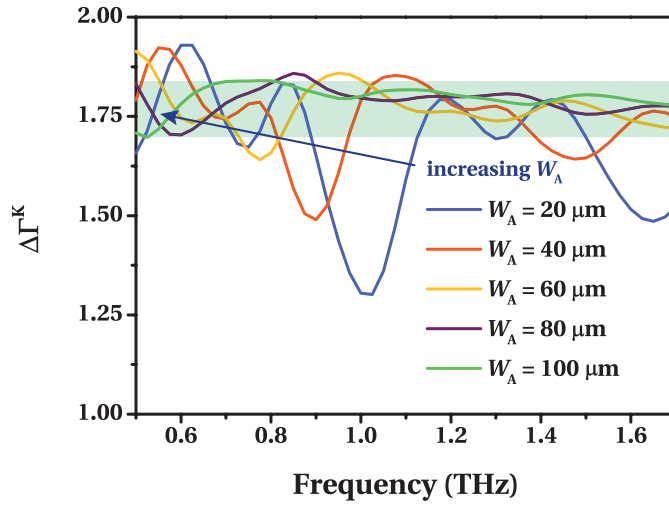


Figure 5.9 – Dependence of $\Delta\Gamma^K$ on frequency for all the simulated values of W_A . The optimized solution for broadband performance ($W_A = 100\mu\text{m}$) is highlighted in green.

of Z_A , with the ideal case given by $Z_{\text{opt}} = \text{real}(Z_A)$.

In the following discussion it is assumed that the switch impedance can be estimated by considering a patterned VO₂ region with the same dimensions of the gap, and that the VO₂ volume is fully switched in the ON state. The values of Z_{OFF} and Z_{ON} can then be easily controlled by modifying the width W and length L of the gap in the bowtie antenna, as reported in equation (3.8). However, especially for small values of L , the ratio W/L has an effect also on the antenna impedance. For this reason, Z_A had to be assessed for each combination of W and L . HFSS simulations from 0.5 THz to 1.7 THz were performed keeping constant $L_A = 60\mu\text{m}$, $W_A = 100\mu\text{m}$ (providing the best results in the previous set of simulations) and $L = 2\mu\text{m}$, while varying the VO₂ switch width W from $2\mu\text{m}$ to $8\mu\text{m}$.

Figure 5.10 shows the dependence on W of the real part of Z_A . In all the cases, $\text{real}(Z_A)$ is quite stable with frequency. By increasing the width from $2\mu\text{m}$ to $8\mu\text{m}$, $\text{real}(Z_A)$ decreases in average from 61.2Ω to 45.2Ω , corresponding to a decrease of 26.1%. Simultaneously, also Z_{opt} decreases but at a higher rate, from $3.16 \times 10^3\Omega$ to $7.90 \times 10^2\Omega$ (75% decrease), suggesting the possibility to match $\text{real}(Z_A)$ and Z_{opt} for larger widths.

However, as shown in Figure 5.11, $|\text{imag}(Z_A)|$ increases considerably with W due to the increased capacitive coupling at the antenna port. Combined with the decrease in $\text{real}(Z_A)$, this makes the imaginary part of Z_A rapidly non-negligible with respect

5.2. VO₂ modulated scatterer for THz applications

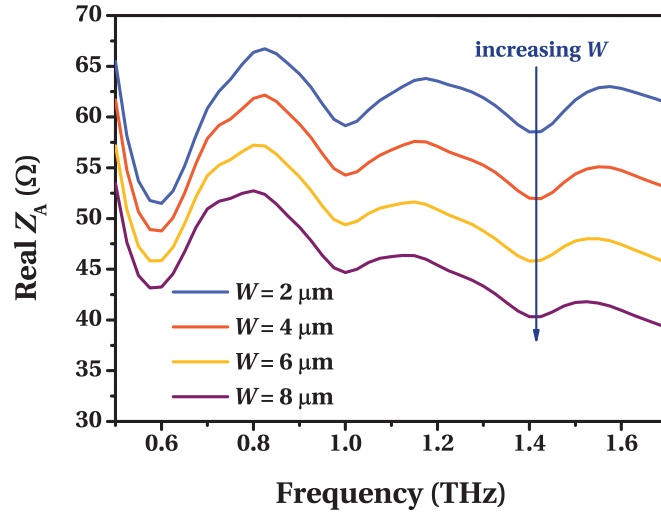


Figure 5.10 – Dependence of the real part of the antenna impedance on the width of the VO₂ switch.

to the real part, which is detrimental for the performance of the MST. Moreover, it must be noted that while $|\text{imag}(Z_A)|$ is fairly stable with frequency after 0.7 THz, it increases steeply lowering the frequency down to 0.5 THz.

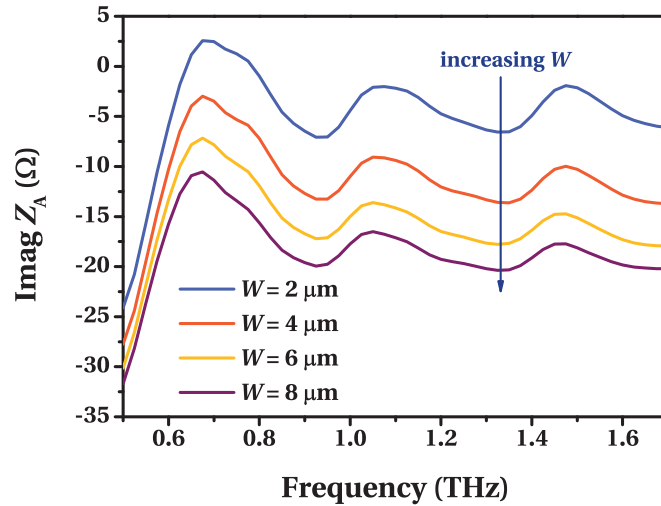


Figure 5.11 – Dependence of the imaginary part of the antenna impedance on the width of the VO₂ switch.

Table 5.2 summarizes the values of Z_{OFF} , Z_{ON} , Z_{opt} , $\text{real}(Z_A)$ and $\text{imag}(Z_A)$ (calculated in average for frequencies > 0.7 THz), for all the simulated geometries in this optimization step. The reported values show the conflict between the two optimization targets: matching $\text{real}(Z_A)$ and Z_{opt} , and having $\text{real}(Z_A) \gg |\text{imag}(Z_A)|$.

Table 5.2 – Dependence on W of the antenna and tunable load impedances.

$W(\mu\text{m})$	$Z_{\text{OFF}}(\Omega)$	$Z_{\text{ON}}(\Omega)$	$Z_{\text{opt}}(\Omega)$	$\text{real}(Z_A)(\Omega)$	$\text{imag}(Z_A)(\Omega)$
2	1.0×10^6	10	3.16×10^3	62.2	-3.86
4	5.0×10^5	5	1.58×10^3	56.1	-10.9
6	3.3×10^5	3.3	1.05×10^3	50.3	-15.3
8	2.5×10^5	2.5	7.90×10^2	45.0	-18.2

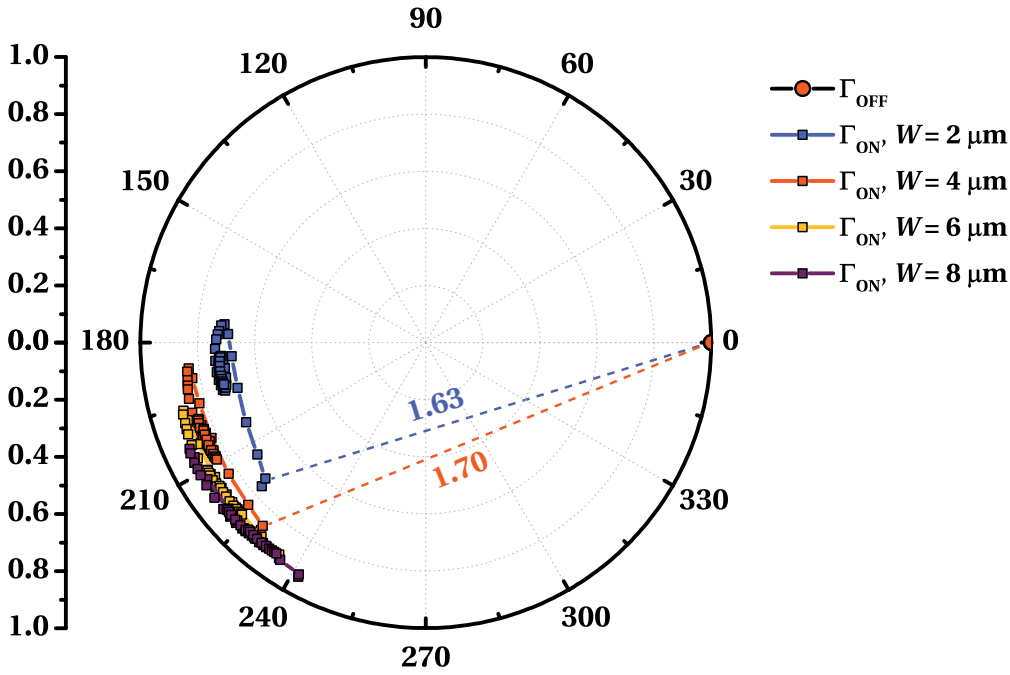


Figure 5.12 – Polar plot of $\Gamma_{\text{ON}}^{\text{K}}$ and $\Gamma_{\text{OFF}}^{\text{K}}$ for all the simulated values of W , from $2 \mu\text{m}$ to $8 \mu\text{m}$ and keeping constant $L = 2 \mu\text{m}$, $W_A = 100 \mu\text{m}$ and $L_A = 60 \mu\text{m}$. Minimum of $\Delta\Gamma^{\text{K}}$ plotted in dashed lines in the best ($W = 4 \mu\text{m}$) and worst ($W = 2 \mu\text{m}$) case.

In order to clarify which effect is more important for the broadband performance of the MST, the analysis of the results proceeds with the calculation of $\Delta\Gamma^{\text{K}}$. Figure 5.12 shows the polar plot of $\Gamma_{\text{OFF}}^{\text{K}}$ and $\Gamma_{\text{ON}}^{\text{K}}$ for all the simulated values of W . With the exception of the $W = 2 \mu\text{m}$ case, which clearly shows worse results with a minimum of $\Delta\Gamma^{\text{K}} = 1.63$, the other geometries present comparable performance.

Due to the increase in $|\text{imag}(Z_A)|$ while decreasing the frequency from 0.7 THz to 0.5 THz, $\Delta\Gamma^{\text{K}}$ decreases and reaches its minimum in that frequency range, for all values of W . This effect is better shown in Figure 5.13, plotting the dependence of $\Delta\Gamma^{\text{K}}$ on frequency. For frequencies higher than 0.7 THz, the simulation with presents in average the best performance.

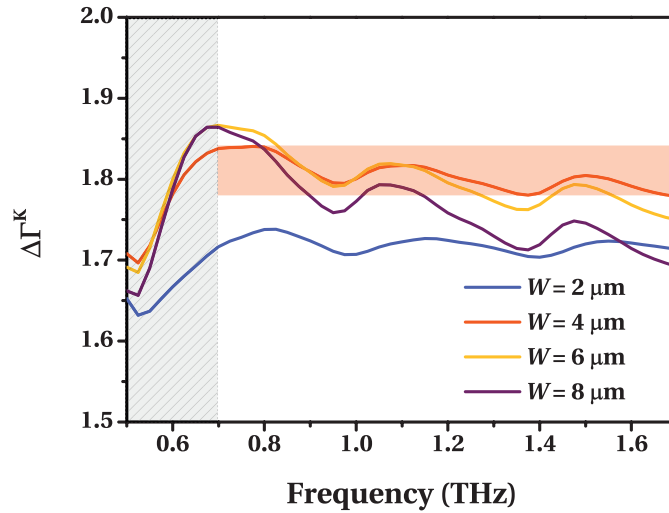


Figure 5.13 – Dependence of $\Delta\Gamma^K$ on frequency for all the simulated values of W . The optimized solution for broadband performance starting from 0.7 THz ($W = 4\mu\text{m}$) is highlighted in red.

Effect of the antenna size

As remarked in the previous optimization section, the MST presents a drop in performance for frequencies lower than 0.7 THz. In order to extend the frequency range of operation of the device, another set of simulations was performed for bowtie antennas with larger dimensions, from 0.1 THz to 1.7 THz. An additional advantage of larger antennas consists in facilitating the measurements, allowing to more easily center the THz beam on the antenna.

Figure 5.14 shows the frequency dependence of the impedance of an optimized bowtie antenna with larger dimensions ($L_A = 300\mu\text{m}$, $W_A = 400\mu\text{m}$), keeping constant the geometry of the VO₂ switch optimized in the previous section ($L = 2\mu\text{m}$, $W = 4\mu\text{m}$), corresponding to $Z_{\text{opt}} = 1.58 \times 10^3 \Omega$. As expected for an optimized bowtie antenna, the impedance presents a very low dependence on frequency; the average of $\text{real}(Z_A)$ in the whole frequency range is 62.6Ω and the average of $\text{imag}(Z_A)$ is -13Ω .

This design provides excellent performance in the whole frequency range, as shown by the polar plot of Γ_{ON}^K and Γ_{OFF}^K in Figure 5.15 (a) and the dependence on frequency of $\Delta\Gamma^K$ in Figure 5.15 (b).

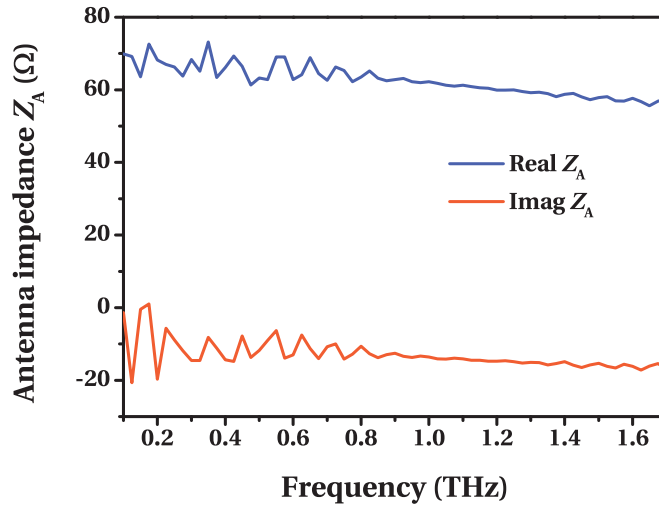


Figure 5.14 – Dependence on frequency of the impedance of the large bowtie antenna.

Optimization of the VO₂ THz MST on HR-Si

As aforementioned, studying the design of the VO₂ THz MST on silicon is interesting because of the lower costs with respect to sapphire and better compatibility with other processing steps that could be required for integration with other devices.

However, as presented in chapter 2, VO₂ films on silicon do not exhibit MIT as steep as the ones on sapphire, with resistance ratios of the order of 3 decades in the best case.

This section deals with the assessment of the THz MST performance on Si/SiO₂ substrates, using the VO₂ resistivity values reported in Table 5.1 (resistance ratio of 545). HFSS simulations from 0.5 THz to 1.7 THz were performed keeping constant the optimized antenna shape ($L_A = 60\mu\text{m}$, $W_A = 100\mu\text{m}$) and the VO₂ switch length $L = 2\mu\text{m}$, while varying W from $4\mu\text{m}$ to $16\mu\text{m}$. Larger widths with respect to the switches on sapphire were needed to take into account the higher resistivity in the ON state of VO₂ deposited on SiO₂. The dependence of the real and imaginary part of the antenna impedance has the same profile as what obtained for the antennas on sapphire (Figures 5.10 and 5.11): increasing the width of the gap in the bowtie antenna decreases $\text{real}(Z_A)$ and increases $\text{imag}(Z_A)$. The results for all the simulated geometries are summarized in Table 5.3.

Despite VO₂ having lower resistivity in the OFF state with respect to VO₂ on sapphire, the resistance in the OFF state is still much higher than $\text{real}(Z_A)$. As a consequence,

5.2. VO₂ modulated scatterer for THz applications

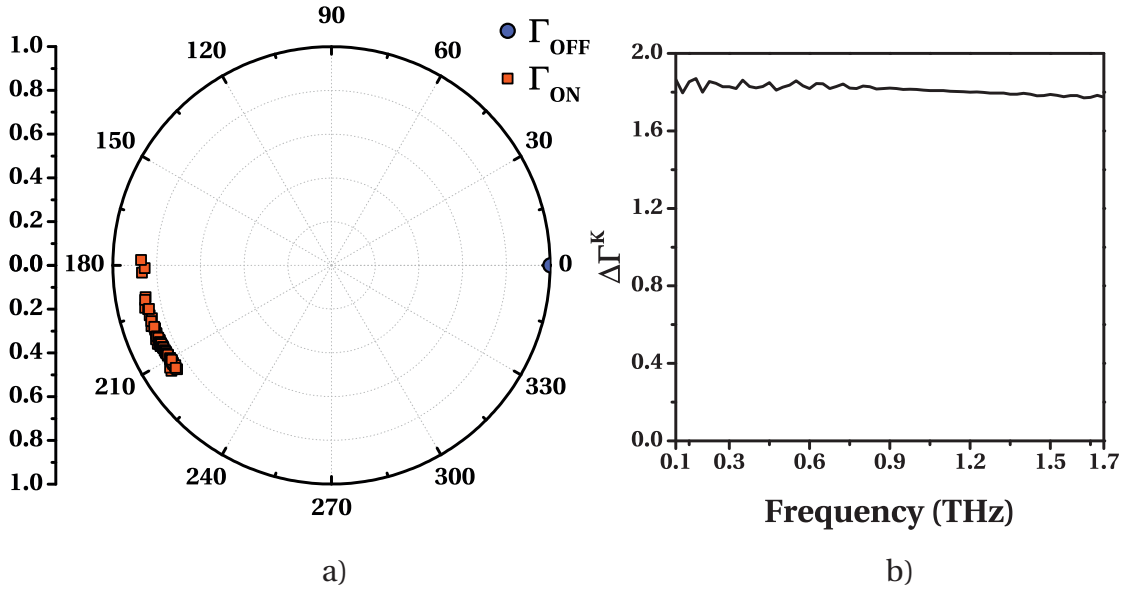


Figure 5.15 – a) Polar plot of $\Gamma_{\text{ON}}^{\text{K}}$ and $\Gamma_{\text{OFF}}^{\text{K}}$ for the optimized large bowtie antenna ($L_{\text{A}} = 300\mu\text{m}$, $W_{\text{A}} = 400\mu\text{m}$, $L = 2\mu\text{m}$, $W = 4\mu\text{m}$). b) Dependence on frequency of $\Delta\Gamma^{\text{K}}$.

as shown in Figure 5.16, $\Gamma_{\text{OFF}}^{\text{K}}$ is at the border of the polar plot and independent of frequency. However, due to the higher resistivity in the ON state, W must be increased greatly to improve the $\text{real}(Z_{\text{A}})/Z_{\text{ON}}$ ratio and achieve acceptable values of $\Delta\Gamma^{\text{K}}$.

As better shown in Figure 5.17, $\Delta\Gamma^{\text{K}}$ improves in the whole frequency range while increasing W from $4\mu\text{m}$ to $12\mu\text{m}$, but it decreases for $W = 16\mu\text{m}$ despite the improved $\text{real}(Z_{\text{A}})/Z_{\text{ON}}$ ratio. For the optimized case ($W = 12\mu\text{m}$) the minimum of $\Delta\Gamma^{\text{K}}$ is 1.2 and the maximum is 1.44.

Table 5.3 – Impedances of the antenna and tunable load for the MST on HR-Si.

$W(\mu\text{m})$	$Z_{\text{OFF}}(\Omega)$	$Z_{\text{ON}}(\Omega)$	$Z_{\text{opt}}(\Omega)$	$\text{real}(Z_{\text{A}})(\Omega)$	$\text{imag}(Z_{\text{A}})(\Omega)$
4	2.4×10^4	44	1.02×10^3	54.1	-9.7
6	1.6×10^4	29.3	6.85×10^2	48.4	-14.0
8	1.2×10^4	22	5.14×10^2	43.4	-16.8
10	9.6×10^3	17.6	4.11×10^2	38.8	-18.4
12	8.0×10^3	14.7	3.42×10^2	35.0	-19.3
14	6.9×10^3	12.6	2.93×10^2	31.3	-19.7
16	6.0×10^3	11	2.56×10^2	28.3	-19.8

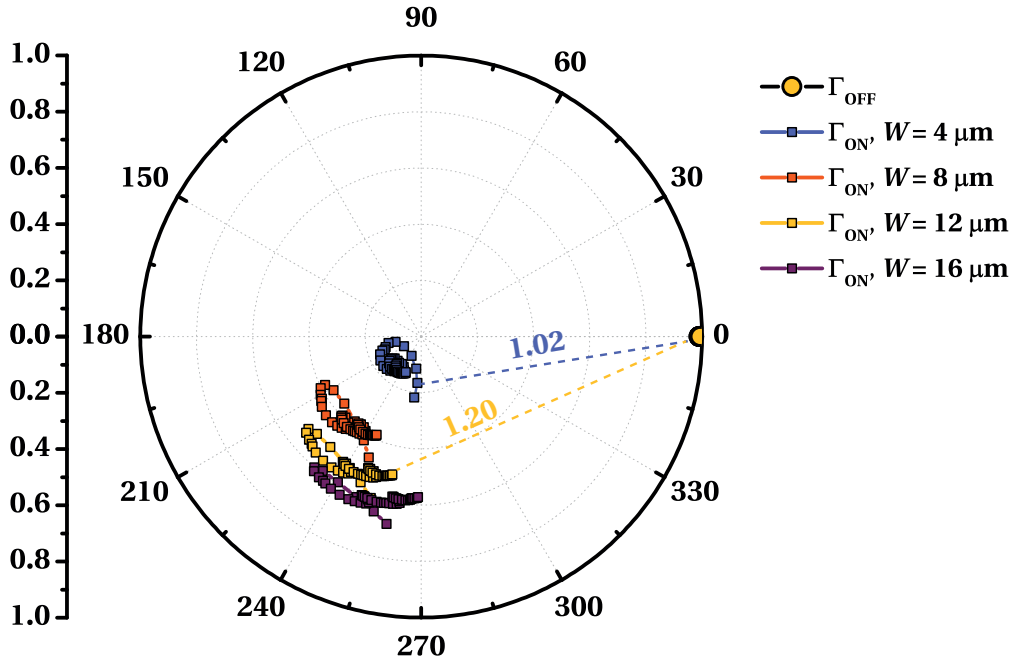


Figure 5.16 – Polar plot of Γ_{ON}^K and Γ_{OFF}^K for the THz MST on HR-Si for selected values of W , from $4\ \mu\text{m}$ to $16\ \mu\text{m}$ and keeping constant $L = 2\ \mu\text{m}$, $W_A = 100\ \mu\text{m}$ and $L_A = 60\ \mu\text{m}$. Minimum of $\Delta\Gamma^K$ plotted in dashed lines in the best ($W = 12\ \mu\text{m}$) and worst ($W = 4\ \mu\text{m}$) case.

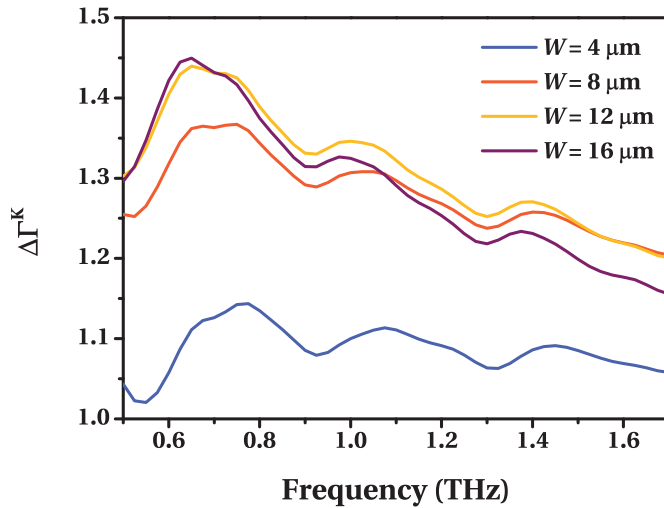


Figure 5.17 – Dependence of $\Delta\Gamma^K$ on frequency for the THz MST on HR-Si for selected values of W .

5.2.3 Fabrication

The VO₂ THz MST presented in this chapter was fabricated in collaboration with LMN at INRS, University of Quebec.

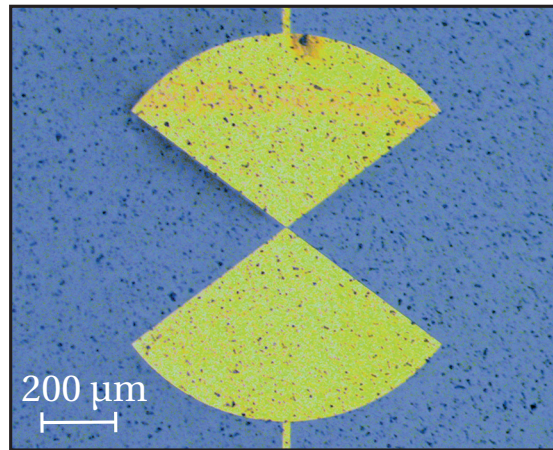


Figure 5.18 – Top view of the characterized VO₂ THz MST.

A 500 nm thick epitaxial VO₂ layer was first deposited on a 1" circular sapphire substrate (Al₂O₃(1 $\bar{1}$ 02) orientation) by PLD, with details on the deposition parameters reported in section 3.4.3. The metallic patterns for the bowtie antennas and the 20 μm wide bias lines used to induce the E-MIT were defined by e-beam lithography and lift-off of a 150 nm Cr/Cu/Au stack. The full layout was included in a 1x1 cm² area, subsequently diced from the substrate. Metal pads were defined at the border of the chip to connect the devices to a printed circuit board (PCB) support.

Figure 5.18 shows an optical microscope image of the characterized device, with dimensions corresponding to the results of the optimization process carried out in the previous section ($L_A = 300\mu\text{m}$, $W_A = 400\mu\text{m}$, $L = 2\mu\text{m}$, $W = 4\mu\text{m}$).

5.2.4 Measurements

DC E-MIT characterization

DC measurements were performed to characterize the actuation of the VO₂ switch integrated in the THz MST antenna. Figure 5.19 shows the resistance modulation for a VO₂ switch actuated with current up to 20 mA. The resistance in the OFF state is $Z_{\text{OFF}} = 1.25\text{k}\Omega$. The switch actuates at $I_{\text{act}} = 1.04\text{mA}$ and the resistance in the ON state can be further decreased depending on the level of the bias current. For instance, Z_{ON} is 149 Ω at 5 mA and 28.5 Ω at 20 mA.

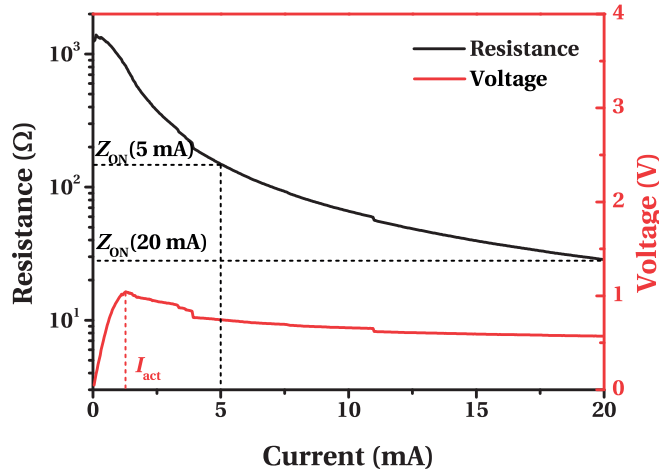


Figure 5.19 – Current actuation of the VO₂ switch used as a tunable load for the VO₂ THz MST.

THz characterization

The substrate was connected to the PCB support by using silver paint; standard wire bonding on the metal pads used for biasing could not be used due to insufficient adhesion of the metal stack on VO₂. The VO₂ MST has been characterized from 0.1 THz to 2 THz with a TERA K15 *MARK II* time-domain THz spectrometer from MenloSystems. The measurement setup is shown in Figure 5.20, in reflective configuration and with a rotary stage used for automatic measurements of the radiation pattern.

The setup has been configured to send a THz pulse towards the MST antenna, with an inclination of 45° with respect to the sample surface. The aim of the measurements is to verify that a modulated signal can be obtained by switching ON and OFF the VO₂ junction of the antenna, and that this modulated signal is scattered not only towards the specular direction of the beam but in multiple directions. This is a fundamental characteristic of the proposed MST, which sets it apart from standard surface modulators and allows the applications described above.

To maximize accuracy, a sequence of measurements was performed on the MST. Each measurement cycle consists of four measurements (*M1*, *M2*, *M3*, *M4*), where the first one is made in the ON state of the switch and the other three are made in the OFF state. The modulated signal is given by subtracting *M1*-*M2* (i.e. ON-OFF). However, THz measurements may be characterized by low signal to noise ratios, so it is important to do also dummy measurements to evaluate the noise floor. This is done by subtracting

5.2. VO₂ modulated scatterer for THz applications

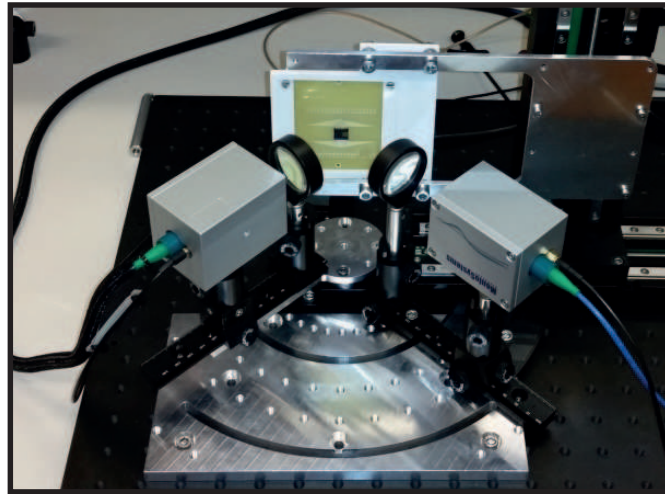


Figure 5.20 – Measurement setup for reflective THz-TDS.

$M3-M4$ (i.e. OFF-OFF), which should cancel out ideally but will give a signal indicating the noise and non-repeatability of the THz setup. The operation of the MST is verified if the modulated signal ($M1-M2$) is much stronger than the noise floor ($M3-M4$).

1000 cycles were performed and averaged in order to obtain lower noise floor. In order to provide results independent of the intensity of the used pulse, both the modulated signal and the noise floor are normalized (in a frequency-wise manner) relatively to the total power emitted by the setup, which can be easily measured in a specular configuration using a gold plated mirror chip.

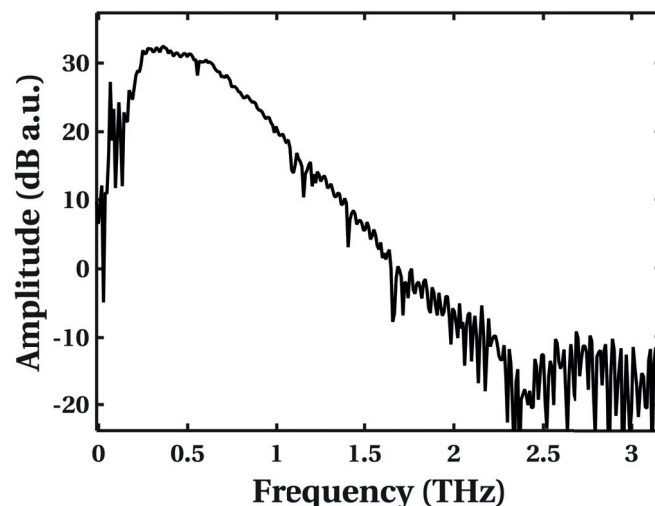


Figure 5.21 – Nominal power spectrum of the THz spectrometer used in this work, measured with a reference mirror.

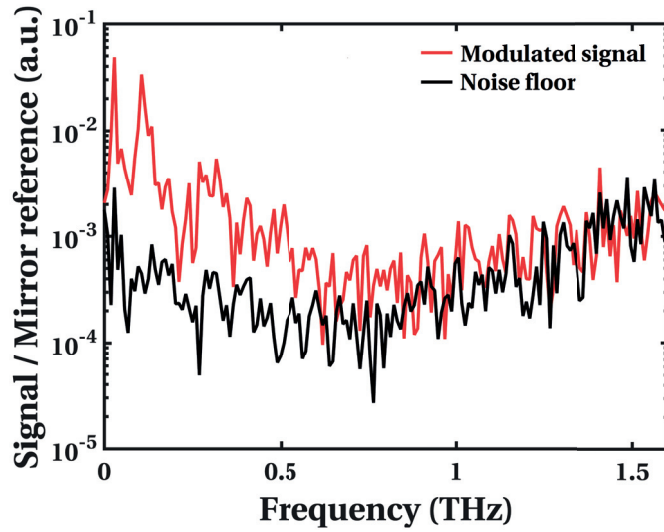


Figure 5.22 – Differential signal and noise floor for incidence at 45° and reception at –10° from the normal. The measurements have been normalized with respect to the mirror power. The results are obtained averaging 1000 cycles.

Figure 5.21 shows the nominal power of our system measured in this way. Excellent dynamical range is available up to 1.6 THz. In order to limit the power consumption and prevent reliability issues due to the high number of planned actuation cycles, in a first set of measurements the current was limited to $I_{DC} = 20$ mA while operating the device. This current level was not high enough to fully actuate the switch and reach the Z_{ON} value used in the design, but still low enough to ensure a good Γ_{ON}^K value.

Figure 5.22 shows the normalized modulated signal, measured at an incident angle of 45° and a reception angle of –10° from the normal. The MST working principle has been validated by measuring a modulated signal up to two orders of magnitude larger than the noise floor, providing maximum SNR at 0.32 THz. The device operation is very broadband, starting from less than 0.1 THz and verified until 0.8 THz, confirming that this is the first MST antenna operating in the THz range.

To obtain a further confirmation that the modulated signal actually came from the antenna, THz imaging has been performed by translating the chip and its support in the XY plane, while leaving unchanged the excitation (45°) and the readout (–10°) angles of the THz setup. Figure 5.23 shows the obtained intensity mapping in linear units, obtained at the frequency of 0.32 THz, both for the noise floor (Figure 5.23 a) and the modulated signal (Figure 5.23 b).

It is possible to observe that the antenna appears as a bright spot in the center of

5.2. VO₂ modulated scatterer for THz applications

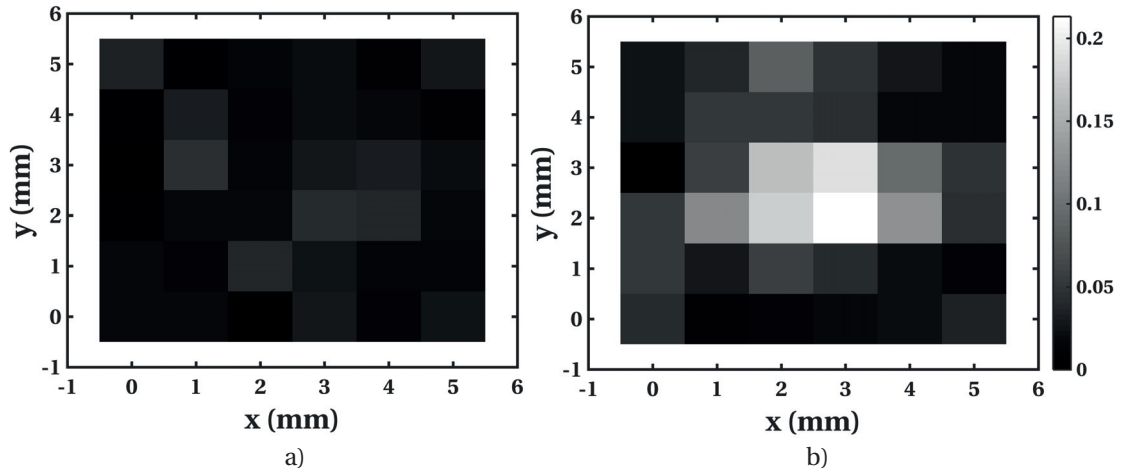


Figure 5.23 – a) Noise floor and b) modulated signal imaging at 0.32 THz. The measurements are obtained averaging 100 cycles.

the scanned area, which is completely absent in the noise floor, confirming that the antenna operated as expected.

In order to obtain a radiation pattern of the VO₂ THz MST, the receiver angle was scanned while keeping constant the transmitter one, and for each configuration the measurements were obtained averaging 100 cycles. It is possible to observe that the radiation pattern slightly at -30° , but it remains fairly omnidirectional as expected for a bowtie antenna. Further investigations are required to explain the drop in the radiation pattern, which might be due to the effect of the substrate.

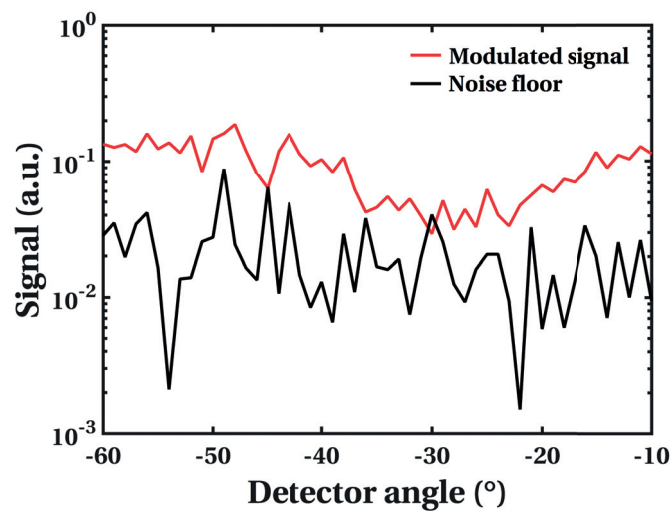


Figure 5.24 – Radiation pattern of the VO₂ THz MST.

5.3 Conclusion

The main contribution of this chapter consists in the demonstration of the first MST antenna in the THz range, enabled by the metal-insulator transition in VO₂.

After a general introduction on the properties of THz waves, the main applications of the MIT in VO₂ for THz devices were reviewed. A common element among all previous applications of VO₂ for reconfigurable THz devices is the fact that a continuous VO₂ film or a repeated pattern of VO₂ junctions is used to modify the electromagnetic properties of a surface. In this work we propose for the first time a THz device based on a single VO₂ junction. The results presented in this chapter can encourage the use of single VO₂ switches for THz reconfigurable electronics, having highlighted their advantages with respect to metasurfaces: operation ensured even when the interrogation and receiver fields are placed at arbitrary angles, reduced power consumption, reduced response time

The proposed device is a VO₂ MST for THz RFID applications. The theory of MSTs is well known, but no MST working in the THz range was ever demonstrated before this work. The design tradeoffs and the optimization process for the MST antenna and the integrated VO₂ switch were discussed by full-wave electromagnetic simulations, and the resulting geometry was fabricated and characterized up to 2 THz using reflective THz-TDS.

The MST working principle has been validated by measuring a modulated signal up to two orders of magnitude larger than the noise floor. The device operation is very broadband, starting from less than 0.1 THz and verified until 0.8 THz, confirming that this is the first MST antenna operating in the THz range, promising for the development of fast and energy-efficient THz communication applications and novel phase-resolved THz imaging systems.

6 Conclusions and perspectives

The aim of this thesis was to study the potential of the MIT in functional oxides for reconfigurable electronics in a wide frequency range, from steep-slope electronic switches for logic, to reconfigurable high-frequency functions up to the THz range.

Vanadium dioxide presents a MIT near room temperature with high contrast in electrical properties between the two structural phases. For this reason, it has been selected as an ideal candidate to discuss the potential of the metal-insulator transition for the applications targeted in this thesis.

A CMOS-compatible process for sputtering deposition of VO₂ and device integration has been optimized and exploited for several devices based on the MIT: steep slope temperature-stable DC switches, highly-reliable low-loss RF switches, novel tunable capacitors and RF filters. The possibility to enable tunable functions at even higher frequency was demonstrated by the design and characterization of the first modulated scatterer working in the THz range.

6.1 Conclusions

The main contributions from the work presented in this thesis can be summarized as follows:

- 1. Development of a high-quality CMOS-compatible technology for VO₂ electronic switches on Si/SiO₂ substrates.**

A fabrication process for VO₂ electronic switches on Si/SiO₂ substrates has been developed with particular focus on CMOS-compatibility. The critical step of the

process was the optimization of the reactive magnetron sputtering deposition on SiO₂, which required a precise control of the O₂ partial pressure in the sputtering chamber. The film exhibited a resistance ratio as high as 3.33×10^3 , decreasing from 5 Ω cm to 1.5×10^{-3} Ω cm increasing the temperature from 25 °C to 95 °C, and a hysteresis of ~ 7 °C. These values are comparable to what achievable with PLD of polycrystalline VO₂, without its drawbacks in terms of homogeneity for large-scale depositions. The resulting CMOS-compatible planar VO₂ electronic switches on Si/SiO₂ substrates had a resistance ratio of $> 1.44 \times 10^3$ when electrically actuated, more than one decade higher than previously reported VO₂ switches on Si/SiO₂ substrates.

2. Comprehensive study of the E-MIT slope in VO₂ switches.

We assessed for the first time the slope of the electrical transition in two-terminal VO₂ switches, reporting values as low as 0.24 mVdec⁻¹ at room temperature. Moreover, we experimentally reported the dependence of the slope on the temperature, increasing only up to 0.38 mVdec⁻¹ at 50 °C, corresponding to a T dependence $< 5.5 \mu\text{V}^\circ\text{C}/\text{dec}$. Moreover, the devices show excellent ON-state conduction, with $I_{\text{ON}} \geq 1.8 \text{ mA}/\mu\text{m}$ at 5.5 V independently of temperature. These results recommend MIT VO₂ switches as future candidates for steep-slope, highly conductive, temperature-stable switches.

3. Method to decrease the actuation voltage by generating high electric fields in VO₂ switches.

We proposed an alternative electrode shape to reduce the actuation voltage V_{act} in VO₂ switches. Triangular-shaped metal “spikes” along the electrode sides of a VO₂ junction allow to decrease the voltage necessary to reach the transition temperature T_{MIT} with respect to standard “flat” junctions. This effect is due to the higher electric field induced at the tip of the spikes, which depends on the spike radius of curvature. For 10 μm long switches, the devices with flat junctions actuated on average at 25.8 V, while the devices with spikes actuated on average at 20.1 V. In the best case, considering the devices which actuated at lower voltage, we obtain a 25.3 % reduction in V_{act} for the 10 μm long devices (from 16.6 V to 12.4 V) and a 38.3 % reduction in V_{act} for the 2 μm long devices (from 8.6 V to 5.3 V).

4. Fabrication and characterization of CMOS-compatible VO₂ RF switches.

We reported for the first time VO₂ RF switches based on a CMOS-compatible

process on Si/SiO₂ substrates. The VO₂ switches present excellent RF performance, around -0.6 dB S_{21-ON} independent of frequency and -10 dB S_{21-OFF} at 40 GHz, comparable with the state-of-the-art of VO₂ RF switches on sapphire. A variability study on 32 instances of the same device ($W = 100\mu\text{m}$, $L = 12.5\mu\text{m}$) was performed, obtaining $R_{ON} = 12 \pm 3\Omega$ and $R_{OFF} = 8.25 \pm 2.25\text{k}\Omega$. A reliability study revealed that the lifetime of voltage-actuated VO₂ RF switches is highly dependent on the rise time of the voltage pulse train and it can be slightly improved decreasing the DC current density, while it is not affected by the duty cycle. A lifetime higher than 10^9 cycles was reported for a pulse train with an amplitude of 15 V, a current density of $5 \times 10^5 \text{ A cm}^{-2}$ and a rise time of 4 μs . These results validate VO₂ RF switches as a promising solution for wideband reconfigurable electronics.

5. Fabrication and characterization of novel VO₂ tunable capacitors.

We proposed a new method to exploit VO₂ for tunable capacitors: the MIT allows tuning the length of a gap between metal lines, and in consequence its parasitic capacitance. Following this approach, a thermally actuated VO₂ tunable capacitor loaded in series configuration on a CPW has been modeled, fabricated and characterized up to 40 GHz. The series capacitor shows two well defined states, switching from 5.8 fF in the VO₂ insulating state to 12.5 fF in the VO₂ conducting state. The VO₂ tunable capacitors offer an alternative to more commonly employed technologies for RF reconfigurable electronics, presenting lower loss than semiconductor varactors at high frequency and easier integration than RF MEMS.

6. Fabrication and characterization of VO₂ RF tunable filters in the K band.

Tunable and switchable bandstop filters based on the VO₂ tunable capacitors were fabricated and characterized. The filters maintain good RF performance in both the insulating and the conducting state, in a frequency range higher than what previously reported using conventional VO₂ RF switches, limited by their parasitic capacitance. The fabricated tunable bandstop filters reached a tunability of 12 % in resonance frequency, from 22.5 GHz to 19.8 GHz. The return loss is about -1.5 dB at the center frequency, the isolation is 17.2 dB in the OFF state and 18.8 dB in the ON state, and the insertion loss is better than -2 dB in the lower and higher conducting bands up to 40 GHz. The fabricated switchable bandstop filter shows a bandstop resonance around 22.5 GHz with high isolation (18 dB) in the OFF state and low insertion loss in the ON state,

better than -2.5 dB up to 40 GHz. The measurements are in good agreement with full-wave 3D electromagnetic simulations, which moreover show that the performance of the VO₂ tunable filter is comparable to the corresponding ideal fixed-frequency filters in both the ON and OFF states.

7. Study of the integration of microheaters in VO₂ tunable capacitors and filters.

We investigated the feasibility of electrothermal actuation of VO₂ tunable capacitors with integrated microheaters, locally heating the VO₂ regions. The tradeoff between power needed for actuation and RF performance has been studied by electrothermal and electromagnetic simulations. A tunable microwave filter employing VO₂ capacitors with integrated microheaters has been simulated, showing performance comparable to the corresponding fixed-frequency filters in both the ON and the OFF state: the resonance frequency varies by only 4.4 % in the OFF state ($f_{0\text{-OFF}} = 26.76$ GHz) and 7.2 % ($f_{0\text{-ON}} = 21.9$ GHz) in the ON state, while the rejection level presents a slight decrease, from -14.72 dB to -12.04 dB in the OFF state and from -14.61 dB to -11.93 dB in the ON state. Importantly, the filter performance is not affected in terms of tunability (18.2 %), demonstrating the potential of the proposed method for electrical control of VO₂ tunable filters in the K band.

8. Fabrication and characterization of the first THz MST.

A modulated scatterer working in the THz range has been demonstrated for the first time, exploiting the MIT in VO₂. Differently from all previously reported THz VO₂ devices, based on the reconfiguration of the electromagnetic properties of a metasurface, in the proposed THz MST the device operation is based on a single VO₂ junction as small as $2\ \mu\text{m} \times 4\ \mu\text{m}$. An optimum design for the VO₂ THz MST was fabricated and characterized up to 2 THz using reflective THz-TDS. The device operation is very broadband, starting from less than 0.1 THz and verified until at least 0.8 THz, confirming that this is the first MST antenna operating in the THz range.

6.2 Future work

This section summarizes the most important research paths for further investigations related to the work presented in this thesis:

1. Low-power steep-slope VO₂ switches.

The method to decrease the actuation voltage in VO₂ switches, presented in section 3.4, has shown promising results. However, the devices had still too high levels of actuation voltage and current to be promising for low-power applications. This can be partially ascribed to the variability of the PLD process employed in this case, therefore it would be interesting to proceed with a second fabrication run based on the sputtering process developed at EPFL. The objective to develop energy efficient switches must be further pursued identifying and testing other methods to reduce the actuation power, like extreme nanopatterning of the VO₂ junction. Combined with the proposed optimized electrode shape for increasing the electric field, this approach is expected to enable ultra-low power steep-slope switches for Beyond CMOS logic.

2. Further applications of VO₂ tunable capacitors.

VO₂ tunable capacitors have been successfully characterized and their potential for reconfigurable microwave circuits has been assessed by fabricating tunable bandstop filters. Further work is encouraged to identify other possible applications for VO₂ tunable capacitors for reconfigurable microwave electronics, like for instance digital phase shifters.

3. Fabrication of integrated microheaters for VO₂ electrothermal actuation.

The electromagnetic simulations of VO₂ tunable bandstop filters with integrated microheaters proved that local electrothermal actuation of VO₂ is a promising method to overcome the limitations of thermal actuation in terms of required power and switching time, because the filter performance is not affected in terms of tunability and only slightly in terms of rejection level. However, these findings have to be validated by measurements, fabricating devices based on the process proposed in Figure 4.26.

4. VO₂ THz MST applications.

The working principle of the VO₂ THz MST has been successfully validated, measuring a modulated signal up to two orders of magnitude larger than the noise floor. Further work involves the development of possible applications based on the MST, such as RFIDs or imaging retinas [265, 266].

6.3 Perspectives

This thesis and other recent works confirm that VO₂ devices have high potential to offer an alternative to competing technologies and open a new design space in a broad frequency range. However, some important challenges in terms of technology and design must be addressed to bring these devices to a maturity level suitable for industrial applications. Important research topics for this purpose include:

1. Optimization of VO₂ technology for industrial scale fabrication.

In order to develop a VO₂ technology platform suitable for industrial scale processes, further work is required in terms of material optimization and integration. The optimization of the films must be driven by well-defined figures of merit for the targeted applications, and the process must achieve fully controlled integration capability on CMOS platforms, focusing on stability during lithographic processing, control of changes in material properties due to processing and long-term stability of the material properties. Atomic layer deposition of VO₂ offers a very attractive route towards an industrial scale deposition of high quality VO₂ with good reproducibility, being a very robust process, capable of nanometer thickness control and able to produce conformal coatings even across trenches.

2. Engineering of VO₂ material to tune the MIT properties.

The MIT in pure VO₂ is well known in terms of electrical properties, with a high contrast in resistivity very attractive for applications in reconfigurable electronics. However, the thermal MIT occurs relatively close to room temperature, while many electronic devices (e.g. for airborne applications) must work up to operating temperatures ~ 125 – 150 °C. Moreover, the resistivity in the insulating state of VO₂ is often too low for applications based on 2-terminal abrupt switches. Both issues can be addressed doping VO₂ with elements that increase its band gap.

3. 3-terminal VO₂ switches.

One of the most important open questions regarding VO₂ devices remains the research for ideal design strategy and switching mechanism enabling 3-terminal VO₂ switches with low power, steep slope and high ON/OFF contrast. Electrothermal and field-effect gating must be further investigated for optimized 3-terminal VO₂ devices.

Bibliography

- [1] J. Bardeen and W. H. Brattain, "The Transistor, A Semi-Conductor Triode," *Physical Review*, vol. 74, pp. 230–231, jul 1948.
- [2] J. S. C. Kilby, "Turning Potential into Realities: The Invention of the Integrated Circuit (Nobel Lecture)," *ChemPhysChem*, vol. 2, pp. 482–489, sep 2001.
- [3] G. Moore, "Cramming More Components Onto Integrated Circuits," *Proceedings of the IEEE*, vol. 86, pp. 82–85, jan 1998.
- [4] R. Dennard, F. Gaensslen, V. Rideout, E. Bassous, and A. LeBlanc, "Design of ion-implanted MOSFET's with very small physical dimensions," *IEEE Journal of Solid-State Circuits*, vol. 9, pp. 256–268, oct 1974.
- [5] "International Technology Roadmap for Semiconductors, 2013 edition,"
- [6] J. A. Rogers, T. Someya, and Y. Huang, "Materials and Mechanics for Stretchable Electronics," *Science*, vol. 327, pp. 1603–1607, mar 2010.
- [7] H. S. P. Wong, H. Y. Lee, S. Yu, Y. S. Chen, Y. Wu, P. S. Chen, B. Lee, F. T. Chen, and M. J. Tsai, "Metal-oxide RRAM," *Proceedings of the IEEE*, vol. 100, no. 6, pp. 1951–1970, 2012.
- [8] M. G. Blamire, J. L. MacManus-Driscoll, N. D. Mathur, and Z. H. Barber, "The Materials Science of Functional Oxide Thin Films," *Advanced Materials*, vol. 21, pp. 3827–3839, oct 2009.
- [9] S. D. Ha and S. Ramanathan, "Adaptive oxide electronics: A review," *Journal of Applied Physics*, vol. 110, no. 7, p. 071101, 2011.
- [10] J. Mannhart and D. G. Schlom, "Oxide Interfaces - an Opportunity for Electronics," *Science*, vol. 327, pp. 1607–11, mar 2010.

Bibliography

- [11] T. Blanquart, J. Niinistö, M. Gavagnin, V. Longo, M. Heikkilä, E. Puukilainen, V. R. Pallem, C. Dussarrat, M. Ritala, and M. Leskelä, “Atomic layer deposition and characterization of vanadium oxide thin films,” *RSC Advances*, vol. 3, no. 4, pp. 1179–1185, 2013.
- [12] X. Cao, X. Li, X. Gao, W. Yu, X. Liu, Y. Zhang, L. Chen, and X. Cheng, “Forming-free colossal resistive switching effect in rare-earth-oxide Gd₂O₃ films for memristor applications,” *Journal of Applied Physics*, vol. 106, no. 7, p. 073723, 2009.
- [13] D. Sacchetto and M. Zervas, “Resistive programmable through-silicon vias for reconfigurable 3-D fabrics,” *IEEE Transactions on Nanotechnology*, vol. 11, no. 1, pp. 8–11, 2012.
- [14] M. Imada, A. Fujimori, and Y. Tokura, “Metal-insulator transitions,” *Reviews of Modern Physics*, vol. 70, pp. 1039–1263, oct 1998.
- [15] F. J. Morin, “Oxides which show a metal-to-insulator transition at the neel temperature,” *Physical Review Letters*, vol. 3, no. 1, pp. 34–36, 1959.
- [16] N. F. Mott, “Metal-insulator transition,” *Reviews of Modern Physics*, vol. 40, no. 4, pp. 677–683, 1968.
- [17] J. B. Goodenough, “The two components of the crystallographic transition in VO₂,” *Journal of Solid State Chemistry*, vol. 3, no. 4, pp. 490–500, 1971.
- [18] R. M. Wentzcovitch, W. W. Schulz, and P. B. Allen, “VO₂: Peierls or Mott-Hubbard? A view from band theory,” *Physical Review Letters*, vol. 72, pp. 3389–3392, may 1994.
- [19] V. R. Morrison, R. P. Chatelain, K. L. Tiwari, a. Hendaoui, a. Bruhacs, M. Chaker, and B. J. Siwick, “A photoinduced metal-like phase of monoclinic VO₂ revealed by ultrafast electron diffraction,” *Science*, vol. 346, pp. 445–448, oct 2014.
- [20] S. Kittiwatanakul, S. A. Wolf, and J. Lu, “Large epitaxial bi-axial strain induces a Mott-like phase transition in VO₂,” *Applied Physics Letters*, vol. 105, p. 073112, aug 2014.
- [21] A. X. Gray, J. Jeong, N. P. Aetukuri, P. Granitzka, Z. Chen, R. Kukreja, D. Higley, T. Chase, A. H. Reid, H. Ohldag, M. A. Marcus, A. Scholl, A. T. Young, A. Doran, C. A. Jenkins, P. Shafer, E. Arenholz, M. G. Samant, S. S. P. Parkin, and H. A. Dürr,

- “Correlation-driven insulator-metal transition in near-ideal vanadium dioxide films,” *arXiv:1503.07892*, 2015.
- [22] B. Mayer, C. Schmidt, A. Grupp, J. Bühler, J. Oelmann, R. E. Marvel, R. F. Haglund, T. Oka, D. Brida, A. Leitenstorfer, and A. Pashkin, “Tunneling breakdown of a strongly correlated insulating state in VO₂ induced by intense multiterahertz excitation,” *Physical Review B*, vol. 91, p. 235113, jun 2015.
- [23] J. Leroy, a. Crunteanu, a. Bessaudou, F. Cosset, C. Champeaux, and J.-C. Orianges, “High-speed metal-insulator transition in vanadium dioxide films induced by an electrical pulsed voltage over nano-gap electrodes,” *Applied Physics Letters*, vol. 100, no. 21, p. 213507, 2012.
- [24] Z. Yang, C. Ko, and S. Ramanathan, “Oxide Electronics Utilizing Ultrafast Metal-Insulator Transitions,” *Annual Review of Materials Research*, vol. 41, pp. 337–367, aug 2011.
- [25] B.-J. Kim, Y. W. Lee, B.-G. Chae, S. J. Yun, S.-Y. Oh, H.-T. Kim, and Y.-S. Lim, “Temperature dependence of the first-order metal-insulator transition in VO₂ and programmable critical temperature sensor,” *Applied Physics Letters*, vol. 90, no. 2, p. 023515, 2007.
- [26] E. Strelcov, Y. Lilach, and A. Kolmakov, “Gas Sensor Based on Metal-Insulator Transition in VO₂ Nanowire Thermistor,” *Nano Letters*, vol. 9, pp. 2322–2326, jun 2009.
- [27] R. M. Briggs, I. M. Pryce, and H. A. Atwater, “Compact silicon photonic waveguide modulator based on the vanadium dioxide metal-insulator phase transition,” *Optics Express*, vol. 18, p. 11192, may 2010.
- [28] P. Markov, R. E. Marvel, H. J. Conley, K. J. Miller, R. F. Haglund, and S. M. Weiss, “Optically Monitored Electrical Switching in VO₂,” *ACS Photonics*, vol. 2, no. 8, pp. 1175–1182, 2015.
- [29] J. Jeong, A. Joushaghani, S. Paradis, D. Alain, and J. K. S. Poon, “Electrically Controllable Extraordinary Optical Transmission in Metallic Surface Gratings on VO₂,” *Optics Letters*, vol. 40, no. 19, pp. 4–5, 2015.
- [30] D. Y. Lei, K. Appavoo, F. Ligmajer, Y. Sonnefraud, R. F. Haglund, and S. a. Maier, “Optically-Triggered Nanoscale Memory Effect in a Hybrid Plasmonic-Phase Changing Nanostructure,” *ACS Photonics*, p. 150814084329004, 2015.

Bibliography

- [31] T. Driscoll, H. T. Kim, B. G. Chae, M. Di Ventra, and D. N. Basov, "Phase-transition driven memristive system," *Applied Physics Letters*, vol. 95, no. 4, pp. 67–69, 2009.
- [32] H. Kim, N. Charipar, E. Breckenfeld, A. Rosenberg, and A. Piqué, "Active terahertz metamaterials based on the phase transition of VO₂ thin films," *Thin Solid Films*, 2015.
- [33] M. Liu, H. Y. Hwang, H. Tao, A. C. Strikwerda, K. Fan, G. R. Keiser, A. J. Sternbach, K. G. West, S. Kittiwatanakul, J. Lu, S. a. Wolf, F. G. Omenetto, X. Zhang, K. a. Nelson, and R. D. Averitt, "Terahertz-field-induced insulator-to-metal transition in vanadium dioxide metamaterial," *Nature*, vol. 487, pp. 345–8, jul 2012.
- [34] Y. Zhu, X. Hu, H. Yang, and Q. Gong, "Switchable cross-polarization conversion in ultrathin metasurfaces," *Journal of Optics*, vol. 17, no. 10, p. 105101, 2015.
- [35] J. Zhu, K. Hippalgaonkar, S. Shen, K. Wang, Y. Abate, S. Lee, J. Wu, X. Yin, A. Majumdar, and X. Zhang, "Temperature-Gated Thermal Rectifier for Active Heat Flow Control," *Nano Letters*, vol. 14, pp. 4867–4872, aug 2014.
- [36] Y. Zhou, X. Chen, C. Ko, Z. Yang, C. Mouli, and S. Ramanathan, "Voltage-Triggered Ultrafast Phase Transition in Vanadium Dioxide Switches," *IEEE Electron Device Letters*, vol. 34, no. 2, pp. 220–222, 2013.
- [37] C. Aurelian, G. Julien, B. Pierre, O. Jean-christophe, C. Corinne, and C. Alain, "Exploiting the semiconductor-metal phase transition of VO₂ materials: a novel direction towards tuneable devices and systems for RF-microwave applications," in *Advanced Microwave and Millimeter Wave Technologies Semiconductor Devices Circuits and Systems*, ch. 3, pp. 35–56, Intech, 2010.
- [38] L. A. Ladd and W. Paul, "Optical and transport properties of high quality crystals of V₂O₄ near the metallic transition temperature," *Solid State Communications*, vol. 7, pp. 425–428, feb 1969.
- [39] C. N. Berglund and H. J. Guggenheim, "Electronic Properties of VO₂ near the Semiconductor-Metal Transition," *Physical Review*, vol. 185, pp. 1022–1033, sep 1969.
- [40] C. H. Griffiths, "Influence of stoichiometry on the metal-semiconductor transition in vanadium dioxide," *Journal of Applied Physics*, vol. 45, no. 5, p. 2201, 1974.

- [41] A. Pergament, G. Stefanovich, and A. Velichko, "Oxide Electronics and Vanadium Dioxide Perspective: A Review," *Journal on Selected Topics in Nanoelectronics and Computing*, vol. 1, no. 1, pp. 24–43, 2013.
- [42] J. Nag and R. F. Haglund Jr, "Synthesis of vanadium dioxide thin films and nanoparticles," *Journal of Physics: Condensed Matter*, vol. 20, p. 264016, jul 2008.
- [43] Y. Cui and S. Ramanathan, "Substrate effects on metal-insulator transition characteristics of rf-sputtered epitaxial VO₂ thin films," *Journal of Vacuum Science & Technology A: Vacuum, Surfaces, and Films*, vol. 29, no. 4, p. 041502, 2011.
- [44] Y. Muraoka and Z. Hiroi, "Metal–insulator transition of VO₂ thin films grown on TiO₂ (001) and (110) substrates," *Applied Physics Letters*, vol. 80, no. 4, p. 583, 2002.
- [45] K. Nagashima, T. Yanagida, H. Tanaka, and T. Kawai, "Influence of ambient atmosphere on metal-insulator transition of strained vanadium dioxide ultrathin films," *Journal of Applied Physics*, vol. 100, no. 6, p. 063714, 2006.
- [46] J. Lu, K. G. West, and S. A. Wolf, "Very large anisotropy in the dc conductivity of epitaxial VO₂ thin films grown on (011) rutile TiO₂ substrates," *Applied Physics Letters*, vol. 93, no. 26, p. 262107, 2008.
- [47] M. Nagashima and H. Wada, "The oxygen deficiency effect of VO₂ thin films prepared by laser ablation," *Journal of Materials Research*, vol. 12, pp. 416–422, feb 1997.
- [48] J. Narayan and V. M. Bhosle, "Phase transition and critical issues in structure-property correlations of vanadium oxide," *Journal of Applied Physics*, vol. 100, no. 10, p. 103524, 2006.
- [49] B.-G. Chae, H.-T. Kim, S.-J. Yun, B.-J. Kim, Y.-W. Lee, and K.-Y. Kang, "Comparative Analysis of VO₂ Thin Films Prepared on Sapphire and SiO₂/Si Substrates by the Sol–Gel Process," *Japanese Journal of Applied Physics*, vol. 46, pp. 738–743, feb 2007.
- [50] K. Okimura, N. Ezreena, Y. Sasakawa, and J. Sakai, "Electric-Field-Induced Multistep Resistance Switching in Planar VO₂/c-Al₂O₃ Structure," *Japanese Journal of Applied Physics*, vol. 48, p. 065003, jun 2009.

Bibliography

- [51] Y. Zhao, J. Hwan Lee, Y. Zhu, M. Nazari, C. Chen, H. Wang, A. Bernussi, M. Holtz, and Z. Fan, "Structural, electrical, and terahertz transmission properties of VO₂ thin films grown on c-, r-, and m-plane sapphire substrates," *Journal of Applied Physics*, vol. 111, no. 5, p. 053533, 2012.
- [52] D. H. Kim and H. S. Kwok, "Pulsed laser deposition of VO₂ thin films," *Applied Physics Letters*, vol. 65, no. 25, p. 3188, 1994.
- [53] D.-H. Youn, J.-W. Lee, B.-G. Chae, H. T. Kim, S.-L. Maeng, and K.-Y. Kang, "Growth optimization and electrical characteristics of VO₂ films on amorphous SiO₂/Si substrates," *Journal of Applied Physics*, vol. 95, no. 3, p. 1407, 2004.
- [54] M. Soltani, M. Chaker, E. Haddad, R. V. Kruzelecky, and D. Nikanpour, "Optical switching of vanadium dioxide thin films deposited by reactive pulsed laser deposition," *Journal of Vacuum Science & Technology A: Vacuum, Surfaces, and Films*, vol. 22, no. 3, p. 859, 2004.
- [55] B. N. Masina, S. Lafane, L. Wu, A. A. Akande, B. Mwakikunga, S. Abdelli-Messaci, T. Kerdja, and A. Forbes, "Phase-selective vanadium dioxide (VO₂) nanostructured thin films by pulsed laser deposition," *Journal of Applied Physics*, vol. 118, no. 16, p. 165308, 2015.
- [56] M. Maaza, K. Bouziane, J. Maritz, D. McLachlan, R. Swanepool, J. Frigerio, and M. Every, "Direct production of thermochromic VO₂ thin film coatings by pulsed laser ablation," *Optical Materials*, vol. 15, pp. 41–45, sep 2000.
- [57] R. E. Marvel, R. R. Harl, V. Craciun, B. R. Rogers, and R. F. Haglund, "Influence of deposition process and substrate on the phase transition of vanadium dioxide thin films," *Acta Materialia*, vol. 91, pp. 217–226, jun 2015.
- [58] A. Razavi, T. Hughes, J. Antinovitch, and J. Hoffman, "Temperature effects on structure and optical properties of radio-frequency sputtered VO₂," *Journal of Vacuum Science & Technology A: Vacuum, Surfaces, and Films*, vol. 7, p. 1310, may 1989.
- [59] A. Razavi, L. Bobyak, and P. Fallon, "The effects of biasing and annealing on the optical properties of radio-frequency sputtered VO₂," *Journal of Vacuum Science & Technology A: Vacuum, Surfaces, and Films*, vol. 8, p. 1391, may 1990.

- [60] P. Jin and S. Tanemura, "Formation and Thermo-chromism of VO₂ Films Deposited by RF Magnetron Sputtering at Low Substrate Temperature," *Japanese Journal of Applied Physics*, vol. 33, pp. 1478–1483, mar 1994.
- [61] J. Cui, D. Da, and W. Jiang, "Structure characterization of vanadium oxide thin films prepared by magnetron sputtering methods," *Applied Surface Science*, vol. 133, pp. 225–229, jul 1998.
- [62] R. Dillon, K. Le, and N. Ianno, "Thermochromic VO₂ sputtered by control of a vanadium-oxygen emission ratio," *Thin Solid Films*, vol. 398-399, pp. 10–16, nov 2001.
- [63] D. Brassard, S. Fourmaux, M. Jean-Jacques, J. C. Kieffer, and M. a. El Khakani, "Grain size effect on the semiconductor-metal phase transition characteristics of magnetron-sputtered VO₂ thin films," *Applied Physics Letters*, vol. 87, no. 5, p. 051910, 2005.
- [64] G. Fu, A. Polity, N. Volbers, and B. K. Meyer, "Annealing effects on VO₂ thin films deposited by reactive sputtering," *Thin Solid Films*, vol. 515, pp. 2519–2522, dec 2006.
- [65] N. R. Mlyuka and R. T. Kivaisi, "Correlation between optical, electrical and structural properties of vanadium dioxide thin films," *Journal of Materials Science*, vol. 41, pp. 5619–5624, jun 2006.
- [66] S. J. Yun, J. W. Lim, J.-S. Noh, B.-G. Chae, and H.-T. Kim, "Vanadium Dioxide Films Deposited on Amorphous SiO₂- and Al₂O₃- Coated Si Substrates by Reactive RF-Magnetron Sputter Deposition," *Japanese Journal of Applied Physics*, vol. 47, pp. 3067–3069, apr 2008.
- [67] Q. Yu, W. Li, J. Liang, Z. Duan, Z. Hu, J. Liu, H. Chen, and J. Chu, "Oxygen pressure manipulations on the metal insulator transition characteristics of highly (0 1 1) oriented vanadium dioxide films grown by magnetron sputtering," *Journal of Physics D: Applied Physics*, vol. 46, p. 055310, feb 2013.
- [68] D.-H. Qiu, Q.-Y. Wen, Q.-H. Yang, Z. Chen, Y.-L. Jing, and H.-W. Zhang, "Electrically-driven metal-insulator transition of vanadium dioxide thin films in a metal-oxide-insulator-metal device structure," *Materials Science in Semiconductor Processing*, vol. 27, pp. 140–144, nov 2014.

Bibliography

- [69] A. Paone, R. Sanjines, P. Jeanneret, H. J. Whitlow, E. Guibert, G. Guibert, F. Bussy, J.-L. Scartezzini, and A. Schüler, "Influence of doping in thermochromic $V_{1-x}W_xO_2$ and $V_{1-x}Al_xO_2$ thin films: Twice improved doping efficiency in $V_{1-x}W_xO_2$," *Journal of Alloys and Compounds*, vol. 621, pp. 206–211, feb 2015.
- [70] D. Ruzmetov, K. T. Zawilski, V. Narayanamurti, and S. Ramanathan, "Structure-functional property relationships in rf-sputtered vanadium dioxide thin films," *Journal of Applied Physics*, vol. 102, no. 11, 2007.
- [71] Z. Yang and S. Ramanathan, "Direct measurement of compositional complexity-induced electronic inhomogeneity in VO_2 thin films grown on gate dielectrics," *Applied Physics Letters*, vol. 98, no. 19, p. 192113, 2011.
- [72] M. S. de Castro, C. L. Ferreira, and R. R. de Avillez, "Vanadium oxide thin films produced by magnetron sputtering from a V_2O_5 target at room temperature," *Infrared Physics & Technology*, vol. 60, pp. 103–107, sep 2013.
- [73] S. Koide and H. Takei, "Epitaxial Growth of VO_2 Single Crystals and Their Anisotropic Properties in Electrical Resistivities," *Journal of the Physical Society of Japan*, vol. 22, pp. 946–947, mar 1967.
- [74] T. Maruyama and Y. Ikuta, "Vanadium dioxide thin films prepared by chemical vapour deposition from vanadium(III) acetylacetonate," *Journal of Materials Science*, vol. 28, no. 18, pp. 5073–5078, 1993.
- [75] T. D. Manning and I. P. Parkin, "Vanadium(IV) oxide thin films on glass and silicon from the atmospheric pressure chemical vapour deposition reaction of $VOCl_3$ and water," *Polyhedron*, vol. 23, pp. 3087–3095, dec 2004.
- [76] H. Zhang, H. Chang, J. Guo, and T. Zhang, "Microstructure of epitaxial VO_2 thin films deposited on (1120) sapphire by MOCVD," *Journal of Materials Research*, vol. 9, pp. 2264–2271, sep 1994.
- [77] M. B. Sahana, G. N. Subbanna, and S. A. Shivashankar, "Phase transformation and semiconductor-metal transition in thin films of VO_2 deposited by low-pressure metalorganic chemical vapor deposition," *Journal of Applied Physics*, vol. 92, no. 11, p. 6495, 2002.
- [78] M. B. Sahana, M. S. Dharmaparakash, and S. A. Shivashankar, "Microstructure and properties of VO_2 thin films deposited by MOCVD from vanadyl acetylacetonate," *Journal of Materials Chemistry*, vol. 12, pp. 333–338, jan 2002.

- [79] D. P. Partlow, S. R. Gurkovich, K. C. Radford, and L. J. Denes, "Switchable vanadium oxide films by a sol-gel process," *Journal of Applied Physics*, vol. 70, no. 1, pp. 443–452, 1991.
- [80] G. Guzman, R. Morineau, and J. Livage, "Synthesis of vanadium dioxide thin films from vanadium alkoxides," *Materials Research Bulletin*, vol. 29, pp. 509–515, may 1994.
- [81] G. Guzman, F. Beteille, R. Morineau, and J. Livage, "Electrical switching in VO₂ sol-gel films," *Journal of Materials Chemistry*, vol. 6, no. 3, p. 505, 1996.
- [82] J. Livage, G. Guzman, F. Beteille, and P. Davidson, "Optical properties of sol-gel derived vanadium oxide films," 1997.
- [83] F. Béteille and J. Livage, "Optical Switching in VO₂ Thin Films," *Journal of Sol-Gel Science and Technology*, vol. 921, pp. 915–921, 1998.
- [84] Y. Dachuan, X. Niankan, Z. Jingyu, and Z. Xiulin, "Vanadium dioxide films with good electrical switching property," 1999.
- [85] S. Lu, L. Hou, and F. Gan, "Surface analysis and phase transition of gel-derived VO₂ thin films," *Thin Solid Films*, vol. 353, pp. 40–44, sep 1999.
- [86] B.-G. Chae, H.-T. Kim, S.-J. Yun, B.-J. Kim, Y.-W. Lee, D.-H. Youn, and K.-Y. Kang, "Highly Oriented VO₂ Thin Films Prepared by Sol-Gel Deposition," *Electrochemical and Solid-State Letters*, vol. 9, no. 1, p. C12, 2006.
- [87] B.-G. Chae, H.-T. Kim, S.-J. Yun, B.-J. Kim, Y.-W. Lee, and K.-Y. Kang, "Comparative Analysis of VO₂ Thin Films Prepared on Sapphire and SiO₂/Si Substrates by the Sol-Gel Process," *Japanese Journal of Applied Physics*, vol. 46, pp. 738–743, feb 2007.
- [88] Q. Shi, W. Huang, J. Wu, Y. Zhang, Y. Xu, Y. Zhang, S. Qiao, and J. Yan, "Terahertz transmission characteristics across the phase transition in VO₂ films deposited on Si, sapphire, and SiO₂ substrates," *Journal of Applied Physics*, vol. 112, no. 3, p. 033523, 2012.
- [89] S. J. Jiang, C. B. Ye, M. S. Khan, and C. G. Granqvist, "Evolution of thermochromism during oxidation of evaporated vanadium films," *Applied optics*, vol. 30, pp. 847–51, mar 1991.

Bibliography

- [90] C.-R. Cho, S. Cho, S. Vadim, R. Jung, and I. Yoo, "Current-induced metal-insulator transition in VO_x thin film prepared by rapid-thermal-annealing," *Thin Solid Films*, vol. 495, pp. 375–379, jan 2006.
- [91] M. Gurvitch, S. Luryi, A. Polyakov, A. Shabalov, M. Dudley, G. Wang, S. Ge, and V. Yakovlev, "VO₂ films with strong semiconductor to metal phase transition prepared by the precursor oxidation process," *Journal of Applied Physics*, vol. 102, no. 3, p. 033504, 2007.
- [92] I. P. Radu, K. Martens, S. Mertens, C. Adelmann, X. Shi, H. Tielens, M. Schaekers, G. Pourtois, S. Van Elshocht, S. De Gendt, M. Heyns, and J. A. Kittl, "Vanadium Oxide as a Memory Material," in *ECS Transactions*, vol. 35, pp. 233–243, 2011.
- [93] J.-R. Liang, M.-J. Wu, M. Hu, J. Liu, N.-W. Zhu, X.-X. Xia, and H.-D. Chen, "Fabrication of VO₂ thin film by rapid thermal annealing in oxygen atmosphere and its metal-insulator phase transition properties," *Chinese Physics B*, vol. 23, p. 076801, jul 2014.
- [94] G. Rampelberg, B. De Schutter, W. Devulder, K. Martens, I. Radu, and C. Detavernier, "In situ X-ray diffraction study of the controlled oxidation and reduction in the V–O system for the synthesis of VO₂ and V₂O₃ thin films," *Journal of Materials Chemistry C*, no. Cvd, pp. 26–29, 2015.
- [95] B. Van Bilzen, P. Homm, L. Dillemans, C.-Y. Su, M. Menghini, M. Sousa, C. Marchiori, L. Zhang, J. W. Seo, and J.-P. Locquet, "Production of VO₂ thin films through post-deposition annealing of V₂O₃ and VO_x films," *Thin Solid Films*, vol. 591, pp. 143–148, 2015.
- [96] P. Dagur, A. U. Mane, and S. Shivashankar, "Thin films of VO₂ on glass by atomic layer deposition: microstructure and electrical properties," *Journal of Crystal Growth*, vol. 275, pp. e1223–e1228, feb 2005.
- [97] I. Povey, M. Bardosova, F. Chalvet, M. Pemble, and H. Yates, "Atomic layer deposition for the fabrication of 3D photonic crystals structures: Growth of Al₂O₃ and VO₂ photonic crystal systems," *Surface and Coatings Technology*, vol. 201, pp. 9345–9348, sep 2007.
- [98] O. M. Osmolowskaya and V. M. Smirnov, "Growth mechanism of nanodimensional vanadium dioxide on silicon surface obtained by ML-ALD method," *Reviews on Advanced Materials Science*, vol. 27, no. 2, pp. 184–188, 2011.

- [99] G. Rampelberg, M. Schaeckers, K. Martens, Q. Xie, D. Deduytsche, B. De Schutter, N. Blasco, J. Kittl, and C. Detavernier, "Semiconductor-metal transition in thin VO₂ films grown by ozone based atomic layer deposition," *Applied Physics Letters*, vol. 98, no. 16, p. 162902, 2011.
- [100] K. Zhang, M. Tangirala, D. Nminibapiel, W. Cao, V. Pallem, C. Dussarrat, and H. Baumgart, "Synthesis of VO₂ Thin Films by Atomic Layer Deposition with TEMAV as Precursor," *ECS Transactions*, vol. 50, pp. 175–182, mar 2013.
- [101] A. Paone and A. Schüler, "Advanced switchable selective absorber coatings for overheating protection of solar thermal collectors. Technical report, SFOE Project-No.: 102016," tech. rep., 2011.
- [102] S. Mertin, V. Hody-Le Caër, M. Joly, I. Mack, P. Oelhafen, J. L. Scartezzini, and A. Schüler, "Reactively sputtered coatings on architectural glazing for coloured active solar thermal façades," *Energy and Buildings*, vol. 68, no. PART C, pp. 764–770, 2014.
- [103] J. Jian, W. Zhang, C. Jacob, A. Chen, H. Wang, J. Huang, and H. Wang, "Roles of grain boundaries on the semiconductor to metal phase transition of VO₂ thin films," *Applied Physics Letters*, vol. 107, no. 10, p. 102105, 2015.
- [104] R. Wickoff, *Crystal Structures 1*. Interscience Publishers, second ed., 1963.
- [105] W. Melitz, J. Shen, A. C. Kummel, and S. Lee, "Kelvin probe force microscopy and its application," *Surface Science Reports*, vol. 66, no. 1, pp. 1–27, 2011.
- [106] C. Ko, Z. Yang, and S. Ramanathan, "Work function of vanadium dioxide thin films across the metal-insulator transition and the role of surface nonstoichiometry," *ACS applied materials & interfaces*, vol. 3, pp. 3396–401, sep 2011.
- [107] A. Sohn, H. Kim, D.-W. Kim, C. Ko, S. Ramanathan, J. Park, G. Seo, B.-J. Kim, J.-H. Shin, and H.-T. Kim, "Evolution of local work function in epitaxial VO₂ thin films spanning the metal-insulator transition," *Applied Physics Letters*, vol. 101, no. 19, p. 191605, 2012.
- [108] T. Lee, A. Efremov, Y.-H. Ham, S. J. Yun, N.-K. Min, M. Hong, and K.-H. Kwon, "Etching characteristics and mechanism of vanadium dioxide in inductively coupled Cl₂/Ar plasma," apr 2009.

Bibliography

- [109] T. Driscoll, J. Quinn, M. Di Ventra, D. N. Basov, G. Seo, Y.-W. Lee, H.-T. Kim, and D. R. Smith, "Current oscillations in vanadium dioxide: Evidence for electrically triggered percolation avalanches," *Physical Review B*, vol. 86, p. 094203, sep 2012.
- [110] H. Madan, M. Jerry, A. Pogrebnyakov, T. Mayer, and S. Datta, "Quantitative Mapping of Phase Coexistence in Mott-Peierls Insulator during Electronic and Thermally Driven Phase Transition," *ACS Nano*, vol. 9, pp. 2009–2017, feb 2015.
- [111] A. Joushaghani, J. Jeong, S. Paradis, D. Alain, J. Stewart Aitchison, and J. K. S. Poon, "Voltage-controlled switching and thermal effects in VO₂ nano-gap junctions," *Applied Physics Letters*, vol. 104, p. 221904, jun 2014.
- [112] N. F. Mott, *Metal-Insulator Transitions*. New York: Taylor & Francis, 1990.
- [113] A. Pergament, "Metal-insulator transition: the Mott criterion and coherence length," 2003.
- [114] A. L. Pergament, G. B. Stefanovich, N. A. Kuldin, and A. A. Velichko, "On the Problem of Metal-Insulator Transitions in Vanadium Oxides," *ISRN Condensed Matter Physics*, vol. 2013, no. 960627, pp. 1–6, 2013.
- [115] M. F. Becker, A. B. Buckman, R. M. Walser, T. Lepine, P. Georges, and A. Brun, "Femtosecond laser excitation of the semiconductor-metal phase transition in VO₂," *Applied Physics Letters*, vol. 65, no. 12, p. 1507, 1994.
- [116] A. Cavalleri, C. Toth, C. W. Siders, J. A. Squier, F. Raksi, P. Forget, and J. C. Kieffer, "Femtosecond Structural Dynamics in VO₂ during an Ultrafast Solid-Solid Phase Transition," *Physical Review Letters*, vol. 87, p. 237401, nov 2001.
- [117] G. Stefanovich, A. Pergament, and D. Stefanovich, "Electrical switching and Mott transition in VO₂," *Journal of Physics: Condensed Matter*, vol. 12, no. 41, pp. 8837–8845, 2000.
- [118] H.-T. Kim, B.-G. Chae, D.-H. Youn, S.-L. Maeng, G. Kim, K.-Y. Kang, and Y.-S. Lim, "Mechanism and observation of Mott transition in VO₂ -based two- and three-terminal devices," *New Journal of Physics*, vol. 6, pp. 52–52, may 2004.
- [119] A. Zimmers, L. Aigouy, M. Mortier, A. Sharoni, S. Wang, K. G. West, J. G. Ramirez, and I. K. Schuller, "Role of Thermal Heating on the Voltage Induced Insulator-Metal Transition in VO₂," *Physical Review Letters*, vol. 110, p. 056601, jan 2013.

- [120] T. S. Jordan, S. Scott, D. Leonhardt, J. O. Custer, C. T. Rodenbeck, S. Wolfley, and C. D. Nordquist, "Model and Characterization of VO₂ Thin-Film Switching Devices," *Electron Devices, IEEE Transactions on*, vol. 61, no. 3, pp. 813–819, 2014.
- [121] S. Rathi, J.-H. Park, I.-y. Lee, J. M. Baik, K. S. Yi, and G.-H. Kim, "Unravelling the switching mechanisms in electric field induced insulator-metal transitions in VO₂ nanobeams," *Journal of Physics D: Applied Physics*, vol. 47, p. 295101, jul 2014.
- [122] J. Yoon, G. Lee, C. Park, B. S. Mun, and H. Ju, "Investigation of length-dependent characteristics of the voltage-induced metal insulator transition in VO₂ film devices," *Applied Physics Letters*, vol. 105, p. 083503, aug 2014.
- [123] A. Joushaghani, J. Jeong, S. Paradis, D. Alain, J. Stewart Aitchison, and J. K. S. Poon, "Electronic and thermal effects in the insulator-metal phase transition in VO₂ nano-gap junctions," *Applied Physics Letters*, vol. 105, p. 231904, dec 2014.
- [124] A. Joushaghani, J. Jeong, S. Paradis, D. Alain, J. Aitchison, and J. Poon, "Characteristics of the Current-Controlled Phase Transition of VO₂ Microwires for Hybrid Optoelectronic Devices," *Photonics*, vol. 2, no. 3, pp. 916–932, 2015.
- [125] A. Cavalleri, T. Dekorsy, H. H. W. Chong, J. C. Kieffer, and R. W. Schoenlein, "Evidence for a structurally-driven insulator-to-metal transition in VO₂: A view from the ultrafast timescale," *Physical Review B - Condensed Matter and Materials Physics*, vol. 70, no. 16, pp. 1–4, 2004.
- [126] C. Kübler, H. Ehrke, R. Huber, R. Lopez, A. Halabica, R. F. Haglund, and A. Leitenstorfer, "Coherent Structural Dynamics and Electronic Correlations during an Ultrafast Insulator-to-Metal Phase Transition in VO₂," *Physical Review Letters*, vol. 99, p. 116401, sep 2007.
- [127] H.-T. Kim, Y. W. Lee, B.-J. Kim, B.-G. Chae, S. J. Yun, K.-Y. Kang, K.-J. Han, K.-J. Yee, and Y.-S. Lim, "Monoclinic and Correlated Metal Phase in VO₂ as Evidence of the Mott Transition: Coherent Phonon Analysis," *Physical Review Letters*, vol. 97, p. 266401, dec 2006.
- [128] B. G. Chae, H. T. Kim, D. H. Youn, and K. Y. Kang, "Abrupt metal-insulator transition observed in VO₂ thin films induced by a switching voltage pulse," *Physica B: Condensed Matter*, vol. 369, no. 1-4, pp. 76–80, 2005.

Bibliography

- [129] A. Kar, N. Shukla, E. Freeman, H. Paik, H. Liu, R. Engel-Herbert, S. S. N. Bharadwaja, D. G. Schlom, and S. Datta, "Intrinsic electronic switching time in ultrathin epitaxial vanadium dioxide thin film," *Applied Physics Letters*, vol. 102, no. 7, p. 072106, 2013.
- [130] S. Hormoz and S. Ramanathan, "Limits on vanadium oxide Mott metal–insulator transition field-effect transistors," *Solid-State Electronics*, vol. 54, pp. 654–659, jun 2010.
- [131] A. Crunteanu, J. Givernaud, J. Leroy, D. Mardivirin, C. Champeaux, J.-C. Orlianges, A. Catherinot, and P. Blondy, "Voltage- and current-activated metal–insulator transition in VO₂ -based electrical switches: a lifetime operation analysis," *Science and Technology of Advanced Materials*, vol. 11, p. 065002, dec 2010.
- [132] I. P. Radu, B. Govoreanu, S. Mertens, X. Shi, M. Cantoro, M. Schaeckers, M. Jurczak, S. De Gendt, A. Stesmans, J. a. Kittl, M. Heyns, and K. Martens, "Switching mechanism in two-terminal vanadium dioxide devices," *Nanotechnology*, vol. 26, no. 16, p. 165202, 2015.
- [133] D. Ruzmetov, G. Gopalakrishnan, C. Ko, V. Narayanamurti, and S. Ramanathan, "Three-terminal field effect devices utilizing thin film vanadium oxide as the channel layer," *Journal of Applied Physics*, vol. 107, no. 11, p. 114516, 2010.
- [134] M. Belyaev, A. Velichko, P. Boriskov, N. Kuldin, V. Putrolaynen, and G. Stefanovitch, "The Field Effect and Mott Transistor Based on Vanadium Dioxide," *Journal on Selected Topics in Nano Electronics and Computing*, vol. 2, no. 1, pp. 26–30, 2014.
- [135] K. Martens, J. W. Jeong, N. Aetukuri, C. Rettner, N. Shukla, E. Freeman, D. N. Esfahani, F. M. Peeters, T. Topuria, P. M. Rice, A. Volodin, B. Douhard, W. Vandervorst, M. G. Samant, S. Datta, and S. S. P. Parkin, "Field Effect and Strongly Localized Carriers in the Metal-Insulator Transition Material VO₂," *Physical Review Letters*, vol. 115, no. 19, p. 196401, 2015.
- [136] P. P. Boriskov, a. a. Velichko, a. L. Pergament, G. B. Stefanovich, and D. G. Stefanovich, "The effect of electric field on metal-insulator phase transition in vanadium dioxide," *Technical Physics Letters*, vol. 28, pp. 406–408, may 2001.

-
- [137] M. Nakano, K. Shibuya, D. Okuyama, T. Hatano, S. Ono, M. Kawasaki, Y. Iwasa, and Y. Tokura, "Collective bulk carrier delocalization driven by electrostatic surface charge accumulation.," *Nature*, vol. 487, pp. 459–62, jul 2012.
- [138] K. Liu, D. Fu, J. Cao, J. Suh, K. X. Wang, C. Cheng, D. F. Ogletree, H. Guo, S. Sengupta, A. Khan, C. W. Yeung, S. Salahuddin, M. M. Deshmukh, and J. Wu, "Dense electron system from gate-controlled surface metal-insulator transition.," *Nano letters*, vol. 12, pp. 6272–7, dec 2012.
- [139] J. Jeong, N. Aetukuri, T. Graf, T. D. Schladt, M. G. Samant, and S. S. P. Parkin, "Suppression of Metal-Insulator Transition in VO₂ by Electric Field-Induced Oxygen Vacancy Formation," *Science*, vol. 339, pp. 1402–1405, mar 2013.
- [140] J. Karel, C. Viol Barbosa, J. Kiss, J. Jeong, N. Aetukuri, M. Samant, X. Kozina, E. Ikenaga, G. Fecher, C. Felser, and S. S. P. Parkin, "Distinct Electronic Structure of the Electrolyte Gate Induced Conducting Phase in Vanadium Dioxide Revealed by High Energy Photoelectron Spectroscopy.," *ACS nano*, vol. 8, no. 6, pp. 5748–5789, 2014.
- [141] J. Jeong, N. B. Aetukuri, D. Passarello, S. D. Conradson, M. G. Samant, and S. S. P. Parkin, "Giant reversible, facet-dependent, structural changes in a correlated-electron insulator induced by ionic liquid gating," *Proceedings of the National Academy of Sciences*, vol. 112, no. 4, pp. 1013–1018, 2015.
- [142] F. Chen, L. Fan, S. Chen, G. Liao, Y. Chen, P. Wu, L. Song, C. Zou, and Z. Wu, "Control of the Metal–insulator Transition in VO₂ Epitaxial Film by Modifying Carrier Density," *ACS Applied Materials & Interfaces*, p. 150309144104002, 2015.
- [143] E. Freeman, A. Kar, N. Shukla, R. Misra, R. Engel-Herbert, D. Schlom, V. Gopalan, K. Rabe, and S. Datta, "Characterization and modeling of metal-insulator transition (MIT) based tunnel junctions," in *70th Device Research Conference*, vol. 56, pp. 243–244, IEEE, jun 2012.
- [144] K. Martens, I. P. Radu, S. Mertens, X. Shi, L. Nyns, S. Cosemans, P. Favia, H. Bender, T. Conard, M. Schaekers, S. De Gendt, V. Afanas'ev, J. a. Kittl, M. Heyns, and M. Jurczak, "The VO₂ interface, the metal-insulator transition tunnel junction, and the metal-insulator transition switch On-Off resistance," *Journal of Applied Physics*, vol. 112, no. 12, p. 124501, 2012.

Bibliography

- [145] J. Sakai, "High-efficiency voltage oscillation in VO₂ planer-type junctions with infinite negative differential resistance," *Journal of Applied Physics*, vol. 103, no. 10, p. 103708, 2008.
- [146] Y. W. Lee, B. J. Kim, J. W. Lim, S. J. Yun, S. Choi, B. G. Chae, G. Kim, and H. T. Kim, "Metal-insulator transition-induced electrical oscillation in vanadium dioxide thin film," *Applied Physics Letters*, vol. 92, no. 16, 2008.
- [147] H.-T. Kim, B.-J. Kim, S. Choi, B.-G. Chae, Y. W. Lee, T. Driscoll, M. M. Qazilbash, and D. N. Basov, "Electrical oscillations induced by the metal-insulator transition in VO₂," *Journal of Applied Physics*, vol. 107, no. 2, p. 023702, 2010.
- [148] J. Leroy, A. Crunteanu, J. Givernaud, J.-C. Orlianges, C. Champeaux, and P. Blondy, "Generation of electrical self-oscillations in two-terminal switching devices based on the insulator-to-metal phase transition of VO₂ thin films," *International Journal of Microwave and Wireless Technologies*, vol. 4, no. 01, pp. 101–107, 2012.
- [149] A. Beaumont, J. Leroy, J.-C. Orlianges, and A. Crunteanu, "Current-induced electrical self-oscillations across out-of-plane threshold switches based on VO₂ layers integrated in crossbars geometry," *Journal of Applied Physics*, vol. 115, no. 15, p. 154502, 2014.
- [150] V. S. Aliev, S. G. Bortnikov, I. V. Mzhelskiy, and I. A. Badmaeva, "Current oscillations as a manifestation of spatio-temporal inhomogeneity of temperature distribution in vanadium dioxide films at semiconductor-metal phase transition," *Applied Physics Letters*, vol. 105, p. 142101, oct 2014.
- [151] N. Shukla, A. Parihar, E. Freeman, H. Paik, G. Stone, V. Narayanan, H. Wen, Z. Cai, V. Gopalan, R. Engel-Herbert, D. G. Schlom, A. Raychowdhury, and S. Datta, "Synchronized charge oscillations in correlated electron systems.," *Scientific reports*, vol. 4, p. 4964, jan 2014.
- [152] P. Maffezzoni, L. Daniel, N. Shukla, S. Datta, and A. Raychowdhury, "Modeling and Simulation of Vanadium Dioxide Relaxation Oscillators," *IEEE Transactions on Circuits and Systems I: Regular Papers*, vol. 62, pp. 2207–2215, sep 2015.
- [153] N. Shukla, A. Parihar, M. Cotter, M. Barth, X. Li, N. Chandramoorthy, H. Paik, D. G. Schlom, V. Narayanan, A. Raychowdhury, and S. Datta, "Pairwise coupled hybrid vanadium dioxide-MOSFET (HVFET) oscillators for non-boolean

- associative computing,” in *2014 IEEE International Electron Devices Meeting*, pp. 28.7.1–28.7.4, IEEE, dec 2014.
- [154] A. Parihar, N. Shukla, S. Datta, and A. Raychowdhury, “Exploiting Synchronization Properties of Correlated Electron Devices in a Non-Boolean Computing Fabric for Template Matching,” *IEEE Journal on Emerging and Selected Topics in Circuits and Systems*, vol. 4, pp. 450–459, dec 2014.
- [155] S. Datta, N. Shukla, M. Cotter, A. Parihar, and A. Raychowdhury, “Neuro Inspired Computing with Coupled Relaxation Oscillators,” *Proceedings of the The 51st Annual Design Automation Conference on Design Automation Conference - DAC '14*, pp. 1–6, 2014.
- [156] I. Radu, B. Govoreanu, and K. Martens, “Vanadium Dioxide for Selector Applications,” *ECS Transactions*, vol. 58, no. 7, pp. 249–258, 2013.
- [157] Y. Zhou and S. Ramanathan, “Mott Memory and Neuromorphic Devices,” *Proceedings of the IEEE*, vol. 103, pp. 1289–1310, aug 2015.
- [158] M.-J. Lee, Y. Park, D.-S. Suh, E.-H. Lee, S. Seo, D.-C. Kim, R. Jung, B.-S. Kang, S.-E. Ahn, C. Lee, D. Seo, Y.-K. Cha, I.-K. Yoo, J.-S. Kim, and B. Park, “Two Series Oxide Resistors Applicable to High Speed and High Density Nonvolatile Memory,” *Advanced Materials*, vol. 19, pp. 3919–3923, nov 2007.
- [159] M. Son, J. Lee, J. Park, J. Shin, G. Choi, S. Jung, W. Lee, S. Kim, S. Park, and H. Hwang, “Excellent selector characteristics of nanoscale VO₂ for high-density bipolar ReRAM applications,” *IEEE Electron Device Letters*, vol. 32, no. 11, pp. 1579–1581, 2011.
- [160] T. Driscoll, H.-T. Kim, B.-G. Chae, B.-J. Kim, Y.-W. Lee, N. M. Jokerst, S. Palit, D. R. Smith, M. Di Ventra, and D. N. Basov, “Memory Metamaterials,” *Science*, vol. 325, pp. 1518–1521, sep 2009.
- [161] H. Coy, R. Cabrera, N. Sepulveda, and F. E. Fernandez, “Optoelectronic and all-optical multiple memory states in vanadium dioxide,” *Journal of Applied Physics*, vol. 108, no. 11, p. 113115, 2010.
- [162] J. Li and J. Dho, “Anomalous optical switching and thermal hysteresis behaviors of VO₂ films on glass substrate,” *Applied Physics Letters*, vol. 99, no. 23, p. 231909, 2011.

Bibliography

- [163] L. Pellegrino, N. Manca, T. Kanki, H. Tanaka, M. Biasotti, E. Bellingeri, A. S. Siri, and D. Marré, “Multistate Memory Devices Based on Free-standing VO₂/TiO₂ Microstructures Driven by Joule Self-Heating,” *Advanced Materials*, vol. 24, pp. 2929–2934, jun 2012.
- [164] G. Seo, B. J. Kim, H. T. Kim, and Y. W. Lee, “Thermally- or optically-biased memristive switching in two-terminal VO₂ devices,” *Current Applied Physics*, vol. 14, no. 9, pp. 1251–1256, 2014.
- [165] B. J. Kim, Y. W. Lee, S. Choi, S. J. Yun, and H. T. Kim, “VO₂ thin-film varistor based on metal-insulator transition,” *IEEE Electron Device Letters*, vol. 31, pp. 14–16, 2010.
- [166] J. Givernaud, A. Crunteanu, J.-C. Orlianges, A. Pothier, C. Champeaux, A. Catherinot, and P. Blondy, “Microwave Power Limiting Devices Based on the Semiconductor-Metal Transition in Vanadium-Dioxide Thin Films,” *IEEE Transactions on Microwave Theory and Techniques*, vol. 58, pp. 2352–2361, sep 2010.
- [167] H. Iwai, “Technology roadmap for 22nm and beyond,” in *2009 2nd International Workshop on Electron Devices and Semiconductor Technology*, pp. 1–4, IEEE, jun 2009.
- [168] K. Bernstein, R. K. Cavin, W. Porod, A. Seabaugh, and J. Welser, “Device and architecture outlook for beyond CMOS switches,” *Proceedings of the IEEE*, vol. 98, no. 12, pp. 2169–2184, 2010.
- [169] A. C. Seabaugh and Q. Zhang, “Low-voltage tunnel transistors for beyond CMOS logic,” *Proceedings of the IEEE*, vol. 98, no. 12, pp. 2095–2110, 2010.
- [170] R. V. Overstraeten, G. Declerck, and P. Muls, “Theory of the MOS transistor in weak inversion-new method to determine the number of surface states,” *IEEE Transactions on Electron Devices*, vol. 22, no. 5, 1975.
- [171] A. M. Ionescu and H. Riel, “Tunnel field-effect transistors as energy-efficient electronic switches,” *Nature*, vol. 479, no. 7373, pp. 329–337, 2011.
- [172] S. Salahuddin and S. Datta, “Use of negative capacitance to provide voltage amplification for low power nanoscale devices,” *Nano Letters*, vol. 8, no. 2, pp. 405–410, 2008.

- [173] N. Abele, R. Fritschi, K. Boucart, F. Casset, P. Ancey, and A. Ionescu, "Suspended-gate MOSFET: bringing new MEMS functionality into solid-state MOS transistor," *IEEE International Electron Devices Meeting, 2005. IEDM Technical Digest.*, 2005.
- [174] K. Gopalakrishnan, P. Griffin, and J. Plummer, "I-MOS: a novel semiconductor device with a subthreshold slope lower than kT/q ," in *Digest. International Electron Devices Meeting.*, pp. 289–292, IEEE, 2002.
- [175] K. Boucart and A. M. Ionescu, "Double-gate tunnel FET with high-k gate dielectric," *IEEE Transactions on Electron Devices*, vol. 54, no. 7, pp. 1725–1733, 2007.
- [176] A. Ozelik, O. Cabarcos, D. L. Allara, and M. W. Horn, "Vanadium oxide thin films alloyed with Ti, Zr, Nb, and Mo for uncooled infrared imaging applications," *Journal of Electronic Materials*, vol. 42, no. 5, pp. 901–905, 2013.
- [177] D. L. Perry, *Handbook of Inorganic Compounds*. CRC Press, second ed., 2011.
- [178] R. Eason, *Pulsed Laser Deposition of Thin Films: Applications-Led Growth of Functional Materials*. John Wiley & Sons, Inc., 2006.
- [179] Z. Yang, S. Hart, C. Ko, A. Yacoby, and S. Ramanathan, "Studies on electric triggering of the metal-insulator transition in VO₂ thin films between 77 K and 300 K," *Journal of Applied Physics*, vol. 110, no. 3, p. 033725, 2011.
- [180] A. Zylbersztein and N. F. Mott, "Metal-insulator transition in vanadium dioxide," *Physical Review B*, vol. 11, pp. 4383–4395, jun 1975.
- [181] D. M. Pozar, *Microwave Engineering*. John Wiley & Sons, Inc., 4th ed., 2012.
- [182] S. M. Sze and N. Kwok, *Physics of Semiconductor Devices*. Interscience, 3rd ed., 2006.
- [183] C. Rauscher, "Reconfigurable bandpass filter with a three-to-one switchable passband width," *Microwave Theory and Techniques, IEEE Transactions on*, vol. 51, pp. 573–577, feb 2003.
- [184] F. Mahe, G. Tanne, E. Rius, and C. Person, "Electronically switchable dual-band microstrip interdigital bandpass filter for multistandard communication applications," *European Microwave Conference*, 2000.

Bibliography

- [185] C. Lugo and J. Papapolymerou, "Electronic switchable bandpass filter using PIN diodes for wireless low cost system-on-a-package applications," *IEEE Proceedings - Microwaves, Antennas and Propagation*, vol. 151, no. 6, p. 497, 2004.
- [186] B. Razavi, *RF Microelectronics*. Prentice Hall, 2nd ed., 2012.
- [187] M. Koochakzadeh, "Multi-Scale Tunable Filter Covering a Frequency Range of 6.5:1," *International Microwave Symposium Digest*, pp. 1023–1026, 2008.
- [188] X.-G. Wang, Y.-H. Cho, and S.-W. Yun, "A Tunable Compline Bandpass Filter Loaded With Series Resonator," *Microwave Theory And Techniques, IEEE Transactions on*, pp. 1–8, 2012.
- [189] G. Suo, X. Guo, B. Cao, B. Wei, X. Zhang, T. Zheng, and G. Zhang, "Superconducting Varactor Tunable Filter With Constant Bandwidth Using Coupling Line," *IEEE Microwave and Wireless Components Letters*, vol. 24, pp. 628–630, sep 2014.
- [190] A. Tagantsev, V. Sherman, K. Astafiev, J. Venkatesh, and N. Setter, "Ferroelectric Materials for Microwave Tunable Applications," *Journal of Electroceramics*, vol. 11, pp. 5–66, sep 2003.
- [191] J. Nath, D. Ghosh, J. Maria, A. Kingon, W. Fathelbab, P. Franzon, and M. Steer, "An electronically tunable microstrip bandpass filter using thin-film Barium-Strontium-Titanate (BST) varactors," *IEEE Transactions on Microwave Theory and Techniques*, vol. 53, pp. 2707–2712, sep 2005.
- [192] J. Papapolymerou, C. Lugo, Z. Zhao, X. Wang, and A. Hunt, "A miniature low-loss slow-wave tunable ferroelectric bandpass filter from 11-14 GHz," *Microwave Symposium Digest, 2006. IEEE MTT-S International*, vol. 11, no. 2, pp. 556–559, 2006.
- [193] H. Jiang, B. Lacroix, K. Choi, Y. Wang, A. T. Hunt, and J. Papapolymerou, "Ka- and U-Band Tunable Bandpass Filters Using Ferroelectric Capacitors," *IEEE Transactions on Microwave Theory and Techniques*, vol. 59, pp. 3068–3075, dec 2011.
- [194] D. Kuylenstierna, E. Ash, A. Vorobiev, T. Itoh, and S. Gevorgian, "X-band Left Handed Phase Shifter using Thin Film Ba_{0.25}SR_{0.75}TiO₃ Ferroelectric Varactors," in *2006 European Microwave Conference*, pp. 847–850, IEEE, sep 2006.

- [195] K. Kim, T. Yun, J. Lee, M. Chaker, C. Park, and K. Wu, "Integration of microwave phase shifter with BST varactor onto TiO₂/Si wafer," *Electronics Letters*, vol. 43, no. 14, p. 757, 2007.
- [196] G. M. Rebeiz, *RF MEMS - Theory, Design, and Technology*. John Wiley & Sons, Inc., 2003.
- [197] G. Rebeiz and J. Muldavin, "RF MEMS switches and switch circuits," *IEEE Microwave Magazine*, vol. 2, no. 4, pp. 59–71, 2001.
- [198] a. Verger, a. Pothier, C. Guines, a. Crunteanu, P. Blondy, J.-C. Orlianges, J. Dhenin, a. Broue, F. Courtade, and O. Vendier, "Sub-hundred nanosecond electrostatic actuated RF MEMS switched capacitors," *Journal of Micromechanics and Microengineering*, vol. 20, no. 6, p. 064011, 2010.
- [199] A. Verger, A. Pothier, C. Guines, P. Blondy, O. Vendier, and F. Courtade, "Nanogap MEMS Micro-Relay with 70 ns Switching Speed," *IEEE International Conference on Micro Electro Mechanical Systems*, no. February, pp. 717–720, 2012.
- [200] C. F. Moldovan, W. a. Vitale, P. Sharma, L. Bernard, and A. M. Ionescu, "Fabrication and characterization of graphene RF NEMS capacitive switches," *Microelectronic Engineering*, vol. 145, pp. 5–8, 2015.
- [201] C. Moldovan, W. Vitale, M. Tamagnone, and A. Ionescu, "Graphene RF NEMS shunt switches for analog and digital phase shifters," in *2015 Transducers - 2015 18th International Conference on Solid-State Sensors, Actuators and Microsystems (TRANSDUCERS)*, pp. 2029–2032, IEEE, jun 2015.
- [202] T. Hallam, C. F. Moldovan, K. Gajewski, A. M. Ionescu, and G. S. Duesberg, "Large area suspended graphene for nano-mechanical devices," *physica status solidi (b)*, vol. 252, pp. 2429–2432, nov 2015.
- [203] T. Rijks, J. van Beek, P. Steeneken, M. Ulenaers, J. De Coster, and R. Puers, "RF MEMS tunable capacitors with large tuning ratio," in *17th IEEE International Conference on Micro Electro Mechanical Systems. Maastricht MEMS 2004 Technical Digest*, pp. 777–780, IEEE.
- [204] D. Peroulis and L. Katehi, "Electrostatically-tunable analog RF MEMS varactors with measured capacitance range of 300%," in *IEEE MTT-S International Microwave Symposium Digest, 2003*, vol. 3, pp. 1793–1796, IEEE.

Bibliography

- [205] Q. Ma, Q. Tran, T.-K. A. Chou, J. Heck, H. Bar, R. Kant, and V. Rao, "Metal contact reliability of RF MEMS switches," in *Proc. SPIE 6463, Reliability, Packaging, Testing, and Characterization of MEMS/MOEMS VI, 646305 (January 19, 2007)*; doi:10.1117/12.702177 (A. L. Hartzell and R. Ramesham, eds.), p. 646305, jan 2007.
- [206] M. Fernandez-Bolanos, D. Tsamados, P. Dainesi, and A. M. Ionescu, "Reliability of RF MEMS Capacitive Switches and Distributed MEMS Phase Shifters using AlN Dielectric," in *2009 IEEE 22nd International Conference on Micro Electro Mechanical Systems*, pp. 638–641, IEEE, jan 2009.
- [207] Y. Chiou and G. Rebeiz, "A Quasi Elliptic Function 1.75–2.25 GHz 3-Pole Bandpass Filter With Bandwidth Control," *Microwave Theory and Techniques, IEEE Transactions on*, vol. 60, no. 99, pp. 1–1, 2012.
- [208] C.-c. Cheng and G. M. Rebeiz, "High-Q 4–6-GHz Suspended Stripline RF MEMS Tunable Filter With Bandwidth Control," *IEEE Transactions on Microwave Theory and Techniques*, vol. 59, no. 10, pp. 2469–2476, 2011.
- [209] Y. Chiou and G. M. Rebeiz, "A Tunable Three-Pole 1.5-2.2-GHz Bandpass Filter With Bandwidth and Transmission Zero Control," *IEEE Transactions on Microwave Theory and Techniques*, vol. 59, no. 11, pp. 2872–2878, 2011.
- [210] N. Zahirovic, S. Fouladi, R. R. Mansour, and M. Yu, "Tunable suspended substrate stripline filters with constant bandwidth," *2011 IEEE MTT-S International Microwave Symposium*, pp. 1–1, jun 2011.
- [211] N. Zhang, Z. Deng, and C. Shu, "Design and Analysis of a Tunable Bandpass Filter Employing RF MEMS Capacitors," *IEEE Electron Device Letters*, vol. 32, no. 10, pp. 1460–1462, 2011.
- [212] M. El-Tanani and G. M. Rebeiz, "High-Performance 1.5-2.5-GHz RF-MEMS Tunable Filters for Wireless Applications," *IEEE Transactions on Microwave Theory and Techniques*, vol. 58, no. 6, pp. 1629–1637, 2010.
- [213] F. Dumas-Bouchiat, C. Champeaux, A. Catherinot, A. Crunteanu, and P. Blondy, "Rf-microwave switches based on reversible semiconductor-metal transition of VO₂ thin films synthesized by pulsed-laser deposition," *Applied Physics Letters*, vol. 91, no. 22, p. 223505, 2007.

- [214] S. D. Ha, Y. Zhou, C. J. Fisher, S. Ramanathan, and J. P. Treadway, "Electrical switching dynamics and broadband microwave characteristics of VO₂ radio frequency devices," *Journal of Applied Physics*, vol. 113, pp. 1–25, 2013.
- [215] C. Hillman, P. Stupar, J. B. Hacker, Z. Griffith, M. Field, and M. Rodwell, "An ultra-low loss millimeter-wave solid state switch technology based on the metal - insulator - transition of vanadium dioxide," in *2014 IEEE MTT-S International Microwave Symposium (IMS2014)*, pp. 1–4, IEEE, jun 2014.
- [216] J. Givernaud, C. Champeaux, A. Catherinot, A. Pothier, P. Blondy, and A. Crunteanu, "Tunable band stop filters based on metal-insulator transition in vanadium dioxide thin films," in *Microwave Symposium Digest, 2008 IEEE MTT-S International*, pp. 1103–1106, 2008.
- [217] A. Crunteanu, J. Givernaud, C. Champeaux, A. Catherinot, A. Pothier, and P. Blondy, "Integration of VO₂ thin films presenting a semiconductor-to-metal phase transition for fabrication of microwave switches and tunable filters," in *French Symposium on Emerging Technologies for Micro-nanofabrication*, 2008.
- [218] D. Bouyge, A. Crunteanu, J.-C. Orlianges, D. Passerieux, C. Champeaux, A. Catherinot, A. Velez, J. Bonache, F. Martin, and P. Blondy, "Reconfigurable bandpass filter based on split ring resonators and vanadium dioxide (VO₂) microwave switches," *2009 Asia Pacific Microwave Conference*, pp. 2332–2335, dec 2009.
- [219] D. Bouyge and A. Crunteanu, "Applications of vanadium dioxide (VO₂)-loaded electrically small resonators in the design of tunable filters," in *European Microwave Conference, 2010*, no. September, pp. 822–825, 2010.
- [220] T. Teeslink, D. Torres, J. Ebel, N. Sepulveda, and D. Anagnostou, "Reconfigurable Bowtie Antenna using Metal-Insulator Transition in Vanadium Dioxide.," *IEEE Antennas and Wireless Propagation Letters*, vol. 1225, no. c, pp. 1–1, 2015.
- [221] S. D. Ha, Y. Zhou, C. J. Fisher, S. Ramanathan, and J. P. Treadway, "Abrupt Insertion Loss Drop by RF-Triggering of the Phase Transition in VO₂ CPW Switches," *IEEE Microwave and Wireless Components Letters*, vol. 24, pp. 575–577, aug 2014.

Bibliography

- [222] M. Fernandez-Bolanos, J. Perruisseau-Carrier, P. Dainesi, and A. Ionescu, "RF MEMS capacitive switch on semi-suspended CPW using low-loss high-resistivity silicon substrate," *Microelectronic Engineering*, vol. 85, pp. 1039–1042, may 2008.
- [223] R. N. Simons, *Coplanar Waveguide Circuits, Components, and Systems*. Wiley Series in Microwave and Optical Engineering, New York, USA: John Wiley & Sons, Inc., mar 2001.
- [224] G. L. Matthaei, *Microwave Filters, Impedance-Matching Networks, and Coupling Structures*. House, Artech, 1964.
- [225] R. Mongia, I. J. Bahl, P. Bhartia, and J. Hong, "RF AND MICROWAVE COUPLED-LINE CIRCUITS," ch. 9, Artech House, 1999.
- [226] J. Hong and M. Lancaster, *Microstrip filters for RF and microwave applications*. John Wiley & Sons Inc, 2011.
- [227] E. Hamad, A. Safwat, and A. Omar, "Controlled capacitance and inductance behaviour of L-shaped defected ground structure for coplanar waveguide," *IEE Proceedings - Microwaves, Antennas and Propagation*, vol. 152, no. 5, p. 299, 2005.
- [228] M. Karim, A. Liu, A. Alphones, X. Zhang, and A. Yu, "CPW band-stop filter using unloaded and loaded EBG structures," *IEE Proceedings on Microwaves, Antennas and Propagation*, vol. 152, no. 6, pp. 434–440, 2005.
- [229] M. F. Karim, A.-q. Liu, A. Alphones, and A. Yu, "A reconfigurable micromachined switching filter using periodic structures," *IEEE Transactions on Microwave Theory and Techniques*, vol. 55, no. 6, pp. 1154–1162, 2007.
- [230] A. Safwat, F. Podevin, P. Ferrari, and A. Vilcot, "Tunable bandstop defected ground structure resonator using reconfigurable dumbbell-shaped coplanar waveguide," *IEEE Transactions on Microwave Theory and Techniques*, vol. 54, no. 9, pp. 3559–3564, 2006.
- [231] M. F. Karim, A. Q. Liut, A. Alphones, and A. B. Yu, "A Novel Reconfigurable Filter Using Periodic Structures," *International Microwave Symposium Digest*, pp. 943–946, 2006.

- [232] Y.-L. Lai and P.-Y. Cheng, "CPW Filters with Defected Ground Structures for RF and Microwave Applications," in *Proceedings of the 9th Joint Conference on Information Sciences (JCIS)*, (Paris, France), Atlantis Press, 2006.
- [233] M.-L. Her, Y.-Z. Wang, C.-M. Chang, and K.-Y. Lin, "Coplanar waveguide (CPW) defected ground structure (DGS) for bandpass filter application," *Microwave and Optical Technology Letters*, vol. 42, pp. 331–334, aug 2004.
- [234] J. Lim, C. Kim, Y. Lee, D. Ahn, and S. Nam, "A spiral-shaped defected ground structure for coplanar waveguide," *Microwave and Wireless Components Letters*, vol. 12, no. 9, pp. 330–332, 2002.
- [235] M. F. Karim, A.-Q. Liu, A. Yu, and A. Alphones, "Micromachined tunable filter using fractal electromagnetic bandgap (EBG) structures," *Sensors and Actuators A: Physical*, vol. 133, pp. 355–362, feb 2007.
- [236] H. Liu, T. Yoshimasu, and L. Sun, "CPW bandstop filter using periodically loaded slot resonators," *Electronics Letters*, vol. 42, no. 6, p. 352, 2006.
- [237] Jia-Sheng Hong and B. Karyamapudi, "A general circuit model for defected ground structures in planar transmission lines," *IEEE Microwave and Wireless Components Letters*, vol. 15, pp. 706–708, oct 2005.
- [238] A. Joushaghani, B. a. Kruger, S. Paradis, D. Alain, J. Stewart Aitchison, and J. K. S. Poon, "Sub-volt broadband hybrid plasmonic-vanadium dioxide switches," *Applied Physics Letters*, vol. 102, no. 6, p. 061101, 2013.
- [239] H. Obloh, W. Muller-Sebert, D. Brink, W. Fehrenbach, C. Nebel, C. Wild, and E. Worner, "Matrix-addressable infrared filters for the protection of highly sensitive detectors," in *2011 Defense Science Research Conference and Expo (DSR)*, pp. 1–5, IEEE, aug 2011.
- [240] P. Bhattacharyya, "Technological Journey Towards Reliable Microheater Development for MEMS Gas Sensors: A Review," *IEEE Transactions on Device and Materials Reliability*, vol. 14, pp. 589–599, jun 2014.
- [241] M. Tamagnone, A. Fallahi, J. R. Mosig, and J. Perruisseau-Carrier, "Fundamental limits and near-optimal design of graphene modulators and non-reciprocal devices," *Nature Photonics*, vol. 8, pp. 556–563, may 2014.

Bibliography

- [242] M. Tamagnone, S. Capdevila, H. Hasani, P. Romano, A. Skrivervik, J. Perruisseau-Carrier, J. R. Mosig, W. A. Vitale, C. Moldovan, and A. M. Ionescu, "Performance evaluation of novel technologies for terahertz reflectarrays," in *2015 10th European Microwave Integrated Circuits Conference (EuMIC)*, pp. 393–396, IEEE, sep 2015.
- [243] H. Park, E. P. J. Parrott, F. Fan, M. Lim, H. Han, V. G. Chigrinov, and E. Pickwell-MacPherson, "Evaluating liquid crystal properties for use in terahertz devices," *Optics Express*, vol. 20, no. 11, p. 11899, 2012.
- [244] Y. Yashchyshyn, K. Derzakowski, and P. Bajurko, "Reconfigurable Semiconductor Antenna for sub-THz Frequencies," No. Antennas and Propagation (EuCAP), 2013 7th European Conference on, pp. 537–540, 2013.
- [245] H.-T. Chen, W. J. Padilla, M. J. Cich, A. K. Azad, R. D. Averitt, and A. J. Taylor, "A metamaterial solid-state terahertz phase modulator," *Nature Photonics*, vol. 3, no. 3, pp. 148–151, 2009.
- [246] M. Kafesaki, N. H. Shen, S. Tzortzakis, and C. M. Soukoulis, "Optically switchable and tunable terahertz metamaterials through photoconductivity," *Journal of Optics*, vol. 14, no. 11, p. 114008, 2012.
- [247] J. Gomez-Diaz, C. Moldovan, S. Capdevila, J. Romeu, L. Bernard, A. Magrez, A. Ionescu, and J. Perruisseau-Carrier, "Self-biased reconfigurable graphene stacks for terahertz plasmonics," *Nature Communications*, vol. 6, p. 6334, mar 2015.
- [248] D. H. Auston, K. P. Cheung, and P. R. Smith, "Picosecond Photoconducting Hertzian Dipoles," *Applied Physics Letters*, vol. 45, no. 3, pp. 284–286, 1984.
- [249] D. Auston and M. Nuss, "Electrooptical generation and detection of femtosecond electrical transients," *IEEE Journal of Quantum Electronics*, vol. 24, no. 2, pp. 184–197, 1988.
- [250] M. C. Nuss, P. M. Mankiewich, M. L. O'Malley, E. H. Westerwick, and P. B. Littlewood, "Dynamic conductivity and coherence peak in YBa₂Cu₃O₇ superconductors," *Physical Review Letters*, vol. 66, pp. 3305–3308, jun 1991.
- [251] M. Nuss and J. Orenstein, *Millimeter and Submillimeter Wave Spectroscopy in Solids*. Springer-Verlag, Berlin Heidelberg New York, 1998.

-
- [252] P. Y. Han, M. Tani, M. Usami, S. Kono, R. Kersting, and X.-C. Zhang, "A direct comparison between terahertz time-domain spectroscopy and far-infrared Fourier transform spectroscopy," *Journal of Applied Physics*, vol. 89, no. 4, p. 2357, 2001.
- [253] Q. Shi, W. Huang, T. Lu, Y. Zhang, F. Yue, S. Qiao, and Y. Xiao, "Nanostructured VO₂ film with high transparency and enhanced switching ratio in THz range," *Applied Physics Letters*, vol. 104, no. 7, p. 071903, 2014.
- [254] D. J. Hilton, R. P. Prasankumar, S. Fourmaux, a. Cavalleri, D. Brassard, M. a. El Khakani, J. C. Kieffer, a. J. Taylor, and R. D. Averitt, "Enhanced photosusceptibility near T_c for the light-induced insulator-to-metal phase transition in vanadium dioxide," *Physical Review Letters*, vol. 99, no. November, pp. 1–4, 2007.
- [255] Z. J. Thompson, A. Stickel, Y.-G. Jeong, S. Han, B. H. Son, M. J. Paul, B. Lee, A. Mousavian, G. Seo, H.-T. Kim, Y.-S. Lee, and D.-S. Kim, "Terahertz-Triggered Phase Transition and Hysteresis Narrowing in a Nanoantenna Patterned Vanadium Dioxide Film," *Nano Letters*, vol. 15, no. 9, pp. 5893–5898, 2015.
- [256] S. Vegesna, Y. Zhu, Y. Zhao, Z. Fan, A. Bernussi, and M. Saed, "Terahertz frequency selective surface with reconfigurable polarization characteristics using vanadium dioxide," *Journal of Electromagnetic Waves and Applications*, vol. 28, pp. 83–90, jan 2014.
- [257] J.-H. Shin, K. Moon, E. S. Lee, I.-M. Lee, and K. Hyun Park, "Metal-VO₂ hybrid grating structure for a terahertz active switchable linear polarizer," *Nanotechnology*, vol. 26, no. 31, p. 315203, 2015.
- [258] T. Driscoll, S. Palit, M. M. Qazilbash, M. Brehm, F. Keilmann, B.-G. Chae, S.-J. Yun, H.-T. Kim, S. Y. Cho, N. M. Jokerst, D. R. Smith, and D. N. Basov, "Dynamic tuning of an infrared hybrid-metamaterial resonance using vanadium dioxide," *Applied Physics Letters*, vol. 93, no. 2, p. 024101, 2008.
- [259] Y. Zhu, S. Vegesna, Y. Zhao, V. Kuryatkov, M. Holtz, Z. Fan, M. Saed, and A. a. Bernussi, "Tunable dual-band terahertz metamaterial bandpass filters.," *Optics letters*, vol. 38, pp. 2382–4, jul 2013.
- [260] M. Seo, J. Kyoung, H. Park, S. Koo, H.-s. Kim, H. Bernien, B. J. Kim, J. H. Choe, Y. H. Ahn, H.-T. Kim, N. Park, Q.-H. Park, K. Ahn, and D.-s. Kim, "Active terahertz

Bibliography

- nanoantennas based on VO₂ phase transition.,” *Nano letters*, vol. 10, pp. 2064–8, jun 2010.
- [261] Y.-G. Jeong, H. Bernien, J.-S. Kyoung, H.-R. Park, H.-S. Kim, J.-W. Choi, B.-J. Kim, H.-T. Kim, K. J. Ahn, and D.-S. Kim, “Electrical control of terahertz nano antennas on VO₂ thin film.,” *Optics express*, vol. 19, pp. 21211–5, oct 2011.
- [262] Y.-G. Jeong, S. Han, J. Rhie, J.-S. Kyoung, J.-W. Choi, N. Park, S. Hong, B.-J. Kim, H.-T. Kim, and D.-S. Kim, “A Vanadium Dioxide Metamaterial Disengaged from Insulator-to-Metal Transition,” *Nano Letters*, vol. 15, pp. 6318–6323, oct 2015.
- [263] S. Capdevila, *RFID Multiantenna Systems for Wireless Communications and Sensing*. PhD thesis, Universitat Politècnica de Catalunya, 2013.
- [264] J. C. Bolomey, S. Capdevila, L. Jofre, and J. Romeu, “Electromagnetic Modeling of RFID-Modulated Scattering Mechanism. Application to Tag Performance Evaluation,” *Proceedings of the IEEE*, vol. 98, pp. 1555–1569, sep 2010.
- [265] M. Abou-Khousa and R. Zoughi, “Multiple Loaded Scatterer Method for E-Field Mapping Applications,” *IEEE Transactions on Antennas and Propagation*, vol. 58, pp. 900–907, mar 2010.
- [266] M. T. Ghasr, M. a. Abou-Khousa, S. Kharkovsky, R. Zoughi, and D. Pommerenke, “Portable Real-Time Microwave Camera at 24 GHz,” *IEEE Transactions on Antennas and Propagation*, vol. 60, pp. 1114–1125, feb 2012.

WOLFGANG AMADEUS VITALE – LIST OF PUBLICATIONS

JOURNAL PAPERS

- [1] **W. A. Vitale**[†], M. Tamagnone[†], N. Émond, B. Le Drogoff, S. C. Capdevila, A. Skrivervik, M. Chaker, J. R. Mosig, and A. M. Ionescu, “Terahertz modulated scatterer technique enabled by current actuated vanadium dioxide switches,” *Applied Physics Letters*, under review, 2016, [† equal contributions](#).
- [2] **W. A. Vitale**, L. Petit, C. F. Moldovan, M. Fernández-Bolaños, A. Paone, A. Schüler, and A. M. Ionescu, “Electrothermal actuation of vanadium dioxide for tunable capacitors and microwave filters with integrated microheaters,” *Sensors and Actuators A: Physical*, Jan. 2016, doi: 10.1016/j.sna.2016.01.027
- [3] C.F. Moldovan[†], **W. A. Vitale**[†], P. Sharma, M. Tamagnone, J. R. Mosig, and A. M. Ionescu, “Graphene quantum capacitors for high frequency tunable analog applications,” *Nano Letters*, under review, 2016, [† equal contributions](#).
- [4] **W. A. Vitale**, C. F. Moldovan, M. Tamagnone, A. Paone, A. Schuler, and A. M. Ionescu, “Steep-Slope Metal–Insulator-Transition VO₂ Switches With Temperature-Stable High ION,” *IEEE Electron Device Letters*, vol. 36, no. 9, pp. 972–974, Sep. 2015, doi: 10.1109/LED.2015.2454535
- [5] **W. A. Vitale**, C. F. Moldovan, A. Paone, A. Schüler, and A. M. Ionescu, “Fabrication of CMOS-compatible abrupt electronic switches based on vanadium dioxide,” *Microelectronic Engineering*, vol. 145, pp. 117–119, Sep. 2015, doi: 10.1016/j.mee.2015.03.055
- [6] C. F. Moldovan, **W. A. Vitale**, P. Sharma, L. Bernard, and A. M. Ionescu, “Fabrication and characterization of graphene RF NEMS capacitive switches,” *Microelectronic Engineering*, vol. 145, pp. 5–8, 2015, doi: 10.1016/j.mee.2015.01.032
- [7] M. Maqueda López, M. Fernández-Bolaños, **W. A. Vitale**, and A. M. Ionescu, “Solid-gap wine-glass mode disks VB-FET resonators applied to biomass sensing,” *Microelectronic Engineering*, vol. 145, pp. 53–57, Sep. 2015, doi: 10.1016/j.mee.2015.03.005
- [8] M. Mohamed, Z. Aksamija, **W. A. Vitale**, F. Hassan, K. H. Park, and U. Ravaioli, “A conjoined electron and thermal transport study of thermal degradation induced during normal operation of multigate transistors,” *IEEE Transactions on Electron Devices*, vol. 61, no. 4, pp. 976–983, 2014, doi: 10.1109/TED.2014.2306422

CONFERENCE PAPERS

- [9] M. Tamagnone, S. Capdevila, H. Hasani, **W. A. Vitale**, C. Moldovan, A. M. Ionescu, A. Skrivervik, J. R. Mosig, “Novel Technologies for Fixed and Tuneable Terahertz Reflectarrays”, [oral presentation in 10th European Conference on Antennas and Propagation \(EuCAP\)](#), Davos, Switzerland, 2016, accepted.
- [10] M. Tamagnone, S. Capdevila, H. Hasani, P. Romano, A. Skrivervik, J. Perruisseau-carrier, J. R. Mosig, **W. A. Vitale**, C. F. Moldovan, and A. M. Ionescu, “Performance evaluation of novel technologies for terahertz reflectarrays,” [oral presentation in 45th European Microwave Conference](#), 2015, doi: 10.1109/EuMIC.2015.7345152.
- [11] **W. A. Vitale**, M. Fernandez-Bolanos, C. F. Moldovan, A. Paone, A. Schuler, and A. M. Ionescu, “Tunable capacitors and microwave filters based on vanadium dioxide metal-insulator

- transition,” [oral presentation in 18th International Conference on Solid-State Sensors, Actuators and Microsystems \(TRANSDUCERS\)](#), pp. 311–314, 2015, doi: 10.1109/TRANSDUCERS.2015.7180923
- [12] C. F. Moldovan, **W. A. Vitale**, M. Tamagnone, and A. M. Ionescu, “Graphene RF NEMS shunt switches for analog and digital phase shifters,” [in 18th International Conference on Solid-State Sensors, Actuators and Microsystems \(TRANSDUCERS\)](#), pp. 2029–2032, 2015, doi: 10.1109/TRANSDUCERS.2015.7181354
- [13] **W. A. Vitale**, M. Fernandez-Bolanos, A. Klumpp, J. Weber, P. Ramm, and A. M. Ionescu, “Ultra fine-pitch TSV technology for ultra-dense high-Q RF inductors,” [oral presentation in 2015 Symposium on VLSI Technology \(VLSI Technology\)](#), pp. T52–T53, 2015, doi: 10.1109/VLSIT.2015.7223700
- [14] **W. A. Vitale**, M. Fernandez-Bolanos, R. Merkel, A. Enayati, I. Ocket, W. De Raedt, J. Weber, P. Ramm, and A. M. Ionescu, “Fine pitch 3D-TSV based high frequency components for RF MEMS applications,” [oral presentation in 2015 IEEE 65th Electronic Components and Technology Conference \(ECTC\)](#), 2015, doi: 10.1109/ECTC.2015.7159650
- [15] C. F. Moldovan, K. Gajewski, M. Tamagnone, R. S. Weatherup, H. Sugime, A. Szumska, **W. A. Vitale**, J. Robertson, and A. M. Ionescu, “Spatial variability in large area single and few-layer CVD graphene,” [oral presentation in EUROSOI-ULIS 2015: 2015 Joint International EUROSOI Workshop and International Conference on Ultimate Integration on Silicon](#), pp. 85–88, 2015, doi: 10.1109/ULIS.2015.7063779.
- [16] **W. A. Vitale**, C. F. Moldovan, A. Paone, A. Schuler, and A. M. Ionescu, “CMOS-compatible abrupt switches based on VO₂ metal-insulator transition,” [oral presentation in EUROSOI-ULIS 2015: 2015 Joint International EUROSOI Workshop and International Conference on Ultimate Integration on Silicon](#), pp. 53–56, 2015, doi: 10.1109/ULIS.2015.7063771
- [17] C. F. Moldovan, **W. A. Vitale**, P. Sharma, J. Perruisseau Carrier, and A. M. Ionescu, “Fabrication and characterization of graphene RF NEMS capacitive switches,” [40th Micro and Nano Engineering](#), 2014
- [18] **W. A. Vitale**, A. Paone, C. F. Moldovan, A. Schuler, and A. M. Ionescu, “Growth optimization of vanadium dioxide films on SiO₂/Si substrates,” [oral presentation in 40th Micro and Nano Engineering](#), 2014
- [19] **W. A. Vitale**, A. Paone, M. Fernandez-Bolanos, A. Bazigos, W. Grabinski, A. Schuler, and A. M. Ionescu, “Steep slope VO₂ switches for wide-band (DC-40 GHz) reconfigurable electronics,” [oral presentation in 72nd Device Research Conference](#), pp. 29–30, 2014, doi: 10.1109/DRC.2014.6872284
- [20] C. F. Moldovan, **W. A. Vitale**, P. Sharma, J. Perruisseau-Carrier, and A. M. Ionescu, “RF NEMS Based on Suspended Graphene Structures,” [oral presentation in 4th National Conference on Nano- and Micromechanics](#), 2014.
- [21] **W. A. Vitale**, M. Fernandez-Bolanos, A. Bazigos, C. Dehollain, and A. M. Ionescu, “RF MEMS power sensors for ultra-low power wake-up circuit applications,” [oral presentation in 2013 Proceedings of the European Solid-State Device Research Conference \(ESSDERC\)](#), pp. 288–291, 2013, doi: 10.1109/ESSDERC.2013.6818875
- [22] R. Gueye, S. W. Lee, **W. A. Vitale**, S. Truax, T. Akiyama, C. Roman, A. Ionescu, C. Hierold, D. Briand, and N. F. De Rooij, “RF-TSVs compatible with harsh-environment post-processing for ‘via-first’ 3D integration,” [in 2013 Transducers and Eurosensors XXVII: The 17th International Conference on Solid-State Sensors, Actuators and Microsystems, TRANSDUCERS and EUROSensors 2013](#), pp. 830–833, 2013, doi: 10.1109/Transducers.2013.6626895

- [23] M. Mohamed, Z. Aksamija, and **W. A. Vitale**, “Interplay between the Electrical and Thermal Transport of Silicon Nanoscale MOSFETs,” in [International Conference on Semiconductor Processes and Devices \(SISPAD\)](#), pp. 372–375, 2012.
- [24] **W. A. Vitale**, M. Fernández-Bolaños, and A. M. Ionescu, “High-Q 3D Embedded Inductors using TSV for RF MEMS Tunable Bandpass Filters (4.65-6.8 GHz),” in [Microwave Conference \(EuMC\), 2012 42nd European](#), 2012.
- [25] J. Cao, **W. A. Vitale**, and A. M. Ionescu, “Self-assembled nano-electro-mechanical tri-state carbon nanotube switches for reconfigurable integrated circuits,” [oral presentation in 2012 IEEE 25th International Conference on Micro Electro Mechanical Systems \(MEMS\)](#), pp. 188–191, 2012, doi: 10.1109/MEMSYS.2012.6170148
- [26] **W. A. Vitale**, M. Mohamed, and U. Ravaioli, “Monte Carlo study of transport properties in junctionless transistors,” in [2010 14th International Workshop on Computational Electronics](#), 2010, doi: 10.1109/IWCE.2010.5677969

Wolfgang Amadeus Vitale

- PhD from EPFL in microsystems and microelectronics.
- Results driven, goal oriented, fast learner, versatile.
- Proven professional proficiency in English, French and Italian.
- Broad experience in micro/nanoelectronics for computing/sensing/RF applications (5+ years design/characterization, 2+ years fabrication).

Av. Jomini 13 p/o J. Vioget
CH-1018, Lausanne
+41 78 622 1305
wolfgang.vitale@gmail.com



EXPERIENCE

Research Scientist: advanced materials for reconfigurable electronics

Swiss Federal Institute of Technology in Lausanne (EPFL)

CH

June 2011 – present

Vanadium Dioxide (VO₂) devices for reconfigurable electronics

- I identified a new material for reconfigurable electronics and introduced it among the main research activities in my group, leading to a European project proposal (acceptance pending).
- I designed, fabricated and characterized devices with novel functionalities and/or state-of-the-art performance exploiting a new material with no standard fabrication processes.

FP7 European project “e-Brains” (15.25 million € budget, 20 partners)

- I had the main role in the design and characterization of state-of-the-art RF devices leading to excellent results for my work package.

FP7 European project “Grafol” (6.9 million € budget, 14 partners)

- I obtained different roles in different groups (design, simulation, fabrication, characterization), according to what was more needed to reach the specified goals. My contributions led to the implementation of novel devices such as graphene NEMS capacitive switches and quantum varactors.

RF MEMS power sensors

- I found a way to exploit previously fabricated devices for a new, more fruitful purpose.

Visiting Researcher: developing a self-consistent thermoelectric 3D Monte Carlo simulator

University of Illinois at Urbana-Champaign (UIUC)

USA

Feb. 2010 – Nov. 2010

- I introduced new key features in the state-of-the-art Monte Carlo simulator developed at UIUC.
- I achieved proficient use of 2 new programming languages in the first month of the project.

Visiting Researcher: developing an algorithm for 3D localization of neurons from MEA recordings

Imperial College London (ICL)

UK

Jun. 2009 – Sept. 2009

- I managed in less than 3 months to obtain a background in neuroscience, learn a new programming language and develop a general-purpose simulation tool for my research group.

EDUCATION

PhD in Microsystems and Microelectronics

Swiss Federal Institute of Technology in Lausanne (EPFL)

CH

June 2011 – Feb. 2016

- 20+ technical articles in peer-reviewed journal and selective international conferences: bit.ly/20Pbsgr

M.Sc. in Micro and Nanotechnologies for Integrated Systems

Swiss Federal Institute of Technology in Lausanne (EPFL), Grenoble
Institute of Technology (INPG), Polytechnic University of Turin (POLITO)

CH/FR/IT

Sept. 2008 – Sept. 2010

- First in his class regarding grades, admitted after competitive entrance exam.

B.Sc. in Information Technology Engineering

Grenoble Institute of Technology (INPG), Polytechnic University of Turin (POLITO)

IT/FR Sept. 2005 – Feb. 2008

- First in his class regarding grades, admitted after competitive entrance exam.

SKILLS

Micro/Nanofabrication of electronic devices in cleanroom environment.

- Photolithography, electron-beam (e-beam) lithography; sputtering growth optimization, e-beam evaporation, atomic layer deposition (ALD); dry and wet etching; rapid thermal annealing.

Electrical, optical and structural characterization.

- Semiconductor parameter analyzer, impedance analyzer, LCR meter, spectrum analyzer, vector network analyzer, cryogenic measurements.
- Ellipsometer, Fourier Transform Infrared Spectroscopy (FTIR).
- Scanning electron microscope (SEM), focused-ion beam (FIB), atomic force microscopy (AFM).

Programming languages.

- Developed projects in MATLAB, Fortran, C, Java, VHDL, NEURON.
- Experience with ADA, SQL, Python.
- Good knowledge of UNIX shell scripting.

Engineering CAD and software.

- Developed projects in HFSS, COMSOL, ADS, Momentum.
- Experience with Cadence Virtuoso platform, Modelsim, Synopsis Design Vision, Synopsis TCAD, Coventorware, Cadence OrCad, Ansys Multiphysics.

LANGUAGES

Italian: mother tongue

English: full professional proficiency

French: full professional proficiency

German: basic knowledge, willing to learn

Spanish: professional working proficiency

AWARDS

- **"Gilbert Hausmann Award"** nomination, as one of the best PhD theses defended at EPFL from Sept. 2015 to Oct. 2016.
- **"Premio Optime"** by the Unione Industriale di Torino as one of the best graduates of the city (over about 100.000 students) in 2011.

PERSONAL INFORMATION

- Italian nationality with Swiss B EU permit.

